Search for the $K_L \to \pi^0 \nu \bar{\nu}$ Decay with 3.3×10^{19} Protons on Target at the J-PARC KOTO Experiment

Ryota Shiraishi

Department of Physics, Graduate School of Science,
The University of Osaka

May 30, 2025

Abstract

This thesis describes the latest search for the rare decay of the neutral kaon, $K_L \to \pi^0 \nu \bar{\nu}$, at the J-PARC KOTO experiment. The branching ratio of the $K_L \to \pi^0 \nu \bar{\nu}$ decay is highly suppressed in the Standard Model (SM), and thus is one of the excellent probes to search for new physics beyond the SM.

The previous data analysis performed in the KOTO experiment using the dataset collected from 2016 to 2018 revealed two new background sources from $K^\pm$ decays and beam-halo $K_L \to 2\gamma$ decays. In this analysis, three signal candidate events were observed in the signal region, which is statistically consistent with the estimated number of background events of 1.22 ± 0.26.

The analysis described in this thesis was based on data collected in 2021 which corresponds to 3.3×10^{19} protons on target. In order to suppress the $K^\pm$ background events, a charged-particle detector was newly developed and installed before the data-taking in 2021. The detector aimed to reject the $K^\pm$ background events by detecting the $K^\pm$ entering the KOTO detector. Using a control sample of $K^\pm$ events collected in 2021, $K^\pm$ detection inefficiency of the charged-particle detector was estimated to be $(7.8^{+0.6}_{-5.2}) \times 10^{-2}$, which reduced the $K^\pm$ background events by a factor of 13. In addition, new event-selection methods were introduced to the $K_L \to \pi^0 \nu \bar{\nu}$ analysis to reduce the beam-halo $K_L \to 2\gamma$ background events. Moreover, a readout method of the electromagnetic calorimeter was upgraded and a new downstream detector was installed, both of which improved suppression of other background events. We achieved a single event sensitivity of $(9.31 \pm 0.06_{\mathrm{stat}} \pm 0.83_{\mathrm{syst}}) \times 10^{-10}$ for the $K_L \to \pi^0 \nu \bar{\nu}$ decay while keeping the expected number of background events to be $0.252 \pm 0.055|_{\mathrm{stat}}{}^{+0.052}_{-0.067}|_{\mathrm{syst}}$. We observed no signal candidate events in the signal region, and set an upper limit on the branching ratio for $K_L \to \pi^0 \nu \bar{\nu}$ as 2.2×10^{-9} at the 90% confidence level. This result improved the previous best limit by a factor of 1.4. We also performed the analysis to search for the $K_L \to \pi^0 X^0$ decay, where X^0 is an invisible particle. Using the same dataset, we obtained an upper limit on the branching ratio for $K_L \to \pi^0 X^0$ as 1.6×10^{-9} at the 90% confidence level for the X^0 mass of $135\,\mathrm{MeV}/c^2$, which also improved the previous limit by a factor of 1.4.

Acknowledgements

I would like to express my deep gratitude to my supervisors, professor Hajime Nanjo and professor emeritus Taku Yamanaka, for guiding me to the field of high energy physics. Their consistent advice on my study, career decision, and any other things that I encountered always helped me to take the first step. I would also like to express my gratitude to associate professor Tatsuya Masubuchi and assistant professor Minoru Hirose for giving me valuable feedback on my research and presentation from the standpoint of non-collaborators.

My thesis was supported by many people from the KOTO collaboration. I would like to appreciate the spokesperson of the KOTO experiment, Tadashi Nomura, for always clarifying a path forward during the analysis. I am deeply grateful to Koji Shiomi for his kind help with anything I asked for.

I would like to express my gratitude to professor Yau W. Wah for giving me the opportunity to stay at the University of Chicago and work with colleagues there. I would also like to express my gratitude to Yu-Chen Tung and Chieh Lin for their kind support in my study. They helped me a lot in understanding detailed work in the analysis. I would like to thank Mario Gonzalez and Joseph Redeker for being the Ph.D. colleagues in the KOTO experiment. Working with you two often helped me mentally and inspired me to continue my research. I would also like to express my thanks to the DAQ group. I always keep in mind that any physics results are outcomes of the stable data-acquisition system.

I would also like to acknowledge the past collaborators, Nobuhiro Shimizu and Satoshi Shinohara. They always helped me a lot even after they left the collaboration. Their pieces of advice for me, particularly in the data analysis, were priceless, as I did not have a senior colleague (*senpai*) close to me during my doctoral program. I would also like to express my special thanks to Yuya Noichi and Taylor Cassidy Nunes, whom I shared the same time with during my master's program. Their work literally contributed to the achievement in the KOTO experiment and helped my thesis significantly as well. I could not have completed it without their studies.

I would like to express my gratitude to the members of the Nanjo group and the former Yamanaka group. In particular, my special thanks go to Lakmin Wickremasinghe for being a colleague in the lab for seven years. Sitting at the desk next to you, having conversations, and encouraging each other during this long journey have become one of the most valuable experiences in my life. My gratitude also goes to the secretaries, Chie Fujisaka, Yuka Nakano, Junko Maeda, and Kiyoko Kiyokawa, for their considerate support during my life at university.

I would like to express my acknowledgements to the Pioneering Quantum Beam Application (PQBA) program and the Support for Pioneering Research Initiated by the Next Generation (SPRING) for financial support through my graduate research. Without these supports, I might not have been able to continue my Ph.D. research.

Finally, I would like to express my deep gratitude to my family. They always respected my decisions on an educational and career path, and supported my life consistently.

Ryota Shiraishi
Osaka, Japan
June, 2025

Contents

List of Figures

List of Tables

Chapter 1

Introduction

The Standard Model (SM) of particle physics describes the nature of elementary particles and interactions between them. It has succeeded to give reasonable explanations to various kinds of experimental observations to date. There are, however, several fundamental questions that still remain mysteries. For instance, one of the biggest questions is what brought about baryon asymmetry of the universe, that is, why matter dominates the universe we see today and antimatter almost disappeared. Cosmology based on the Big Bang nucleosynthesis theory and the observation of the cosmic microwave background have revealed that the current universe originated from an excess of $O(10^{-9})$ of matter over antimatter in the early universe [1, 2]. One of the conditions to be satisfied for generating this baryon asymmetry is the violation of CP-symmetry (CP-violation). Although the CP-violation is incorporated in the SM, the size of the violation is not enough to explain the baryon asymmetry of the universe.

To elucidate such remaining issues, particle physicists have been trying to find a physics mechanism beyond the SM, "New Physics (NP)", in both theoretical and experimental approaches. The SM is considered to be the low-energy effective theory, and thus NP should exist in the higher energy scale. In order to find a clue to NP, many experimental studies are performed all around the world. Direct-search experiments with the Large Hadron Collider, for instance, are exploring the energy frontier though no significant findings have been reported. In the light of wide range of studies in different flavor sectors, indirect-search experiments with high-intensity beams have been crucial as well. The rare decays of the K meson (kaon), $K_L \to \pi^0 \nu\bar{\nu}$ and $K^+ \to \pi^+ \nu\bar{\nu}$, can provide a probe to search for NP beyond the SM in the energy scale of tens of TeV or more [3].

In this chapter, underlying theories on neutral kaon physics, quark mixing, and CP-violation will be introduced, followed by physics motivation behind the study of $K_L \to \pi^0 \nu\bar{\nu}$. Next, past and current experimental searches for $K_L \to \pi^0 \nu\bar{\nu}$ will be reviewed, which leads to the purpose of this thesis. At the end of this chapter, the outline of the thesis and author's contributions in this study will be clarified.

1.1 Underlying Theory

This section describes the fundamental property of kaon, the mechanism of CP-violation, and the Cabibo-Kobayashi-Maskawa model, which contributed to the establishment of the SM.

1.1.1 Physics of Neutral Kaon

Kaon is one of the subatomic particles in the group of meson, and it involves an s quark or an $\bar{s}$ quark. Historically, kaon has played important roles in the establishment of the SM. Neutral kaons K^0 ($d\bar{s}$) and $\bar{K}^0$ ($\bar{d}s$), in particular, have unique features. It was observed that they decay into the same final states such as two or three pions.This implies that they are indistinguishable based on the decay products. On the other hand, K^0 and $\bar{K}^0$ can transform into each other, as shown in Figure 1.1. If the rate of this mixing between K^0 and $\bar{K}^0$ is the same, one can define the following states:

$$|K_1\rangle = \frac{|K^0\rangle + |\bar{K}^0\rangle}{\sqrt{2}}, \tag{1.1}$$

$$|K_2\rangle = \frac{|K^0\rangle - |\bar{K}^0\rangle}{\sqrt{2}}. \tag{1.2}$$

These are the CP eigenstates because

$$CP\,|K_1\rangle = \frac{|\bar{K}^0\rangle + |K^0\rangle}{\sqrt{2}} = +\,|K_1\rangle\,, \tag{1.3}$$

$$CP\,|K_2\rangle = \frac{|\bar{K}^0\rangle - |K^0\rangle}{\sqrt{2}} = -\,|K_2\rangle\,. \tag{1.4}$$

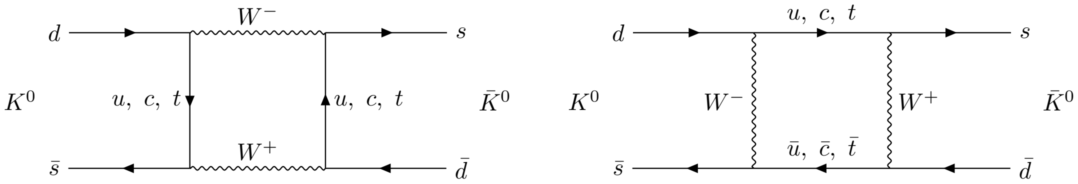

Figure 1.1: Feynman diagrams for $K^0 - \bar{K}^0$ mixing.

The CP eigenvalues of $\pi\pi$ and $\pi\pi\pi$ systems are given as $CP(\pi\pi) = +1$ and $CP(\pi\pi\pi) = -1$. Equations 1.3 and 1.4 tell that K_1 decays into two-pion final state while K_2 decays into three-pion final state if CP were conserved in the weak interaction.

Actually, two different kaons, the long-lived neutral kaon (K_L) and the short-lived neutral kaon K_S, were observed. K_L mainly decays into $3\pi^0$ while K_S mainly decays into $2\pi^0$. Due to the difference in the phase space available for each decay, K_L and K_S have the different lifetimes. The lifetimes of K_L and K_S are 51 ns and 90 ps, respectively [1]. The relationship among K_L, K_S, K_1, and K_2 will be explained in Section 1.1.2.

1.1.2 CP Violation in the Neutral Kaon System

Although CP was assumed to be conserved in weak interactions in the above discussion, J. Cronin and V. Fitch observed some long-lived kaons decaying into two pions in 1964 [4]. This means that CP is not exactly conserved in the weak interaction. Taking this into account, the states of K_S and

K_L can be written as

$$|K_S\rangle = \frac{1}{\sqrt{1+|\epsilon|^2}}(|K_1\rangle + \epsilon\,|K_2\rangle), \tag{1.5}$$

$$|K_L\rangle = \frac{1}{\sqrt{1+|\epsilon|^2}}(|K_2\rangle + \epsilon\,|K_1\rangle), \tag{1.6}$$

where the parameter ϵ represents the mixing between K_1 and K_2 and thus shows the amount of CP-violation. In the current measurements, the size of ϵ was obtained from the global fit as

$$|\epsilon| = (2.228 \pm 0.011) \times 10^{-3} \quad [1]. \tag{1.7}$$

Due to the small value of $|\epsilon|$, K_S and K_L states can be approximated as

$$K_S \approx K_1, \tag{1.8}$$

$$K_L \approx K_2. \tag{1.9}$$

1.1.3 Cabbibo-Kobayashi-Maskawa Model

In the framework of the SM, the Cabibo-Kobayashi-Maskawa (CKM) matrix[5, 6] plays an important role to describe interactions involving quark transitions. The CKM matrix (V_{CKM}) is a 3×3 unitary matrix that specifies the transition probability from one quark to another. It connects the quark mass eigenstates (d, s, b) to the weak eigenstates (d', s', b') as

$$\begin{pmatrix} d' \\ s' \\ b' \end{pmatrix} = V_{\mathrm{CKM}} \begin{pmatrix} d \\ s \\ b \end{pmatrix}, \tag{1.10}$$

where

$$V_{\mathrm{CKM}} = \begin{pmatrix} V_{ud} & V_{us} & V_{ub} \\ V_{cd} & V_{cs} & V_{cb} \\ V_{td} & V_{ts} & V_{tb} \end{pmatrix}. \tag{1.11}$$

The CKM matrix can be parametrized by three mixing angles θ_{12}, θ_{23}, θ_{13}, and a CP-violating phase δ as

$$\begin{aligned} V_{\mathrm{CKM}} &= \begin{pmatrix} 1 & 0 & 0 \\ 0 & c_{23} & s_{23} \\ 0 & -s_{23} & c_{23} \end{pmatrix} \begin{pmatrix} c_{13} & 0 & s_{13}e^{-i\delta} \\ 0 & 1 & 0 \\ -s_{13}e^{i\delta} & 0 & c_{13} \end{pmatrix} \begin{pmatrix} c_{12} & s_{12} & 0 \\ -s_{12} & c_{12} & 0 \\ 0 & 0 & 1 \end{pmatrix} \\ &= \begin{pmatrix} c_{12}c_{13} & s_{12}c_{13} & s_{13}e^{-i\delta} \\ -s_{12}c_{23} - c_{12}s_{23}s_{13}e^{i\delta} & c_{12}c_{13} - s_{12}s_{23}s_{13}e^{i\delta} & s_{23}c_{13} \\ s_{12}s_{23} - c_{12}c_{23}s_{13}e^{i\delta} & -c_{12}s_{23} - s_{12}c_{23}s_{13}e^{i\delta} & c_{23}c_{13} \end{pmatrix}, \end{aligned} \tag{1.12}$$

where $s_{ij} = \sin\theta_{ij}$, $c_{ij} = \cos\theta_{ij}$. Equation 1.12 can also be expressed with the Wolfenstein parameterization[7] using four real parameters λ, A, ρ, and η as

$$V_{\mathrm{CKM}} = \begin{pmatrix} 1-\lambda^2/2 & \lambda & A\lambda^3(\rho - i\eta) \\ -\lambda & 1-\lambda^2/2 & A\lambda^2 \\ A\lambda^3(1-\rho-i\eta) & -A\lambda^2 & 1 \end{pmatrix} + O(\lambda^4). \tag{1.13}$$

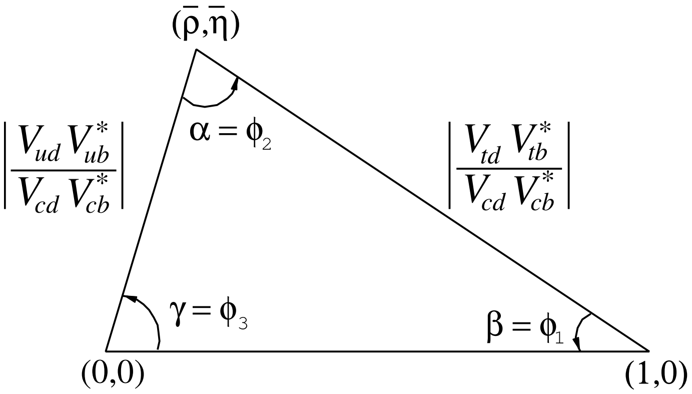

Figure 1.2: CKM unitarity triangle on the $\bar{\rho}$-$\bar{\eta}$ plane. The figure is quoted from Ref. [1].

The parameters are defined as

$$\lambda \equiv \frac{|V_{us}|}{\sqrt{|V_{ud}|^2 + |V_{us}|^2}}, \tag{1.14}$$

$$A \equiv \frac{1}{\lambda}\left|\frac{V_{cb}}{V_{us}}\right|, \tag{1.15}$$

$$\rho \equiv \mathrm{Re}\left\{\frac{V_{ub}^*}{A\lambda^3}\right\}, \tag{1.16}$$

$$\eta \equiv \mathrm{Im}\left\{\frac{V_{ub}^*}{A\lambda^3}\right\}. \tag{1.17}$$

$$\tag{1.18}$$

These parameters are determined with experimental measurements, which is important to test the unitarity of the CKM matrix. For example, the following equation

$$V_{ud}V_{ub}^* + V_{cd}V_{cb}^* + V_{td}V_{tb}^* = 0, \tag{1.19}$$

is one of the unitary relations. The three terms in the sum are complex numbers, and thus this relation can be represented as a triangle on the complex plane. Equation 1.19 can be expressed as

$$\frac{V_{ud}V_{ub}^*}{V_{cd}V_{cb}^*} + 1 + \frac{V_{td}V_{tb}^*}{V_{cd}V_{cb}^*} = 0. \tag{1.20}$$

This is one the common notations to illustrate the CKM unitarity triangle as shown in Figure 1.2. The parameters $\bar{\rho}$ and $\bar{\eta}$ written in Figure 1.2 are defined as

$$\bar{\rho} + i\bar{\eta} = -\frac{V_{ud}V_{ub}^*}{V_{cd}V_{cb}^*}. \tag{1.21}$$

In the Wolfenstein parameterization, $\bar{\rho}$ and $\bar{\eta}$ are expressed as $\bar{\rho} \sim \rho(1-\lambda^2/2)$ and $\bar{\eta} \sim \eta(1-\lambda^2/2)$. Various measurements have been performed so far to check whether the triangle is closed completely or not. Figure 1.3 shows the unitarity triangle with the parameters constrained by

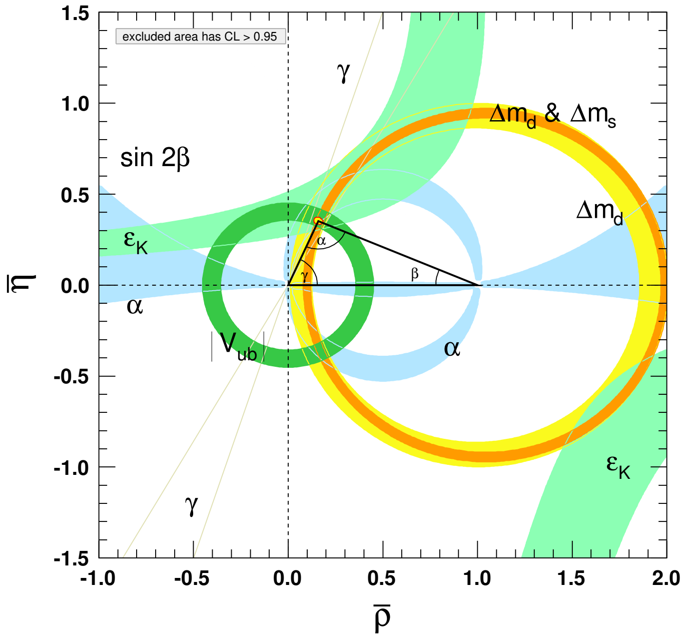

Figure 1.3: Constraints on the $\bar{\rho}$-$\bar{\eta}$ plane. The figure is quoted from Ref. [1].

experiments. The latest global fit [1] for the Wolfenstein parameters gives

$$\lambda = 0.22501 \pm 0.00068, \tag{1.22}$$

$$A = 0.826^{+0.016}_{-0.015}, \tag{1.23}$$

$$\bar{\rho} = 0.1591 \pm 0.0094, \tag{1.24}$$

$$\bar{\eta} = 0.3523^{+0.0073}_{-0.0071}. \tag{1.25}$$

The parameter $\bar{\eta}$ (or η), which is the height of the unitarity triangle, carries the imaginary part of the CKM matrix. Thus, the measurement of this parameter can be interpreted as the determination of the size of the CP-violation.

1.2 Physics Motivation for $K_L \to \pi^0 \nu \bar{\nu}$

In this section, physics of $K_L \to \pi^0 \nu \bar{\nu}$ and the relation with $K^+ \to \pi^+ \nu \bar{\nu}$ in the SM are explained. After that, various NP scenarios which imply possible deviations of the branching ratio are briefly reviewed.

1.2.1 $K_L \to \pi^0 \nu \bar{\nu}$ in the Standard Model

The rare decay of the neutral kaon, $K_L \to \pi^0 \nu \bar{\nu}$, is one of the golden modes in kaon decays. Since flavor-changing neutral current (FCNC) processes are forbidden at tree level in the SM, $K_L \to \pi^0 \nu \bar{\nu}$ proceeds through a loop diagram. Figure 1.4 shows examples of Feynman diagrams of $K_L \to \pi^0 \nu \bar{\nu}$ predicted in the SM.

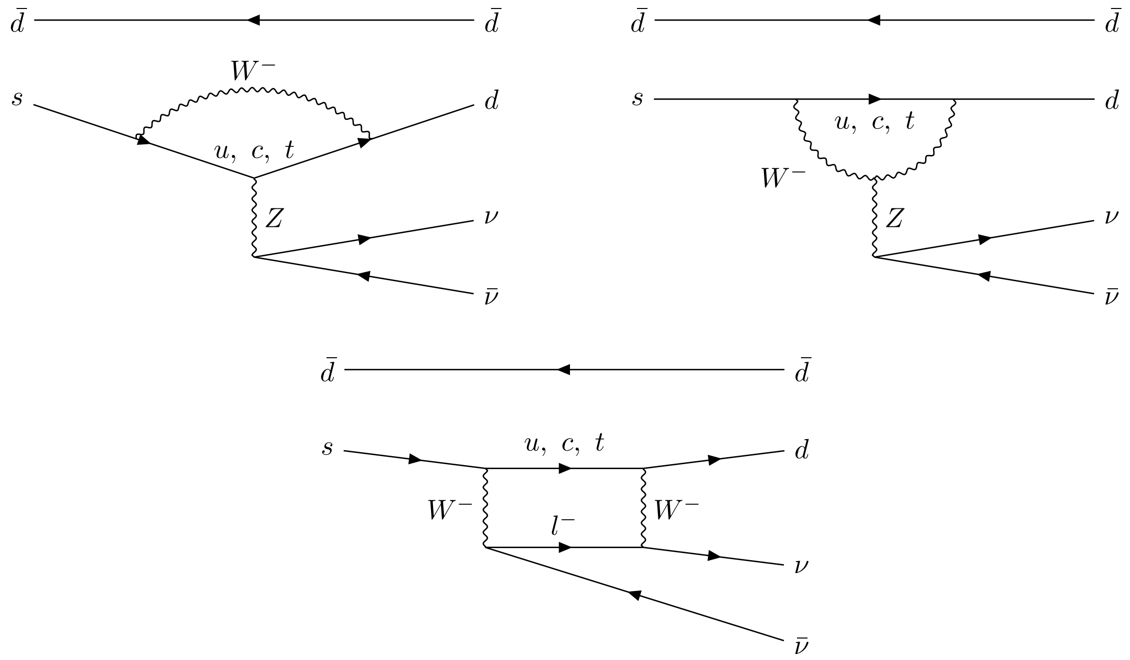

Figure 1.4: Examples of Feynman diagrams of $\bar{K}^0 \to \pi^0\nu\bar{\nu}$ in the SM.

The quark-level amplitude of this process $\mathcal{A}(s \to d\nu\bar{\nu})$ can be expressed as,

$$\begin{aligned}\mathcal{A}(s \to d\nu\bar{\nu}) &\sim \sum_{q=u,c,t} \lambda_q X_{\mathrm{SM}}(x_q) \\ &\sim \frac{m_t^2}{M_W^2}\lambda_t + \frac{m_c^2}{M_W^2}\ln\frac{M_W}{m_c}\lambda_c + \frac{\Lambda_{\mathrm{QCD}}^2}{M_W^2}\lambda_u \quad [8],\end{aligned} \tag{1.26}$$

where $\lambda_q = V_{qs}^* V_{qd}$ and $x_q = m_q^2/M_W^2$. The index q in Equation 1.26 runs over all the internal up-type quarks (u, c, and t) running in the loop of the diagrams. This formula represents suppressions by the CKM parameters shown as λ_q as well as the Glashow-Iliopoulos-Maiani (GIM) mechanism[9] where the unitarity of the CKM matrix ($\sum_{q=u,c,t}\lambda_q = \lambda_u + \lambda_c + \lambda_t = 0$) with the quark mass difference gives the non-perfect cancellation. Considering the masses of the charm quark ($m_c = 1.28\,\mathrm{GeV}/c^2$), top quark ($m_t = 173\,\mathrm{GeV}/c^2$), and the W boson ($M_W = 80.4\,\mathrm{GeV}/c^2$), and the QCD energy scale ($\Lambda_{\mathrm{QCD}} \sim 200\,\mathrm{MeV}$), Equation 1.26 implies that the top quark contribution amounts to $\sim$ 68% of the amplitude $\mathcal{A}(s \to d\nu\bar{\nu})$ while the charm and up quark contributions amount to $\sim$ 29% and $\sim$ 3%, respectively [8].

The $K_L \to \pi^0\nu\bar{\nu}$ decay amplitude can be written as

$$\begin{aligned}\mathcal{A}(K_L \to \pi^0\nu\bar{\nu}) &\sim \frac{1}{\sqrt{2}}\left(\mathcal{A}(K^0 \to \pi^0\nu\bar{\nu}) - \mathcal{A}(\bar{K}^0 \to \pi^0\nu\bar{\nu})\right) \\ &\propto V_{ts}V_{td}^* - V_{ts}^*V_{td} \\ &\sim -A\lambda^2\left(A\lambda^3(1-\rho+i\eta) - A\lambda^3(1-\rho-i\eta)\right) \\ &= -2iA^2\lambda^5\eta \\ &\propto \eta.\end{aligned} \tag{1.27}$$

Thus, $K_L \to \pi^0\nu\bar{\nu}$ can purely extract the CP-violation parameter η. This implies that $K_L \to \pi^0\nu\bar{\nu}$ can determine the height of the unitarity triangle by drawing a horizontal band in the $\bar{\rho}$–$\bar{\eta}$ plane.

The recent prediction of $\mathcal{B}(K_L \to \pi^0\nu\bar{\nu})$ in the SM is

$$\mathcal{B}(K_L \to \pi^0\nu\bar{\nu}) = (2.94 \pm 0.15) \times 10^{-11} \quad [10]. \tag{1.28}$$

The relevant hadronic matrix elements can be extracted from the well-measured $K^+ \to \pi^0 e^+ \nu_e$ decay [11], which allows for the accurate prediction of $\mathcal{B}(K_L \to \pi^0\nu\bar{\nu})$. Since the charm quark contribution drops out to be less than 1% in $K_L \to \pi^0\nu\bar{\nu}$ [12], uncertainties induced from it are eliminated. As studied in References [13, 12], the uncertainty is dominated by parametric errors from the CKM matrix. It is worthwhile to mention that intrinsic theory uncertainties are only about 2% for $\mathcal{B}(K_L \to \pi^0\nu\bar{\nu})$ though the determination of the CKM parameters should be improved by future measurements. The sources of the uncertainty are detailed in Appendix A.

In the context of NP searches, the strong suppression of the SM contribution to $K_L \to \pi^0\nu\bar{\nu}$ is a great advantage to look for an additional contribution of NP as a relatively large effect. In addition, the accurate prediction helps to distinguish the measured value from the predicted one. Thus, even a small deviation can indicate a clear sign of NP.

1.2.2 $K^+ \to \pi^+\nu\bar{\nu}$ and the Grossman-Nir Bound

Another golden mode in kaon decays, $K^+ \to \pi^+\nu\bar{\nu}$, also undergoes the FCNC via $s \to d\nu\bar{\nu}$ process. This decay is also highly suppressed as well as theoretically clean. The branching ratio in the SM is

$$\mathcal{B}(K^+ \to \pi^+\nu\bar{\nu}) = (8.60 \pm 0.42) \times 10^{-11} \quad [10]. \tag{1.29}$$

One of the important features for $K_L \to \pi^0\nu\bar{\nu}$ and $K^+ \to \pi^+\nu\bar{\nu}$ is that $\mathcal{B}(K_L \to \pi^0\nu\bar{\nu})$ and $\mathcal{B}(K^+ \to \pi^+\nu\bar{\nu})$ have a model-independent relation that can be derived from the isospin symmetry. Y. Grossman and Y. Nir obtained the following inequality called the Grossmann-Nir bound [14]:

$$\begin{aligned} \mathcal{B}(K_L \to \pi^0\nu\bar{\nu}) &< \frac{1}{r_{is}} \cdot \frac{\tau_{K_L}}{\tau_{K^+}} \cdot \mathcal{B}(K^+ \to \pi^+\nu\bar{\nu}) \\ &= 4.3 \cdot \mathcal{B}(K^+ \to \pi^+\nu\bar{\nu}), \end{aligned} \tag{1.30}$$

where τ_{K_L} and τ_{K^+} are the lifetimes of K_L and K^+, respectively, and $r_{is}(= 0.954)$ is the isospin breaking factor [15].

From the experimental point of view, Equation 1.33 gives an indirect upper limit on $\mathcal{B}(K_L \to \pi^0\nu\bar{\nu})$ depending on a measured value of $\mathcal{B}(K^+ \to \pi^+\nu\bar{\nu})$. $\mathcal{B}(K^+ \to \pi^+\nu\bar{\nu})$ was first measured by the E787 and E949 experiments at Brookhaven National Laboratory (BNL) as

$$\mathcal{B}(K^+ \to \pi^+\nu\bar{\nu}) = \left(1.73^{+1.15}_{-1.05}\right) \times 10^{-10} \quad [16], \tag{1.31}$$

which agrees with the SM prediction within errors. Recently, the NA62 experiment at CERN has been performing more precise measurements of $\mathcal{B}(K^+ \to \pi^+\nu\bar{\nu})$. In 2025, NA62 first observed $K^+ \to \pi^+\nu\bar{\nu}$ decays with a significance above 5σ, and obtained

$$\begin{aligned} \mathcal{B}(K^+ \to \pi^+\nu\bar{\nu}) &= \left(13.0^{+3.0}_{-2.7}|_{\text{stat}}{}^{+1.3}_{-1.3}|_{\text{syst}}\right) \times 10^{-11} \\ &= \left(13.0^{+3.3}_{-3.0}\right) \times 10^{-11} \quad [17], \end{aligned} \tag{1.32}$$

which agrees with the SM prediction within 1.7σ. Based on this result with one standard deviation of the error taken into account, the Grossmann-Nir bound can be calculated to be

$$\mathcal{B}(K_L \to \pi^0\nu\bar{\nu}) < 7.1 \times 10^{-10}. \tag{1.33}$$

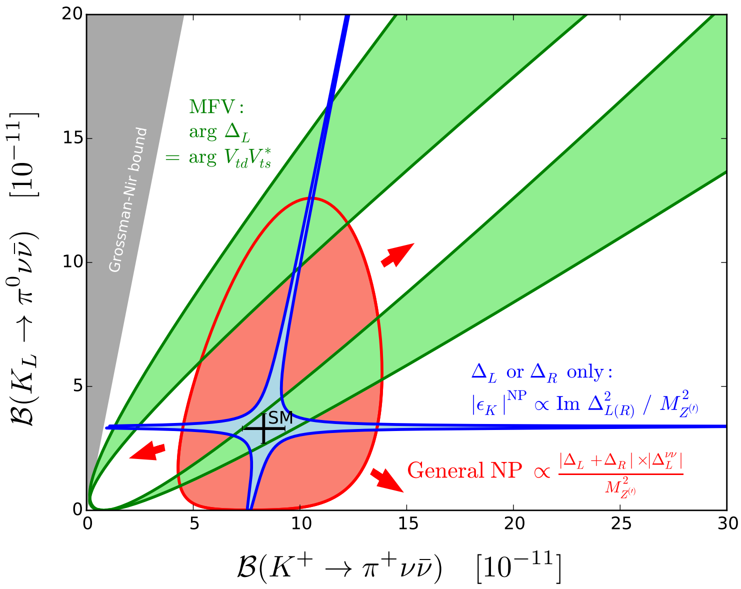

Figure 1.5: Correlation between $\mathcal{B}(K_L \to \pi^0\nu\bar{\nu})$ and $\mathcal{B}(K^+ \to \pi^+\nu\bar{\nu})$ under various scenarios. Note that some of these models are partially excluded from the measurement of $\mathcal{B}(K^+ \to \pi^+\nu\bar{\nu})$ by NA62, as described in Section 1.2.2. The figure is quoted from Ref. [18].

1.2.3 $K_L \to \pi^0\nu\bar{\nu}$ Beyond the Standard Model

There are many theory models for physics beyond the SM which allow for deviations of $\mathcal{B}(K_L \to \pi^0\nu\bar{\nu})$ from the SM prediction [18, 19, 3, 20]. To identify the model from various possible scenarios, it is important to consider correlations of $\mathcal{B}(K_L \to \pi^0\nu\bar{\nu})$ with other observables. Figure 1.5 shows various NP models and their correlations between $\mathcal{B}(K_L \to \pi^0\nu\bar{\nu})$ and $\mathcal{B}(K^+ \to \pi^+\nu\bar{\nu})$. The green region shows the models that have a CKM-like structure in flavor interactions, such as the Minimal Flavor Violation (MFV) models [21]. The two green branches shown in Figure 1.5 are partially ruled out by other experimental constraints [22, 23]. The blue region shows the models where only left or right-handed couplings are assumed to be present with the constraint from the parameter ϵ_K (denoted as ϵ in Equation 1.7). For example, the Littlest Higgs model with T-parity[24, 25, 26] and models with Z or Z′ FCNC scenarios with pure left-handed or right-handed couplings to quarks at tree level[27, 3] belong to this class of model. The red region shows models in which the correlation between ϵ_K and $K \to \pi\nu\bar{\nu}$ is weak or absent, such as Z′ models with both left-handed and right-handed couplings[3] and the Randall-Sundrum model with custodial protection[28]. In addition to the models discussed above, many other NP scenarios have also been considered, such as general minimum supersymmetric standard models[23, 29] and models with lepton-flavor universality violation[30, 31]. As a concrete example, the models with a 3-TeV Z′ are shown in Figure 1.6.

Scenarios with two-Higgs-doublet models are also discussed [32, 33]. In particular, the model studied in Ref. [34] was motivated by electroweak baryogenesis which is one of the scenarios to give rise to the baryon asymmetry of the universe. This model implies that branching ratios of $K^+ \to \pi^+\nu\bar{\nu}$ and $K_L \to \pi^0\nu\bar{\nu}$ can deviate from the SM prediction by the order of 10% and 1%, respectively.

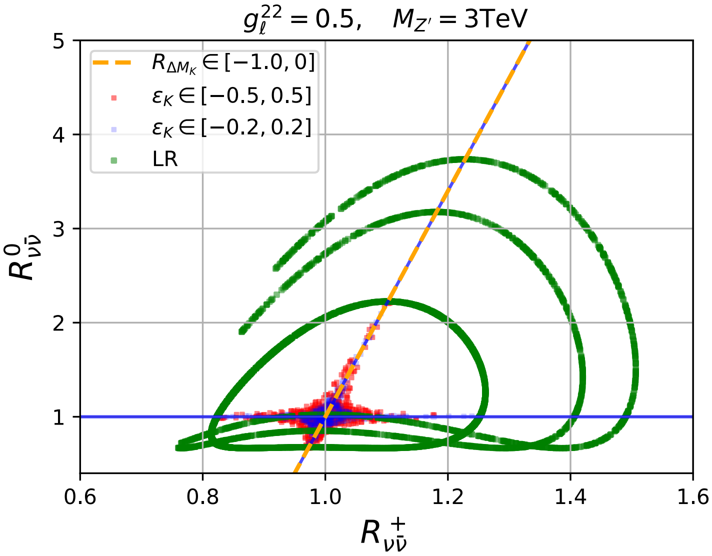

Figure 1.6: Correlation between between $K_L \to \pi^0 \nu \bar{\nu}$ and $K^+ \to \pi^+ \nu \bar{\nu}$ for a Z′ with its mass of 3 TeV studied in Ref. [20]. The horizontal (vertical) axis represents the branching ratio of $K^+ \to \pi^+ \nu \bar{\nu}$ ($K_L \to \pi^0 \nu \bar{\nu}$) normalized to its SM prediction defined as $R^+_{\nu\bar{\nu}} = \mathcal{B}(K^+ \to \pi^+ \nu \bar{\nu})/\mathcal{B}(K^+ \to \pi^+ \nu \bar{\nu})_{\mathrm{SM}}$ ($R^0_{\nu\bar{\nu}} = \mathcal{B}(K_L \to \pi^0 \nu \bar{\nu})/\mathcal{B}(K_L \to \pi^0 \nu \bar{\nu})_{\mathrm{SM}}$). The green region indicates the model with both left-handed and right-handed couplings. The blue (red) region indicates the left-handed scenario with a constraint of $\epsilon_K \in [-0.2, 0.2]$ ($\epsilon_K \in [-0.5, 0.5]$). The figure is quoted from Ref. [20].

Finally, while many of the NP models respect the model-independent Grossman-Nir bound as the SM does, recent studies have pointed out that some exotic models could violate the Grossman-Nir bound under particular assumptions [35, 36, 37, 38]. The model discussed in Ref. [36], for instance, considers the K-π transition via the isospin change by $\Delta I = 3/2$, while the Grossman-Nir bound assumes the $\Delta I = 1/2$ transition which is considered to be the dominant process in the SM. Figure 1.7 shows branching ratios for $K_L \to \pi^0 \nu \bar{\nu}$ and $K^+ \to \pi^+ \nu \bar{\nu}$ in this model where both $\Delta I = 1/2$ and $\Delta I = 3/2$ interactions are considered.

1.2.4 $K_L \to \pi^0 X^0$

In the NP model assuming the existence of an invisible particle X^0, the $K_L \to \pi^0 \nu \bar{\nu}$ signal can also be interpreted as $K_L \to \pi^0 X^0$. Assuming that X^0 is an invisible long-lived particle, the $K_L \to \pi^0 X^0$ decay could give a similar signature to $K_L \to \pi^0 \nu \bar{\nu}$ because one can only see two photons from the π^0 decay in the final state. Thus, this decay can be studied together with $K_L \to \pi^0 \nu \bar{\nu}$ under various assumptions of the X^0 mass (m_{X^0}). For instance, the models studied in Refs. [40, 41] are motivated by the anomalous magnetic dipole moment of the muon [42, 43, 44, 45], and may explain the anomaly by introducing a new light gauge boson Z' for X^0.

Although the $K \to \pi X^0$ decay is being studied via the charged mode, $K^+ \to \pi^+ X^0$ by NA62 [46], there is an experimental loophole around the π^0 mass (m_{π^0}) for the following reason. In the study of $K^+ \to \pi^+ \nu \bar{\nu}$ by NA62, they measure the squared missing mass defined as $m^2_{\mathrm{miss}} = (P_K - P_\pi)^2$ where P_K and P_π represent the four-momenta of the K^+ and π^+ candidates.

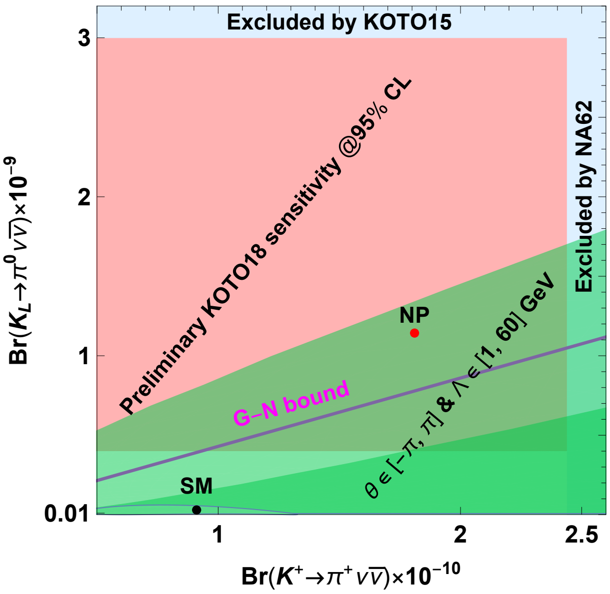

Figure 1.7: Branching ratio predictions for $K_L \to \pi^0\nu\bar{\nu}$ and $K^+ \to \pi^+\nu\bar{\nu}$ based on the model discussed in Ref. [36]. The variable Λ and θ in the figure are the parameters representing the NP scale and some phase, respectively. The allowed region demonstrated in this model is shown in the green region. The purple line indicates the Grossman-Nir bound. The black dot labeled SM corresponds to the SM prediction and the red dot labeled NP corresponds to the case with $(\Lambda, \theta) = (39\,\text{GeV}, -\pi/4)$ in this model. Note that the excluded region for $\mathcal{B}(K^+ \to \pi^+\nu\bar{\nu})$ has been updated in the recent measurement by NA62 [39]. The figure is quoted from Ref.[36].

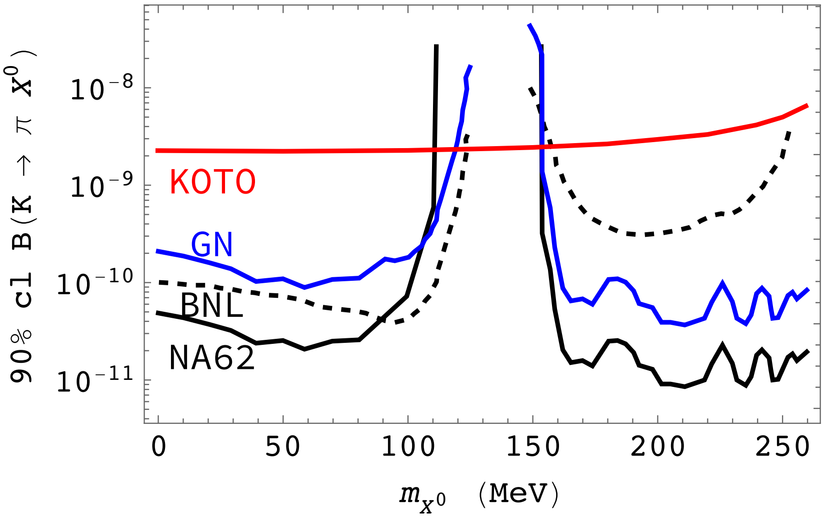

Figure 1.8: Constraints on the branching ratio of $K \to \pi X^0$ with an assumption that X^0 is stable. The black solid (dashed) line shows the exclusion limit for $K^+ \to \pi^+ X^0$ from the NA62 experiment at CERN (the E787 and E949 experiments at BNL) [46, 16]. The blue line shows the corresponding Grossman-Nir bound. The red line shows the constraint on $K_L \to \pi^0 X^0$ from the KOTO experiment [50]. The figure is quoted from Ref. [1].

This quantity corresponds to the momentum that a neutrino pair in the final state carries away. For the $K^+ \to \pi^+ \nu \bar{\nu}$ signal selection, they reject the region of $0.010 < m^2_{\text{miss}} < 0.026\,\text{GeV}^2/c^4$ to suppress the large background contribution from $K^+ \to \pi^+ \pi^0$ decays. Figure 1.8 shows the constraints on the branching ratio of $K \to \pi X^0$ as a function of m_{X^0}. A separate study in NA62 covers the m_{X^0} region around m_{π^0} [51]. Figure 1.9 shows the results obtained from this search. On the other hand, the $K_L \to \pi^0 X^0$ search has no such kinematical constraints, and is capable of exploring the region of $m_{X^0} \sim m_{\pi^0}$, as shown in Figure 1.8.

The models with X^0 under other assumptions, such as an unstable case, are also considered [47], and some studies may be found in Refs. [48, 49].

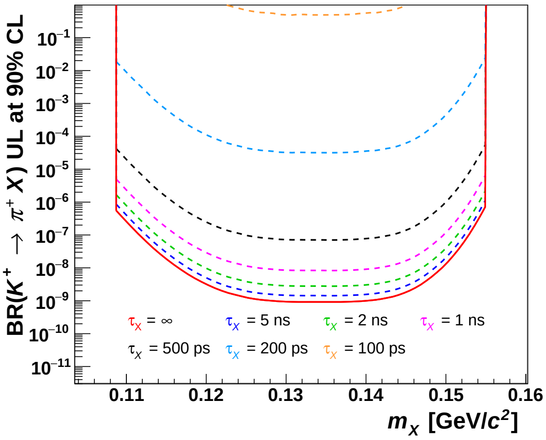

Figure 1.9: Upper limits on the branching ratio for $K^+ \to \pi^+ X^0$ obtained from the search for the decay of the π^0 to invisible particles by the NA62 experiment. The red solid line corresponds to the case where X^0 is assumed to be a long-lived particle. The other dashed lines assumed that X^0 has the lifetime of τ_X shown in the figure. The figure is quoted from Ref. [51].

1.3 Previous Experimental Searches for $K_L \to \pi^0 \nu \bar{\nu}$

1.3.1 Search History

Although $K_L \to \pi^0 \nu \bar{\nu}$ is considered to be among the most promising decay modes to explore NP beyond the SM from a theoretical point of view, an experimental search for this decay is challenging. To observe the $K_L \to \pi^0 \nu \bar{\nu}$ decay that rarely occurs due to its small branching ratio, a large number of K_L's are needed. In addition, reduction of background events is critical to discriminate them from the $K_L \to \pi^0 \nu \bar{\nu}$ signal. As a consequence, the $K_L \to \pi^0 \nu \bar{\nu}$ decay has not been observed yet to date.

In spite of these difficulties, long-lasting efforts by various experiments in the past decades have been pushing the upper limit on $\mathcal{B}(K_L \to \pi^0 \nu \bar{\nu})$ down to the level of two orders of magnitude larger than the SM prediction. Figure 1.10 shows upper limits on $\mathcal{B}(K_L \to \pi^0 \nu \bar{\nu})$ obtained from past searches. Single event sensitivity in Figure 1.10 means a branching ratio equivalent to an observation of one signal event. Starting with the E391a experiment, recent searches have been performed by the experiments dedicated to the $K_L \to \pi^0 \nu \bar{\nu}$ study.

1.3.2 Dedicated Experiments

In order to search for the ultra rare decay, dedicated experiments, E391a and KOTO shown in Figure 1.10, were developed. In this section, the experimental principle of the dedicated experiments is introduced. After that, the first dedicated experiment, E391a, and its successor experiment, KOTO, will be briefly reviewed.

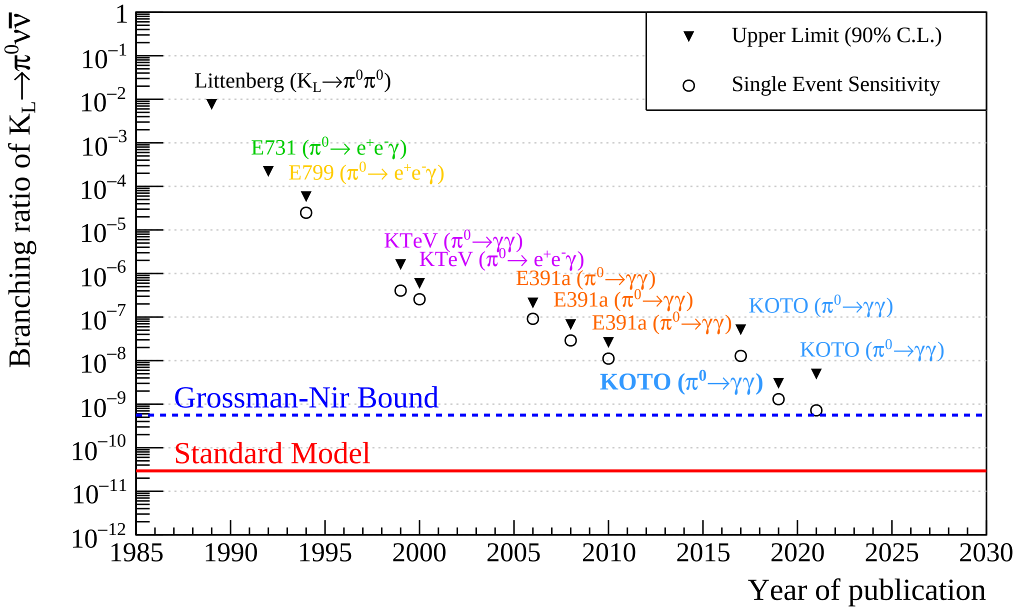

Figure 1.10: Upper limit on $\mathcal{B}(K_L \to \pi^0\nu\bar{\nu})$ at the 90% C.L. (black triangle) and the single event sensitivity (black circle). The values are quoted from Refs. [52, 53, 54, 55, 56, 57, 58, 59, 60, 50, 61]. The red line indicates the SM prediction of $\mathcal{B}(K_L \to \pi^0\nu\bar{\nu})$. The blue dashed line indicates the current Grossman-Nir bound.

1.3.2.1 Experimental Principle

A π^0 decays into two photons with the mean lifetime of 8.43×10^{-17} s and the branching ratio of 98.8% [1]. Therefore, there are only two photons and undetected neutrinos in the final state of $K_L \to \pi^0\nu\bar{\nu}$. The $K_L \to \pi^0\nu\bar{\nu}$ signal was identified by detecting the two photons from the π^0 decay while ensuring that there are no extra detectable particles in each event. A volume for K_L to decay is fully sealed with veto detectors so that extra particles can be detected, as shown in Figure 1.11.

1.3.2.2 KEK E391a Experiment

The E391a experiment performed the first dedicated search for $K_L \to \pi^0\nu\bar{\nu}$ at the High Energy Accelerator Research Organization (KEK) in Japan. E391a used the 12-GeV proton beam provided from the proton synchrotron (KEK-PS) to generate the neutral beam including K_L. The upper limits on $\mathcal{B}(K_L \to \pi^0\nu\bar{\nu})$ were set in 2006 [57], 2008 [58], and 2010 [59]. The final result by E391a is

$$\mathcal{B}(K_L \to \pi^0\nu\bar{\nu}) < 2.6 \times 10^{-8} \quad \text{(90\% C.L.)} \quad [59]. \tag{1.34}$$

1.3.2.3 J-PARC KOTO Experiment

The KOTO experiment was proposed in 2006 to be the successor to the E391 experiment [62]. The experiment is conducted at the Japan Proton Accelerator Research Complex (J-PARC) in Japan [63]. J-PARC provides a 30-GeV proton beam with the two orders of magnitude higher intensity

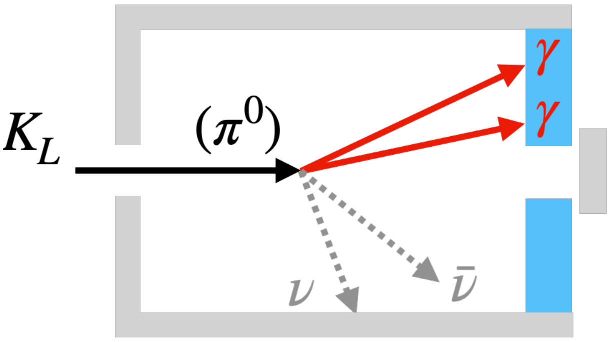

Figure 1.11: Illustration of $K_L \to \pi^0 \nu\bar{\nu}$ signal detection. The K_L in the beam enters the detector. The blue boxes represent a detector to identify $\pi^0 \to 2\gamma$. The grey boxes represent veto detectors to ensure that there are no extra detectable particles other than two photons.

than that of KEK-PS. The experimental principle for the $K_L \to \pi^0 \nu\bar{\nu}$ search at KOTO is basically the same as the method in E391a, and its details will be described in Chapter 2.

At present, the KOTO experiment is the only place where the search for $K_L \to \pi^0 \nu\bar{\nu}$ is performed in the world. The experimental project to study $K_L \to \pi^0 \nu\bar{\nu}$ at J-PARC was designed to be carried out by taking a step-by-step approach. Toward the observation of the $K_L \to \pi^0 \nu\bar{\nu}$ signal event, the sensitivity goal in KOTO (Step 1)[1] was set below 10^{-10}. KOTO is improving the sensitivity and trying to find a contribution of NP to $K_L \to \pi^0 \nu\bar{\nu}$ predicted in the current sensitivity region. A measurement of $\mathcal{B}(K_L \to \pi^0 \nu\bar{\nu})$ with dozens of signal events is planned to be carried out by the next-generation experiment called KOTO II (Step 2) [64] after KOTO's data-taking is completed.

Figure 1.12 shows the history of the data-taking at the KOTO experiment, and Table 1.1 summarizes the datasets used for the $K_L \to \pi^0 \nu\bar{\nu}$ search. KOTO has been accumulating data during accelerator operations at J-PARC since the first data-taking in 2013. KOTO has published results of the $K_L \to \pi^0 \nu\bar{\nu}$ search in 2017 [60], 2019 [50], and 2021 [61]. From the results published in 2019 [50], the most stringent upper limit on $\mathcal{B}(K_L \to \pi^0 \nu\bar{\nu})$ was set as

$$\mathcal{B}(K_L \to \pi^0 \nu\bar{\nu}) < 3.0 \times 10^{-9} \quad (90\%\ \text{C.L.}) \quad [50]. \tag{1.35}$$

This limit is still above the current Grossman-Nir bound shown in Equation 1.33. Therefore, it is of great importance to improve the experimental sensitivity for the $K_L \to \pi^0 \nu\bar{\nu}$ search independently of the $K^+ \to \pi^+ \nu\bar{\nu}$ decay to scrutinize the unexplored region below the indirect limit. The results published in 2021 [50] are described in Section 1.4.

---

[1] In the proposal, the current KOTO experiment was referred to as "Step 1".

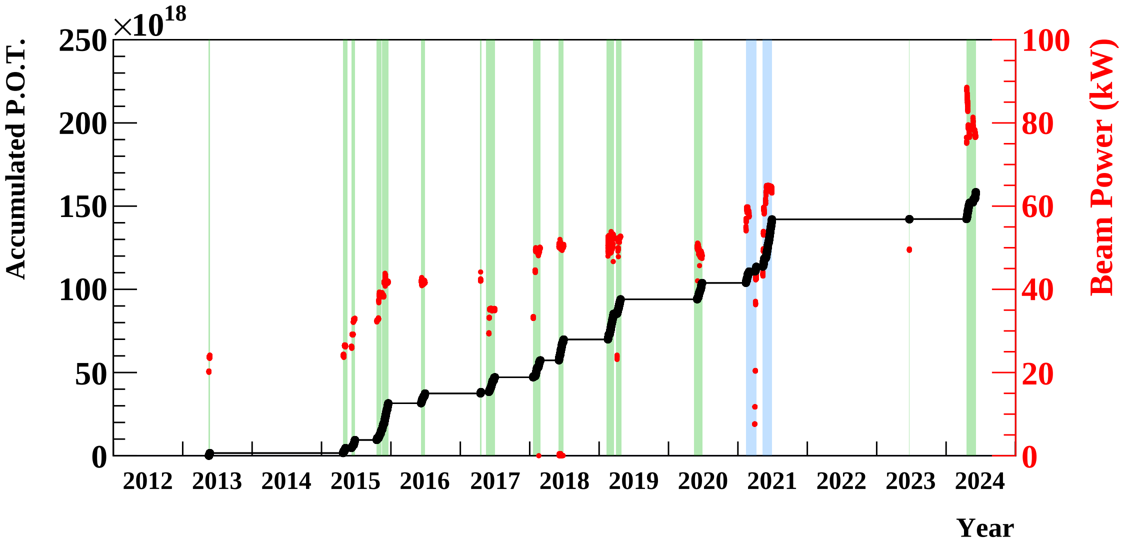

Figure 1.12: Data-taking history of the KOTO experiment as of 2024. The black points show the accumulated number of POT. The red points shows the power of the beam provided at J-PARC. The area shaded in blue corresponds to the data collected in 2021, which is focused in this thesis.

Table 1.1: Summary of the data-taking at the KOTO experiment. Analyses of the data collected until 2018 have been already completed (denoted as ✓) and the results were published in the papers listed in the column for references. The third column from the left shows the number of protons on target (POT) used for the physics data analysis.

Data-taking year	Analysis status	POT	Reference
2013	✓	1.6×10^{18}	[60]
2015	✓	2.2×10^{19}	[50]
2016–2018	✓	3.1×10^{19}	[61]
2019	ongoing	2.1×10^{19}[a]	n/a
2020	ongoing[b]	8.9×10^{18}[a]	n/a
2021	covered in this thesis	3.3×10^{19}	[65]

[a] The number is still preliminary.

[b] Control data collected in 2020 was used to study background events for the 2016–2018 data analysis.

1.4 Results from 2016–2018 Data in KOTO

In the last search for $K_L \to \pi^0 \nu \bar{\nu}$ at KOTO using the data collected from 2016 to 2018 [61], three events were observed in the signal region as shown in Figure 1.13. In this analysis, two new background sources were found. One is from $K^\pm$ decays and the other is from beam-halo $K_L \to 2\gamma$ decays. Among the $K^\pm$-induced events, the $K^\pm \to \pi^0 e^\pm \nu$ decay shown in Figure 1.14 was the main cause of the background. If the two photons from the π^0 decay are detected and the $e^\pm$ is not detected, such events could be misidentified as a signal. Since neutrinos are undetected escaping from the detector, $e^\pm$ is the only particle available for veto decision, and thus the $K^\pm \to \pi^0 e^\pm \nu$ decay is the dangerous background source. The background mechanism of the beam-halo $K_L \to 2\gamma$ decay is explained in Section 2.1.2.

Table 1.2 shows the numbers of expected events from various background sources in this analysis. Based on the fact that the total number of background events was estimated to be 1.22 ± 0.26, it was concluded that the number of observed events was statistically consistent with the background expectation.

The upper limit on the branching ratio obtained in this analysis was $\mathcal{B}(K_L \to \pi^0 \nu \bar{\nu}) < 4.9 \times 10^{-9}$ at the 90% C.L. This result did not improve the best upper limit obtained from the 2015 data. In this analysis, the single event sensitivity was $(7.20 \pm 0.05_{\mathrm{stat}} \pm 0.66_{\mathrm{syst}}) \times 10^{-10}$, which is more than one order of magnitude above the SM sensitivity. Since more background events are expected along with an improvement of a sensitivity in the future, these background events must be reduced.

Table 1.2: Summary of the expected numbers of background events in the 2016–2018 data analysis.

Source		Number of events
K_L	$K_L \to 3\pi^0$	0.01 ± 0.01
	$K_L \to 2\gamma$ (beam halo)	0.26 ± 0.07 [a]
	Other K_L decays	0.005 ± 0.005
$K^\pm$		0.87 ± 0.25 [a]
Neutron	Hadron cluster	0.017 ± 0.002
	CV η	0.03 ± 0.01
	Upstream π^0	0.03 ± 0.03
Total		1.22 ± 0.26

[a] Background sources studied after looking inside the blind region.

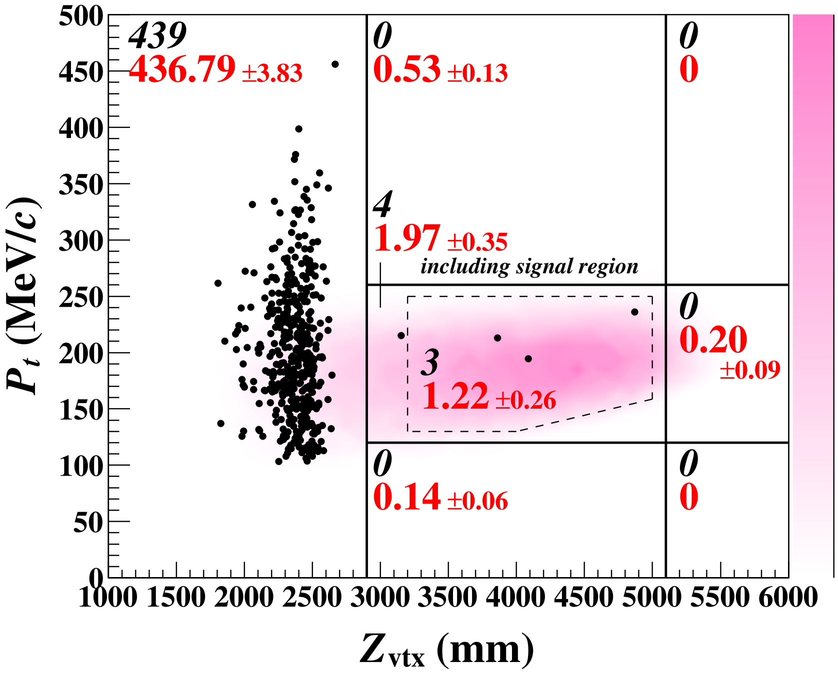

Figure 1.13: Reconstructed π^0 transverse momentum (P_t) versus π^0 decay vertex position (Z_{vtx}) for events after imposing the $K_L \to \pi^0\nu\bar{\nu}$ selection criteria in the 2016–2018 data analysis. The region surrounded by dashed lines is the signal region. The black dots represent observed events, and the shaded contour indicates the $K_L \to \pi^0\nu\bar{\nu}$ distribution from the Monte Carlo simulation. The black italic (red regular) numbers indicate the number of observed (background) events for different regions. The figure is quoted from Ref. [61].

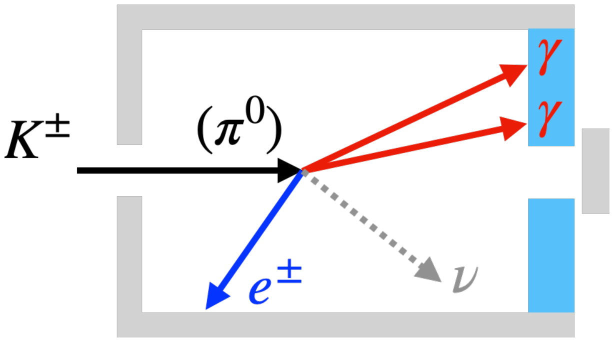

Figure 1.14: Illustration of the $K^\pm \to \pi^0 e^\pm \nu$ background. The blue boxes represent a detector to identify $\pi^0 \to 2\gamma$. The grey boxes represent veto detectors to ensure that there are no extra detectable particles other than two photons. Since neutrinos escape undetected, $e^\pm$ in $K^\pm \to \pi^0 e^\pm \nu$ is the only particle available for veto decision.

1.5 KOTO Detector Upgrade after 2018

The detector condition in the KOTO experiment was changed after the data-taking in 2018. As described in Section 1.4, reduction of the $K^{\pm}$ background is crucial, and thus detection of $K^{\pm}$ in the beam at the entrance of the KOTO detector was considered as a possible solution. By installing an in-beam charged particle detector, one can directly detect $K^{\pm}$'s and reject background events associated with them. This idea, however, has a negative aspect for the following reason. An in-beam detector at the detector entrance enhances scattering of incident beam particles. This can be a cause to increase background events and accidental activities. Therefore, a thin detector with low material budget was desired to mitigate scattering effects while its $K^{\pm}$ detection efficiency is high enough to reduce background events. A prototype of charged particle detector for this purpose was installed before the data-taking in 2020, and it was used during a part of the beam operation at J-PARC in 2020. After this beam operation, the prototype detector was replaced with a new detector before the data-taking in 2021. This detector is called Upstream Charged Veto (UCV) and its details are described in Section 2.5.

In addition to UCV, there were two other upgrades of the KOTO detector. The electromagnetic calorimeter was upgraded to have a new signal readout system, and one of the detectors located in the downstream section of the KOTO detector was replaced with a new detector. These were also motivated by improvements of the background reduction. Details are described in Section 2.5.

1.6 Purpose of This Thesis

As mentioned in Section 1.3, the search for $K_L \to \pi^0 \nu \bar{\nu}$ is currently performed only at the KOTO experiment in the world. The most stringent upper limits on the branching ratios of $K_L \to \pi^0 \nu \bar{\nu}$ and $K_L \to \pi^0 X^0$ were obtained from the data collected in 2015 (“2015 data"), and the best single event sensitivity was achieved with the data collected in 2016–2018 (“2016–2018 data"). After the observation of the three signal candidate events in the 2016–2018 data was reported, it triggered various theory discussions, aiming to build a model assuming the observed events as signals[2]. The corresponding branching ratio for $K_L \to \pi^0 \nu \bar{\nu}$ would have exceeded the Grossman-Nir bound if the observed events had been considered as signals. Therefore, NP models that can even break the Grossman-Nir bound were proposed, as already described in Section 1.2.3.

The purpose of this thesis is to describe the latest analysis of the $K_L \to \pi^0 \nu \bar{\nu}$ search at the KOTO experiment using the data collected in 2021. We aimed to suppress the background events which were found in the previous analysis with the upgraded detector system and the new analysis methods. Based on the results from this search, the thesis aims to give new insights into the understanding of the background contributions and to discuss the impacts of the obtained results.

---

[2] When the observed events were first reported in the public conference, the background sources of $K^{\pm}$ and beam-halo $K_L \to 2\gamma$ decays had not been found. Thus, the total number of background events was estimated to be 0.05 ± 0.02 with a single event sensitivity of 6.9×10^{-10} [66].

1.7 Outline and Author's Contribution

The rest of this thesis is organized as follows. Chapter 2 describes experimental methods and apparatus. Chapter 3 describes data-taking conditions in 2021. Chapter 4 describes the procedure of event reconstruction. Chapter 5 describes the simulation process. Chapter 6 describes the analysis of the 2021 data and summarizes results. Chapter 7 describes discussions on the 2021 data analysis and future strategy. Chapter 8 concludes the study of 2021 data analysis and clarifies the outcome from it.

This study was done with collaborators in the KOTO experiment, ranging from the developments and upgrades of the detector system to the data-taking and the analysis. Particularly, the following contributions are author's main work in this study.

- Development and installation of a new detector (UCV). This is described in Section 2.5.2.
- Performance evaluation of UCV for the $K_L \rightarrow \pi^0 \nu \bar{\nu}$ search. This is described in Sections 6.2.2.1, 6.3.6.2, and Appendix D.
- Evaluation of the single event sensitivity and its systematic uncertainties for the $K_L \rightarrow \pi^0 \nu \bar{\nu}$ analysis. These are described in Section 6.2.3.
- Evaluation of the $K^{\pm}$ decay background and its systematic uncertainties for the $K_L \rightarrow \pi^0 \nu \bar{\nu}$ analysis. These are described in Section 6.3.6.
- Analysis for the $K_L \rightarrow \pi^0 X^0$ decay. This is described in Section 6.5.

Chapter 2

The KOTO Experiment

In this chapter, experimental methods to search for $K_L \rightarrow \pi^0 \nu \bar{\nu}$ in the KOTO experiment is introduced. Next, experimental facilities and apparatuses used for the KOTO experiment are detailed. The design of the KOTO experiment can also be found in Refs. [62, 67].

2.1 Basic Strategy

Detection of $K_L \rightarrow \pi^0 \nu \bar{\nu}$ is expected to be challenging since the branching ratio of the signal decay is extremely small. This means that a large number of K_L particles are needed to study $K_L \rightarrow \pi^0 \nu \bar{\nu}$. In addition, events from non-signal sources are all backgrounds in finding the signal. Since all the particles in both the initial state and the final state are neutral, charged-particle tracking is not usable, and no information on the incident K_L is available. Therefore, separation of signal events from background events is indispensable. This section describes the strategy of KOTO to find the signal and what kind of background sources are expected.

2.1.1 Signal Identification

The signature of the $K_L \rightarrow \pi^0 \nu \bar{\nu}$ signal is "($\pi^0 \rightarrow$) 2γ + *nothing else*"; two photons from the π^0 decay are the only visible particles in the final state. A pair of neutrinos escape undetected and take away a part of the momentum of the initial K_L. Consequently, the π^0 has a large transverse momentum with respect to the direction of the K_L. If we are able to reconstruct a π^0 from 2γ, we can utilize the transverse momentum of the π^0 as one of the kinematical features for the signal identification.

Figure 2.1 shows a conceptual design to produce the neutral beam including K_L. Secondary particles are generated by the collision of the proton beam with the production target. Short-lived particles and charged particles can be eliminated with a long beam line and a magnet, respectively. Thus, only photons, neutrons, and K_L remain at the exit of the beam line. Collimators shape the beam and make it narrow. The narrow beam is one of the key ingredients in the process of the π^0 reconstruction explained later. Details of the proton beam delivery, the production target, and the beam line components will be covered in Section 2.2, Section 2.3, and Section 2.4, respectively.

By using K_L generated in this way, the signal detection is performed as shown in Figure 2.2. The KOTO detector is composed of an electromagnetic calorimeter and veto detectors. The

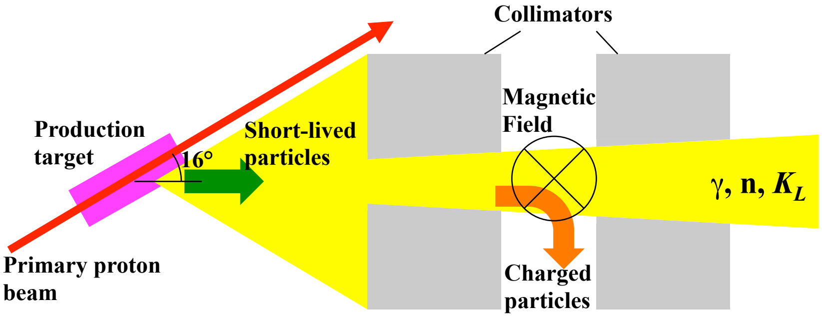

Figure 2.1: Conceptual design of the neutral beam production. The figure is quoted from Ref. [68].

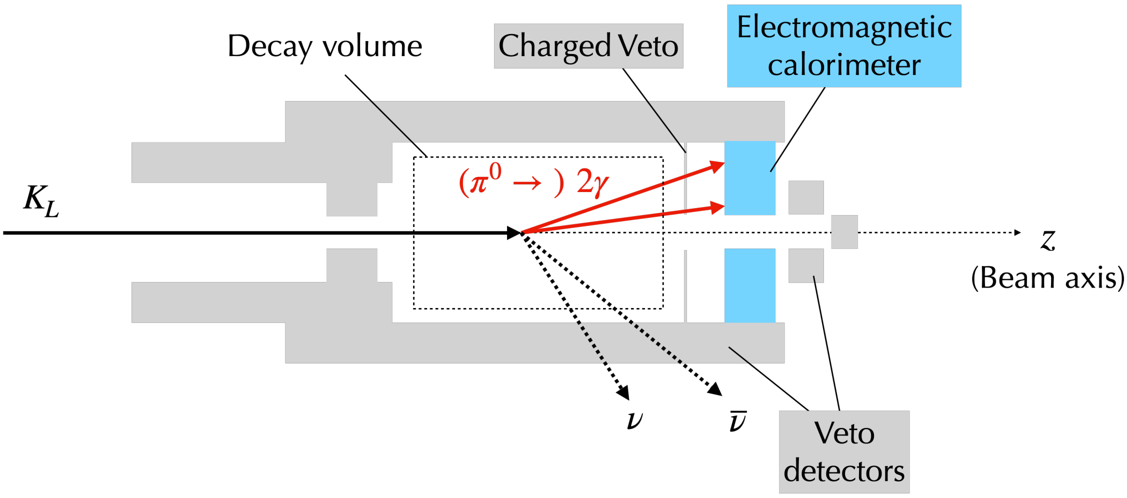

Figure 2.2: Schematic view of the signal detection with the KOTO detector. The blue boxes represent an electromagnetic calorimeter and the grey boxes represent veto detectors. The charged-veto counters detect charged particles hitting the electromagnetic calorimeter. The veto detectors surround the decay volume to detect any extra particles if such exist.

charged-veto detector detects charged particles entering the calorimeter. The $K_L \to \pi^0 \nu \bar{\nu}$ decay is identified by detecting the two photons at the calorimeter. The electromagnetic calorimeter is responsible for measuring energies and positions of the two photons. All the other veto detectors are needed to ensure that there are no other detectable particles. Each detector component is detailed in Section 2.5.

With the two photons detected in the electromagnetic calorimeter, the π^0 is reconstructed in the following steps. The conservation law of four-momentum for $\pi^0 \to 2\gamma$ gives

$$\begin{aligned} M_{\pi^0}^2 &= (E_1 + E_2)^2 - (\boldsymbol{p}_1 + \boldsymbol{p}_2)^2 && (2.1) \\ &= 2E_1E_2(1 - \cos\theta), && (2.2) \end{aligned}$$

where M_{π^0} represents the nominal mass of π^0[1], and $E_{1(2)}$ and $\boldsymbol{p}_{1(2)}$ represent the energy and the momentum of γ_1 (γ_2). The variable θ represents the opening angle between the two photons.

---

[1] $M_{\pi^0} = 134.9768\,\mathrm{MeV}/c^2$ [1].

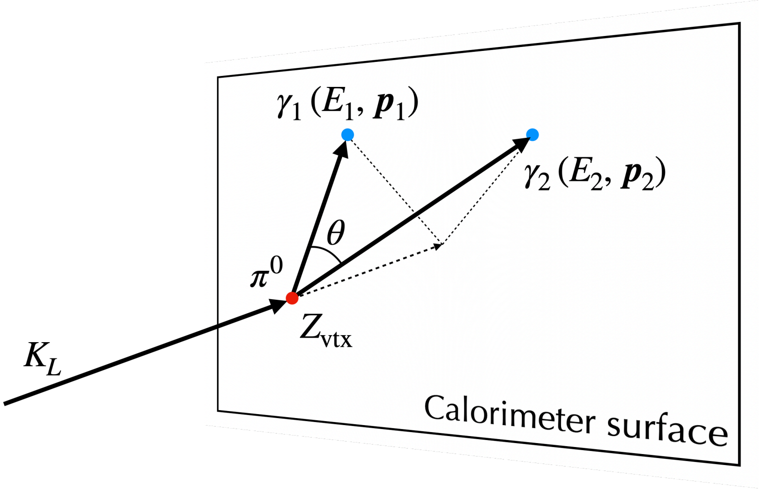

Figure 2.3: Schematic explanation of the reconstruction of the decay vertex position. The beam center lies along the z-axis. The red point represents the vertex position of the π^0 decay. The blue points represent the hit positions of the two photons (γ_1 and γ_2) on the surface of the electromagnetic calorimeter.

Equation 2.2 can then be transformed into

$$\cos\theta = 1 - \frac{M_{\pi^0}^2}{2E_1E_2}. \tag{2.3}$$

Owing to the narrow beam, one can make an assumption that the π^0 decays on the beam axis that is defined as the z-axis in the KOTO coordinate system to determine the vertex position along the z-axis (Z_{vtx}), as shown in Figure 2.3. After Z_{vtx} is reconstructed, the directions of the two photons are determined, and then $\boldsymbol{p}_1$ and $\boldsymbol{p}_2$ can be reconstructed. From the reconstructed two photons, the π^0 can also be reconstructed.

As mentioned, the transverse momentum of π^0 (P_t) is a quantity that characterizes $K_L \to \pi^0\nu\bar{\nu}$. In addition, Z_{vtx} is also a useful quantity for discrimination between the $K_L \to \pi^0\nu\bar{\nu}$ events and background events as explained later in Section 2.1.2.2. Using P_t and Z_{vtx}, we define a signal region in which signal events are expected to distribute, as shown in Figure 2.4. During an analysis of the $K_L \to \pi^0\nu\bar{\nu}$ search, we mask a certain region (blind region) including the signal region in the two-dimensional space of P_t versus Z_{vtx}. This is because we should eliminate a possible bias that could be introduced by looking at events in the signal region. This strategy is called the blind analysis, and the detailed procedure in the analysis is described in Section 6.1.

2.1.2 Background

Rejection of background events is the key to the search for $K_L \to \pi^0\nu\bar{\nu}$. As mentioned already, various background events are expected from many other K_L decays since their branching ratios are considerably larger than that of $K_L \to \pi^0\nu\bar{\nu}$. However, there are other background events originating from the so called beam-halo particles. The following sections briefly describe the sources of main background events and their mechanisms. Details are explained in Chapter 6.

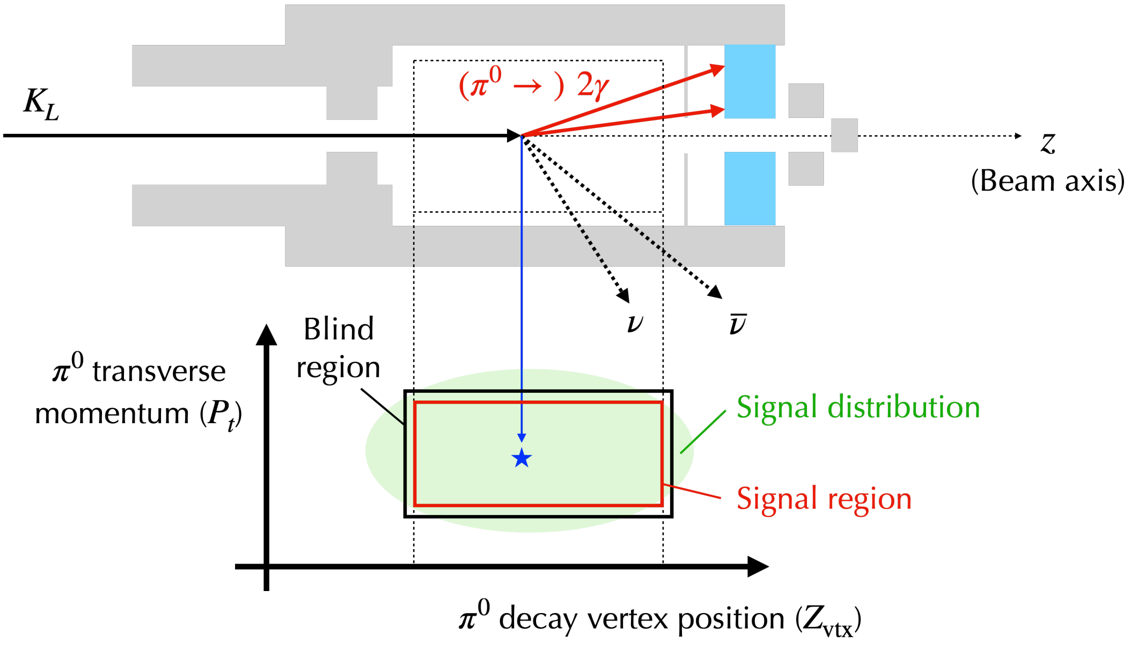

Figure 2.4: Schematic explanation of the signal region. The blue star represents a point of (Z_{vtx}, P_t) for a reconstructed π^0. The green region represents an expected signal distribution. The red and black boxes represent the signal region and the blind region, respectively.

2.1.2.1 Backgrounds from K_L Decays

Decays of K_L can be sources of background events. Depending on the decay mode, they have different background mechanisms. Main K_L decay modes are listed in Table 2.1. $K_L \rightarrow \pi^\pm e^\mp \nu_e$, $K_L \rightarrow \pi^\pm \mu^\mp \nu_\mu$, and $K_L \rightarrow \pi^+\pi^-$ have two charged particles in the final state. They can leave two hits in the electromagnetic calorimeter. These events need to be rejected by detecting charged-particles with a charged-veto detector (CV) located in front of the calorimeter. $K_L \rightarrow 3\pi^0$, $K_L \rightarrow \pi^+\pi^-\pi^0$, and $K_L \rightarrow \pi^0\pi^0$ have more than two particles in the final state. These events need to be rejected by detecting extra photons or $\pi^\pm$ with hermetic veto detectors.

$K_L \rightarrow 2\gamma$ has only two photons in the final state, which is exactly the same as the signal case. This decay, however, can be rejected based on kinematics of the two-body decay. Transverse momenta of the two photons in $K_L \rightarrow 2\gamma$ should be balanced, and thus reconstructed π^0 P_t tends to be small while the signal tends to have large P_t. The hit positions of the two photons from the $K_L \rightarrow 2\gamma$ decay are located symmetrically around the beam axis. Based on these differences, the background events from $K_L \rightarrow 2\gamma$ can be distinguished. Figure 2.5 shows schematic views of background events from $K_L \rightarrow \pi^\pm e^\mp \nu_e$, $K_L \rightarrow \pi^0\pi^0$, and $K_L \rightarrow 2\gamma$.

2.1.2.2 Backgrounds from Scattered Particles

Most of the beam particles reach the detector entrance without scatterings and are localized in the central beam region. However, small amount of beam particles that are scattered at some components in the beam line can also reach the detector and be sources of background events. The former beam component is referred to as the “beam-core” particles and the latter is referred to as the “beam-halo" particles. If beam-halo particles get into the KOTO detector and decay into

Table 2.1: Main decay modes of K_L and their branching ratios [1].

Decay mode	Branching ratio
$K_L \to \pi^\pm e^\mp \nu_e$	$(40.55 \pm 0.11)\%$
$K_L \to \pi^\pm \mu^\mp \nu_\mu$	$(27.04 \pm 0.07)\%$
$K_L \to 3\pi^0$	$(19.52 \pm 0.12)\%$
$K_L \to \pi^+\pi^-\pi^0$	$(12.54 \pm 0.05)\%$
$K_L \to \pi^+\pi^-$	$(1.967 \pm 0.010) \times 10^{-3}$
$K_L \to \pi^0\pi^0$	$(8.64 \pm 0.06) \times 10^{-4}$
$K_L \to 2\gamma$	$(5.47 \pm 0.04) \times 10^{-4}$

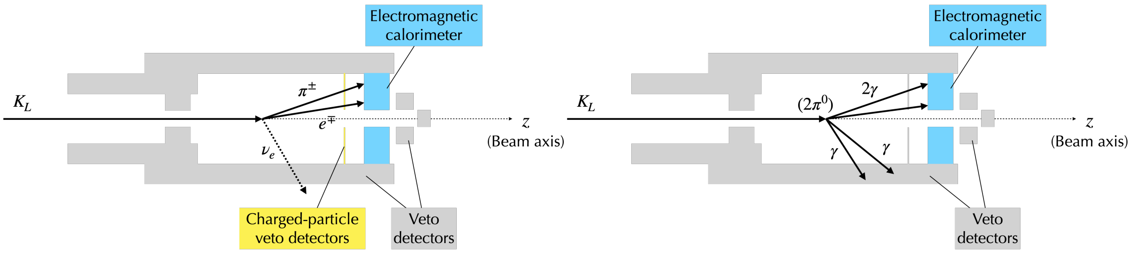

(a) $K_L \to \pi^\pm e^\mp \nu_e$ (b) $K_L \to \pi^0\pi^0$

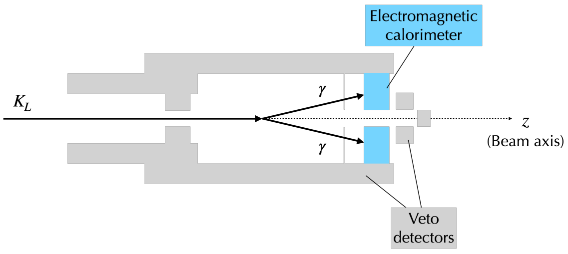

(c) $K_L \to 2\gamma$

Figure 2.5: Examples of background events from (a)$K_L \to \pi^\pm e^\mp \nu_e$, (b)$K_L \to \pi^0\pi^0$, and (c)$K_L \to 2\gamma$. In order not to misidentify these events as a signal event, veto detectors should never miss charged particles and extra photons. Besides, event selection based on kinematic variables such as P_t should be required. Otherwise, these events could fake a signal event.

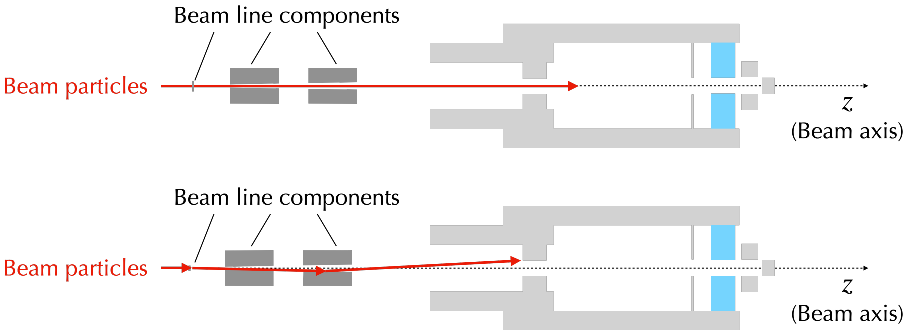

Figure 2.6: Schematic view of incident particles. Beam-core particles (top) come into the KOTO detector directly while beam-halo particles (bottom) undergo scatterings at beam line components before they reach the detector.

daughter particles or hit some detector material generating secondary particles, they could fake a signal event. Figure 2.6 shows schematic views of beam-core and beam-halo particles. Details of the beam line are described in Section 2.4.

Beam-halo neutrons are the sources of three types of background events: the hadron-cluster background, the CV-η background, and the upstream π^0 background. The hadron-cluster background occurs when a beam-halo neutron hits the calorimeter leaving two hadronic showers, as shown in Figure 2.7. A neutron produced in the primary shower induced by the incident neutron can also make a secondary shower in the calorimeter.

The CV-η background occurs when a beam-halo neutron hits the CV detector and generates an η meson which decays[2] into two photons with a branching ratio of 39.4% [1], as shown in Figure 2.7. Although CV is located downstream of the signal region, the reconstructed Z_{vtx} can be shifted upstream into the signal region because the invariant mass for the signal case is m_{π^0}, which is about four times smaller than the η mass[3].

The upstream π^0 background occurs when a beam-halo neutron hits the upstream detector and generates a π^0, which decays into two photons, as shown in Figure 2.7. Although the upstream detectors are located outside the signal region, the reconstructed Z_{vtx} can be shifted downstream into the signal region if energies of the two photons are mismeasured in the calorimeter.

Beam-halo K_L's are also a source of background events. As mentioned in Section 2.1.2.1, the $K_L \to 2\gamma$ decay can be distinguished from the signal case using the difference in the P_t distribution and the back-to-back decay property. However, the beam-halo K_L scattered away from the beam core does not decay on the beam axis, and also the assumed invariant mass of π^0 is smaller than the actual mass of K_L. For these reasons, the reconstructed P_t can be large enough to be in the signal region. Figure 2.8 shows a schematic view of the beam-halo $K_L \to 2\gamma$ background.

Finally, it turned out that the neutral beam contains a small amount of $K^\pm$'s which are also a source of background events, as already mentioned. $K^\pm$'s are generated due to interactions of K_L or $\pi^\pm$ produced from decays of K_L at the downstream collimator, and they can enter the detector. In particular, the $K^\pm \to \pi^0 e^\pm \nu$ decay is the most dominant background. In this decay, the π^0 decays into two photons and the $e^\pm$ is the only other detectable particle. When the $e^\pm$ is emitted backward, it tends to have low energy and not to be detected. Figure 2.9 shows a schematic view

---

[2] The lifetime of η is about 5×10^{-19} s [1].

[3] $M_\eta = 547.862\,\mathrm{MeV}/c^2 (\sim 4 \times M_{\pi^0})$ [1].

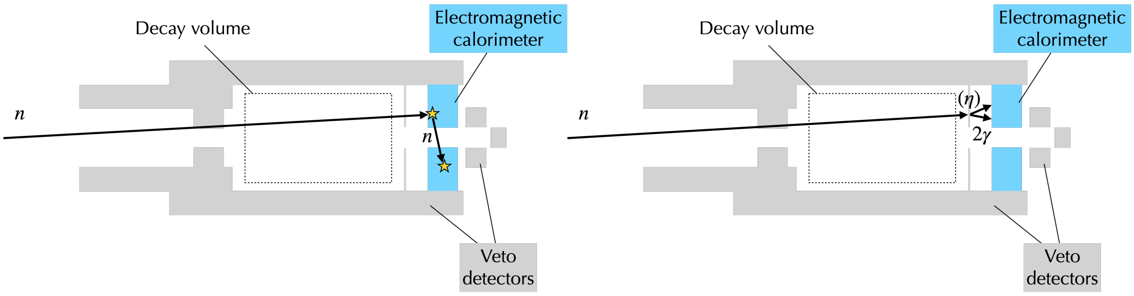

(a) Hadron-cluster background (b) CV-η background

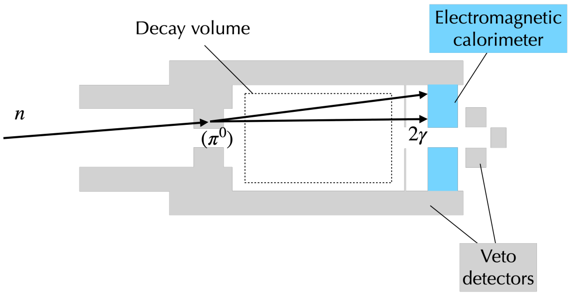

(c) Upstream π^0 background

Figure 2.7: Schematic views of the background events from beam-halo neutrons.

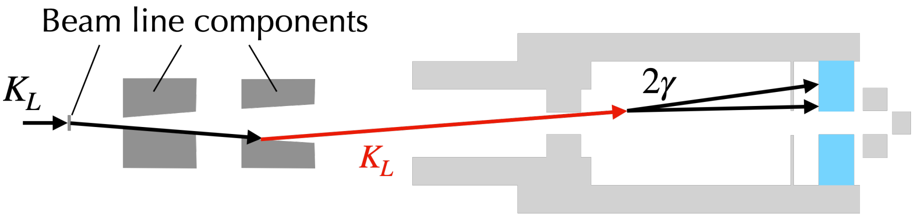

Figure 2.8: Schematic view of the beam-halo $K_L \to 2\gamma$ background.

of the $K^\pm \to \pi^0 e^\pm \nu$ background.

2.1.3 Branching Ratio and Single Event Sensitivity

The branching ratio for $K_L \to \pi^0 \nu \bar{\nu}$ obtained by a measurement can be written as

$$\mathcal{B}(K_L \to \pi^0 \nu \bar{\nu})^{\text{meas}} = \frac{N_{K_L \to \pi^0 \nu \bar{\nu}}}{N_{K_L\,\text{decay}}} \tag{2.4}$$

$$= \frac{N_{\text{sig}}}{N_{K_L\,\text{decay}} \cdot \epsilon_{\text{sig}}}. \tag{2.5}$$

The number of $K_L \to \pi^0 \nu \bar{\nu}$ decays ($N_{K_L \to \pi^0 \nu \bar{\nu}}$) can be obtained from the expected number of signal events (N_{sig}) divided by the signal detection efficiency (ϵ_{sig}). As will be described in Chapter 6, the number of K_L decays ($N_{K_L\,\text{decay}}$) can be measured with $K_L \to \pi^0 \pi^0$ decays that are collected simultaneously with the $K_L \to \pi^0 \nu \bar{\nu}$ data and the signal detection efficiency can be estimated using the GEANT4-based [69, 70, 71] Monte Carlo (MC) simulation.

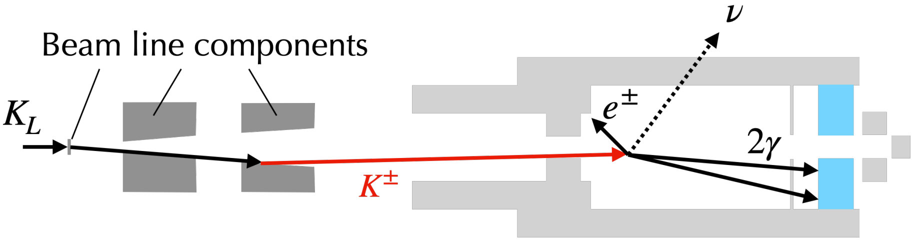

Figure 2.9: Schematic view of the $K^\pm \to \pi^0 e^\pm \nu$ background.

To introduce a quantity called the single event sensitivity (SES), Equation 2.5 can be transformed into the following,

$$\mathcal{B}(K_L \to \pi^0 \nu \bar{\nu})^{\text{meas}} = N_{\text{sig}} \cdot SES, \tag{2.6}$$

where

$$SES = \frac{1}{N_{K_L \text{ decay}} \cdot \epsilon_{\text{sig}}}. \tag{2.7}$$

By definition, SES represents the branching ratio equivalent to the observation of one signal event. Thus, the expected number signal events can be expressed as $\mathcal{B}(K_L \to \pi^0 \nu \bar{\nu})/SES$. As can be seen in Equation 2.6, the branching ratio can be determined or constrained by estimating N_{sig} and SES obtained from an experiment.

2.2 J-PARC Accelerator

J-PARC provides a world-class high-energy proton beam using three acceleration systems: a 400-MeV linear accelerator (Linac) [72, 73], a 3-GeV rapid cycling synchrotron (RCS) [74], and a 30-GeV[4] main ring (MR) [75], as shown in Figure 2.10. In the Linac, 50-keV negative hydrogen ions (H^-) are provided and accelerated up to 400 MeV. The accelerated H^- ions make protons via charge-exchange with a stripper foil at the RCS injection. The RCS has a three-fold symmetric lattice over its circumference of 348.333 m. In the RCS, two bunches of protons are accelerated up to 3 GeV at a repetition rate of 25 Hz. The RCS beam is transported to the Materials and Life science experimental Facility (MLF) and the MR. The MR has a three-fold symmetry and a circumference of 1567.5 m. In the MR, two bunches of protons from the RCS are injected four times, and a total of eight bunches are accelerated up to 30 GeV.

The MR has two beam extraction modes: fast extraction (FX) and slow extraction (SX), each of which delivers the beam to a different facility, as shown in Figure 2.11. The FX mode delivers the beam to the neutrino beam line using fast-kicker magnets which extract all of the beam bunches within a one-turn time period after the beam energy has been ramped up to 30 GeV. On the other hand, the SX mode delivers the beam to the Hadron Experimental Facility slowly with a duration of two seconds called a spill. The beam extraction cycle is then repeated with each repetition rate for the beam delivery. The KOTO experiment is conducted at the Hadron Experimental Facility and thus uses the beam during the MR operation with the SX mode. One of the important

---

[4] The design value of the beam energy is 50 GeV.

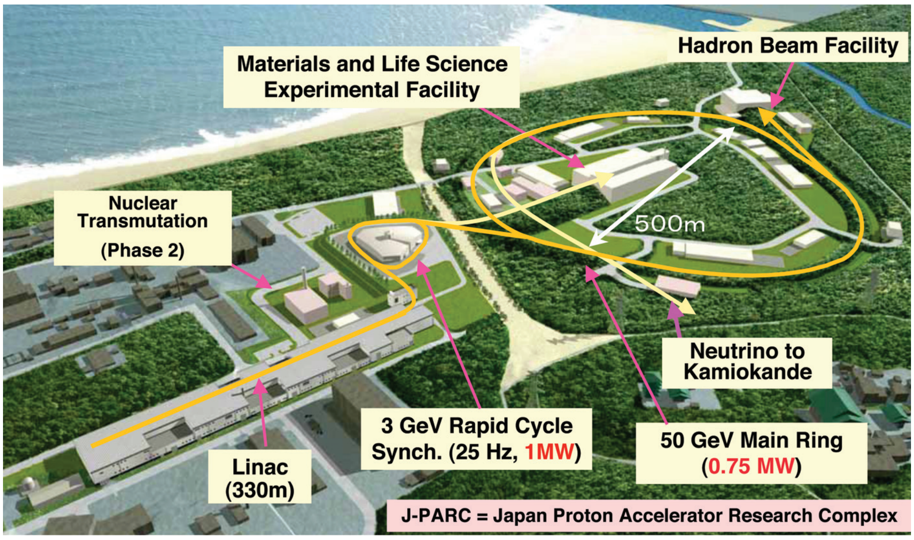

Figure 2.10: Entire view of J-PARC. The figure is quoted from Ref. [63].

measures to show the beam performance is the beam power defined as

$$P = \frac{N_p}{t_{\text{cycle}}} \cdot E_p, \tag{2.8}$$

where N_p represents the number of protons provided during a spill, t_{cycle} represents a repetition cycle, and E_p represents the proton energy. From the viewpoint of accumulating a large number of K_L particles to study $K_L \to \pi^0 \nu \bar{\nu}$, a higher beam power is more desirable. An extraction process with a typical operation cycle for both the FX and SX modes is shown in Figure 2.12. During the beam operation with the SX mode in 2021, the maximum beam power was 64 kW and the repetition cycle was 5.2 seconds.

In the SX mode, the beam is debunched by switching off the radio frequency power at 30 GeV in order for a spill to have a flat time structure in the beam intensity. The reason of making a flat spill structure is that, for experiments using the SX beam, a low instantaneous rate of beam particles is important to avoid event pileups in particle detectors. Although a flat time structure of spills is ideal, there exist spike-like time structures arising from current ripples of the MR power supplies [75]. The spill flatness can be quantified with the spill duty factor defined as

$$\frac{\left\{\int_0^T I(t)dt\right\}^2}{\int_0^T dt \cdot \int_0^T I^2(t)dt}, \tag{2.9}$$

where $I(t)$ represents the spill intensity and T represents the spill duration of 2 s in our case. The perfectly flat spill structure corresponds to a duty factor of 100%.

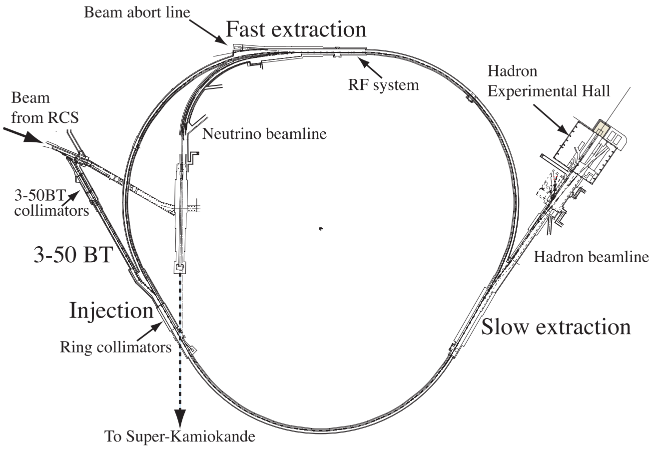

Figure 2.11: Schematic view of the MR. The figure is quoted from Ref. [75].

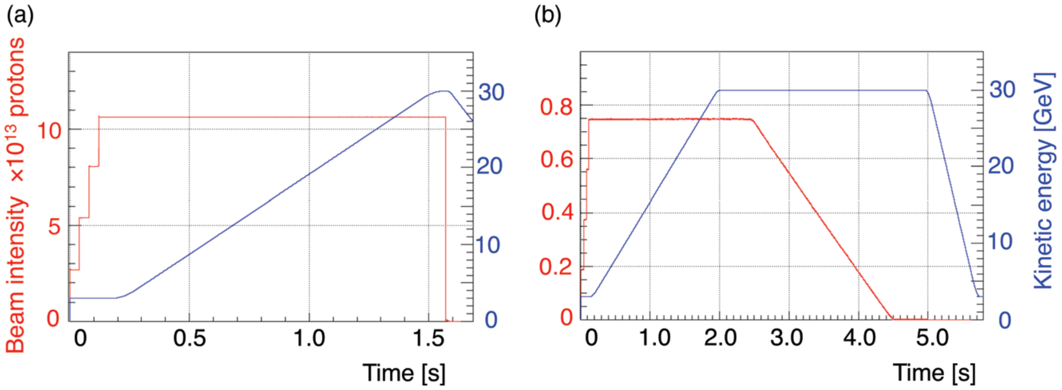

Figure 2.12: Intensity and kinetic energy profiles of a typical operation cycle for the (a) FX and (b) SX modes. The figure is quoted from Ref. [75]. For this figure, the repetition cycle times and delivered beam powers are 2.56 s and 200 kW for the FX mode and 6.0 s and 6 kW for the SX mode. Note that these parameters have been updated in the recent beam operations. During the beam operation with the SX mode in 2021, the maximum beam power was 64 kW and the repetition cycle was 5.2 seconds.

2.3 Hadron Experimental Facility

One of the beam destinations from the MR is the Hadron Experimental Facility (HEF), in which the KOTO experimental area is located. The proton beam is transported through a beam-switching yard (SY) to the HEF [76]. A schematic layout of the SY and the HEF is shown in Figures 2.14 and 2.13. The protons hit the production target in the HEF and create many secondary particles such as kaons and pions, which are used for various experiments. The production target is called the T1 target and was replaced several times in the past to accept a higher beam power. The T1 target used from 2014 to 2019 [77] was replaced in November, 2019 with the current target [78]. Figure 2.15 shows schematic drawings and a photograph of the current T1 target. Two 66-mm-long gold blocks are placed on a copper block in which cooling water pipes are embedded. This structure is basically the same as the previous target. For the current target, a gold block is vertically separated into two with a gap of 0.3 mm to cope with the thermal expansion. The maximum beam power with the new target is considered to be 95 kW for a 5.2 s beam duration [78].

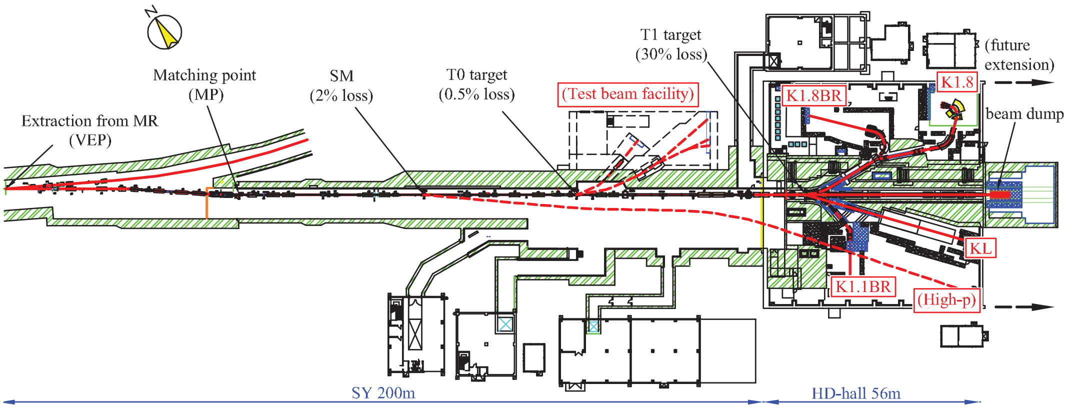

Figure 2.13: Schematic layout of the beam lines from the MR to the HEF. The figure is quoted from Ref. [76].

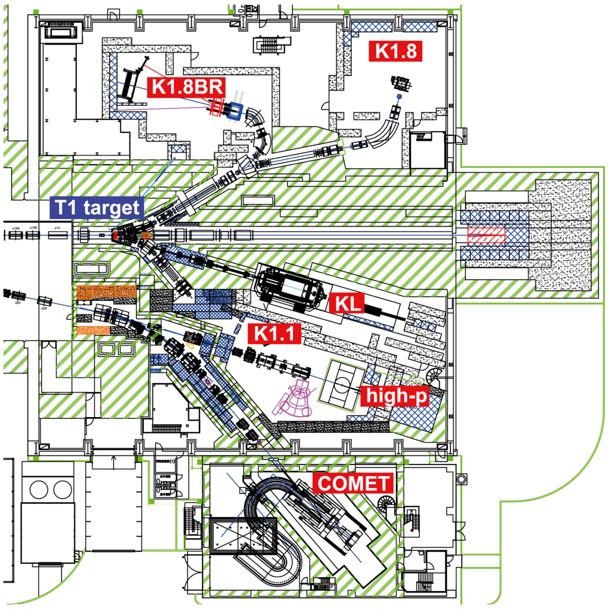

Figure 2.14: Schematic layout of the HEF. Many nuclear and particle physics experiments including KOTO are conducted in the HEF. The names shown in red indicate their locations in the HEF. The KOTO experimental area is denoted as KL. The figure is quoted from Ref. [79].

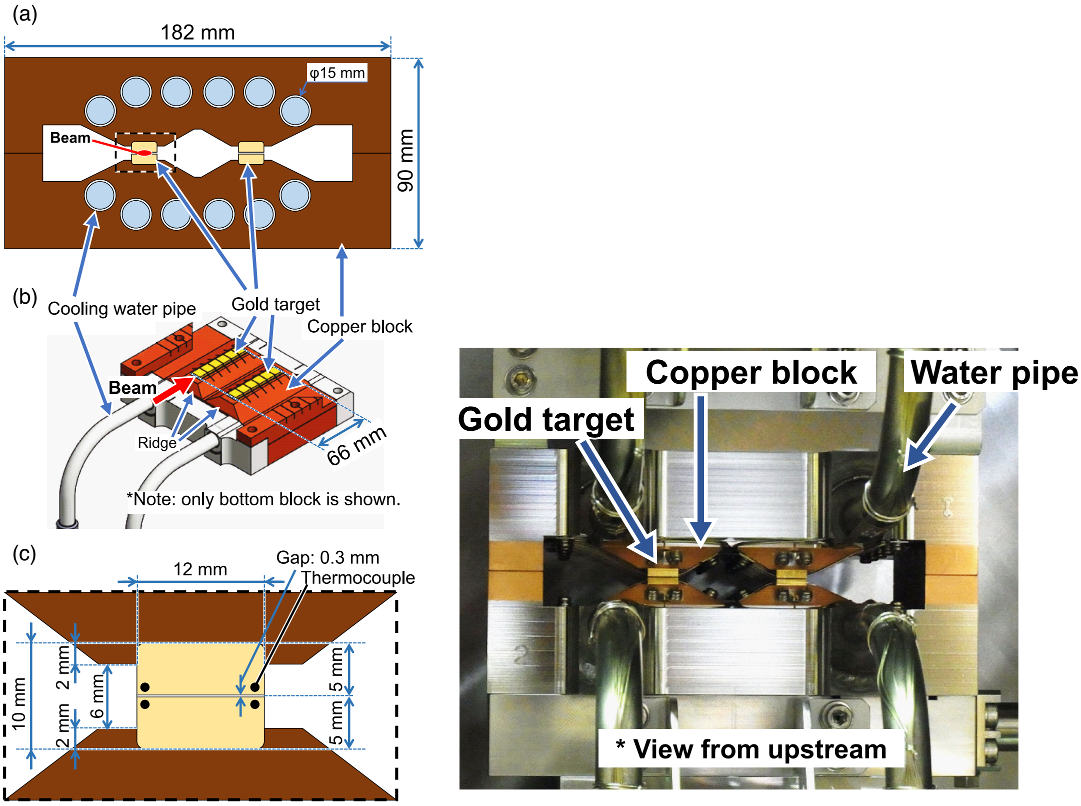

Figure 2.15: Schematic drawings (left) and a photograph (right) of the T1 target. The left drawings show the cross-sectional view (a), the lower half of the target (b), and the expanded view (c). The figures are quoted from Ref. [78].

2.4 KL Beamline

Particles generated at the T1 target are then guided to the experimental area for KOTO through a 20-m-long beam line, as shown in Figure 2.16. The beam line for KOTO, "KL beamline", is located at a production angle of 16° with respect to the primary proton beam line. The KL beamline was designed based on the requirements stated in Section 2.1.1 [80]. Figure 2.17 shows a schematic layout of the KL beamline components. The KL beamline is long enough to eliminate short-lived particles such as K_S and hyperons. A 7-cm-thick lead absorber is placed at the most upstream region in the KL beamline to reduce the number of photons in the beam. There are two collimators: the 1st collimator located upstream with a length of 4 m and the 2nd collimator located downstream with a length of 5 m. These collimators were designed to reduce beam-halo neutrons. The size of the beam at the exit of the beam line is $8 \times 8\,\mathrm{cm}^2$.

The magnet located between the two collimators applies a magnetic field of 1.2 T[5] to sweep out charged particles. There is a rotational beam plug made of brass right behind the sweeping magnet, as shown in Figure 2.16 (not shown in Figure 2.17). The plug is shaped like a disk with a diameter of 600 mm and a height of 250 mm, and has a horizontal hole with a diameter of 150 mm, as shown in Figure 2.18. When the plug is closed, its effective thickness along the beam axis is 450 mm. The nuclear interaction length (λ_I) of brass is 165 mm [1], and thus the plug thickness corresponds to $2.7\lambda_I$. The plug can be closed to stop most of the beam particles except for ones with high penetration, such as charged pions and muons. This enables us to enter the experimental area at lower radiation level during accelerator operation and also to take data for detector calibration using charged pions and muons.

The K_L momentum was measured in the past experiments [81, 82] and has a peak around $1.4\,\mathrm{GeV}/c$, as shown in Figure 2.19. The K_L flux was measured to be 2.1×10^{-7} $K_L's$ per proton on target (POT) [83].

---

[5] The design value of the magnetic field strength was 2 T, as written in Figure 2.17.

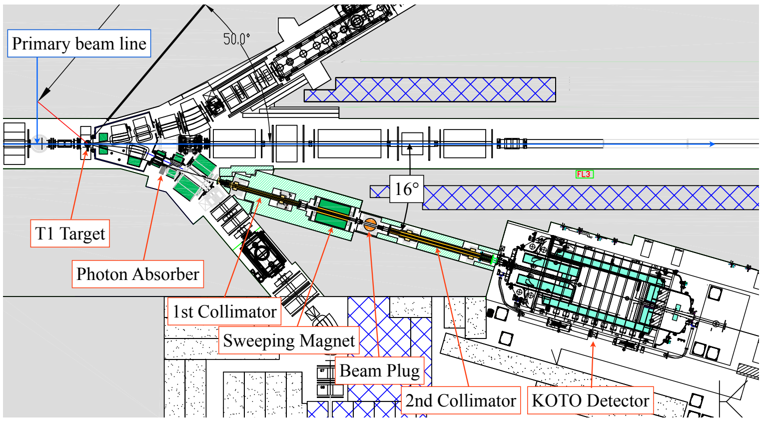

Figure 2.16: Schematic top view of the KL beamline and the KOTO experimental area in the HEF. The KL beamline guides secondary particles generated at the T1 target with an extraction angle of 16° to the KOTO detector.

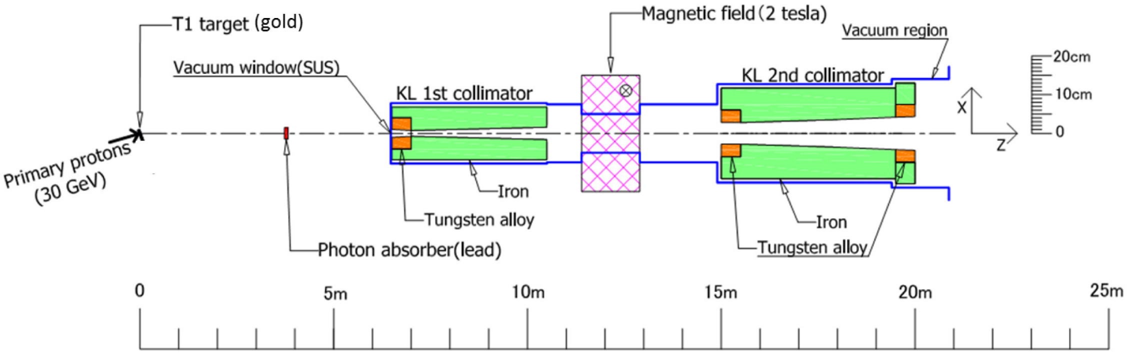

Figure 2.17: Schematic layout of the KL beamline. The figure is quoted from Ref. [84].

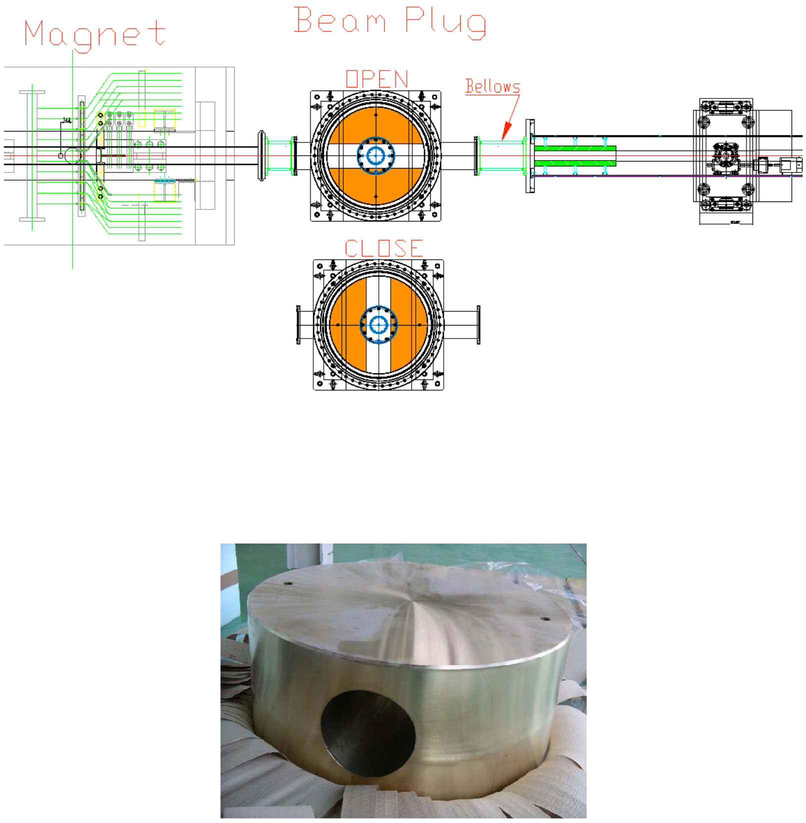

Figure 2.18: Schematic top view (top) and a photograph (bottom) of the rotational beam plug. The plug is open during usual data-taking, while it is closed by 90°-rotation when access to the experimental area or data-taking for detector calibration is needed.

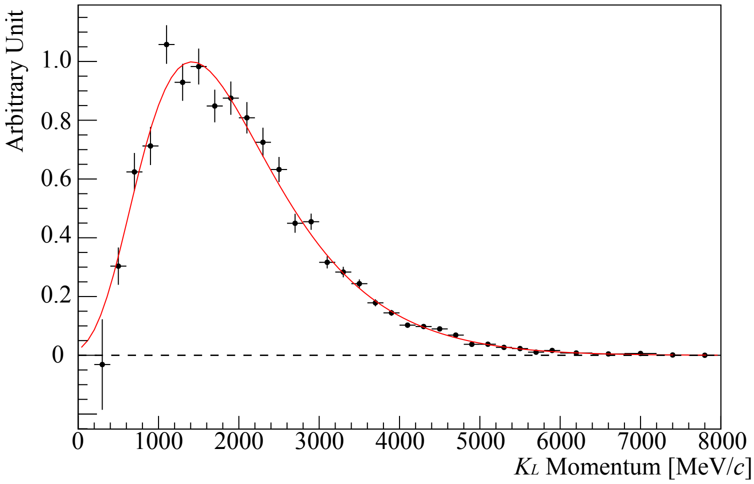

Figure 2.19: Distribution of the K_L momentum at the exit from the beam line. The black points are experimental data and the red curve is a Gaussian fit. The figure is quoted from Ref. [82].

2.5 KOTO Detector

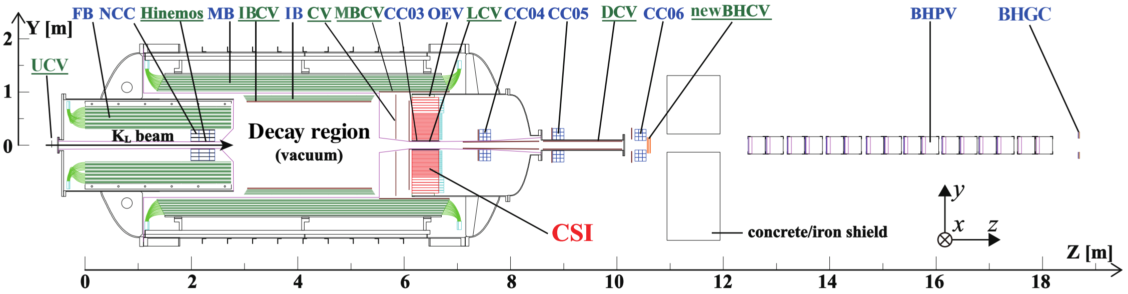

Figure 2.20: Cross-sectional view of the KOTO detector. The beam enters from the left. Detector components with their abbreviated names written in blue (in green and underlined) are photon (charged-particle) veto counters.

The KOTO detector is located 21.5 m away from the T1 target[6]. The detector was designed to be dedicated to the $K_L \to \pi^0 \nu \bar{\nu}$ search, and the subdetectors can be categorized into two types based on their roles:

1. Electromagnetic calorimeter (denoted as CSI in Figure 2.20) to measure energies and positions of two photons produced from the π^0 decay.

2. Veto detectors to ensure that there are no other detectable particles.

As emphasized in Section 2.1.2, the veto detectors are required not to miss any extra particles to reject background events. Therefore, the decay volume is fully surrounded by hermetic veto detectors. Figure 2.20 shows a schematic view of the KOTO detector. The x-axis (horizontal) and y-axis (vertical) are defined using the right-handed coordinate system. As shown in Figure 2.20, the origin of the z-axis is the upstream edge of the detector named FB.

The decay volume is kept in vacuum at $O(10^{-5})$ Pa so that production of π^0's due to beam neutrons interacting with residual gas can be suppressed. The decay volume is separated from the detector space with thin films called the “membranes" drawn in purple lines in Figure 2.1.2 because of outgassing from the detector components. Thus, the detector space is kept at a lower vacuum level of 0.1 Pa, and the many subdetectors are required to work under this vacuum condition.

As described in Section 1.5, the KOTO detector system was upgraded to improve the background reduction capability. Table 2.2 summarizes the upgraded subdetectors. The following sections describe details on each subdetector.

2.5.1 CsI Electromagnetic Calorimeter

The CsI electromagnetic calorimeter (CSI) is composed of undoped CsI crystals [85] whose properties are shown in Table 2.3. These crystals were originally used for the KTeV experiment at Fermi National Accelerator Laboratory [86]. The primary role of CSI is to measure energies and positions of photons. Figure 2.21 shows a schematic view of CSI. Inside a stainless steel cylinder

---

[6] 1.5 m downstream from the KL beamline exit.

Table 2.2: Upgrades of the KOTO detector system after the data-taking in 2018.

Subdetector	Installation/upgrade period	Purpose
Front-side readout of CSI	Between the data-takings in 2018 and 2019	Suppression of the hadron-cluster background by upgrading the signal readout system
DCV	Between the data-takings in 2018 and 2019	Suppression of the background from $K_L \to \pi^+\pi^-\pi^0$ by replacing the downstream charged-veto detector with a new detector
UCV	Between the data-takings in 2020 and 2021	Suppression of the $K^\pm$ background by installing an upstream charged-veto detector

with a diameter of 1.9 m, there are 2716 undoped CsI crystals with a length of 50 cm along the z-axis. The radiation length (X_0) of CsI is 1.85 cm [1], and thus the length of CsI crystals is equivalent to $27X_0$. The 2240 small crystals have a cross-sectional area of $2.5 \times 2.5\,\mathrm{cm}^2$, and are stacked in the central $1.2 \times 1.2\,\mathrm{m}^2$ region. The innermost $20 \times 20\,\mathrm{cm}^2$ region around the beam axis has no crystals so as to allow beam particles to pass through[7]. The other 476 large crystals have a cross-sectional area of $5.0 \times 5.0\,\mathrm{cm}^2$, and are stacked in the peripheral region around the small crystals. The outermost edge inside the cylinder is filled with another subdetector named OEV which is described in Section 2.5.9.

A photon hitting CSI causes an electromagnetic shower spreading over multiple crystals . The scintillation light generated in each crystal is collected from the downstream end of the crystal with a photomultiplier tube (PMT). There is a UV transmitting filter inserted between the crystal and the PMT to eliminate a slow component of the scintillation light emitted in CsI.

Table 2.3: Properties of undoped CsI crystals [1].

Parameter	Value
Radiation length (X_0)	1.86 cm
Nuclear interaction length (λ_I)	39.3 cm
Decay time (τ_{decay})	10 ns and 36 ns (fast component)[a] $\sim 1\,\mu$s (slow component)[b]
Molière radius (R_M)	3.57 cm

[a] The fast component with maximum light output at a wavelength of 315 nm.

[b] The slow component with maximum light output at a wavelength of 480 nm. As explained in the text, this component is cut by a filter.

---

[7] As shown in Figure 2.20, the detectors called LCV and CC03 are placed at the inner surfaces of this space. Thus, the area of the actual hole region is $15 \times 15\,\mathrm{cm}^2$.The detail of each detector is described in Section 2.5.10.

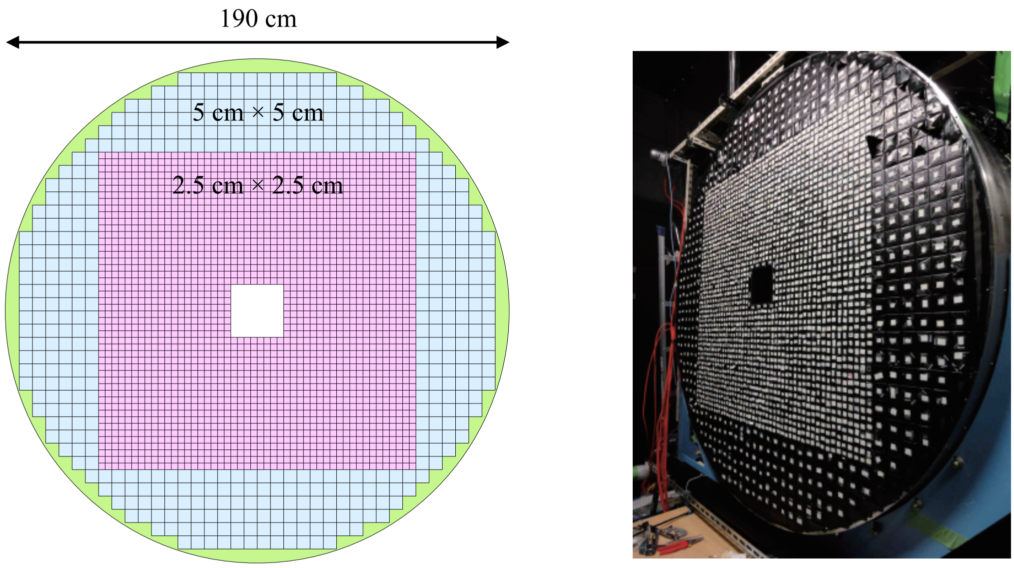

Figure 2.21: Schematic front view (left) and a picture (right) of CSI. The purple (blue) area represents the region composed of the small (large) crystals. The empty region at the center corresponds to the beam hole. The outer green region is filled with OEV.

As described in Section 2.1.2, the hadron-cluster background is one of the dangerous backgrounds in the $K_L \to \pi^0 \nu \bar{\nu}$ search, and it only makes two hadronic showers in CSI. Suppression of this background motivated an introduction of a both-end readout method for CSI. This background can be suppressed based on "*depth*" of the interaction by the beam-halo neutron for the following reason. As shown in Table 2.3, the nuclear interaction length of CsI is much larger than the radiation length. In other words, incident neutrons are likely to interact in CsI crystals over a broad range along the z-axis while incident photons from $K_L \to \pi^0 \nu \bar{\nu}$ interact in a shallow region from the upstream end.

The depth of the interaction position can be translated into the difference in arrival timings of scintillation light between the upstream and downstream ends of the crystal. Thus, silicon photomultipliers called the Multi-Pixel Photon Counter (MPPC) were attached on the upstream surface of CSI to measure a timing difference. Figure 2.22 shows a schematic explanation of the both-end readout method for each crystal using a PMT and an MPPC. In 2018, a total of 4080 MPPCs were installed in CSI [87]. The small crystal has one MPPC on its upstream surface while the large crystal has four MPPCs. In order to reduce the number of readout channels, output signals are connected and summed as shown in Figure 2.23. Details on this connection scheme can be found in Ref. [88]. This method reduced the total number of readout channels for MPPCs to be 256, as shown in Figure 2.24. Figure 2.25 shows photographs of MPPCs that are attached on CSI. Since the MPPCs are irradiated by the neutral beam particles such as neutrons during accelerator operations, degradation of the performance on the discrimination between photon showers and hadronic showers is one of the concerns. The effect of radiation damage was thus studied in Ref. [89] concluding that the performance during the data-taking in 2021 was still at the required level. Details on the upgrade of CSI are also available in Refs. [90, 91, 92, 93, 94].

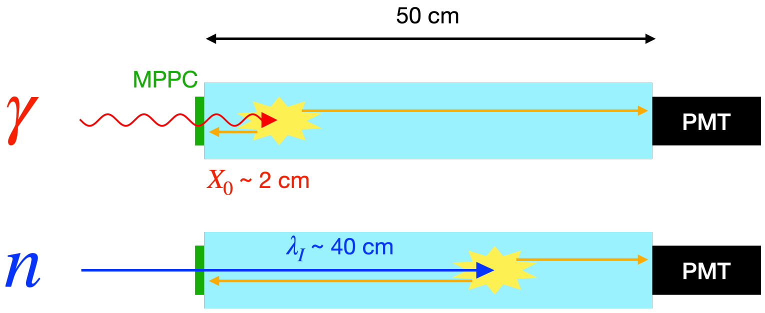

Figure 2.22: Concept of the both-end readout. While photons typically interact in the upstream region of the crystals (top), neutrons can go deep inside (bottom). The depth of the interaction position can be extracted by measuring arrival timings of scintillation light both at the upstream and downstream ends of the crystal.

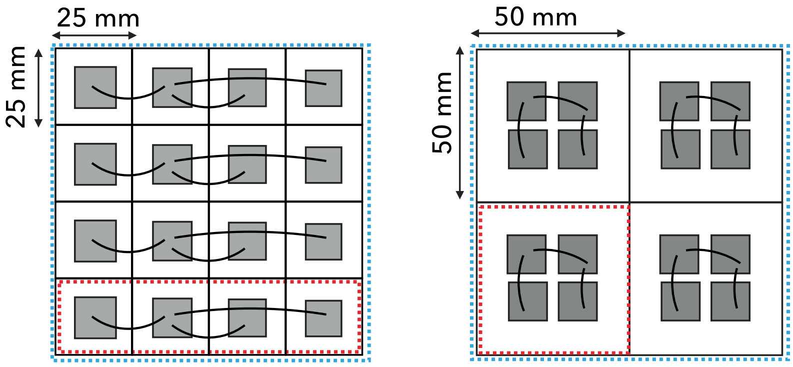

Figure 2.23: Schematic view of the connection of readout channels among MPPCs for 16 small crystals (left) and 4 large crystals (right). The grey squares represent MPPCs and the black lines represent cables connecting output signals across MPPCs. The output from every four MPPCs surrounded by a red dashed line are then summed into a single readout channel with the other three sets of outputs that are connected in the same manner. The figure is quoted from Ref. [93].

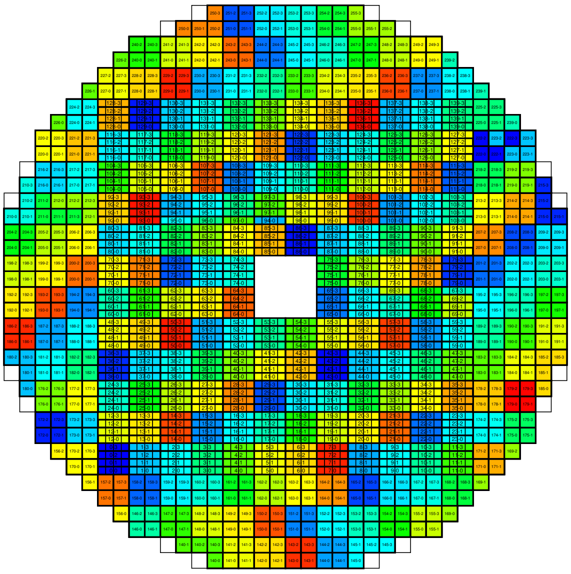

Figure 2.24: Alignment of the 256 readout channels for MPPCs. The output signals from adjacent crystals are displayed in the same color and read out as common channels. MPPCs are not attached to some of the outermost crystals shown in white. Due to misconnection of readout cables, a few channels do not properly sum signals from the adjacent crystals.

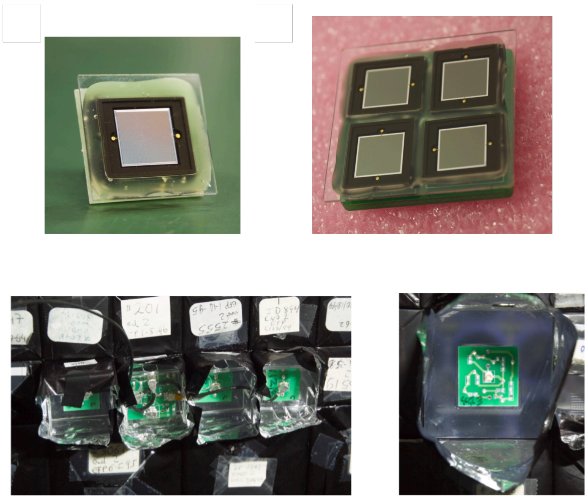

Figure 2.25: Photographs of MPPCs attached on the upstream surface of CsI crystals. The top two photographs show MPPCs that are used for a small (left) and a large (right) crystal. On the front surface of MPPC with a photosensitive area, a 0.5-mm-thick quartz plate is attached to make a flat surface. The bottom two photographs show the front view of small (left) and (large) crystals after installing MPPCs. The MPPC is equipped with its own circuit board for a power supply and signal readout. The top and bottom figures are quoted from Ref. [95] and Ref. [93], respectively.

2.5.2 Upstream Charged Veto

As described in Section 1.4, the top priority issue after the 2016–2018 data analysis was to establish a method to suppress the background from $K^{\pm}$ decays. Therefore, the Upstream Charged Veto (UCV) detector was developed in 2020 and installed before the data-taking in 2021. This detector was developed by the author of this thesis with collaborators in Osaka University. Figure 2.26 shows a photograph of UCV. As the name suggests, UCV is located at the upstream end ($z = -920\,\mathrm{mm}$) of the KOTO detector and is required to detect $K^{\pm}$'s contaminating the neutral beam. Before UCV was installed at this position, there was a vacuum chamber[8] in which a 3-mm-thick aluminum plate (Al target) can be inserted remotely to collect a neutron control sample described in Section 3.2.3.1. However, the location for this chamber was the only place in which UCV can be installed due to geometrical constraints. Thus, the vacuum chamber was replaced with a new one that is spacious enough to accommodate both the Al target and UCV together.

The basic design concept for UCV was to keep efficiency for $K^{\pm}$ with a small amount of material in the beam-core region. This is because placing UCV in the beam does not only mean that it works to detect $K^{\pm}$ but also that it could be a source of scatterings for beam particles. If incident particles are scattered, they might cause an increase in background events and accidental hits on other veto detectors, leading to extra loss of signal acceptance.

Therefore, we decided to develop UCV with 0.5-mm-square scintillating fibers[9]. Every 16 fibers are grouped into a unit of module as shown in Figure 2.27. The fibers are bundled at one of the fiber ends being fixed with a carbon sleeve and an optical epoxy at this end. The scintillation

---

[8] This vacuum chamber was used until the data-taking in 2020.

[9] Type SCSF-78 produced by Kuraray Co., Ltd. [96] was used.

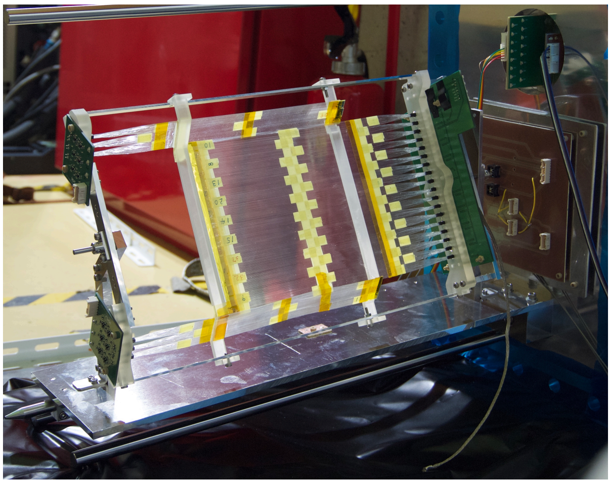

Figure 2.26: Picture of UCV taken from the downstream side before installation.

light generated in fibers is collected with MPPCs[10]. Figure 2.28 shows schematic views of the fixture of fiber modules and MPPCs. The module-end forms a 4×4 matrix of fibers corresponding to the cross-sectional area of $2\times2\,\mathrm{mm}^2$. They are attached to the photosensitive area of $3\times3\,\mathrm{mm}^2$ at each MPPC. The other ends of the fiber modules are covered with aluminized mylar.

A total of 18 modules are aligned to form a single-layer plane tilted by 25° from the perpendicular to the beam axis, as shown in Figure 2.29. By tilting the fiber plane, inefficiency arising from the inactive region of the fiber[11] for $K^{\pm}$ can be reduced while the effective material thickness along the beam axis increases[12]. Additionally, three more modules are placed both at the upper and lower regions with a small overlap with the center fiber plane in the vertical direction to expand the detection coverage. These modules are tilted by 45° from the center plane in the opposite direction. Signals from these modules are read out from the opposite side to the center modules so that UCV can fit in the vacuum chamber without geometrical constrains. On the bottom side of UCV, there is an LED to monitor the output signal.

Figure 2.30 shows the entire setup of UCV. The central coverage of $160\,\mathrm{mm}\times144\,\mathrm{mm}$ is large enough[13] for incident $K^{\pm}$'s specifically in the case where $K^{\pm}$'s pass through the beam-hole region at the z-position of the NCC detector described in Section 2.5.3. The $K^{\pm}$'s in such events are expected to distribute in the region of approximately $100\,\mathrm{mm}\times100\,\mathrm{mm}$ at the z-position of UCV, according to the simulation study as shown in Figure 2.31. Output signals from the MPPCs for a total of 24 modules are read out through the front-end circuit boards where the signal waveforms are shaped and amplified. To reduce the number of readout channels, every two output signals from the adjacent modules are summed into a single channel at another circuit board placed outside the vacuum chamber, which results in a total of 12 readout channels. Details on the development of UCV are available in Refs. [98, 99, 100]. UCV is an in-beam detector being highly irradiated, and thus MPPCs are expected to suffer from radiation damage similarly to CSI. During the accelerator operation in 2021, the accidental activities including a noise effect increased as dark current increased. The MPPCs were once replaced with new ones while the beam operation

---

[10] Type S13360-3075CS produced by HAMAMATSU PHOTONICS K.K. [97] was used.

[11] The single cladding thickness accounts for 2% of the entire fiber thickness [96].

[12] Angle optimization was studied in Ref. [98].

[13] The vertical length of 144 mm with the tilt of 0° corresponds to 131 mm with the tilt of 25°, which is still wide enough.

was suspended on the day for facility maintenance.

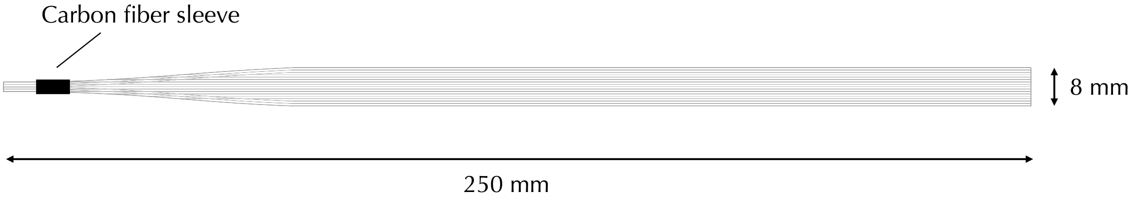

Figure 2.27: Schematic view of a fiber module. Each module is composed of 16 fibers that are aligned side by side. The fibers are bundled with a carbon fiber sleeve (black) around one of the module ends.

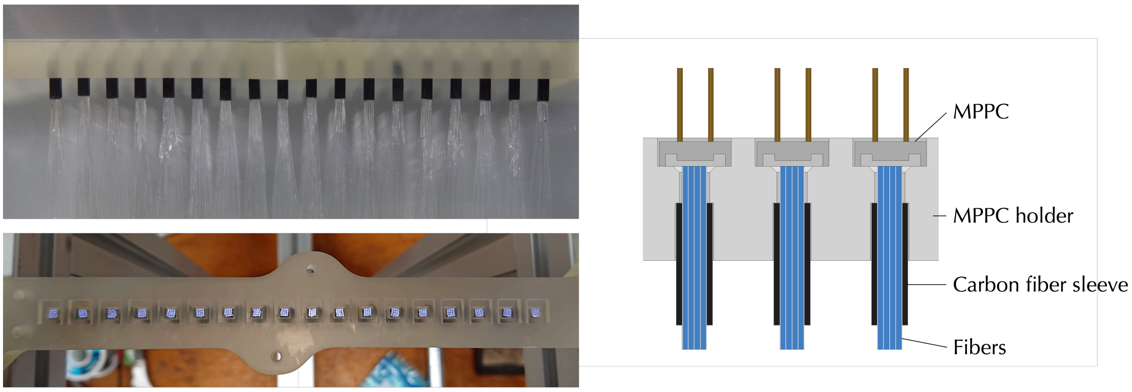

Figure 2.28: Schematic views of fixture of fibers and MPPCs. The left figures show a side view (top) and a cross-sectional view (bottom) of the fibers fixed to the support structure (MPPC holder) before putting MPPCs. The right figure shows the attachment of MPPCs to the fibers. Every16 fibers (blue) are bundled with a carbon fiber sleeve (black) and inserted into a hole in the MPPC holder (grey) made of plastic. Each MPPC (dark grey) is put in a dent from the opposite side with its photosensitive area oriented to the fiber end. The right figure is quoted from Ref. [98] with modifications.

2.5.3 Front Barrel

The Front Barrel (FB) detector is a photon-veto detector covering the upstream region of the decay volume. It is important to veto background events induced from K_L decays such as $K_L \to \pi^0\pi^0$ and $K_L \to 3\pi^0$ by detecting photons hitting the upstream region. FB is a 2.75-m-long cylindrical detector centered along the beam axis. It consists of 16 modules of lead-plastic sandwich detectors with a radial thickness of $16.5X_0$, as shown in Figure 2.32. Each module consists of 27 inner and 32 outer layers stacked in the radial direction. Each layer consists of 1.5-mm-thick lead and 5-mm-thick plastic scintillator sheets. Scintillation light is read out through wavelength-shifting (WLS) fibers embedded in scintillator layers. The scintillation light from the inner and outer layers of scintillator sheets for each module is collected by two separate PMTs from the upstream end. In total, the number of readout channels for FB is 32. Details on FB are available in Ref. [101].

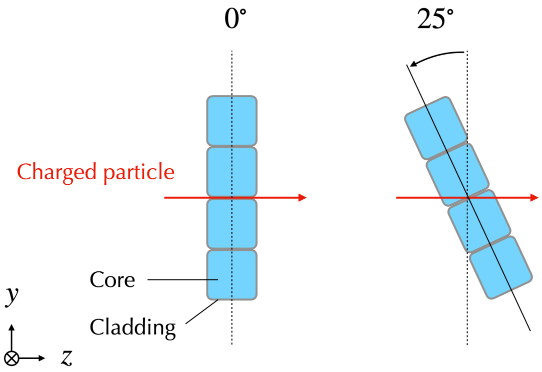

Figure 2.29: Cross-sectional view of the fibers at different angles. Tilting the fiber plane allows to reduce the number of events in which incident charged particles pass only through the cladding part of the fibers.

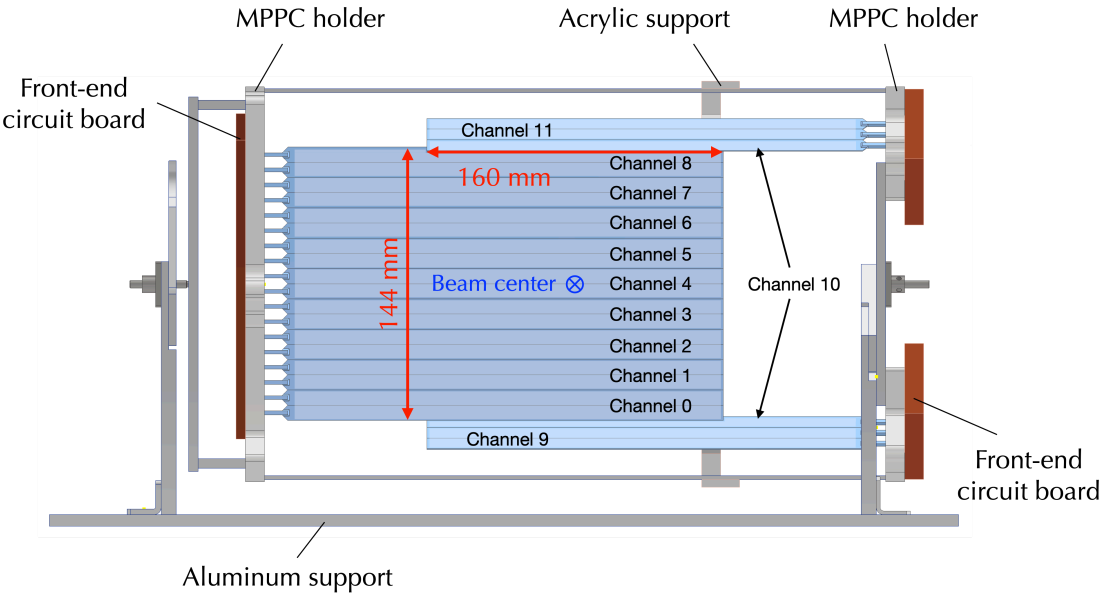

Figure 2.30: Schematic view of the entire setup of UCV from the upstream side. For this figure, the tilting angle is set to 0°. Only the channel 10 has a nonadjacent pair of inputs from the inner modules at the upper and lower regions. The figure is quoted from Ref. [98] with modifications.

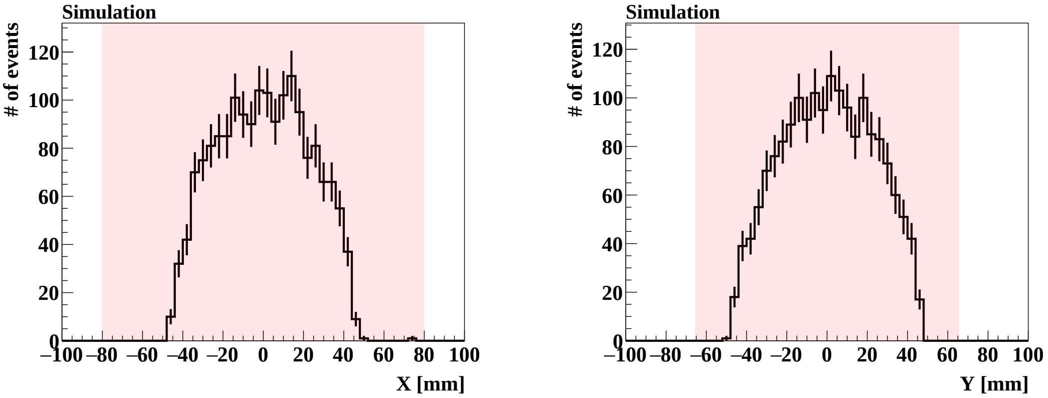

Figure 2.31: $K^{\pm}$ profile at the z-position of UCV estimated by simulation. The red shaded area indicates the region covered by UCV.

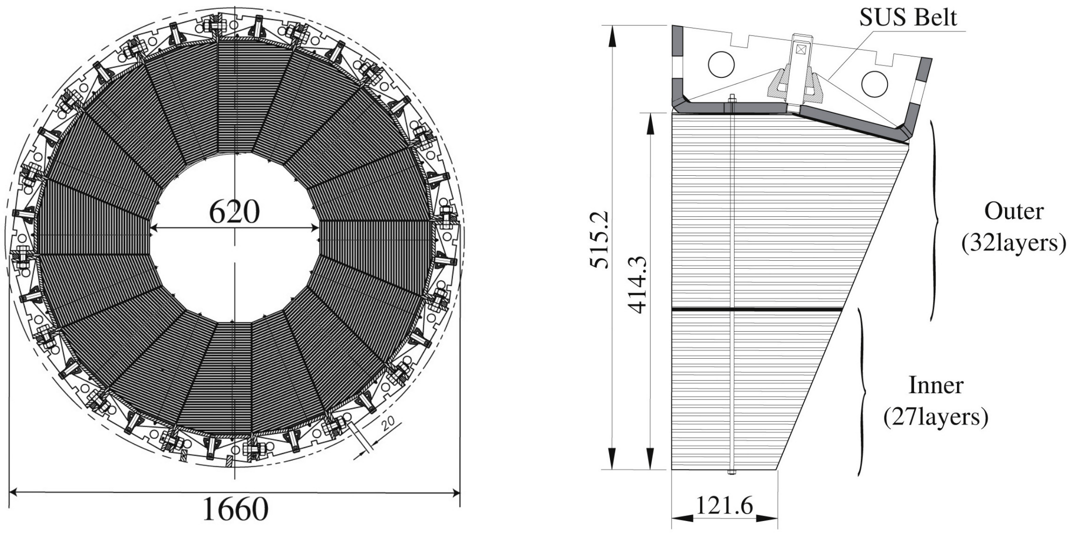

Figure 2.32: Cross-sectional view of FB (left) and an individual module (right). Scales in the figures are in units of mm. The figures are quoted from Ref. [101].

2.5.4 Neutron Collar Counter and Hinemos

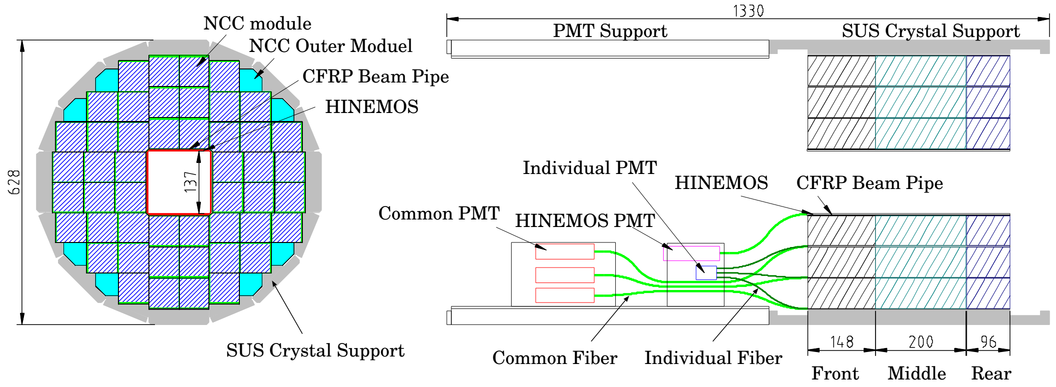

Figure 2.33: Schematic illustration of NCC. The left figure shows a cross-sectional view and the right figure shows a cut view where beam particles come from the left side. The figure is quoted from Ref. [68].

The Neutron Collar Counter (NCC)[102] is placed inside the downstream region of FB surrounding the beam axis. It is a photon-veto detector to reject background events induced from K_L decays by detecting photons. NCC is close to the beam and suffers from the relatively large flux of beam-halo neutrons. A large number of π^0's can be produced at NCC, and it can result in the upstream-π^0 background as described in Section 2.1.2.2. Thus, NCC should also detect secondary particles generated in the interaction of beam-halo neutrons.

NCC is composed of undoped CsI crystals with a length of about 45 cm in the beam direction. As shown in Figure 2.33, the majority of the detector region is filled with 48 inner modules and the rest is filled with 8 outer modules. For the inner modules, scintillation light from a crystal is read out through WLS fibers and is collected with a PMT. Each crystal used for inner modules is divided into three individual crystals referred to as a front, middle, and rear crystal, and they are optically separated. There are two different readout methods for inner modules: common readout and individual readout. The common readout collects output signals from all three individual crystals while the individual readout collects the output signal from each individual crystal separately. For the outer modules, crystals are not divided, and the output signal from each crystal is just read out with a PMT attached to the surface of the crystal. Details on NCC can also be found in Refs. [103, 104].

Even though the inner modules provide position-dependent information in the beam direction with the individual readout, data for individual crystals was not used for the main physics analysis in KOTO[14]. However, we utilized the data with individual readout for the 2021 data analysis for the following reason. As described in Section 1.4, there were three signal candidate events inside the signal region in the analysis of the 2016–2018 data. Investigation on these events revealed that one event out of three included significant waveforms in NCC which can be seen in Figure 2.34. In the common readout channel, the peak position is located outside the time window for veto (veto window), and thus, this event was not vetoed based on this waveform. However, there existed

---

[14] The data itself was recorded and stored as well as the common readout.

a clear peak in the individual rear channel within the veto window, while the front and middle crystals showed waveforms with different timings. This implies that the pulse located inside the veto window in the common channel was overlapped with an additional large pulse which is likely caused by an accidental hit, and consequently the time used for the veto decision was deviated. Although the probability of observing one event or more from this background was estimated to be only 2.2% in the 2016–2018 data analysis [61, 105], the individual readout channels were introduced in the 2021 data analysis aiming at further suppression of the background events due to pulse-overlaps.

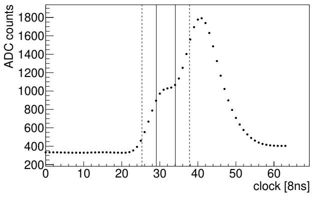

(a) NCC-Common

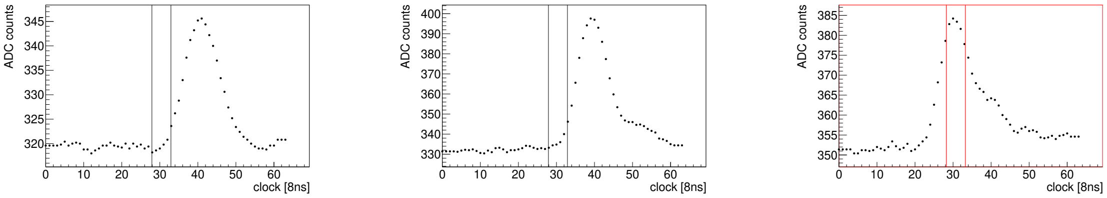

(b) NCC-Individual (front) (c) NCC-Individual (middle) (d) NCC-Individual (rear)

Figure 2.34: Waveforms observed in the common (top) and individual (bottom) readout channels. The analog waveform was digitized in the front-end electronics as explained in Section 2.6. The range between the solid (dashed) lines represents the time window (widened time window) used for the veto decision. The peak position of the pulse in the common channel shown in (a) indicates the time of the activity observed in the corresponding crystal. The figures are quoted from Ref. [105].

NCC modules are stacked with a 2-mm-thick beam pipe made of carbon fiber reinforced plastic (CFRP) in order to form a square-shape beam hole at the center as shown in Figure 2.33. The CFRP pipe, however, is an inactive material which could make a background source. For instance, a single $\pi^\pm$ produced from the $K_L \to \pi^+\pi^-\pi^0$ decay in the region of the second collimator might hit the CFRP pipe generating a π^0 through the charge-exchange interaction, and the rest of the decay products might hit the collimator wall leaving no information. In this case, such an event could be a background in the same way that the upstream π^0 event does.

Thus, a charged-veto detector named Hinemos[15] was installed further inside the CFRP pipe. The Hinemos detector consists of four plastic scintillator sheets covering the inner surface of the pipe. Scintillation light generated in each sheet is read out through WLS fibers and collected by a PMT. Details on the development of Hinemos can be found in Ref. [106].

---

[15] The name stands for the Horizontal Inner NCC Edge Mounted Scintillator.

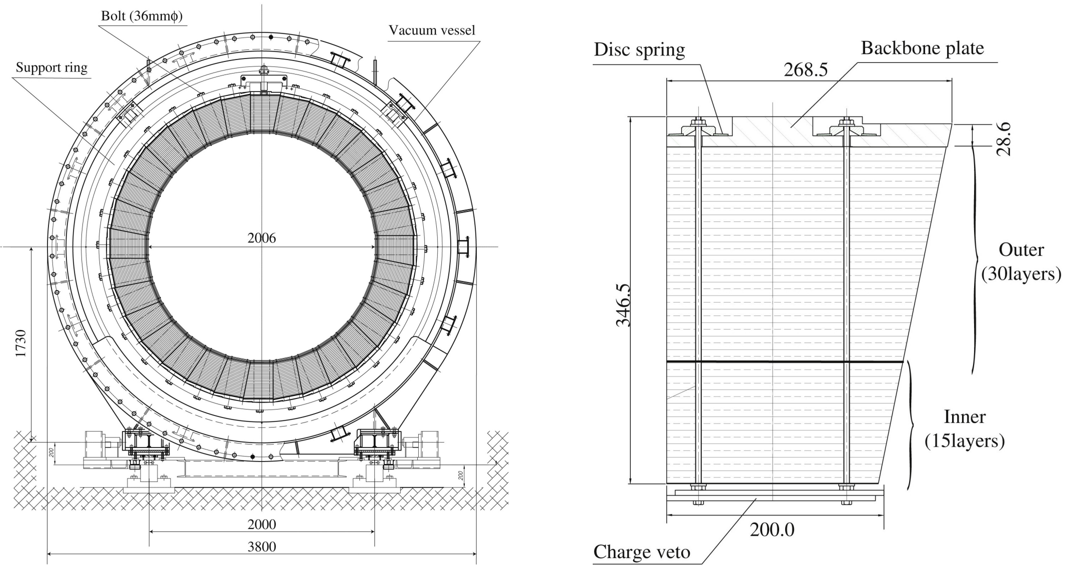

Figure 2.35: Cross-sectional view of MB (left) and an individual module (right). Charged veto written in the right figure illustrates a charged-particle detector that was used until the data-taking in 2015. This detector was replaced with another detector which is detailed in Section 2.5.7. Scales in the figures are in units of mm. The figures are quoted from Ref. [101].

2.5.5 Main Barrel

The Main Barrel (MB) detector is a photon-veto detector located in the middle section of the KOTO detector surrounding the decay volume. MB is required to detect photons to reject background events induced from the K_L decays. Figure 2.35 shows schematic views of MB. MB is a 5.5-m-long cylindrical detector with an outer diameter of 3.5 m. It consists of 32 modules of lead-plastic sandwich detectors with a radial thickness of $14.0X_0$, as shown in Figure 2.35. The design of each module is similar to FB. Each module consists of 15 inner and 30 outer layers stacked in the radial direction. Each layer consists of 1-mm-thick (2-mm-thick) lead and 5-mm-thick plastic scintillator sheets for inner (outer) modules as shown in Figure 2.36. Scintillation light is read out through WLS fibers embedded in scintillator layers. The scintillation light from the inner and outer layers of scintillator sheets for each module is collected by separate PMTs in the same manner for FB, but is also collected from the downstream end with the same configuration. In total, the number of readout channels for MB is 128, which is four times larger than that of FB. Details on MB are available in Ref. [101].

2.5.6 Inner Barrel

The Inner Barrel (IB) detector is a photon-veto detector located inside MB. IB was installed before the data-taking in 2016 to further suppress the $K_L \to \pi^0\pi^0$ background events by a factor of three [107]. The key to the rejection of the $K_L \to \pi^0\pi^0$ background where two extra photons are generated in the final state is the small photon inefficiency of veto detectors. By adding more granular sampling modules inside MB, total material thickness in the radial direction was

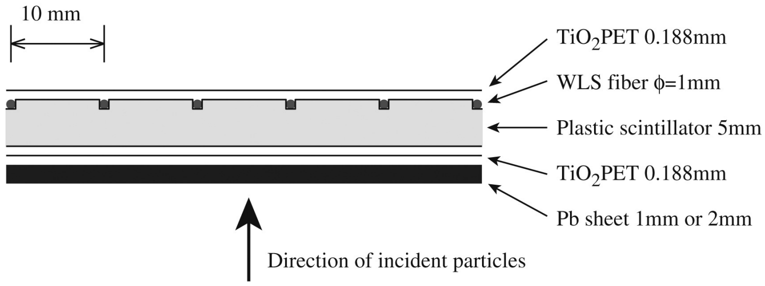

Figure 2.36: One layer of the MB module. The figure is quoted from Ref. [101].

increased, and thus it reduced the photon inefficiency due to the so called punch-through effect and the sampling effect.

Figure 2.37 shows schematic views of IB. IB is a 2.8-m-long cylindrical detector with an (inner) outer diameter of 1.5 m (1.9 m). It consists of 32 modules of lead-plastic sandwich detectors with a radial thickness of $5.0X_0$. Each module consists of 25 layers stacked in the radial direction. Each layer consists of 1-mm-thick lead and 5-mm-thick plastic scintillator sheets. Scintillation light is read out through WLS fibers embedded in scintillator layers and collected by PMTs from the both ends of the modules. In total, the number of readout channels for IB is 64. Details on IB are available in Refs. [107, 108].

2.5.7 Main Barrel Charged Veto and Inner Barrel Charged Veto

The Main Barrel Charged Veto (MBCV) and the Inner Barrel Charged Veto (IBCV) detectors are attached to the inner surface of MB and IB, respectively. These detectors were installed in 2016 together with IB, and the former detector used for charged-veto at the inner surface of MB before the installation of IB was then uninstalled accordingly. These detectors are responsible for detecting charged particles produced from decays of K_L and $K^{\pm}$ in the decay volume. Figure 2.38 shows a schematic view of IBCV and MBCV. IBCV covers the full length of IB along the z-axis while MBCV covers the region between downstream ends of IB and MB. IBCV (MBCV) consists of 32 plastic scintillator sheets with a thickness of 5 mm (10 mm). Scintillation light is read out through WLS fibers embedded in each scintillator sheet and Polymer Light Guides[16] leading to PMTs from the both ends for IBCV and the downstream end for MBCV. Every two output signals from the neighboring scintillator sheets for MBCV are readout together in the same channel. In total, the numbers of readout channels for IBCV and MBCV are 64 and 16, respectively.

2.5.8 Charged Veto

The Charged Veto (CV) detector is located in front of CSI to identify whether a particle hitting CSI is neutral or charged. CV is required to have high detection efficiency to charged particles in order to reject background events from K_L decays with a high branching ratio such as $K_L \to \pi^{\pm}e^{\mp}\nu_e$ and $K_L \to \pi^{\pm}\mu^{\mp}\nu_{\mu}$. At the same time, a material budget for CV must be as small as possible so as not to increase the production of η leading to the CV-η background, as described in Section 2.1.2.2. As shown in Figure 2.39, CV consists of two layers of detectors called Front CV (FCV) and Rear

---

[16] Soft acrylic resin tubes with a diameter of 14 mm.

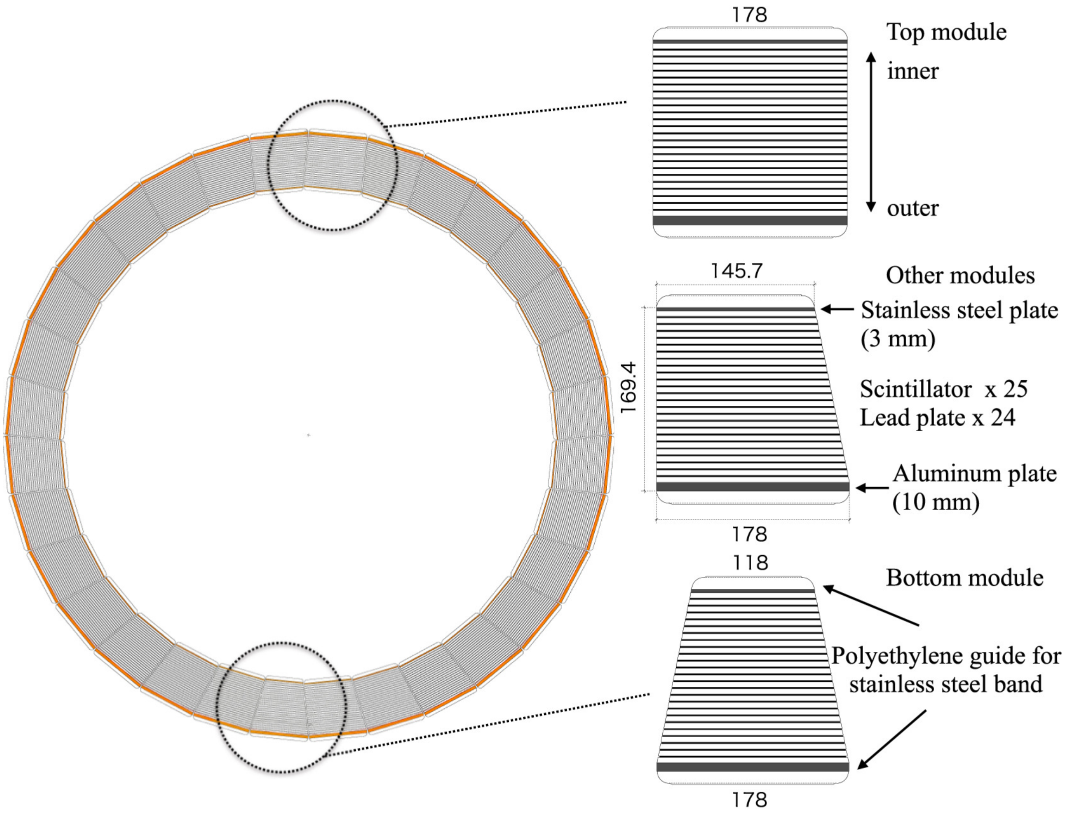

Figure 2.37: Cross-sectional view of IB (left) and an individual module (right). Scales in the figures are in units of mm. The figure is quoted from Ref. [107].

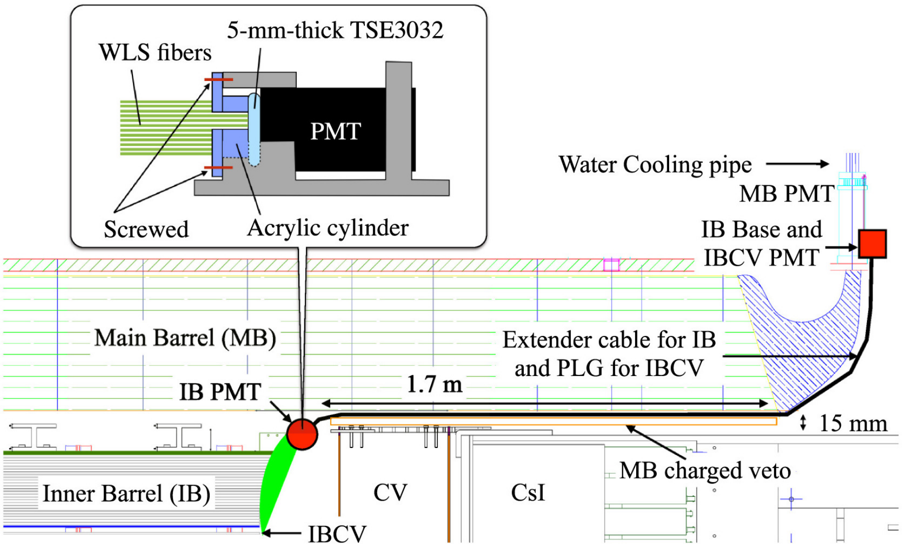

Figure 2.38: Cut view of IB, MB, IBCV, and MBCV at the downstream region of the decay volume. The figure is quoted from Ref. [107].

Figure 2.39: Photograph of CV. The figure is quoted from Ref. [110].

CV (RCV). FCV (RCV) is placed 30 cm (5 cm) upstream from the CSI surface. Figure 2.40 shows a schematic design of each CV layer. The FCV (RCV) layer is composed of 48 (44) plastic scintillator strips arranged in four quadrants with a square beam hole at the center. The strips are placed on the 0.8-mm-thick CFRP plate to be a rigid structure. Each strip is made of 70.7-mm-wide and 3-mm-thick plastic scintillator. Scintillation light from each strip is read out through WLS fibers embedded in the strip and collected by two MPPC that are attached at both ends of the fibers. The number of readout channels is therefore 96 (88) for the FCV (RCV) layer. Details on CV are available in Ref. [109].

2.5.9 Outer Edge Veto

The Outer Edge Veto (OEV) detector is a photon-veto detector to prevent photons from being absorbed by inactive materials in the outer-edge region. OEV is composed of 44 modules that fill the gaps between the outer-edge of CSI and the cylindrical support. Figure 2.41 shows a schematic front view of the OEV modules. Each module is made of lead-plastic sandwich layers stacked in directions perpendicular to the beam axis. Scintillation light from each module is read out through WLS fibers embedded in the scintillator layer and collected by a PMT. Details on OEV are available in Ref. [111].

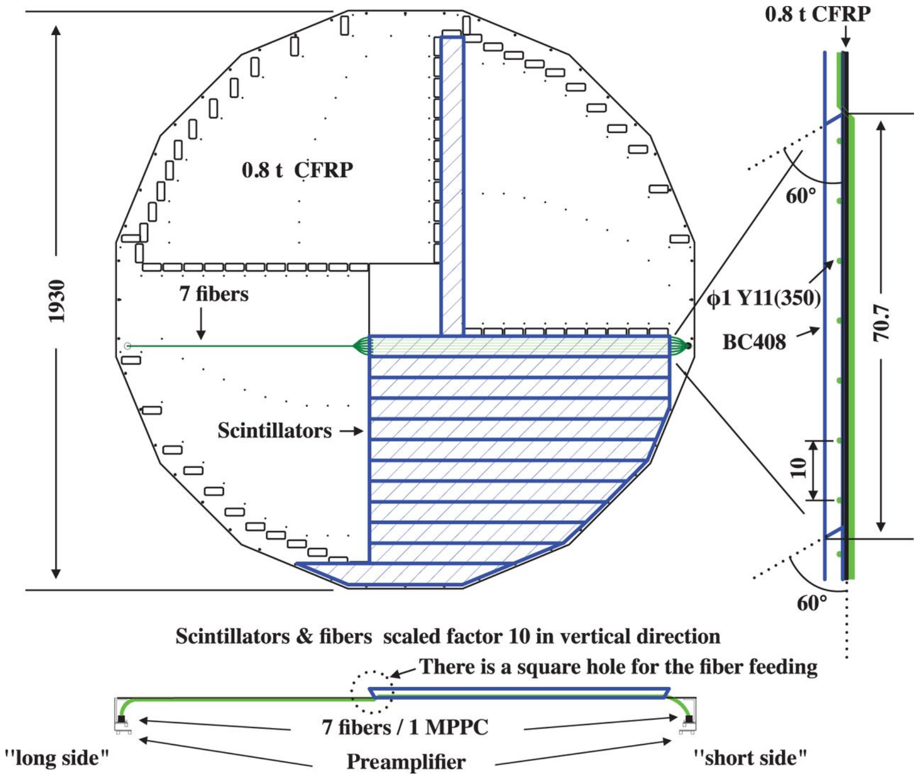

Figure 2.40: Schematic view of a CV layer. Scales in the figure are in units of mm. The figure is quoted from Ref. [109].

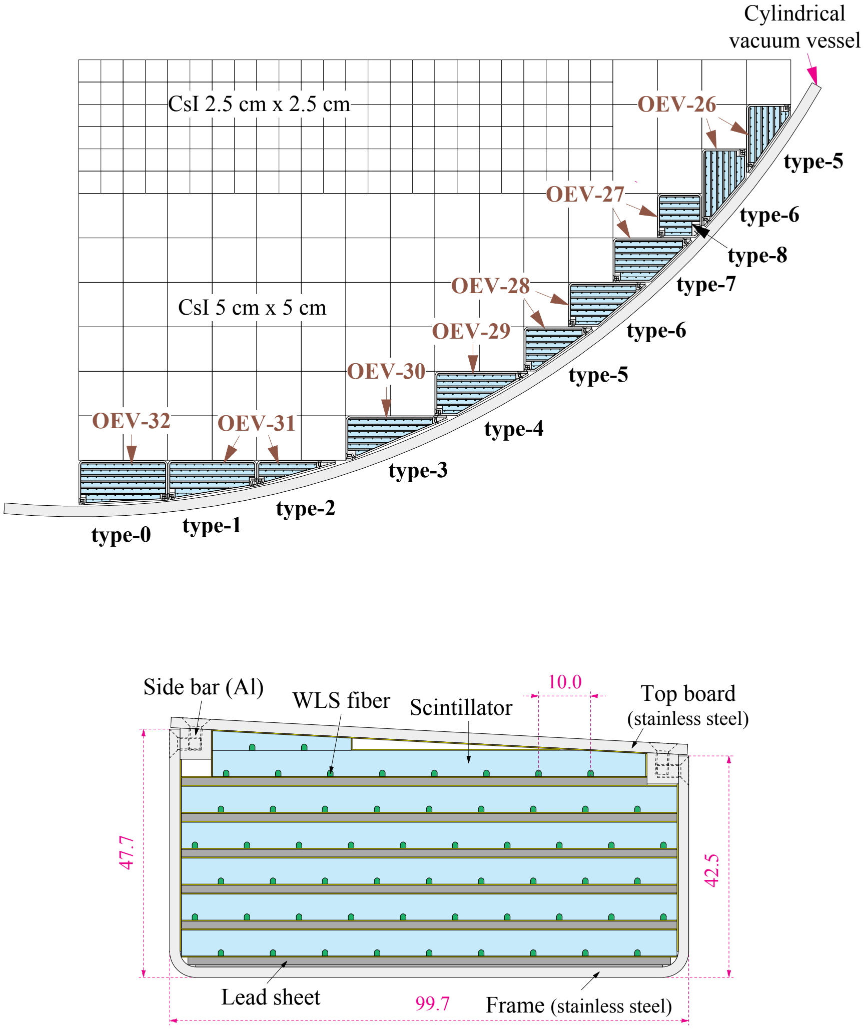

Figure 2.41: Frontl view of OEV (top) and one of the individual modules (bottom). There are several types of the cross-sectional shape for the modules. Scales in the figure are in units of mm. The figures are quoted from Ref. [111].

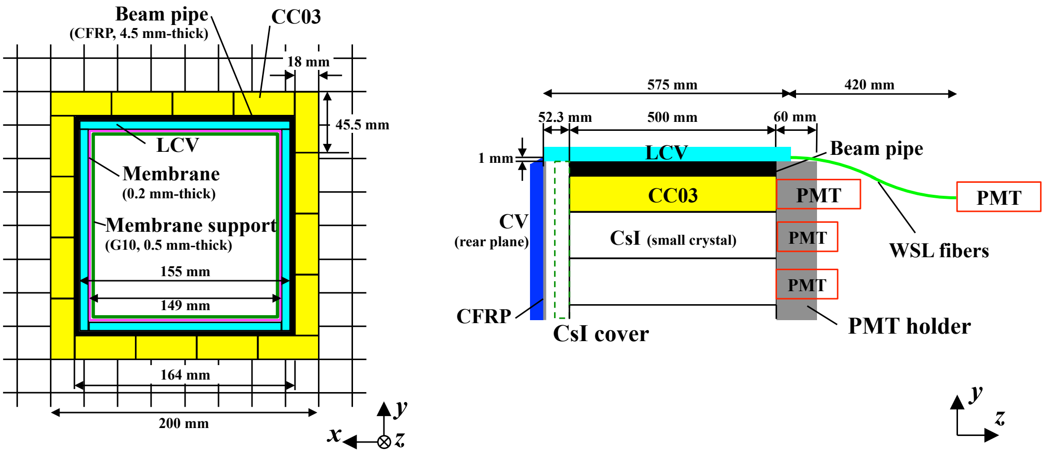

Figure 2.42: Schematic front (left) and side (right) views of CC03 and LCV. The figure is quoted from Ref. [68].

2.5.10 Collar Counter 3 and Liner Charged Veto

The Collar Counter 3 (CC03) is a photon-veto detector placed inside the beam hole at CSI. The main role of CC03 is to reject events where photons coming from K_L decays hit the region just around the beam hole at CSI. CC03 is composed of 16 crystals of undoped CsI as shown in Figure 2.42. Each crystal has a length of 500 mm and a cross-sectional area of $45.5 \times 18\,\mathrm{mm}^2$. Scintillation light generated in each crystal is read out with two PMTs from the downstream end. In total, the number of readout channels for CC03 is 32.

The structure of CC03 is supported by the beam pipe that is a 4.5-mm-thick CFRP square-tube placed inside CC03. Further inside the beam pipe, a charged-veto detector called Liner Charged Veto (LCV) is installed. LCV is required to detect charged particles hitting the beam pipe before they get absorbed. LCV is composed of four plastic scintillator plates with a thickness of 3 mm. LCV fully covers the inner surface of CC03 from the z-position at RCV as shown in Figure 2.42. Scintillation light from each scintillator plate is read out through WLS fibers embedded in the plate and collected with a PMT.

2.5.11 Downstream Collar Counters

There are three different Collar Counter (CC) detectors located in the downstream section of the KOTO detector: CC04, CC05, and CC06. These detectors are responsible for detecting photons and charged particles from K_L decays such as $K_L \to \pi^0\pi^0$ and $K_L \to \pi^+\pi^-\pi^0$. These particles can escape in the beam hole at CSI, and thus they need to be detected in the downstream region in such a case. As shown in Figure 2.43, each detector consists of undoped CsI crystals stacked around the beam pipe for photon detection and plastic scintillator plates placed just in front of the crystals for charged-particle detection. As can be seen in Figure 2.20, only CC04 is placed in the vacuum tank while the others are located outside. For all detectors, scintillation light from each crystal is read out by one PMT at its end, and scintillation light from each plastic scintillator plate is read out by one (two) PMT(s) for the middle two (top and bottom two) scintillator plates.

2.5.12 Downstream Charged Veto

The Downstream Charged Veto (DCV) detector is required to detect charged particles produced from K_L decays. This detector is particularly important to suppress background events from the $K_L \to \pi^+\pi^-\pi^0$ decay. According to the past studies [83, 105, 112], the $K_L \to \pi^+\pi^-\pi^0$ background events remained in the signal region when two charged pions in the final state escaped in the beam hole at CSI and were absorbed by the inactive material at the downstream section in the KOTO detector as shown in Figure 2.44 (left). During the 2016-2018 data-taking, the charged-particle detector named the Beam Pipe Charged Veto (BPCV)[113, 105] was used at the downstream section between CC05 and CC06 to suppress the $K_L \to \pi^+\pi^-\pi^0$ background, as shown in Figure 2.44 (right). BPCV was placed just around a 5-mm-thick aluminum vacuum pipe. It detected charged pions that escaped in the beam hole. If they stopped in the vacuum pipe and generated secondary charged particles, those particles were also detected by BPCV.

To detect the charged pions directly before the absorption, DCV was installed at the downstream section after the data-taking in 2018, as shown in Figure 2.45. DCV is divided into two square-pipes, DCV1 and DCV2. DCV1 was placed inside the membrane in the endcap region and DCV2 was installed inside the downstream vacuum pipe. Each square-pipe for DCV consists of four plastic scintillator sheets with a thickness of 5 mm. As shown in Figure 2.46, each scintillator sheet has a total of 18 WLS fibers that are embedded in grooves. The scintillation light is read out by four MPPCs attached at the ends of the scintillator sheet. Two MPPCs out of four collect photons through the same nine fibers from the both ends. Figure 2.47 shows photographs of the scintillator sheet and the installation of DCV. In line with the installation of DCV, BPCV was uninstalled from the KOTO detector. Details on DCV are available in Ref. [112].

2.5.13 Beam Hole Charged Veto

The Beam Hole Charged Veto (newBHCV[17]) detector is located behind CC06 and covers the beam-core region. newBHCV is required to detect charged particles coming from K_L decays such as $K_L \to \pi^+\pi^-\pi^0$. Though the detector needs to be sensitive to charged particles, it should be insensitive to neutral particles since the detector is placed in the beam with a high flux of neutral particles. To achieve this requirement, newBHCV was developed as a wire chamber detector with a low material budget. The newBHCV detector consists of three wire chambers that are aligned along the beam axis. Figure 2.48 shows a schematic view of a newBHCV chamber. Each chamber is composed of 160 gold-plated tungsten wires with a length of 30 cm and a diameter of 50 μm for anode wires and graphite-coated polyimide films with a thickness of 50 μm for cathode planes. As shown in Figure 2.49, the chamber is filled with a mixture of tetrafluoromethane (CF_4) and n-Pentane gases for an ionization material which provides fast response. The number of readout channels for each chamber is 16. Details on newBHCV are available in Refs. [115, 116].

---

[17] “new" in the abbreviated name means that the previous BHCV detector was replaced by the current one in 2015.

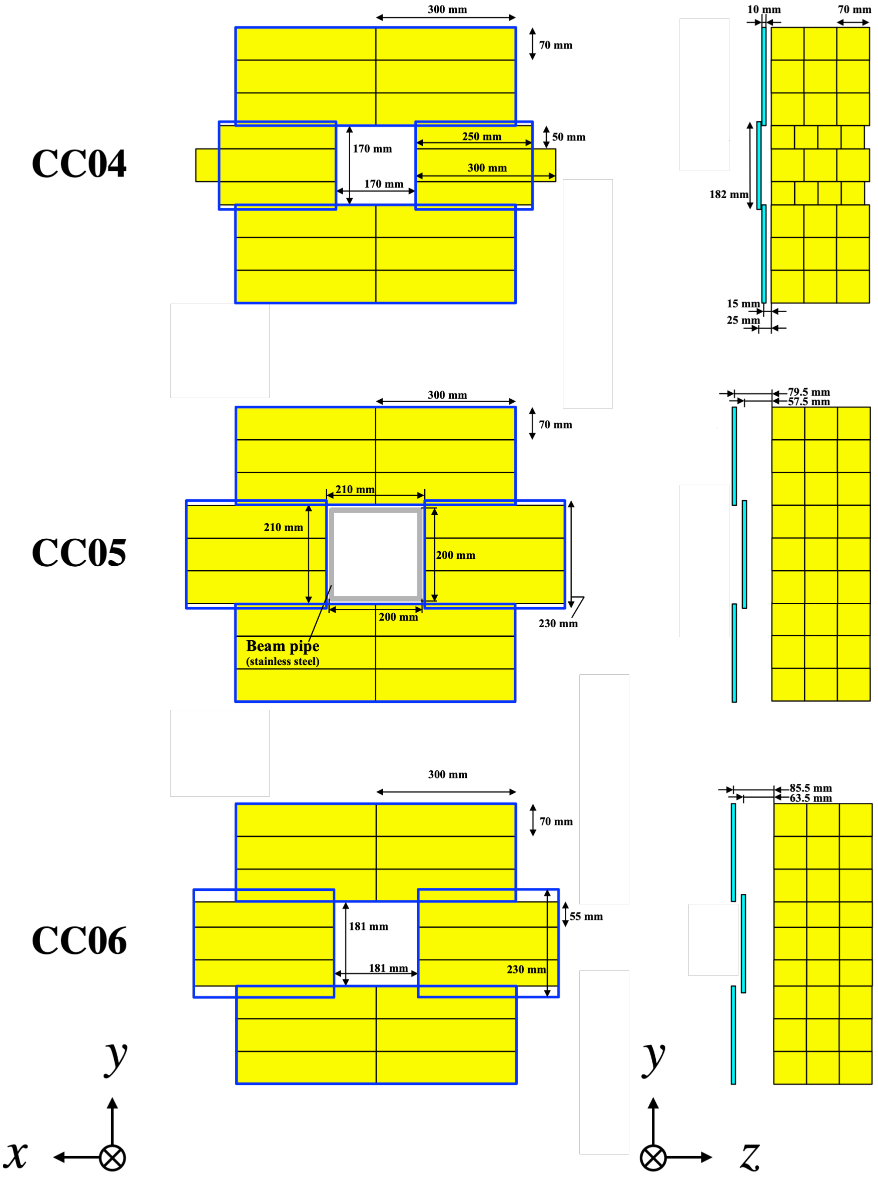

Figure 2.43: Schematic front (left) and side (right) views of CC04, CC05, and CC06. The yellow blocks represent CsI crystals and the blue lines (cyan boxes) in the left (right) figures represent plastic scintillators. The figure is quoted from Ref. [68] with modifications.

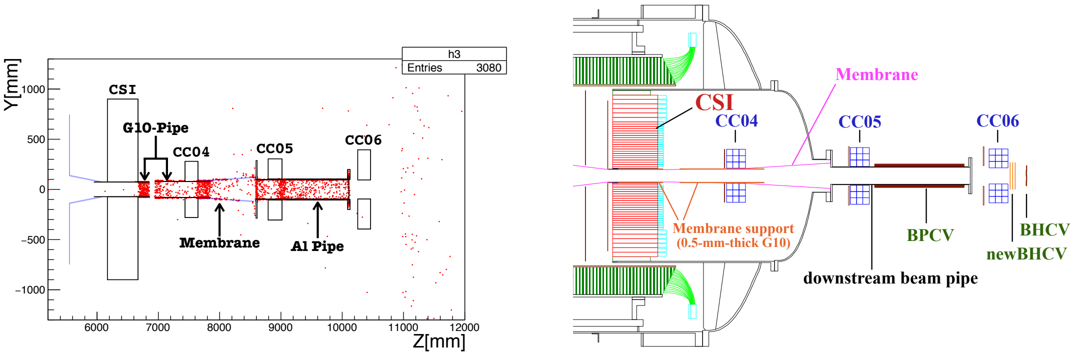

Figure 2.44: Downstream section of the KOTO detector during the 2016-2018 data-taking. The left figure shows interaction positions of charged pions from $K_L \rightarrow \pi^+\pi^-\pi^0$ predicted by simulation. The right figure shows a cross-sectional view of the KOTO detector. BPCV was located between CC05 and CC06 and surrounding the downstream beam pipe. The left and right figures are quoted from Ref. [112] and Ref. [105], respectively.

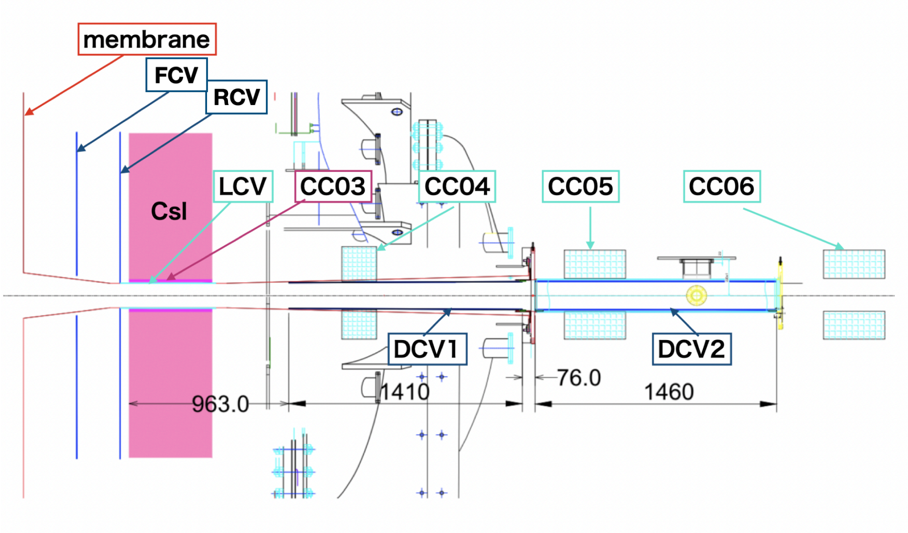

Figure 2.45: Configuration of the downstream section after the data-taking in 2018. Scales in the figure are in units of mm.

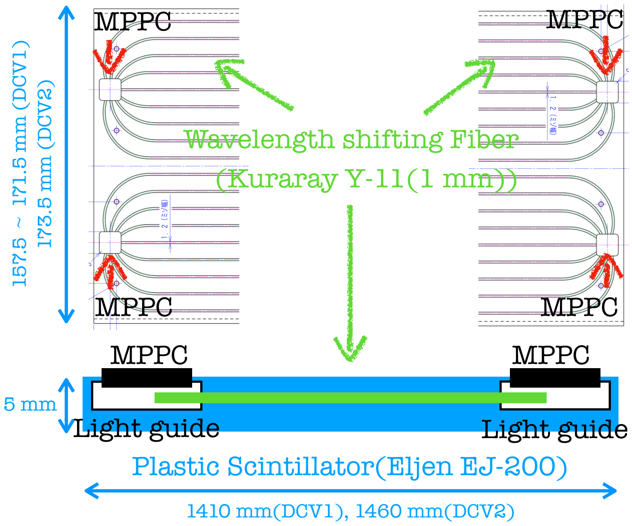

Figure 2.46: Schematic illustration of one of the scintillator sheets with WLS fibers and MPPCs for DCV. The figure is quoted from Ref. [112].

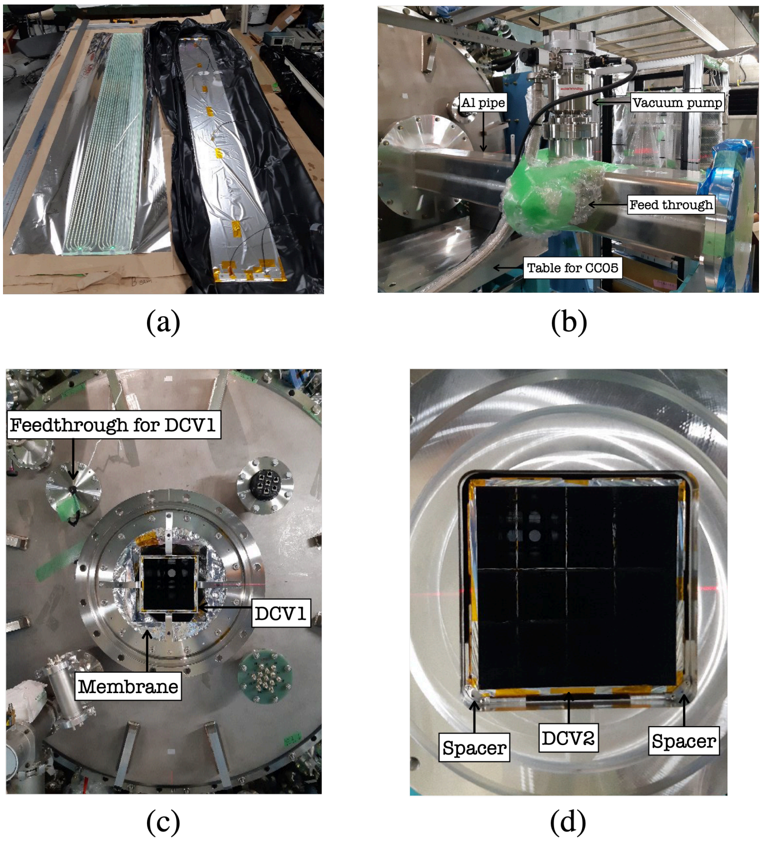

(a) (b) (c) (d)

Figure 2.47: Photographs of DCV. (a) Scintillator sheet before and after being wrapped with aluminized mylars. (b) Downstream view of the vacuum pipe. (c) Downstream view of DCV1. (d) Downstream view of DCV2. The figures are quoted from Ref. [114].

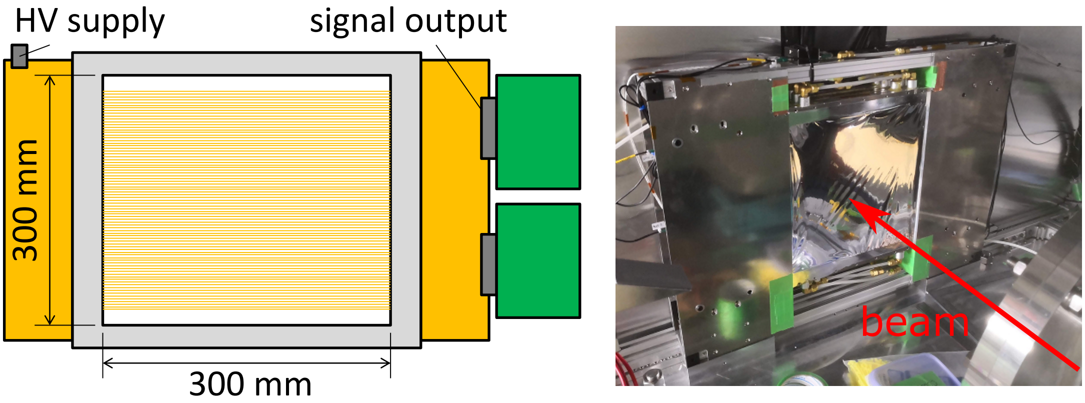

Figure 2.48: Schematic view of a newBHCV chamber (left) and a photograph of the upstream view (right). The figures are quoted from Ref. [117].

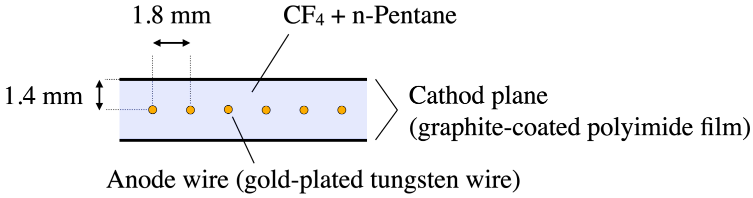

Figure 2.49: Schematic view of the structure in the newBHCV chamber.

2.5.14 Beam Hole Photon Veto

The Beam Hole Photon Veto (BHPV) detector is located at the downstream section behind newBHCV. The role of BHPV is to detect photons coming from K_L decays such as $K_L \to \pi^0\pi^0$. BHPV consists of 16 modules of lead-aerogel Čherenkov detectors placed along the beam axis as shown in Figure 2.50. The total converter thickness in the beam direction is equivalent to $6.2X_0$ for the whole BHPV detector. Figure 2.51 shows a schematic view of an individual module. An incident photon is converted into an electron-positron pair in the lead sheet, and Čherenkov light is emitted in the aerogel tile. The Čherenkov light generated in each module is collected with mirrors and read out by two PMTs from both sides. As seen in Figure 2.50, there is a concrete shield located at the upstream side of BHPV to suppress showers splashing back to upstream detectors. Details on BHPV are available in Ref. [118, 68].

2.5.15 Beam Hole Guard Counter

The Beam Hole Guard Counter (BHGC) is a photon-veto detector located at the most downstream position in the KOTO detector system, as shown in Figure 2.52. BHGC is required to detect in-beam photons that pass through the edge region of BHPV and secondary particles produced in the edge region. It is also required to be insensitive to neutrons passing through the beam hole. It consists of four modules of lead-acrylic Čherenkov detectors surrounding the beam center. Each module is composed of lead and acrylic plates, as shown in Figure 2.53. An incident photon is

Figure 2.50: Entire view of BHPV from the downstream side. There are 16 modules implemented in the KOTO detector system at present while only 12 modules can be seen in the picture which was taken in 2013. The figure is quoted from Ref. [68].

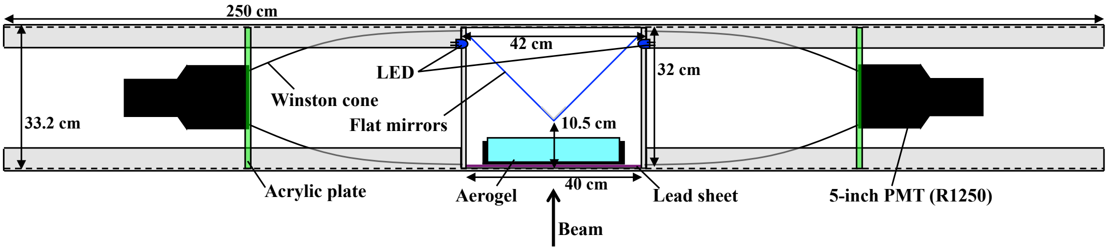

Figure 2.51: Schematic top view of an individual module of BHPV. Each module is composed of a lead converter, an aerogel radiator, and light-collecting mirrors. The figure is quoted from Ref. [118].

converted into an electron-positron pair in the lead plate, and Čherenkov light is emitted in the acrylic plate. The Čherenkov light generated in each module is collected with a light guide and read out by two PMTs from both sides, as shown in Figure 2.53. Details on BHGC are available in Refs. [119, 120].

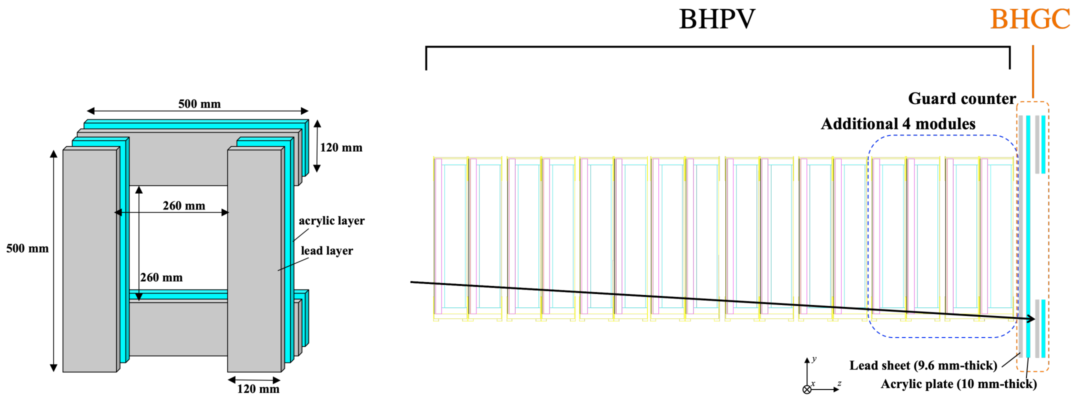

Figure 2.52: Schematic view of BHGC. The left figure shows a front view of BHGC. The right figure shows the location of BHGC with BHPV. The figure is quoted from Ref. [68] with modifications.

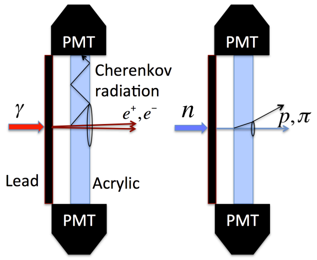

Figure 2.53: Schematic view of an individual module of BHGC. The lead (acrylic) layer works as a converter (Čherenkov radiator). Since charged particles generated from neutrons tend to be slow, it is hard to exceed the Čherenkov threshold. Even if the Čherenkov light is generated, that is not collected by PMTs unless the total reflection condition is satisfied. The figure is quoted from Ref. [119].

2.5.16 Summary of Subdetectors

Table 2.4 summarizes the subdetectors for the KOTO detector system.

Table 2.4: Summary of the subdetectors. In the column for material, scint. and cryst. represent plastic scintillators and undoped CsI crystals, respectively.

Subdetector	Material	Readout	# of channels	Primary role
CSI	cryst.	both-end	2972[a]	$\pi^0 \to 2\gamma$ detection
UCV	scint.	single-end	12	charged veto
FB	scint. & lead	single-end	32	photon veto
NCC	cryst.	single-end	200[b]	photon veto
Hinemos	scint.	single-end	4	photon veto
MB	scint. & lead	both-end	128	photon veto
IB	scint. & lead	both-end	64	photon veto
MBCV	scint.	single-end	16	charged veto
IBCV	scint.	both-end	64	charged veto
CV	scint.	both-end	184 [c]	charged veto
OEV	scint. & lead	single-end	44	photon veto
LCV	scint.	single-end	4	charged veto
CC03	cryst.	single-end	32	photon veto
CC04	cryst. & scint.	single-end[d]	64[d]	photon & charged veto
CC05	cryst. & scint.	single-end[e]	60[e]	photon & charged veto
CC06	cryst. & scint.	single-end[e]	60[e]	photon & charged veto
DCV	scint.	both-end	32	charged veto
newBHCV	CF_4 & n-Pentane	single-end	48	charged veto
BHPV	lead & aerogel	both-end	34	photon veto
BHGC	lead & acrylic	both-end	8	photon veto

[a] 2716 channels with the downstream readout by PMTs and 256 channels with the upstream readout by MPPCs.

[b] 192 channels for inner modules with the common and individual readouts and 8 channels for outer modules.

[c] 96 channels for FCV and 88 channels for RCV.

[d] Both-end readout only for two out of four plastic scintillators. 58 channels for crystals and 6 channels for plastic scintillators.

[e] Both-end readout only for two out of four plastic scintillators. 54 channels for crystals and 6 channels for plastic scintillators.

2.6 Data Acquisition and Trigger Systems

The data acquisition (DAQ) system for the KOTO experiment was designed based on the pipeline readout where the data is stored while waiting for a trigger decision [121, 122]. This design allows to avoid dead time and make versatile requirements for triggers at the online data-processing stage during beam operation. This section briefly describes the overview of the DAQ and trigger systems, hardware components for the front-end electronics, and triggering strategies. Detailed information with the configuration for the data-taking in 2021 can be found in Refs. [123, 49].

2.6.1 Overall Architecture

Figure 2.54 shows a digram of the KOTO DAQ and trigger systems. To collect data efficiently according to the requirements for target events, all output signals from the KOTO detector are first put into waveform digitizers, the modules of the analog-to-digital converter (ADC) either with 125-MHz sampling frequency with a filter or 500-MHz sampling frequency. The total number of output signals from all the subdetectors is more than 4000 channels as summarized in Section 2.5.16, and all of them are continuously digitized with 5.2-μs pipeline depth in the ADC modules. During this period, energy and timing information extracted from each waveform can be analyzed and used for trigger decisions. Once a trigger is issued to ACD modules, digitized waveforms are sliced into either 64 or 256 samples. The ADC modules are also responsible for lossless data-compression to reduce the data size [122], which mitigates limitations of the data transfer speed and the storage resource at the downstream stage. The data are sent to the downstream module for package assembly[18]. The assembled data are then sent to the PC farm which is the last stage of the DAQ system. This PC farm is responsible for event building as well as temporary data storage. Finally, the complete form of data are sent to the KEK Computer Research Center in Tsukuba.

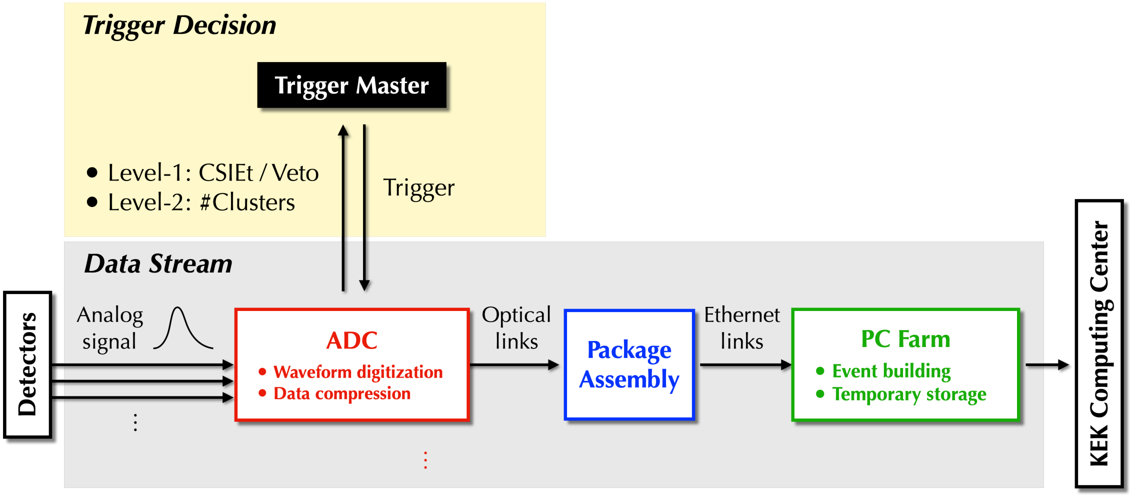

Figure 2.54: Simplified diagram of the data flow and trigger scheme in KOTO.

2.6.2 Front-End Electronics

The ADC modules were developed for the KOTO experiment, and are categorized into two types according to their sampling frequency: 125-MHz ADC [124] and 500-MHz ADC [125]. Figure

---

[18] This module was used to calculate a position of the center of deposited energy (COE) in CSI during a part of data-takings from 2016 to 2018. In 2021, it was only used for the data assembly.

2.55 shows photographs of the ADC modules. Table 2.5 summarizes the types of ADC modules used for each subdetector.

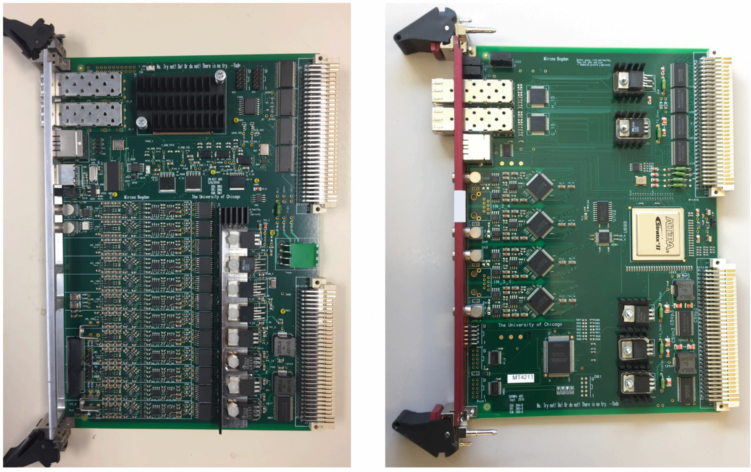

Figure 2.55: Photographs of a 125-MHz ADC module (left) and a 500-MHz ADC module (right). Each 125-MHz (500-MHz) ADC module has 16 (4) input channels to receive signals sent from detectors. The figures are quoted from Ref. [49].

Table 2.5: ADC type used for each subdetector.

ADC type	Subdetector
125-MHz ADC	CSI[a], FB, NCC, MB, MBCV, IBCV, CV, OEV, CC03–06, LCV, DCV
500-MHz ADC	UCV, IB, newBHCV, BHPV, BHGC

[a] Waveforms from both of PMTs and MPPCs were recorded by 125-MHz ADC modules.

The 125-MHz ADC modules are used for most of the subdetectors. This ADC module converts an analog signal into 64 digitized samples with an interval of 8 ns and a dynamic range of 14 bits. One of the features of the ADC modules of this type is that they are equipped with a ten-pole Bessel filter to widen and shape the analog signal waveforms into a Gaussian-like form before digitization [121]. This is because an original pulse with a sharp rising edge is too narrow to be recorded with 8 ns intervals. Figure 2.56 shows an input analog waveform and Figure 2.57a shows a waveform digitized by a 125-MHz ADC module.

The 500-MHz ADC modules are used for subdetectors with high hit rate. This ADC module converts an analog signal into 256 digitized samples with an interval of 2 ns and a dynamic range of 12 bits. Since waveforms are not widened with a filter, they provide a better pulse-separation capability, as shown in Figure 2.57b.

For both types of ADC modules, a waveform is recorded with a 512-ns-wide[19] time range, and that corresponds to the time window for each event in the KOTO data analysis.

---

[19] 512 ns = 8 ns/clock × 64 clocks (125-MHz ADC)= 2 ns/clock × 256 clocks (500-MHz ADC).

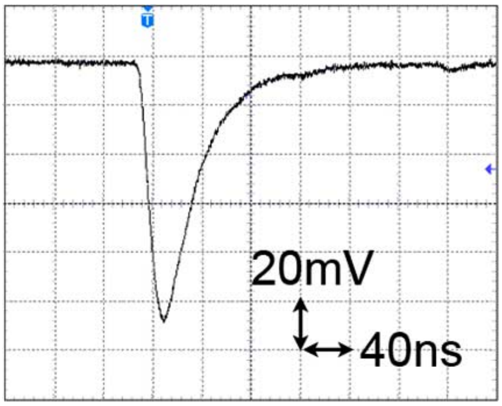

Figure 2.56: An analog signal from a CsI crystal with a PMT recorded by an oscilloscope. The figure is quoted from Ref. [121].

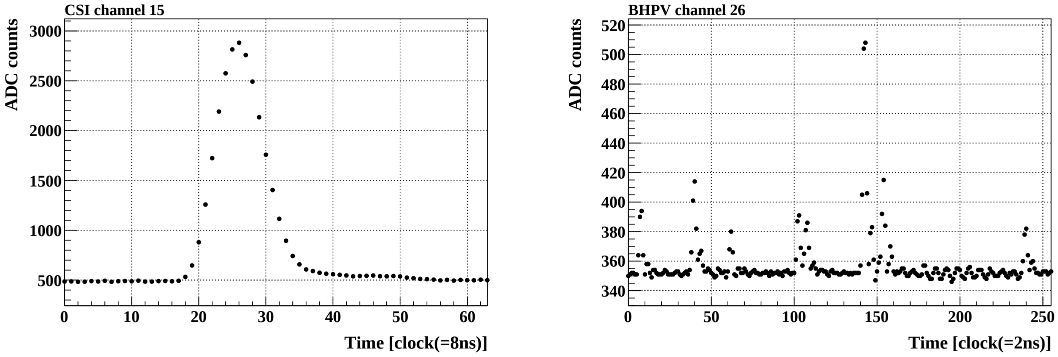

(a) Waveform recorded by 125-MHz ADC.

(b) Waveform recorded by 500-MHz ADC.

Figure 2.57: Example of waveforms recorded by a 125-MHz ADC module and a 500-MHz ADC module.

2.6.3 Trigger Algorithm

By putting together the raw level information of energy and timing in waveforms from ADC modules, advanced features for each event such as total deposited energy in a particular detector and the number of electromagnetic showers in CSI can be obtained. Those pieces of information are then utilized for trigger requirements. In the current KOTO trigger system, the following two-stage trigger decisions are made in combination. Specific requirements that were used during the data-taking in 2021 are described in Chapter 3.

2.6.3.1 Level-1 Trigger

For the identification of the $K_L \to \pi^0 \nu \bar{\nu}$ signal with the KOTO detector, total energy deposition in CSI, referred to as "CSIEt", is used as a minimum criterion; the value of CSIEt is required to be greater than 550 MeV. In addition, hit information in veto detectors can be examined by a pulse height in comparison with a given threshold for each detector. Thus, absence of coincident hits in some of the veto detectors (referred to as the online veto) can also be required to enhance the likelihood of observing no detectable particles other than two photons hitting CSI. As will be described in Section 3.2, the online veto was applied to CV, NCC, MB, IB, and CC03-06. The energy thresholds for the online veto were set approximately to 0.2 MeV for CV, 20 MeV for NCC, and 10 MeV for MB, IB, and CC03-06[20]. These fundamental requirements on CSIEt and veto detectors are called "level-1 trigger" as a first stage of trigger decision.

2.6.3.2 Level-2 Trigger

Since an electromagnetic shower observed in CSI deposits energy across multiple crystals, such a shower is detected as a cluster as shown in Figure 2.58. In the KOTO trigger system, the number of clusters can be counted by the cluster-finding algorithm[21] [123, 49]. This algorithm is based on a pattern-recognition of the hit map in CSI. Hit decision is made for each crystal by judging whether it has energy deposit over a given threshold[22]. As shown in Figure 2.59, CSI crystals is scanned every 2×2 crystal array to count the number of turns at corners. The total number of clusters is thus calculated as the number of turns divided by four because any shape of a single cluster gives four turns for one loop. The requirement on the specific number of clusters is called "level-2 trigger" or online clustering trigger and is used as a second stage of trigger decision. The level-2 trigger is evaluated if the level-1 trigger condition is satisfied.

---

[20] These thresholds are slightly looser than the energy thresholds used in the offline analysis.

[21] This algorithm is different from the clustering algorithm used in the offline analysis described in Section 4.2.1.

[22] Energy threshold for small (large) crystals is set to 22 MeV (44 MeV).

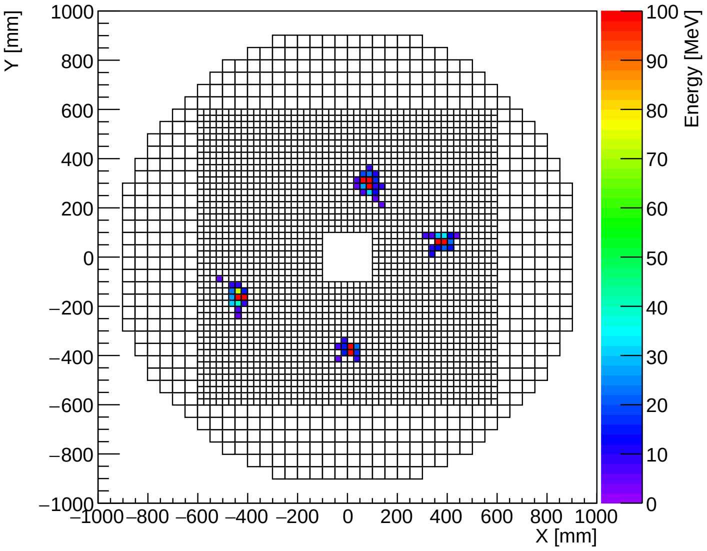

Figure 2.58: Example of electromagnetic showers observed in CSI. In this event display, four electromagnetic showers can be found as different clusters.

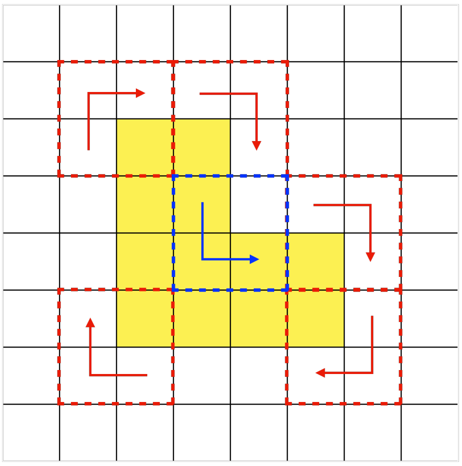

Hit pattern in 2x2 crystal array	Contour	#Turns
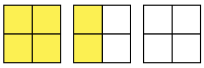	No corners	0
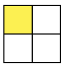	One convex corner	+1
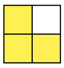	One concave corner	-1
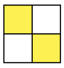	Two concave corners	-2

Figure 2.59: Online cluster-finding algorithm. The crystals shown in yellow represent the ones with deposited energy greater than the threshold. The right table shows possible patterns of 2 × 2 crystals. Each pattern (and its rotationally symmetric pattern) has a unique number of turns. In the left example, there are five convex corners (red) and one concave corner (blue). Thus, the resulting sum of turns is $4\,(= +1 \times 5 + (-1) \times 1)$.

Chapter 3

Data Taking in 2021

This chapter describes the detailed data-taking condition in 2021.

3.1 Beam Condition

In 2021, the MR accelerator operation with the SX mode at J-PARC was conducted from February 9 to April 7 and from May 11 to June 30. The former (latter) term is called Run86 (Run87) according to the name of accelerator operation programs at J-PARC. Details of the performance of the accelerator operation in 2021 can be found in Ref. [126]. During these periods, the beam was extracted to the HEF with a spill repetition cycle of 5.2 s which was the same as in the previous beam operation, and the spill duty factor of 78% was achieved. During Run86, the SX beam power was gradually increased after the accelerator trouble with the electrostatic septum. The maximum beam power during the whole beam operation period was 64 kW, which was the highest beam power ever as of 2021. The accumulated number of protons on target (POT) for the physics data analysis is summarized in Table 3.1. A total of 3.26×10^{19} POT were used for the physics data analysis. This is the largest number of POT ever used in the past data analyses published from the KOTO experiment[1].

---

[1] The total POT for the 2015 (2016–2018) data analysis was 2.19×10^{19} (3.05×10^{19}) [50, 61].

Table 3.1: Summary of the physics data collection at KOTO in 2021. The subperiods are listed in chronological order from the top row to the bottom.

Period	Run	Beam power	POT
Period-0	Run86	60 kW	3.60×10^{18}
Period-1	Run86	10 kW	6.84×10^{16}
Period-2	Run86	15 kW	1.07×10^{17}
Period-3	Run86	25 kW	1.27×10^{17}
Period-4	Run86	40 kW	3.07×10^{17}
Period-5	Run86	45 kW	2.10×10^{18}
Period-6	Run87	46 kW	4.68×10^{17}
Period-7	Run87	51 kW	1.74×10^{17}
Period-8	Run87	56 kW	7.61×10^{18}
Period-9	Run87	60 kW	3.60×10^{18}
Period-10	Run87	64 kW	2.13×10^{19}
	Total		3.26×10^{19}

3.2 Run Type and Trigger Condition

For each data-taking, we utilized the level-1 and level-2 triggers to collect events of our interests efficiently. With different criteria on trigger requirements, we collected various data samples. Each data-taking process managed by the KOTO DAQ system is called a run, and Table 3.2 summarizes types of runs conducted in 2021. Following sections describe details of each run.

Table 3.2: Summary of run types during the data-taking in 2021.

Run type	Purpose
Physics run	To collect data for the $K_L \to \pi^0 \nu \bar{\nu}$ search.
Calibration run	To collect data for detector calibrations.
Al-target run	To collect control data for evaluation of the hadron-cluster background.
Special run for UCV	To collect $K^\pm$ data to study the performance of UCV.

3.2.1 Physics Run

The physics run accounts for the majority of the data-taking time during beam operation. During this data-taking, we collected data using multiple trigger conditions simultaneously. Table 3.3 shows trigger conditions used during physics runs. The following sections explain each trigger condition for physics runs.

3.2.1.1 Physics Trigger

The physics trigger was used to collect a $K_L \to \pi^0 \nu \bar{\nu}$ sample. In order to collect $K_L \to \pi^0 \nu \bar{\nu}$ signal candidate events, CSIEt and the online veto were required by the level-1 trigger. The online veto

Table 3.3: Summary of the trigger conditions for physics runs. The symbols &, |, and ! represent the logical AND, OR, and NOT, respectively. Online veto is expressed as a logical NOT. The numbers in the rightmost column represent the number of clusters required for each trigger type.

Trigger type	Level-1	Level-2
Physics trigger	CSIEt & !(CV | NCC | MB | IB | CC03–CC06)	2
Normalization trigger	CSIEt & !(CV | NCC | MB | IB | CC03–CC06)	–
Minimum–bias trigger	CSIEt	–
$K^{\pm} \to \pi^{\pm}\pi^0$ trigger	CSIEt & CV & !(FCV | RCV | NCC | MB | IB | CC03–CC06)	3
Less-biased $K^{\pm}$ trigger	CSIEt & CV & !(NCC | MB | IB | CC03)	3
$K_L \to 3\pi^0$ trigger	CSIEt & !(CV | NCC | MB | IB | CC03–CC06)	6

was applied to CV, CC03, CC04, CC05, CC06, NCC, MB, and IB. On top of that, the number of clusters observed in CSI was required to be exactly two by the level-2 trigger.

3.2.1.2 Normalization Trigger

The normalization trigger was used to collect K_L decays, particularly, events from three decay modes called the normalization modes: $K_L \to \pi^0\pi^0$, $K_L \to 3\pi^0$, and $K_L \to 2\gamma$. Events collected by this trigger were used to estimate the K_L yield. In each period, the number of recorded events were reduced with a certain prescale factor, p_{norm}[2]. We set a prescale factor for the normalization trigger considering the variation of beam power as shown in Table 3.4. Except for the requirement on the number of clusters, the trigger condition was the same as the physics trigger.

Table 3.4: Summary of prescale factors for the normalization trigger (p_{norm}) and the minimum-bias trigger (p_{min}).

Period	Beam power	Prescale factor (p_{norm})	Prescale factor (p_{min})
Period-0	60 kW	30	900
Period-1	10 kW	2	30
Period-2	15 kW	3	60
Period-3	25 kW	5	100
Period-4	40 kW	10	300
Period-5	45 kW	20	600
Period-6	46 kW	20	600
Period-7	51 kW	30	900
Period-8	56 kW	30	900
Period-9	60 kW	30	900
Period-10	64 kW	30	900

---

[2] For example, if the prescale factor is 3, one third of the whole events were selected randomly and stored.

3.2.1.3 Minimum-Bias Trigger

The minimum-bias trigger was used to collect events with the least bias. Namely, the only requirement to be satisfied was CSIEt by the level-1 trigger. Using events collected by this trigger, one can study effects of online veto. As is the case with the normalization trigger, a prescale factor (p_{min}) was applied. The value of p_{min} for each period is summarized in Table 3.4.

3.2.1.4 $K^{\pm} \rightarrow \pi^{\pm}\pi^{0}$ Trigger

As described in Section 2.4, there is a magnet located between two collimators to sweep out charged particles from the KL beamline, leaving only neutral particles. However, it was found out that small amount of $K^{\pm}$'s that were generated at the downstream collimator contaminated the neutral beam.

In order to evaluate the $K^{\pm}$ flux and inefficiency of UCV, the $K^{\pm} \rightarrow \pi^{\pm}\pi^{0}$ decay was considered as a promising decay mode for $K^{\pm}$ data collection. The branching ratio of $K^{\pm} \rightarrow \pi^{\pm}\pi^{0}$ is 20.67% [1], which is relatively high among various decay modes. Because of the kinematical simplicity of the two-body decay, the $K^{\pm}$ can be reconstructed successfully. Although this trigger was intended to collect a $K^{\pm}$ decay sample, most of the events collected by this trigger were dominated by $K_L \rightarrow \pi^{+}\pi^{-}\pi^{0}$ decays. Details of the mechanism of the $K^{\pm}$ production, the reconstruction method for $K^{\pm} \rightarrow \pi^{\pm}\pi^{0}$, and the analysis of the collected sample are described in Chapter 6.

At the trigger stage, CSIEt and the online veto on NCC, MB, IB, and CC03–CC06 were imposed. In addition, energy deposition at CV was also required[3] to ensure that there was a $\pi^{\pm}$ hit. The criteria on FCV and RCV at the level-1 trigger shown in Table 3.3 are meant that the number of hits both at FCV and RCV was required to be less than three[4]. Finally, the number of clusters in CSI was required to be three at the Level-2 trigger because one from a $\pi^{\pm}$ hit and the other two from two photons from the π^{0} decay were expected. Figure 3.1 shows a schematic view of the $K^{\pm}$ sample collection.

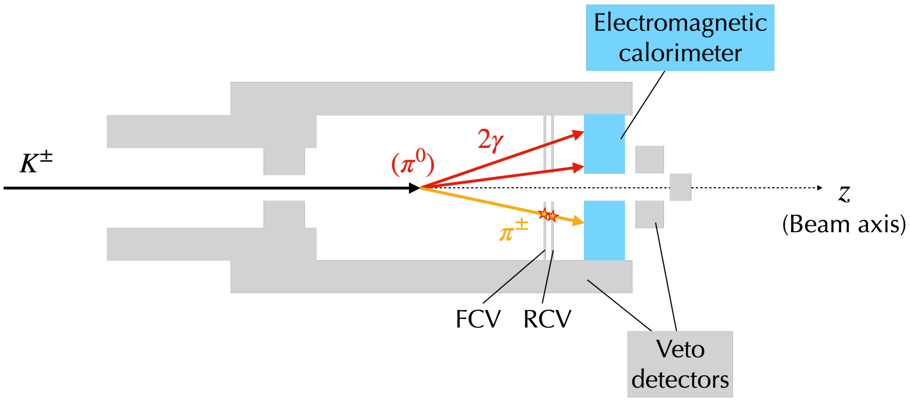

Figure 3.1: Schematic view of the $K^{\pm}$ data-taking with the $K^{\pm} \rightarrow \pi^{\pm}\pi^{0}$ trigger.

---

[3] A hit with the maximum energy deposition among CV modules greater than the online veto threshold (0.2 MeV) was required.

[4] A hit in FCV and RCV was defined as a module in each CV layer with deposited energy greater than 0.25 MeV.

3.2.1.5 Less-Biassed $K^{\pm}$ Trigger

The less-biased $K^{\pm}$ trigger was used to evaluate the flux of K_L contained in three-cluster events. The trigger condition is the same as the $K^{\pm} \to \pi^{\pm}\pi^{0}$ trigger except for FCV, RCV, and CC04–CC06. For this trigger, a prescale factor of 30 was applied.

3.2.1.6 $K_L \to 3\pi^0$ Trigger

As the name suggests, the $K_L \to 3\pi^0$ trigger was used to collect events from $K_L \to 3\pi^0$ decays. Such events were used for energy calibration of CSI and estimation of flux for beam-halo K_L. The $K_L \to 3\pi^0$ trigger has the same level-1 trigger condition as the normalization trigger but it requires six clusters in CSI at the level-2 trigger, as shown in Table 3.3. In addition, no prescale factor was applied to this trigger. Therefore, this trigger made it possible to collect numerous events from $K_L \to 3\pi^0$ decays.

3.2.1.7 External Triggers

In addition to the trigger types shown in Table 3.3, there are several external triggers that do not use any information of the KOTO detector to make the triggers. These triggers were included during physics runs to monitor beam and detector conditions. They include the following:

- Target Monitor Trigger

  The target monitor (TMON) consists of three layers of plastic scintillators placed at an angle of 50° from the primary proton beam line [76]. A trigger is issued whenever secondary particles generated at the T1 target are detected by the TMON as a triple-coincident hit. Using events collected by the TMON trigger, effects of accidental activities by beam particles can be extracted. In KOTO, these events were used to reflect accidental activities in simulated samples, as will be described later in Chapter 5.

- Clock Trigger

  The clock trigger was issued at 10 Hz. This trigger was used to collect events randomly triggered and to check fundamental situation of detectors, such as counting rate and baseline fluctuation of output signal waveforms.

- LED and Laser Triggers

  The LED and laser triggers were issued by flashing them at 10 and 5 Hz, respectively. These triggers were used to collect events to check detector responses.

3.2.2 Calibration Run

In addition to physics runs, data-taking for the purpose of detector calibrations was also done. Each run is briefly described in this section.

3.2.2.1 Cosmic Ray Run

Cosmic ray data was used to calibrate the following detectors: CSI, FB, NCC, Hinemos, MB, IB, MBCV, IBCV, OEV, CSI, LCV, CC03, CC04, CC05, and CC06. The data was collected before

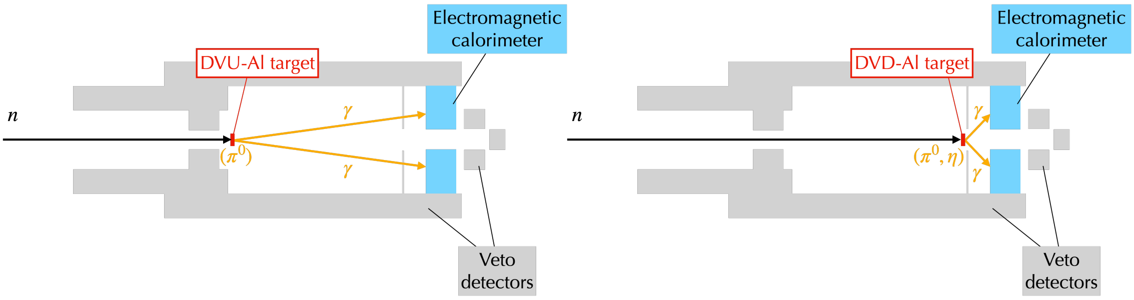

(a) DVU-Al target run (b) DVD-Al target run

Figure 3.2: Schematic views of the aluminum target runs.

and after the beam-operation periods and during periods for accelerator maintenance conducted every week. Events were triggered based on deposited energies in CSI, NCC, MB, IB, CC04, CC05, and CC06.

3.2.2.2 Plug-Closed Run

As described in Section 2.4, the rotational beam plug placed in the KL beamline can be closed to enhance particles with high penetration, such as charged pions and muons. Such data was collected for the calibration of UCV, CV, CC04, CC05, CC06, DCV, BHPV, and BHGC.

3.2.2.3 Aluminum Target Run

The KOTO detector is equipped with two aluminum target plates near the decay volume, as shown in Figure 3.2. One is a 5-mm-thick aluminum plate called the decay volume upstream (DVU-Al), and the other is a 3-mm-thick aluminum plate called the decay volume downstream (DVD-Al). Both of them were placed far away from the beam center during physics runs. Each of them was moved to the beam region during aluminum target runs. DVU-Al is located around the downstream end of FB ($z \sim 2800\,\mathrm{mm}$). In the DVU-Al run, the target was inserted in the beam. Neutrons hitting the target produce π^0's, and the $\pi^0 \to 2\gamma$ decay was used for the precise energy calibration for CSI using $\pi^0 \to 2\gamma$ decays. Events were triggered under the condition where the requirement of six clusters for the level-2 trigger was further added to the physics trigger described in Section 3.2.1.1.

DVD-Al is located upstream of FCV ($z \sim 5500\,\mathrm{mm}$). In addition to the π^0 production, η particles can also be produced at an aluminum target, and thus the run with DVD-Al was conducted to check the yield of η with respect to that of π^0. Although this run was not used for the purpose of detector calibration, it was utilized in the estimation of the systematic uncertainty on the CV-η background as will be described in Section 6.3.5. The DVD-Al run was not conducted in 2021 but done in 2019. Events were triggered under the same condition as the physics trigger[5] described in Section 3.2.1.1.

---

[5] The physics trigger condition in 2019 was the same as the one in 2021.

3.2.3 Special Run

Finally, other types of runs with special data-taking conditions are described in this section.

3.2.3.1 Special Run for the Hadron-Cluster Background

In addition to the aluminum targets described in Sectioin 3.2.2.3, there exists another aluminum target located near the origin of the z-axis (Z0-Al)[6]. The Z0-Al target is a 3-mm-thick aluminum plate[7], and was used to collect control sample for the study of the hadron-cluster background, as shown in Figure 3.3. During this run, the Z0-Al target plate, which was usually positioned outside the beam-core region, was inserted perpendicularly to the beam axis. Since neutrons scattered at the Z0-Al target increase the component of beam-halo neutrons, events in which a neutron hitting CSI generates two clusters can be collected efficiently. Events were triggered under the same condition as the one for the DVU-Al run described in Section 3.2.2.3.

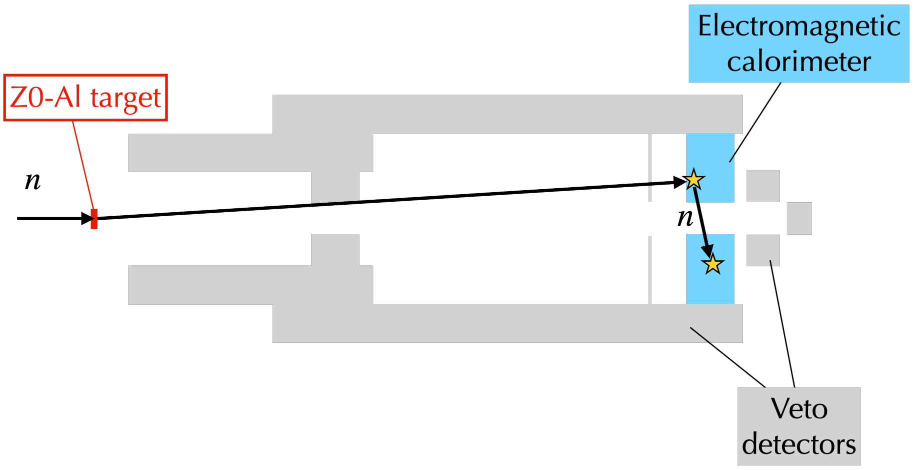

Figure 3.3: Schematic view of the Z0-Al target run to collect a neutron control sample.

3.2.3.2 Special Run for UCV

The special run for UCV was performed in order to collect $K^{\pm}$-rich data that was available for the measurement of the K^{+} detection inefficiency of UCV. Since UCV was intended to reduce the $K^{\pm}$ background, its performance needed to be evaluated. The inefficiency of UCV was therefore measured using events selected by the $K^{\pm}$ trigger in physics runs as will be described in Section 6.3.6. However, the flux of $K^{\pm}$ can be significantly enhanced by turning off the sweeping magnet in the KL beamline and letting charged particles directly reach the KOTO detector. Thus, this special run was conducted under the same trigger condition as the physics run. This run allowed for quick data-taking and large statistics for the $K^{\pm}$ sample. A study on the inefficiency measurement gave the systematic uncertainty on the $K^{\pm}$ background, and will be described in Section 6.3.6.

---

[6] Technically, the location of the Z0-Al target is not $z = 0$ mm but $z = -836$ mm. Note that this is downstream of the UCV position ($z = -920$ mm).

[7] An aluminum target plate with a thickness of 10 mm had been used until it was replaced with the current one in 2019.

Chapter 4

Event Reconstruction

This chapter first describes how deposited energy and hit timing were calculated for every single detector channel. Next, the procedures of clustering and reconstructing π^0 and K_L in CSI are explained. Finally, the procedure to reconstruct veto information is detailed.

4.1 Energy and Timing Reconstruction from Waveform

We determined deposited energy and timing given by particles hitting detectors or random noise activities for every single channel from each waveform. Depending on whether signals were recorded with 125-MHz or 500-MHz sampling chennels, we used different methods to calculate energy and timing.

4.1.1 Baseline

Waveform baselines are not equal to zero ADC counts due to the offset voltage applied in the ADC modules. Thus, the ADC count corresponding to the baseline level needs to be determined to calculate deposited energy from waveforms. The baseline was calculated for every waveform using either first or last nine sampling points[1] . The baseline value was defined as the mean of the ADC counts of the nine samples that have smaller standard deviation. Figure 4.1 shows an example of the baseline determination in the case of a 125-MHz sampling channel. This method was adopted for all the detectors but DCV. This is because we often observed undershoot after a main pulse in waveforms of DCV. To avoid inaccurate estimation of the baseline level, the baseline calculation for DCV was based only on the first nine samples.

---

[1] The 0th and 63rd (255th) clocks among 64 (256) samples for 125-MHz (500-MHz) sampling detectors were excluded for this calculation. The sample at 0th clock was used to calculate a baseline for the trigger system.

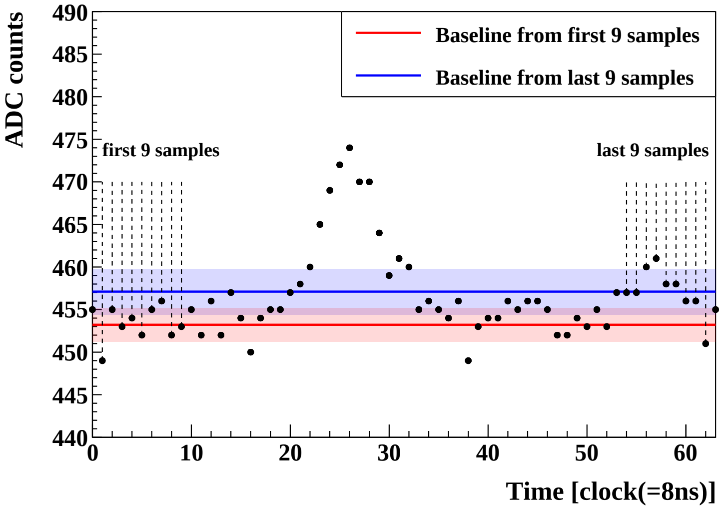

Figure 4.1: Baseline of a waveform. The red (blue) line corresponds to the mean value of the first (last) nine samples, and the band in the same color shows the range of one standard deviation. In this example, the first nine samples give smaller standard deviation, and thus the red line is selected as a baseline value.

4.1.2 Detector with 125-MHz Sampling ADC

4.1.2.1 Energy

Deposited energy for 125-MHz sampling detectors was calculated by summing ADC counts across all the 64 samples with subtraction of the baseline described in in Section 4.1.1. The sum of ADC counts were then translated into the corresponding energy in MeV by multiplying a scale factor (calibration constant).

4.1.2.2 Timing for CSI

Timing of a pulse recorded in CSI channels was defined as the time at which a rising-edge slope exceeded the half of the peak height of the pulse. We refer to it as the constant-fraction timing. To obtain the constant-fraction timing, we first looked for a sample with the maximum ADC counts among all the 64 samples. We then identified two adjacent samples[2] that satisfy the relation

$$S_j < h/2 + B \leq S_{j+1}, \tag{4.1}$$

where S_j (S_{j+1}), h, and B represent ADC counts of the sample at the clock of j ($j+1$), the peak height of the pulse, and the baseline level, respectively. The constant-fraction time (t^{CF}) was obtained by linear interpolation between the two samples as

$$t^{\mathrm{CF}} = j + \frac{h/2 + B - S_j}{S_{j+1} - S_j}. \tag{4.2}$$

Figure 4.2 illustrates the algorithm of this method.

---

[2] The adjacent samples were scanned in the region before the maximum peak position.

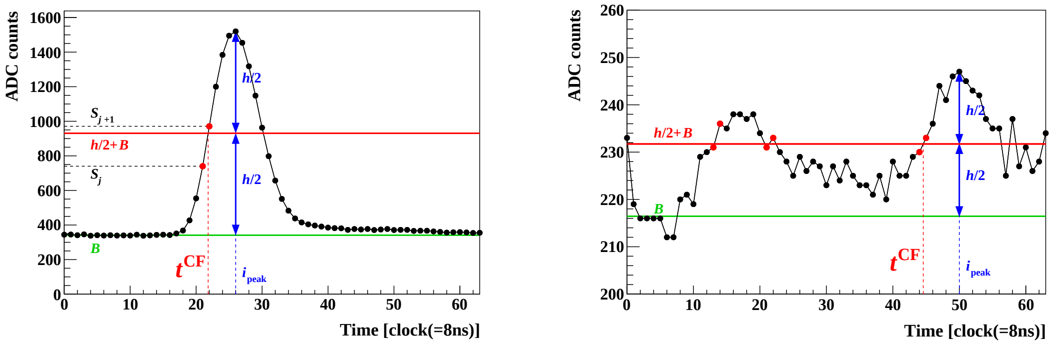

Figure 4.2: Determination of the constant-fraction timing (t^{CF}). The green line shows the baseline level (B). The peak height of the pulse (h) is found at the clock of i_{peak}. The constant-fraction timing shows when the rising-edge exceeds the half of the peak height (red solid line). As shown in the right figure, if more than one candidate of the adjacent samples (red dots) satisfying Equation 4.1 is found, the one closest to i_{peak} is selected.

The constant-fraction timing described above has an upside of mitigating a timing fluctuation depending on the pulse height (i.e., deposited energy) in comparison with the peak timing (shown as i_{peak} in Figure 4.2). As studied in Ref. [127], the constant-fraction time still has dependence on deposited energy due to distortion of the pulse shape, and thus a timing correction for each channel was made for waveforms with deposited energy greater than 400 MeV.

4.1.2.3 Timing for Veto Detectors

One of the concerns regarding the timing determination for veto detectors is an effect of pulse overlaps by accidental hits. Figure 4.3 shows an example of deviation of the constant-fraction timing due to an additional pulse. If the measured timing is shifted outside the veto window, it can lead to an increase in the background. Therefore, we took a different method to determine the timing for 125-MHz-sampling veto detectors. We used a parabola timing (t^{P}) defined as the axis of symmetry of a parabola curve. First, we smoothed a waveform by taking the moving average of five consecutive samples so that the noise in the waveform would not make a peak. After that, we looked for a local maximum peak satisfying

$$\bar{S}_{j-1} < \bar{S}_j \leq \bar{S}_{j+1}, \tag{4.3}$$

where $\bar{S}_j$ represents the ADC counts of the sample at the clock of j for the smoothed waveform. This peak-finding was performed for $\bar{S}_j$ greater than a given threshold so as not to detect the one around the baseline if any. We then solved the vertex of the parabola based on the above three consecutive samples. If multiple candidates satisfying Equation 4.3 existed, we selected the one closest to the nominal timing[3] determined for each detector. Figure 4.4 shows the algorithm of this method.

---

[3] The nominal timing is decided for each detector as a typical timing where the hits in the detector tend to be detected.

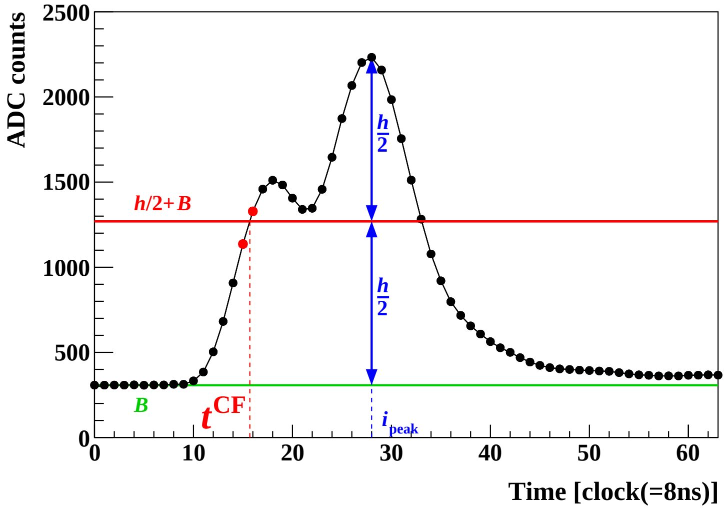

Figure 4.3: Timing shift due to an additional pulse. In this example, the pulse peaking at 29th clock is partially overlapped by another pulse in the rising-edge slope. The constant-fraction timing is thus deviated from the expected position around 20th clock.

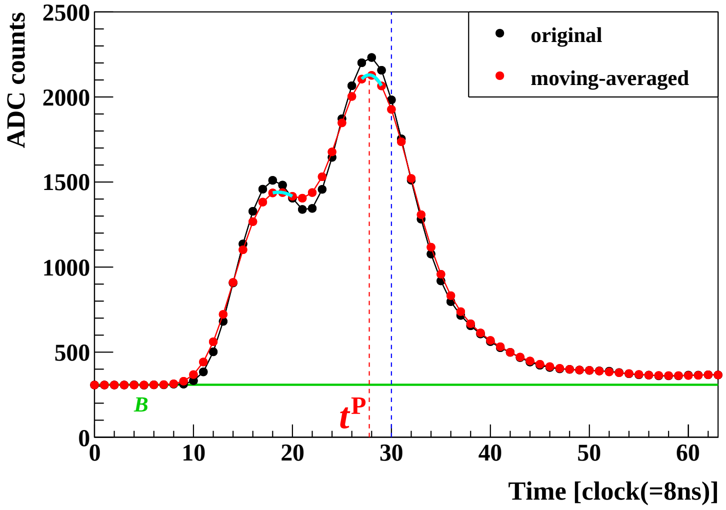

Figure 4.4: Example of waveform smoothing and the parabolic interpolation. The black dots show the original waveform while the red dots show the moving-averaged waveform. In this example, the blue dashed line at 30th clock represents the nominal timing. The moving-averaged waveform has two peak candidates around 19th clock and 29th clock. The parabolic interpolation (cyan line) is performed for these two, and the one closest to the nominal timing is selected.

4.1.3 Detector with 500-MHz Sampling ADC

4.1.3.1 Pulse Identification

As described in Section 2.6.2, the 500-MHz-sampling ADC modules were used for detectors with high hit rate. The peak-finding for each pulse was performed for the moving-averaged waveform. To avoid the detection of fake pulses, the requirement tighter than Equation 4.3 was imposed as

$$\bar{S}_{j-2} < \bar{S}_{j-1} < \bar{S}_{j} \leq \bar{S}_{j+1} < \bar{S}_{j+2}, \tag{4.4}$$

where $\bar{S}_j$ was further required to be greater than a given threshold for each detector. The deposited energy and timing were calculated for each pulse using the original waveform[4]. The appropriate candidate of the pulse for the veto was selected after adjusting the timing, as will be described in Section 4.3.

4.1.3.2 Energy and Timing

Deposited energy corresponding to an observed pulse was calculated by summing ADC counts around the pulse for IB, newBHCV, BHPV, and BHGC. The clock range for summation was determined for each detector. For UCV, peak height of each pulse was used to calculate deposited energy. In both cases, baseline given in Section 4.1.1 was subtracted, and the ADC counts were converted to the energy in units of MeV or the number of photoelectrons (p.e.) based on each calibration constant.

The timing of each pulse was calculated based on the algorithm of the constant-fraction timing using the original waveform.

4.2 Event Reconstruction with CSI

Based on the reconstructed energy and timing for CSI, the clustering of electromagnetic showers and the reconstruction of π^0 was performed. In some cases, K_L was also reconstructed.

4.2.1 Clustering

The procedure of cluster identification in the offline analysis (hereinafter referred to as the offline clustering) is different from the cluster-finding algorithm used in the level-2 trigger system described in Section 2.6.3.2. To define a cluster in CSI, we first selected crystals that had the deposited energy greater than 3 MeV and the timing within a 150-ns-wide window. Such crystals are called the cluster seeds. Next, we grouped any cluster seeds within a radius of 71 mm from each into the same cluster, as illustrated in Figure 4.5. If the grouping ended up in a single crystal (isolated-hit crystal), that was not defined as a cluster, but used for the veto purpose, as will described in Section 4.3.1.1.

---

[4] The moving-averaged waveform was used only to identify peak positions.

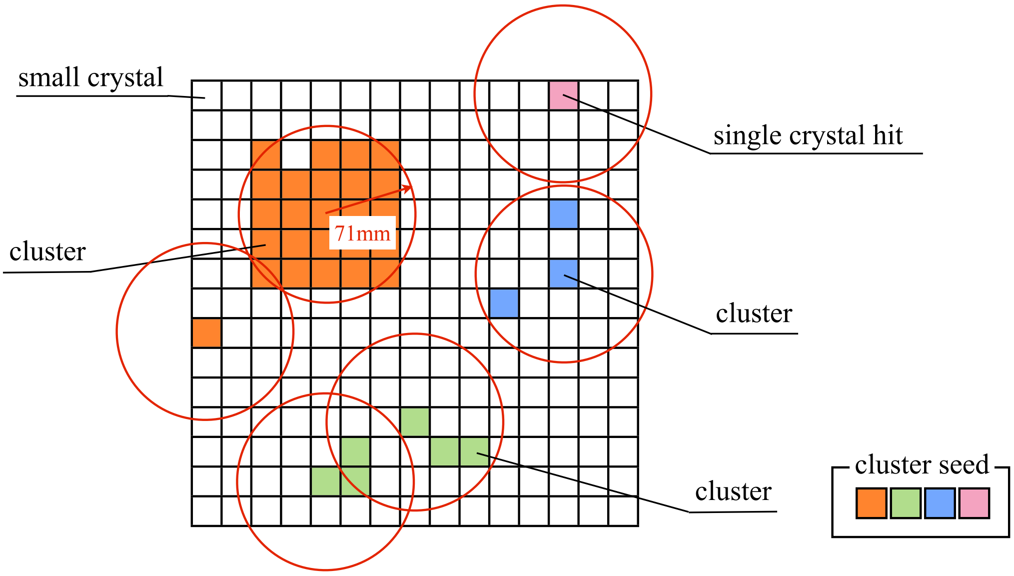

Figure 4.5: Grouping of cluster seeds. The grid represents small crystals. Cluster seeds are shown in different colors. The red circles represent the region for grouping. There are three cluster candidates (orange, green, and blue) and one single crystal hit (pink). The figure is quoted from Ref. [127].

The cluster energy (e_{clus}), x-y position ($\boldsymbol{r}_{\mathrm{clus}}$), and timing ($t_{\mathrm{clus}}$) were calculated as

$$e_{\mathrm{clus}} = \sum_i^n e_i, \tag{4.5}$$

$$\boldsymbol{r}_{\mathrm{clus}} = \frac{\sum_i^n \boldsymbol{r}_i e_i}{\sum_i^n e_i}, \tag{4.6}$$

$$t_{\mathrm{clus}} = \frac{\sum_i^n t_i \sigma_t^2}{\sum_i^n 1/\sigma_t^2}, \tag{4.7}$$

where n is the number of crystals in the cluster, and e_i, $\boldsymbol{r}_i$, and t_i are the energy, x-y position, and timing of each crystal, respectively. σ_t is the timing resolution of crystals as a function of energy, and was measured in the past test as $\sigma_t = 5/e_i \oplus 3.63/\sqrt{e_i} \oplus 0.13$, where σ_t and e_i are in the units of ns and MeV, respectively [81].

Since clusters could contain accidental hits which should be distributing randomly in time, we removed such crystals based on the timing cut. Figure 4.6 shows the distribution of the timing for crystals. The $\pm 5\sigma$ region in the timing distribution is allowed. For crystals with the timing outside this region, a timing deviation defined as $|t_i - t_{\mathrm{clus}}|/\sigma$ was calculated for each crystal. The one with the maximum deviation was excluded from cluster seeds, and used for the veto cut as is the case with the isolated-hit crystal. The whole procedure described above was repeated until the maximum timing-deviation went below 5.

In addition to the above treatment, the cluster timing itself was also examined because the whole cluster may be induced from an accidental hit. A cluster with the maximum timing difference from the average timing of all the cluster candidates was excluded and not used for

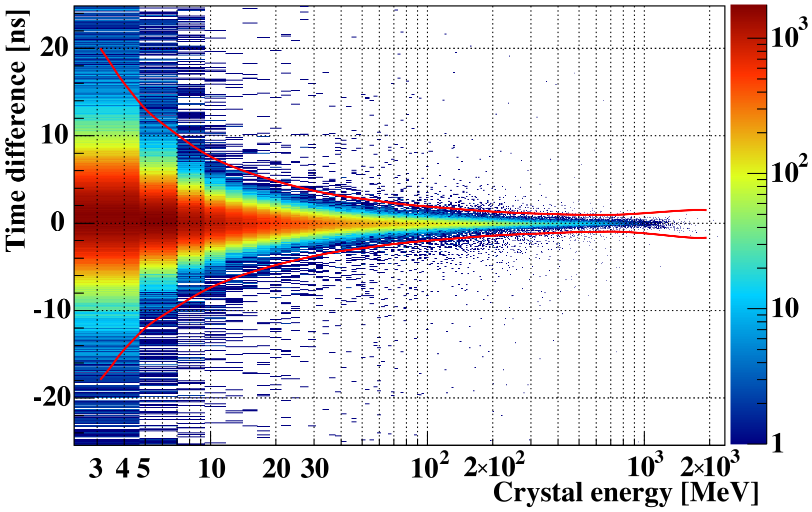

Figure 4.6: Distribution of the timing for crystals relative to the cluster timing as a function of the crystal energy. Color represents the number of events in arbitrary units. The redlines indicate the boundaries of the $\pm5\sigma$ region. The figure is quoted from Ref. [127].

the $\pi^0 \rightarrow 2\gamma$ reconstruction. If that cluster satisfied the photon cluster requirement described in the next section, that was categorized as an extra cluster. The extra cluster was used for the veto purpose, as will be described in Section 4.3.1.2. This process was repeated until the timing difference between the earliest and latest cluster became less than 30 ns.

4.2.2 π^0 Reconstruction

This section describes reconstruction procedure for π^0. Using the cluster information obtained in Section 4.2.1, π^0's were reconstructed through $\pi^0 \rightarrow 2\gamma$ decays. Figure 4.7 shows the procedure of π^0 reconstruction. First, each cluster was required to have the energy of 20 MeV or more as preliminary qualification to be a photon cluster. If we found more than two photon clusters, we selected two of them giving the closest cluster timing to each other. The π^0 information was then reconstructed with these two photon clusters, as described below.

4.2.2.1 Reconstruction of the π^0 Decay Vertex

The vertex position along the z-axis, Z_{vtx} was obtained in the following steps. The opening angle θ between the two photon momenta was determined from Equation 2.3. In addition to Equation 2.3, the opening angle θ also satisfies the laws of cosines for the triangle consisting of the vertex position on the beam axis (red point in Figure 2.3) and the hit positions of the two photons (γ_1 and γ_2) on the CSI surface (blue points in Figure 2.3). The hit positions were determined from Equation 4.6. The resulting relation can be expressed as

$$\cos\theta = \frac{|\boldsymbol{r}_{\gamma_1}|^2 + |\boldsymbol{r}_{\gamma_2}|^2 - |\boldsymbol{r}_{\gamma_1} - \boldsymbol{r}_{\gamma_2}|^2}{2|\boldsymbol{r}_{\gamma_1}||\boldsymbol{r}_{\gamma_2}|}, \tag{4.8}$$

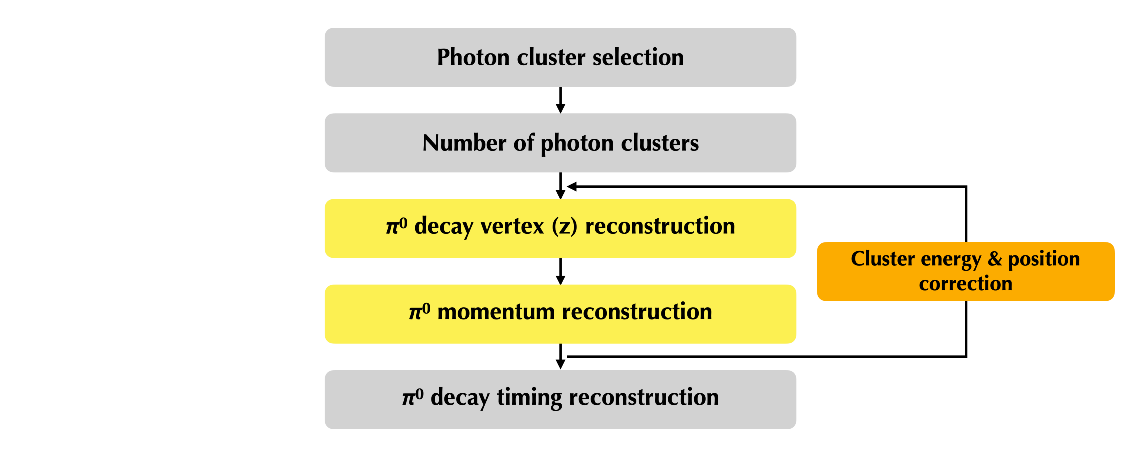

Figure 4.7: Flow of the π^0 reconstruction.

where $\boldsymbol{r}_{\gamma_{1(2)}}$ represents a position vector determined from $(0, 0, Z_{\mathrm{vtx}})$ to $(x_{\mathrm{clus}}, y_{\mathrm{clus}}, Z_{\mathrm{CSI}})$[5] for $\gamma_{1(2)}$. Using Equation 2.3 and Equation 4.8, one can obtain Z_{vtx} from the following relation:

$$(1-\cos^2\theta)dZ^4 + \left\{2\boldsymbol{r}_1\cdot\boldsymbol{r}_2 - (r_1^2+r_2^2)\cos^2\theta\right\}dZ^2 + (\boldsymbol{r}_1\cdot\boldsymbol{r}_2)^2 - r_1^2r_2^2\cos^2\theta = 0, \tag{4.9}$$

where $dZ(= Z_{\mathrm{CSI}} - Z_{\mathrm{vtx}})$ is the distance between the vertex position and the CSI surface and $\boldsymbol{r}_{1(2)}$ is the cluster position ($\boldsymbol{r}_{\mathrm{clus}}$) of $\gamma_{1(2)}$. Equation 4.9 gives at most two solutions for dZ^2. If both of them are the positive values, such events were discarded.

4.2.2.2 Reconstruction of the π^0 Momentum

Once Z_{vtx} was solved, the energies and directions of the two photons were determined. Subsequently, the π^0 momentum in the transverse (longitudinal) direction, P_t (P_z), was reconstructed as

$$P_t = \left|\sum_{i=1}^{2}\frac{E_i\boldsymbol{r}_i}{\sqrt{r_i^2+dZ^2}}\right|, \tag{4.10}$$

$$P_z = \sum_{i=1}^{2}\frac{E_i dZ}{\sqrt{r_i^2+dZ^2}}, \tag{4.11}$$

where E_i and $\boldsymbol{r}_i$ are the cluster energy (e_{clus}) and position ($\boldsymbol{r}_{\mathrm{clus}}$) of γ_i, respectively.

4.2.2.3 Correction for the Position and Energy

After the π^0 momentum was once reconstructed, the cluster energy and position were corrected based on the incident angle of the photon. The cluster position obtained in Equation 4.6 was calculated as the center of energy, and that was assumed to be the incident hit position in the π^0 reconstruction. However, the cluster position does not match with the hit position, as shown in

---

[5] $Z_{\mathrm{CSI}} = 6168$ mm is the z-position of the CSI surface.

Figure 4.8. In order to make a correction, the average distance of the electromagnetic shower (L_{s}) between the incident position and the shower maximum was calculated as

$$L_{\mathrm{s}} = \left(p_0 + p_1 \ln(e_{\mathrm{clus}})\right) X_0, \tag{4.12}$$

where $X_0 (= 18.5\,\mathrm{mm})$ is the radiation length of CsI, e_{clus} is the cluster energy in GeV, and $p_0 (= 6.490)$ and $p_1 (= 0.993)$ are the parameters obtained from a simulation. The incident hit position was then calculated using the photon incident angle θ_{clus}[6] as

$$\boldsymbol{r}_{\mathrm{inc}} = \left(1 - \frac{L_{\mathrm{s}} \sin\theta_{\mathrm{clus}}}{r_{\mathrm{clus}}}\right) \cdot \boldsymbol{r}_{\mathrm{clus}}. \tag{4.13}$$

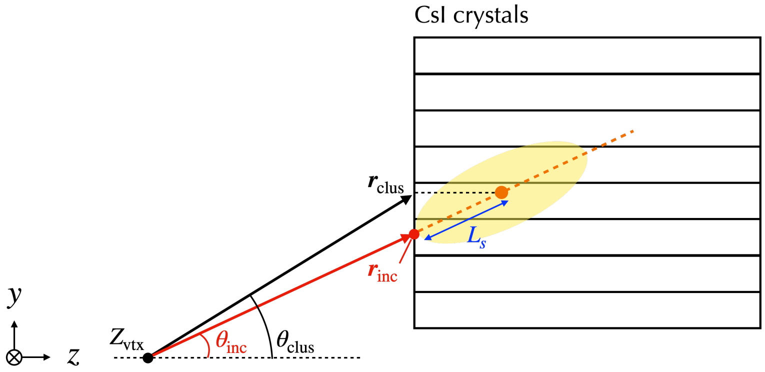

Figure 4.8: Correction for the photon hit position. The black (red) arrow represents the photon direction before (after) the correction. The yellow area represents the shower development in CSI. The cluster position ($\boldsymbol{r}_{\mathrm{clus}}$) and the incident hit position ($\boldsymbol{r}_{\mathrm{inc}}$) do not match depending on the shower depth (L_s).

The cluster energy obtained in Equation 4.5 does not consider possible energy leaks due to shower leakage and the energy threshold of 3 MeV for cluster seeds. Thus, the energy was corrected as

$$e_{\mathrm{clus}} \longrightarrow e_{\mathrm{clus}} \cdot \left(1 + f(E,\, \theta)\right), \tag{4.14}$$

where $f(E,\, \theta)$ is the correction term as a function of the photon cluster energy and incident angle obtained by a simulation.

The incident photon energy and momentum were then reconstructed based the corrected cluster energy and position, and the reconstructed vertex position. After the above corrections were applied, the reconstruction procedures described in Sections 4.2.2.1 and 4.2.2.2 were repeated again. Details of corrections for positions and energies can be found in Ref. [85].

4.2.2.4 Reconstruction of the π^0 Decay Timing

The photon timing at the $\pi^0 \to 2\gamma$ decay vertex (vertex time) was calculated using the cluster timing and the time of flight between $(0,\, 0,\, Z_{\mathrm{vtx}})$ and $\boldsymbol{r}_{\mathrm{inc}}$ as

$$t^i_{\mathrm{vtx}} = t^i_{\mathrm{clus}} - \sqrt{r_i^2 + dZ^2}/c, \tag{4.15}$$

---

[6] As shown in Figure 4.8, the angle denoted as θ_{inc} is the true incident angle. However, the angle θ_{inc} is unknown at this stage, and thus θ_{clus} was used for the correction instead.

where r_i^2 is r_{inc}^2 of γ_i and c is the speed of light. The $\pi^0 \to 2\gamma$ decay timing (event vertex time) was then obtained with the vertex timings of the two photons as

$$T_{\mathrm{vtx}} = \frac{\sum_{i=1}^{2} t_{\mathrm{vtx}}^{i}/\sigma_t^2(E_i)}{\sum_{i=1}^{2} 1/\sigma_t^2(E_i)}, \tag{4.16}$$

where $\sigma_t(E\,[\mathrm{MeV}]) = 3.8/\sqrt{E\,[\mathrm{MeV}]} \oplus 0.19$ is the vertex timing resolution in the unit of ns as a function of the photon energy.

4.2.3 K_L Reconstruction for Normalization Decay Modes

This section describes reconstruction procedures for $K_L \to \pi^0\pi^0$, $K_L \to 3\pi^0$, and $K_L \to 2\gamma$. As mentioned in Section 2.1.3, these decay modes were used to normalize the number of K_L decays for the $K_L \to \pi^0\nu\bar{\nu}$ analysis. The number of photons in the final state (N_γ) is four (six) in the decay chain of $K_L \to \pi^0\pi^0 \to 4\gamma$ ($K_L \to 3\pi^0 \to 6\gamma$) and two in the $K_L \to 2\gamma$ decay. Reconstruction of K_L required detection of all these photons at CSI. Figure 4.9 shows the reconstruction procedures for $K_L \to \pi^0\pi^0$ and $K_L \to 3\pi^0$, and Figure 4.10 shows that for $K_L \to 2\gamma$. Details are described in the following sections.

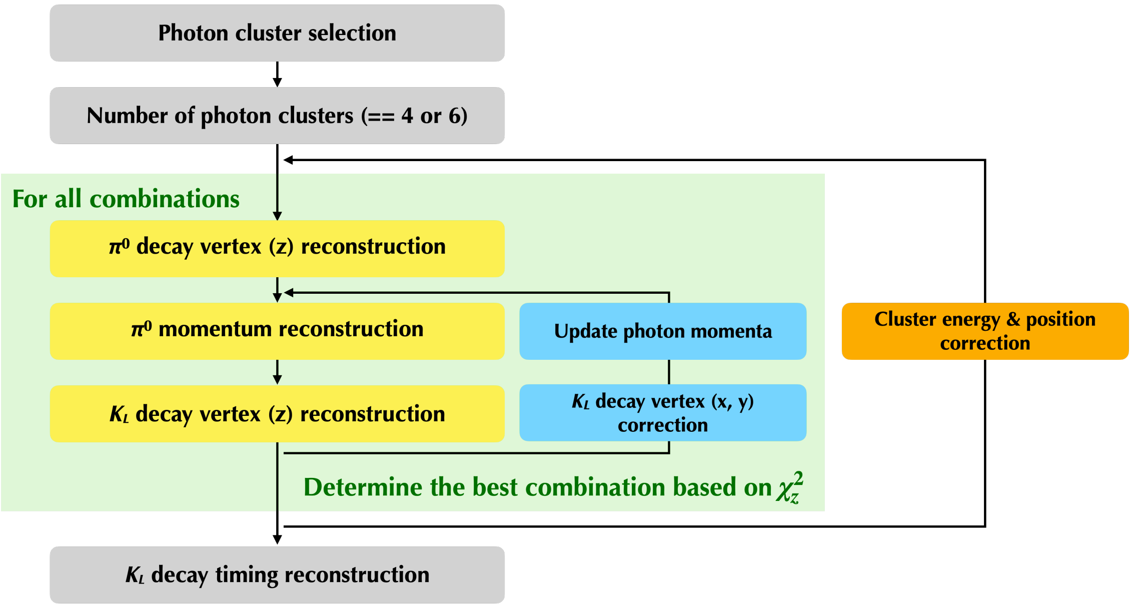

Figure 4.9: Flow of the $K_L \to \pi^0\pi^0$ and $K_L \to 3\pi^0$ reconstructions.

4.2.3.1 Reconstruction of $K_L \to \pi^0\pi^0$ and $K_L \to 3\pi^0$

Each π^0 in $K_L \to \pi^0\pi^0$ and $K_L \to 3\pi^0$ was reconstructed from two photon clusters in the same manner as one described in Section 4.2.2. If we found more than N_γ photon clusters, we selected N_γ photon candidates out of them such that the closest proximity in cluster timings was achieved. Since $K_L \to \pi^0\pi^0$ ($K_L \to 3\pi^0$) has 3 (15) possible combinations of photon pairings for reconstructing two (three) π^0's[7], we performed reconstructions for all the combinations. Among

---

[7] The number of combinations is given as $({}_4C_2 \times {}_2C_2)/2! = 3$ for $K_L \to \pi^0\pi^0$ and $({}_6C_2 \times {}_4C_2 \times {}_2C_2)/3! = 15$ for $K_L \to 3\pi^0$.

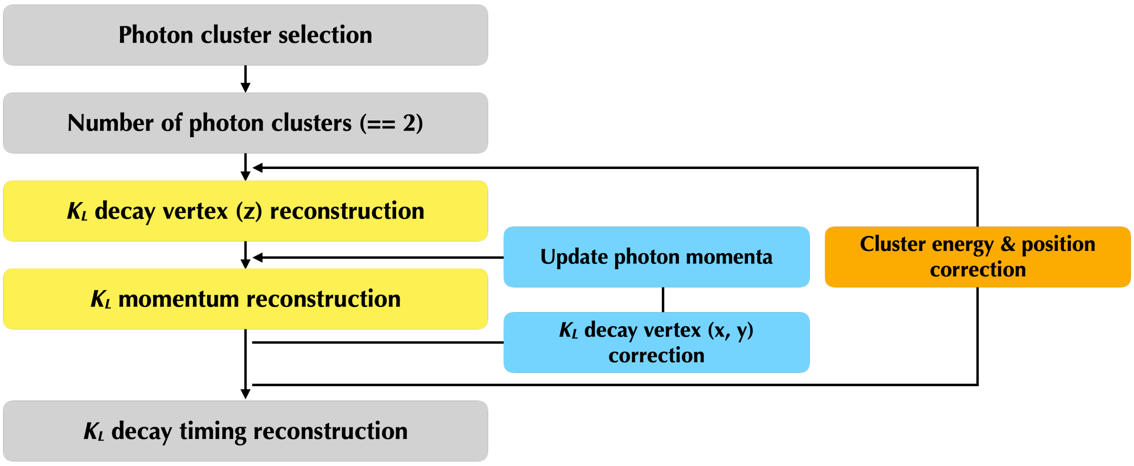

Figure 4.10: Flow of the $K_L \to 2\gamma$ reconstruction.

these combinations, we selected the one based on the consistency of reconstructed Z_{vtx} calculated for K_L and π^0's as described below.

The z-position at the K_L decay vertex ($Z_{\text{vtx}}^{K_L}$) was determined from the Z_{vtx} of π^0's, because of the negligible lifetime of π^0. The value of $Z_{\text{vtx}}^{K_L}$ was calculated as

$$Z_{\text{vtx}}^{K_L} = \frac{\sum_{i=1}^{N_{\pi^0}} Z_{\text{vtx}}^i/\sigma_i^2}{\sum_{i=1}^{N_{\pi^0}} 1/\sigma_i^2}, \tag{4.17}$$

where N_{π^0} ($= N_\gamma/2$) is the number of π^0's in the decay, σ_i and Z_{vtx}^i are the resolution of the reconstructed vertex position as a function of two photon energies and the reconstructed z-position at the $\pi^0 \to 2\gamma$ decay vertex for the i-th π^0, respectively. In order to evaluate the consistency of vertex positions, we defined a variable χ_z^2 as,

$$\chi_z^2 = \sum_{i=1}^{N_{\pi^0}} \left(\frac{Z_{\text{vtx}}^i - Z_{\text{vtx}}^{K_L}}{\sigma_i} \right)^2, \tag{4.18}$$

where the index i (j) represents the i-th (j-th) π^0. We took the photon-pairing combination giving the smallest χ_z^2 value for the reconstruction. The consistency of the vertex positions can also be defined as

$$\Delta Z_{\text{vtx}} = \max\left(|Z_{\text{vtx}}^i - Z_{\text{vtx}}^j| \right), \tag{4.19}$$

where the index i (j) represents the i-th (j-th) π^0. Equations 4.18 and 4.19 are used for the event selection in the normalization mode analysis

4.2.3.2 Reconstruction of $K_L \to 2\gamma$

The $K_L \to 2\gamma$ decay directly makes two photons without involving a π^0. The decay was reconstructed in the similar way to the π^0 reconstruction, but the invariant mass of the two photons was assumed to be the K_L mass instead of the π^0 mass in Equation 2.3.

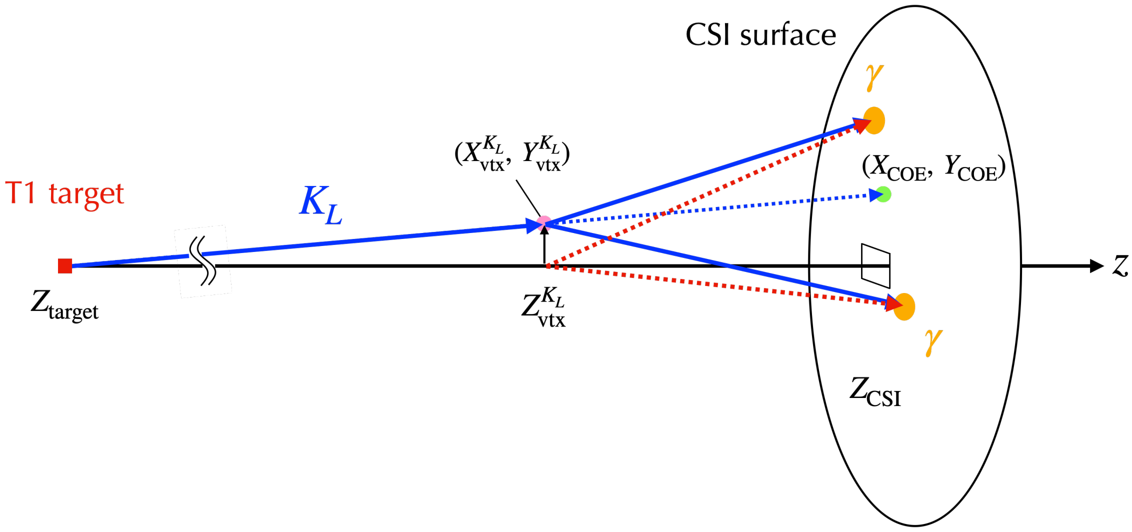

Figure 4.11: Schematic view of the K_L vertex position. The red point indicates the production target (T1 target). The pink and green points indicate the vertex position of the K_L decay and the COE position, respectively. The blue arrows show the trajectories of K_L and two photons produced from the π^0 or K_L decay. The blue dashed arrow shows the trajectory extrapolated from the vertex to the CSI surface. The vertex was first assumed to be on the beam axis, and the photon directions are determined as the red dashed arrows. By the correction, the vertex is shifted to the pink point.

4.2.3.3 Correction for the K_L Decay Position

Before completing the reconstruction procedures, the following correction was applied. The reconstructions for the above three K_L decays assumed that the decays occurred on the z-axis. In other words, the x-y position of the decay vertex, $\boldsymbol{R}_{\mathrm{vtx}}^{K_L} = (X_{\mathrm{vtx}}^{K_L}, Y_{\mathrm{vtx}}^{K_L})$, was set as

$$X_{\mathrm{vtx}}^{K_L} = Y_{\mathrm{vtx}}^{K_L} = 0. \tag{4.20}$$

However, the actual vertex position on the x-y plane could be deviated from the z-axis. The reconstruction for the normalization decay modes allowed for correction of $\boldsymbol{R}_{\mathrm{vtx}}^{K_L}$ because all the final-state photons were fully detected. The correction took the following steps. First, we calculated the center-of-energy (COE) position on the CSI surface, $\boldsymbol{R}_{\mathrm{COE}}$ (= $X_{\mathrm{COE}}, Y_{\mathrm{COE}}$), defined as

$$\boldsymbol{R}_{\mathrm{COE}} = \frac{\sum_{i=1}^{N_\gamma} E_i \boldsymbol{r}_i}{\sum_{i=1}^{N_\gamma} E_i}, \tag{4.21}$$

where E_i and $\boldsymbol{r}_i$ are the energy and incident hit position of γ_i, respectively. As shown in Figure 4.11, the COE position can be considered as the extrapolated position where K_L would hit if it did not decay on the way. After calculating the $\boldsymbol{R}_{\mathrm{COE}}$ position for each photon hit, the $\boldsymbol{R}_{\mathrm{vtx}}^{K_L}$ (= $X_{\mathrm{vtx}}^{K_L}, Y_{\mathrm{vtx}}^{K_L}$) position was corrected as

$$\boldsymbol{R}_{\mathrm{vtx}}^{K_L} = \frac{Z_{\mathrm{vtx}}^{K_L} - Z_{\mathrm{target}}}{Z_{\mathrm{CSI}} - Z_{\mathrm{target}}} \cdot \boldsymbol{R}_{\mathrm{COE}}, \tag{4.22}$$

where Z_{target}(= −21507 mm) is the z-position of the T1 target.

Based on the obtained vertex position, all the photon momenta were updated, and subsequently, all the π^0 momenta, energies, and invariant masses were also recalculated, accordingly. Finally, additional correction for photon energies and hit positions described in Section 4.2.2.3 was applied. After that, all the procedures described above were repeated again, and the momentum, energy, and invariant mass for K_L was reconstructed.

4.2.3.4 Reconstruction of the K_L Decay Timing

The event vertex time for the K_L decay ($T_{\mathrm{vtx}}^{K_L}$) was obtained in the same manner as one described in Section 4.2.2.4, and was calculated as

$$T_{\mathrm{vtx}}^{K_L} = \frac{\sum_{i=1}^{N_\gamma} t_{\mathrm{vtx}}^i / \sigma_t^2(E_i)}{\sum_{i=1}^{N_\gamma} 1/\sigma_t^2(E_i)}, \tag{4.23}$$

where $\sigma_t(E)$ is the same as in Equation 4.16.

4.3 Reconstruction of Veto Information

4.3.1 CSI

As described in Section 4.2.1, isolated-hit crystals and extra clusters were utilized for the veto purpose. The veto cuts based on the CSI information were intended to reject events where an extra photon hitting CSI was not identified as a photon cluster due to the photo-nuclear reaction in the shower propagation. This section explains the criteria of the veto cuts by CSI using isolated-hit crystals and extra clusters.

4.3.1.1 Isolated-Hit Crystal Veto

If the timing of an isolated-hit crystal was within ±10 ns of the timing of its nearest cluster and the deposited energy was greater than a given threshold, the event was vetoed. The energy requirement for accepted events was determined as

$$\begin{cases} E \leq 10\,\mathrm{MeV} & (d \leq 200\,\mathrm{mm}) \\ E \leq 10 - 7 \cdot (d - 200)/400\,\mathrm{MeV} & (200 < d \leq 600\,\mathrm{mm}) \\ E \leq 3\,\mathrm{MeV} & (d \geq 600\,\mathrm{mm}), \end{cases} \tag{4.24}$$

where E and d are the deposited energy and the distance from the nearest cluster, respectively.

In addition to the above requirement, the deposited energies in isolated-hit crystals with d larger than 200 mm was further evaluated with a tighter threshold determined from the noise level of each CSI channel. The noise level, σ, was obtained from data collected by the random trigger. If the energy was larger than the tight energy threshold corresponding to 3σ ($E_{3\sigma}$), such events were discarded. This tight requirement was given as

$$\begin{cases} E \leq 10\,\mathrm{MeV} & (d \leq 200\,\mathrm{mm}) \\ E \leq 10 - 7 \cdot (d - 200)/400\,\mathrm{MeV} & (200 < d \leq d_{3\sigma}\,\mathrm{mm}) \\ E \leq E_{3\sigma}\,\mathrm{MeV} & (d \geq d_{3\sigma}\,\mathrm{mm}), \end{cases} \tag{4.25}$$

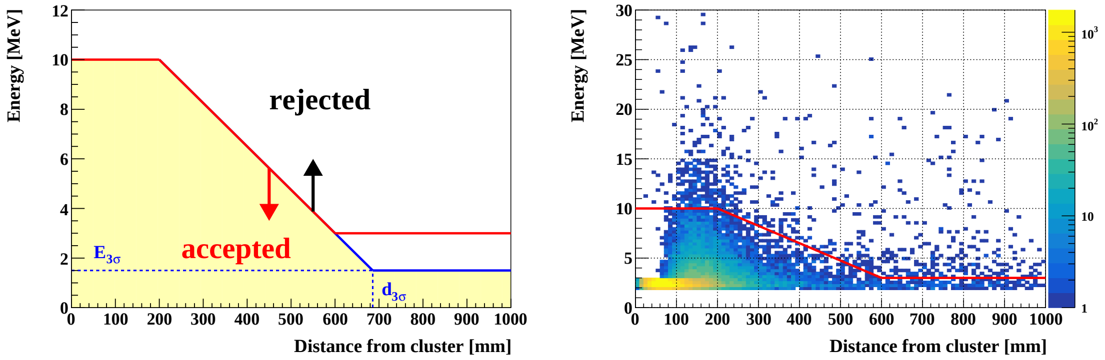

Figure 4.12: Criteria for the isolated-hit crystal veto. The left figure shows the cut boundaries on the plane of the deposited energy and the distance from the nearest cluster. The red (blue) line indicates the energy threshold with the standard (tight) condition. The case with $E_{3\sigma}$ of 1.5 MeV is demonstrated. The yellow area represents the accepted region when the veto cut with the tight condition is applied. The right figure shows $K_L \to \pi^0 \nu \bar{\nu}$ MC events including all the CSI channels on the cut plane. The red line indicates the cut boundary with the standard condition.

where

$$d_{3\sigma} = 200 + \frac{400}{7}(10 - E_{3\sigma}). \tag{4.26}$$

Figure 4.12 shows the cut boundary on the d-E plane and the distribution of $K_L \to \pi^0 \nu \bar{\nu}$ MC events. For the tight condition, most of the CSI channels had $E_{3\sigma}$ threshold values below 3 MeV, as shown in Figure 4.13. Either Equation 4.24 or 4.25 was chosen for the veto criterion depending on the analysis.

4.3.1.2 Extra-Cluster Veto

The requirement for the extra-cluster veto was determined based on the timing of extra clusters. If the vertex times calculated from the extra clusters were within ±10 ns of the event vertex time, such events were discarded.

4.3.2 Veto Detectors

4.3.2.1 General Strategy

The criteria of veto cuts relied on the deposited energy and timing in each detector. The energy for the veto decision should be large enough to discriminate hits from K_L decay products and random noise fluctuations. The timing of each detector was adjusted with the time-of-flight (TOF) determined from the decay vertex to the hit position so that a narrow peak in the timing distribution can be obtained. The module-veto-timing ($t^{\mathrm{veto}}_{\mathrm{mod}}$), the timing for each detector module with respect to the event vertex time, was calculated as

$$\begin{aligned} t^{\mathrm{veto}}_{\mathrm{mod}} &= t_{\mathrm{mod}} - T_{\mathrm{vtx}} - \mathrm{TOF} \\ &= t_{\mathrm{mod}} - T_{\mathrm{vtx}} - D/c, \end{aligned} \tag{4.27}$$

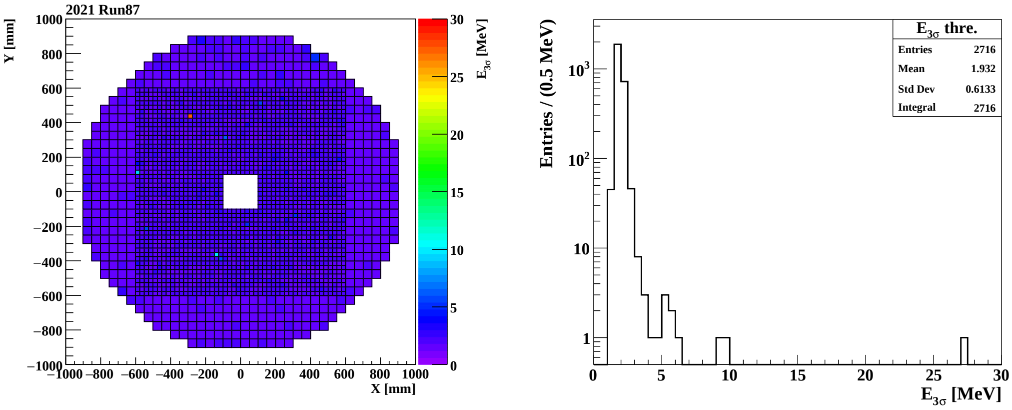

Figure 4.13: Distributions of the $E_{3\sigma}$ threshold values. The left two-dimensional distribution is the CSI map where the z-axis shows $E_{3\sigma}$. The right figure shows the projection of the left distribution to the z-axis.

where t_{mod} is the timing of each module (module-timing), T_{vtx} is the event vertex time, D is the distance between the decay vertex and the hit position at the detector. It should be noted that the distance D is dependent on the Z_{vtx} position. The reconstructed quantity Z_{vtx} could deviate from the true vertex position in a particular case such as the $K_L \to \pi^0\pi^0$ background with the mis-combination of π^0's. That may result in the incorrect calculation of the timing. Therefore, the timing correction was treated in different ways for each detector. To evaluate the veto decision, we selected one of the modules which represented the energy and timing for the detector. We opened a certain width of time window (veto window) around the nominal timing for each detector to judge whether the module-veto-timing was within the time window or not. As a general strategy, the module with the maximum energy deposition (module-energy)[8] within the veto window was selected as the module for the veto decision. Such energy and timing are referred to as the veto energy and the veto timing. The energy threshold for each detector is defined with respect to the veto energy.

As an example, the following section briefly explains the case for FB, NCC, Hinemos, and UCV. Details on other detectors may be found in Appendix B and Refs. [68, 83, 105, 49]. All the criteria for the veto cuts will be shown in Chapter 6.

4.3.2.2 FB, NCC, Hinemos, and UCV

For FB, NCC, Hinemos, and UCV, the TOF was corrected using the z-position of CSI instead of the hit position. With this method, the module-veto-timing can be reduced to the simple form as

$$\begin{aligned} t_{\mathrm{mod}}^{\mathrm{veto}} &= t_{\mathrm{mod}} - \left(T_{\mathrm{CSI}} - \left(\frac{Z_{\mathrm{CSI}} - Z_{\mathrm{vtx}}}{c}\right)\right) - \left(\frac{Z_{\mathrm{CSI}} - Z_{\mathrm{vtx}}}{c}\right) \\ &= t_{\mathrm{mod}} - T_{\mathrm{CSI}} \end{aligned} \tag{4.28}$$

where the dependence on the reconstructed Z_{vtx} was removed.

---

[8] For detectors with the both-end readout, energies at the both ends are summed to calculate the energy for each module.

In the case of UCV, for instance, deposited energy for each hit found in the 512-ns window in each module was calculated, and the one with the maximum energy was selected as the module-energy for each module. The maximum module-energy from all the modules was then selected as the veto energy. Description on the calibration for UCV is given in Appendix D.1.

4.3.2.3 Veto Acceptance for $K_L \to \pi^0\nu\bar{\nu}$

Although the veto cuts need to reject background events, they are expected to be quiet for the $K_L \to \pi^0\nu\bar{\nu}$ signal decay because of no extra detectable particles. Thus, it seems as if one can achieve the large signal acceptance of the veto cut (veto acceptance). In reality, however, the veto acceptance highly suffers from accidental activities. Accidental hits originate from beam particles and decay products from them, such as K_L, neutrons, and photons. They constantly hit detectors anytime during a spill regardless of triggers. If accidental hits are detected within the veto window with deposited energy greater than a threshold, such events are discarded even though they have nothing to do with $K_L \to \pi^0\nu\bar{\nu}$ signals or background events. This results in the loss of the signal acceptance. The probability of the acceptance loss due to accidental hits (accidental loss) can be estimated as

$$\begin{aligned} L &= 1 - P(k = 0; \lambda = R \cdot T) \\ &= 1 - e^{-R\cdot T}, \end{aligned} \tag{4.29}$$

where $P(k; \lambda)$ is the Poisson probability function of observing k events with the mean of λ, and R and T are the accidental hit rate and the width of the veto window for the veto detector, respectively. Since the rate of accidental hits depends on the beam power, the loss becomes larger when the beam is provided at the higher power. In addition, the noise fluctuation observed in waveforms could also make fake hits satisfying the veto criteria on the energy and timing. Thus, the counting rate of the noise contribution is another factor that affects the accidental loss. Although the accidental loss is governed by the above conditions, the width of the veto window is under control in the analysis stage. As can be seen in Equation 4.29, the wider veto window leads to the larger accidental loss. Thus, the width of the veto window was determined for each detector so that it can cover the time range wide enough to reject background events and it can be narrow to avoid the unnecessary loss.

Additionally, the effect called the backsplash loss exists. The backsplash is a phenomenon where electromagnetic showers produced in CSI emit photons or $e^{\pm}$ upstream. If such particles splash back toward veto detectors and hit them, satisfying the veto condition on the energy and timing, the event is also discarded. Figure 4.14 illustrates the signal loss induced from accidental hits and the backsplash effect.

4.3.2.4 Extension of Veto Windows for FB, NCC, and CV

Although the narrower veto window is ideal from the viewpoint of reducing the accidental loss, one could fail to veto events that should be rejected if it is too narrow. Particularly, it can happen in the case where a pulse is overlapped with another, leading to a shift of the measured timing. Therefore, the veto windows of FB, NCC, and CV were widened to reduce the inefficiency against the background.

The decision on whether the veto window should be widened or not was made by the pulse shape discrimination method. For this method, a template of single-hit waveforms was prepared

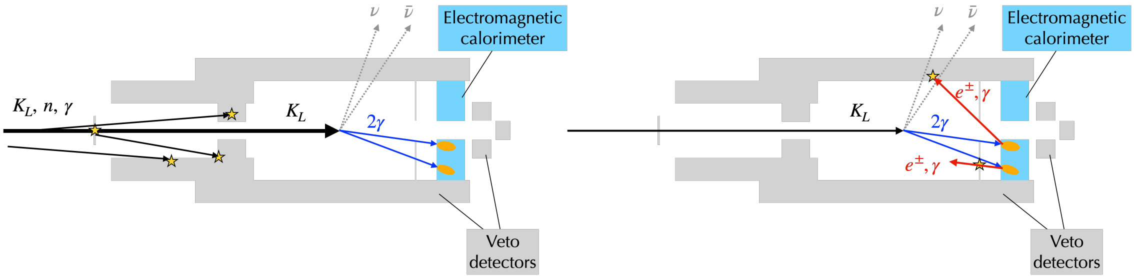

(a) Accidental hit (b) Backsplash

Figure 4.14: Examples of the signal loss due to accidental hits and backsplash effects.

from the data collected in the physics run. Pulses in the collected waveforms were categorized into different energy bins according to the pulse height of each waveform. The pulses in each energy bin were normalized to have the same area and were shifted to have the same timing at the peak. At each sampling point, the mean value of the height was calculated. If the deviation of the height from the mean value is smaller than the pedestal fluctuation for all the data points, such waveforms were selected as the single-hit waveforms.

We applied a fast Fourier transform (FFT) to the template waveforms. The mean value and standard deviation of the magnitude of the FFT output were calculated They were used in the evaluation of a χ^2 value defined as

$$\chi^2_{\mathrm{FFT}} = \sum_{i=1}^{5} \left(\frac{h_i - \mu_i}{\sigma_i} \right)^2, \tag{4.30}$$

where h_i is the hight of the FFT output of the waveform to be evaluated, μ_i is the mean height of the FFT output of the template, and σ_i is the standard deviation of the FFT output of the template. The index i denotes the i-th frequency component. In the calculation of χ^2_{FFT}, the lowest five components were used because the high frequency components were governed by the baseline fluctuation. The veto window was widened when the χ^2_{FFT} value of the waveform was larger than a given threshold. Detailed descriptions on this algorithm can be found in Refs. [105, 49].

Chapter 5

Monte Carlo Simulation

In this chapter, we describe a procedure for generating events using the Monte Carlo (MC) simulation.

5.1 Overview

In the KOTO analysis, the MC simulation is used to estimate the acceptances of $K_L \to \pi^0\nu\bar{\nu}$ and the normalization-mode decays ($K_L \to \pi^0\pi^0$, $K_L \to 3\pi^0$, and $K_L \to 2\gamma$). It is also used to understand various background events, which is often difficult in evaluating the contributions only with data. The simulation procedure mainly consists of the following steps:

1. Generation of incident particles that enter the KOTO detector.
2. Simulation of decays and interactions with detector material based on the software toolkit, GEANT4 version 10.5.1. The simulation results in the time-dependent hit information with deposited energy in each detector.
3. Generation of waveforms from the time-dependent energy deposition with detector responses applied

5.2 Generation of Incident Particles

The MC simulations begin with generation of incident particles to shoot into the KOTO detector. Such seeds for the MC simulation are categorized into two types: beam-core seed to simulate the beam-core K_L and the beam-line seed to simulate the beam-halo particles, such as beam-halo K_L, beam-halo neutrons, and $K^\pm$.

5.2.1 Beam-Core K_L Seed

The beam-core K_L was generated according to the empirical momentum spectrum based on the past measurement [91]. The spectrum can be expressed as

$$f(p,\, \mu,\, \sigma_0,\, A,\, S) = \exp\left\{-\frac{(p-\mu)^2}{2(\sigma_0(1-(A+Sp)\cdot(p-\mu)))^2}\right\}, \tag{5.1}$$

where p represents the K_L momentum in GeV/c and μ, σ_0, A, and S represent fitting parameters. From the past study [91], the fitting parameters were determined to be $(\mu, \sigma_0, A, S) = (1.420, 0.8102, -0.3014, 0.01709)$. Figure 5.1 shows the momentum spectrum for the beam-core K_L.

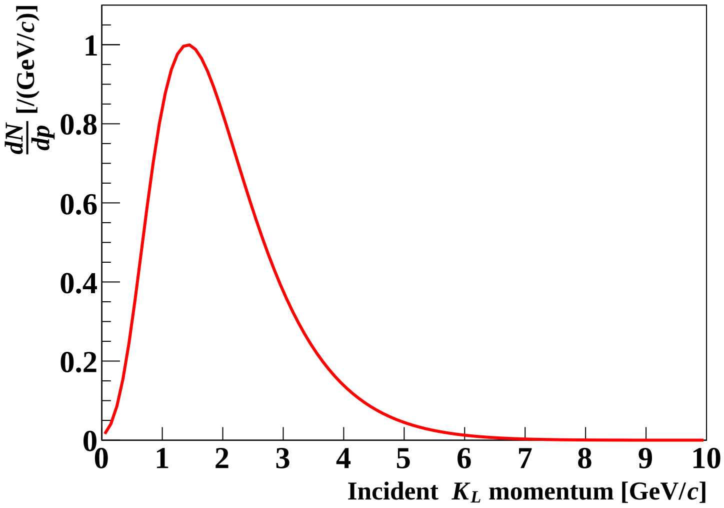

Figure 5.1: K_L momentum spectrum at the beam exit. The momentum peaks around 1.4 GeV/c.

The K_L position and direction at the beam exit were given by the simulation based on the uniform angular production within the solid angle defined with the collimator. The x-y position distribution (target image) was obtained by another simulation of 30-GeV protons hitting the production target. Figure 5.2 shows the target image and the collimator lines. By extrapolating the K_L position from the target position to the beam exit, the position distributions at the beam exit (beam profile) was obtained as shown in Figure 5.3.

5.2.2 Beam-Line Seed

Alternative way to generate incident particles is to fully rely on the simulation including beam-line components (beam-line simulation). Sine the beam-core seed does not consider particles scattered at the beam-line components, such particles are instead treated in the beam-line seed obtained from the beam-line simulation. This method helps to understand the beam-halo particles and the origins of background events associated with them.

In the beam-line simulation, we first simulated 30-GeV proton collisions at the production target. Secondary particles going inside the entrance of the 1st collimator were recorded at a position 1 m away from the target and 16° away from the primary beam line. Next, we simulated decays of the particles selected from the recorded ones, and their interactions with beam-line components. Finally, particles reaching the beam exit were recorded as the beam-line seed. Figure 5.4 shows the particle content in the beam-line seed. As can be seen in Figure 5.5, the tail region of the position distribution is more enhanced in the beam-line seed than the beam-core seed due to scatterings with the beam-line components.

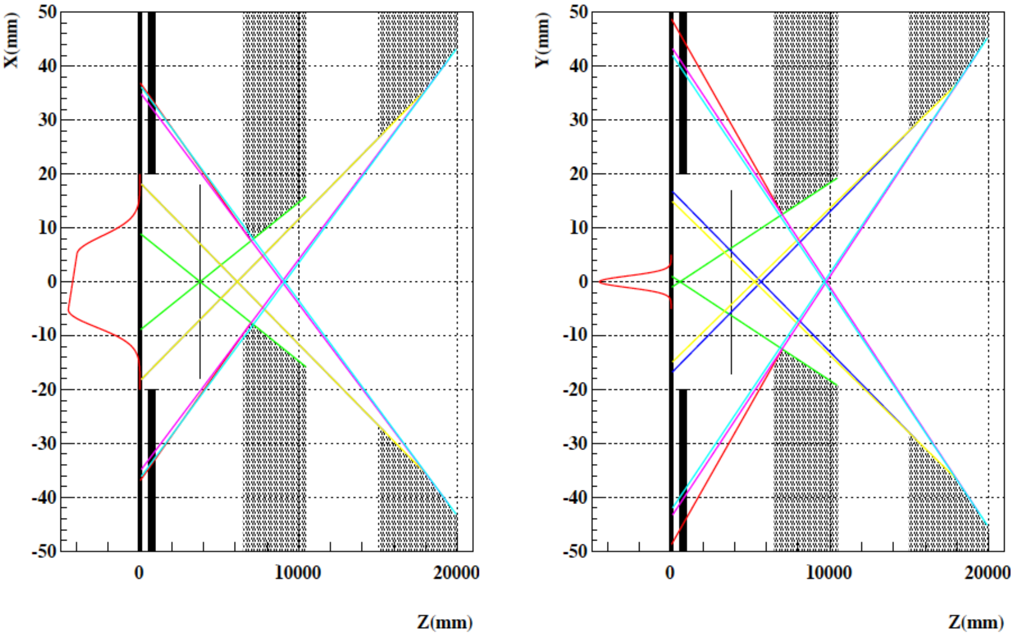

Figure 5.2: Target image (red lines drawn in $Z < 0$ mm) and collimator lines (colored straight lines drawn in $Z > 0$ mm) in X-Z (left) and Y-Z (right) planes. The shaded regions around $6500 < Z < 10500$ mm and $15000 < Z < 20000$ mm indicate the upstream and downstream collimators, respectively. In these figures, the origin of Z is defined to be the target position, and thus the exit from the KL beamline corresponds to the position of $Z = 20000$ mm in the figures. The figures are quoted from Ref. [83].

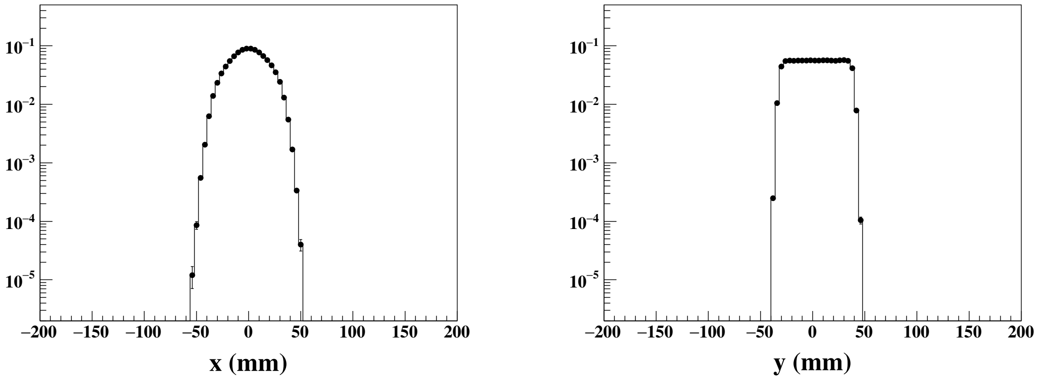

Figure 5.3: Position distributions of the beam-core seeds at the beam exit. The figures are quoted from Ref. [105].

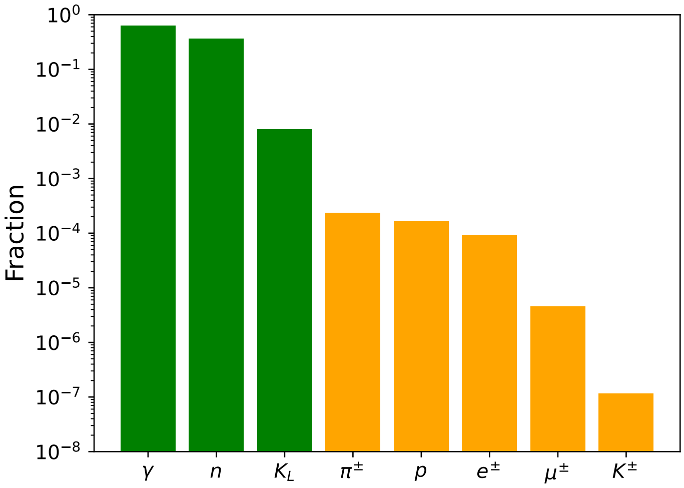

Figure 5.4: Particle content in the beam-line seeds with 10^{12} POT. Although the great majority of beam particles are neutral (green), small amount of charged particles (orange) also exit. In this simulation, photons (γ), electrons ($e^{\pm}$), neutrons (n), and protons (p) with the kinetic energy less than 300 MeV were not recorded.

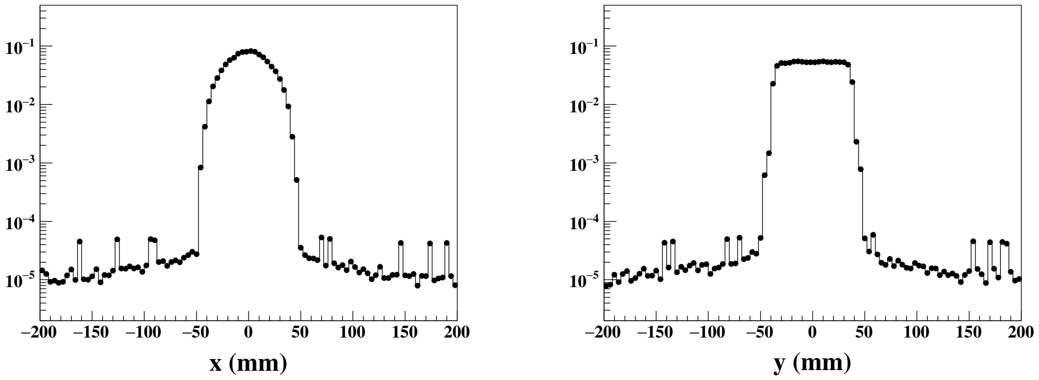

Figure 5.5: Position distributions of the beam-line seeds at the beam exit. The spiky structure is due to the repeated usage of the particles recorded in the first step of the simulation. The figures are quoted from Ref. [105].

5.3 Interaction with Detector Material

Simulation with detector material was based on Geant4 with the QGSP BERT physics list. Particle trajectories were tracked step by step, and then deposited energy, interaction time, and interaction position were recorded in each step. To realize the realistic output signal observed in each detector, the detector response was taken into account for these quantities, as described in Section 5.4.

5.4 Detector Response

All the subdetectors in the KOTO detector system are implemented in the KOTO simulation package. Each of them has its own response reproduced by some model function. Detailed descriptions on the detector response for each detector are found in Refs. [68, 83, 105, 49]. For UCV, scintillating fibers were placed according to its real geometry, as shown in Figure 5.6. However, the detector response was not fully implemented. In addition, as will be described in Sections 6.2.2.1 and 6.3.6.2, the effect of accidental activity on UCV and the $K^{\pm}$ detection inefficiency were evaluated with real data in order to reflect the realistic behavior. Thus, any output information of UCV given by the MC simulation was not used in the $K_L \to \pi^0 \nu \bar{\nu}$ analysis. The only exception was that the effect of particle scatterings at UCV. This effect was taken into account in the evaluation of the beam-halo $K_L \to 2\gamma$ background by shooting incident K_L from the position further upstream of UCV in the MC simulation.

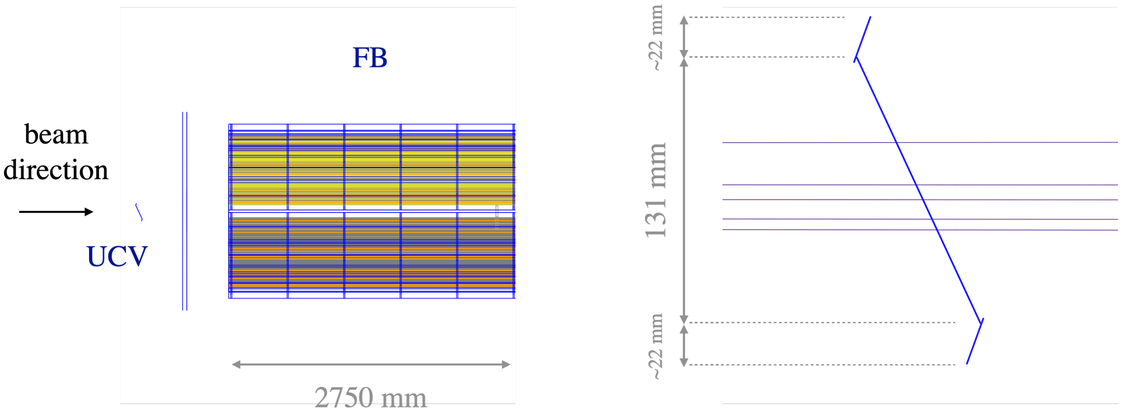

Figure 5.6: Geometry of UCV implemented in the KOTO simulation package. The left figure shows the side view of UCV (left) with FB (right). The right figure shows the expanded view of UCV with example tracks of incident particles shown as horizontal lines. Every single fiber with a thickness of 0.5 mm is placed, forming a tilted plate.

5.5 Accidental Overlay

As mentioned in the previous section, accidental activities and noise contributions in each detector needs to be taken into account in the MC simulation. Events collected by the TMON trigger provide each detector with waveforms representing the accidental activity. By overlaying them on the waveforms generated in the MC simulation, we reflected the effect of accidental activity to the simulation. This method is referred to as the accidental overlay. Energy and timing for simulated events were reconstructed from the waveforms obtained in this procedure. Figure 5.7 shows an example of the accidental overlay.

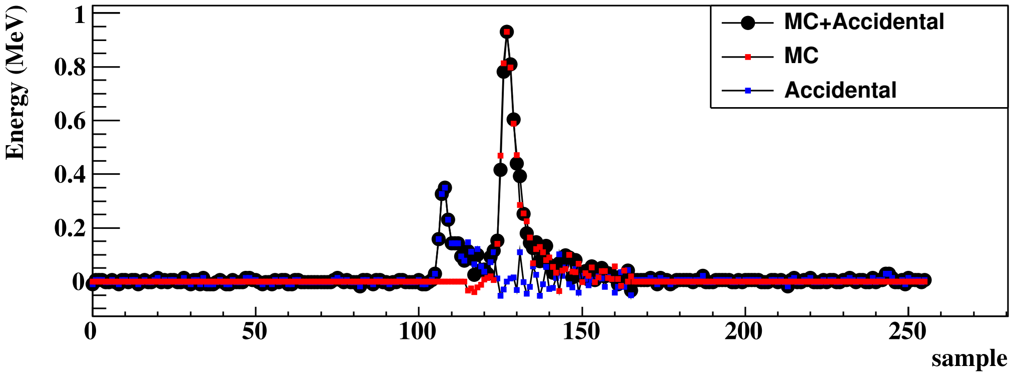

Figure 5.7: Example of accidental overlay. In this figure, an accidental overlay on a waveform in IB is demonstrated. The red points show the waveform generated by the MC simulation and the blue points show the waveform for the accidental activity. The black points are the sum of these two waveforms. The figure is quoted from Ref. [105].

Chapter 6

Analysis of the $K_L \to \pi^0 \nu \bar{\nu}$ and $K_L \to \pi^0 X^0$ Searches

This chapter describes the analysis of the 2021 data to search for the $K_L \to \pi^0 \nu \bar{\nu}$ decay. After the analysis overview is introduced in Section 6.1, the estimation of the single event sensitivity, the expected number of background events, and the results obtained from this search are explained. In Section 6.5, the analysis to search for the $K_L \to \pi^0 X^0$ decay is also described.

6.1 Outline

The analysis for the $K_L \to \pi^0 \nu \bar{\nu}$ search using the 2021 data was performed. Before getting into the detailed analysis, detector calibrations and the data quality checks were done. The two important studies are the estimations of SES and the number of background events that are expected to remain in the signal region. As explained in Section 2.1.1, the signal region had been blinded until the event selection criteria for $K_L \to \pi^0 \nu \bar{\nu}$ were determined. Technically, for two-cluster events in which the reconstructed π^0 P_t and Z_{vtx} satisfied the requirement for the signal region ($130 < P_t < 250\,\mathrm{MeV}/c$ and $3200 < Z_{\mathrm{vtx}} < 5000\,\mathrm{mm}$), they were removed from the dataset at the clustering stage. After that, the blinded region was opened and examined (unblinding). Based on the contents in the signal region, the results on the $K_L \to \pi^0 \nu \bar{\nu}$ search was extracted. For the $K_L \to \pi^0 X^0$ search, the same selection criteria as the $K_L \to \pi^0 \nu \bar{\nu}$ analysis were imposed.

The estimation of SES requires the yield of K_L. It is also used for the background evaluation to normalize the number of events from K_L decays generated by the MC simulation. Thus, the K_L yield was first estimated and used to determine the sensitivity in Section 6.2.3. The normalization of the K_L decays for MC simulation samples for the background evaluation was applied in Section 6.3, based on the result of the K_L yield estimation.

6.2 Single Event Sensitivity Estimation

To estimate SES from Equation 2.7, the two quantities, $N_{K_L\,\mathrm{decay}}$ and ϵ_{sig} defined in Section 2.1.3, need to be determined. For the convenience in the analysis, we introduce the decay probability of K_L (P_{decay}), and define the following:

$$N_{K_L} = N_{K_L\,\mathrm{decay}}/P_{\mathrm{decay}}, \tag{6.1}$$

$$A_{\mathrm{sig}} = P_{\mathrm{decay}} \cdot \epsilon_{\mathrm{sig}}. \tag{6.2}$$

N_{K_L} is the number of incident K_L's at the exit of the KL beamline. A_{sig} is the acceptance of the events for $K_L \to \pi^0\nu\bar{\nu}$ decays. These are simply referred to as the K_L yield and the signal acceptance, respectively. With these definitions, SES can be transformed as

$$SES = \frac{1}{N_{K_L\,\mathrm{decay}} \cdot \epsilon_{\mathrm{sig}}} = \frac{1}{N_{K_L} \cdot A_{\mathrm{sig}}}. \tag{6.3}$$

In this analysis, the K_L yield was estimated using the $K_L \to \pi^0\pi^0$ decay as

$$N_{K_L} = \frac{N_{K_L\to\pi^0\pi^0}}{A_{K_L\to\pi^0\pi^0} \cdot \mathcal{B}(K_L \to \pi^0\pi^0)}. \tag{6.4}$$

$N_{K_L\to\pi^0\pi^0}$ and $A_{K_L\to\pi^0\pi^0}$ represent the number of $K_L \to \pi^0\pi^0$ candidate events and the acceptance of the events for $K_L \to \pi^0\pi^0$ decays, respectively. $\mathcal{B}(K_L \to \pi^0\pi^0)$ is the branching ratio of the $K_L \to \pi^0\pi^0$ decay quoted from Ref. [1]. Using Equation 6.4, Equation 6.3 can be expressed as

$$SES = \frac{A_{K_L\to\pi^0\pi^0}}{A_{\mathrm{sig}}} \cdot \frac{\mathcal{B}(K_L \to \pi^0\pi^0)}{N_{K_L\to\pi^0\pi^0}}. \tag{6.5}$$

As described in Section 3.2.1, the $K_L \to \pi^0\nu\bar{\nu}$ sample and the $K_L \to \pi^0\pi^0$ sample were collected simultaneously during physics runs using the physics trigger and the normalization trigger, respectively. This allowed for cancellation of possible systematic uncertainties that exist in the both samples.

6.2.1 K_L Yield

We used the $K_L \to \pi^0\pi^0$ decay to estimate the K_L yield because the branching ratio of this mode was measured precisely and its kinematical features are similar to $K_L \to \pi^0\nu\bar{\nu}$, which leads to a cancellation of systematic uncertainties between $A_{K_L\to\pi^0\pi^0}$ and A_{sig}. We reconstructed a $K_L \to \pi^0\pi^0$ sample from four-cluster events. In Equation 6.4, $N_{K_L\to\pi^0\pi^0}$ was determined from the data sample while $A_{K_L\to\pi^0\pi^0}$ was determined from the MC sample. The data sample was collected with the normalization trigger described in Section 3.2.1.2. Since the number of recorded events was prescaled by a factor of p_{norm}, the number of $K_L \to \pi^0\pi^0$ candidate events is given as

$$N_{K_L\to\pi^0\pi^0} = N^{\mathrm{obs}}_{K_L\to\pi^0\pi^0} \cdot p_{\mathrm{norm}}, \tag{6.6}$$

where $N^{\mathrm{obs}}_{K_L\to\pi^0\pi^0}$ is the number of events that were actually observed in the available sample. If the purity of the $K_L \to \pi^0\pi^0$ sample is not perfect, other decays can contaminate the data sample as background events. Thus, $N^{\mathrm{obs}}_{K_L\to\pi^0\pi^0}$ was corrected as

$$N^{\mathrm{obs}}_{K_L\to\pi^0\pi^0} = N^{\mathrm{obs}} \cdot \mu, \tag{6.7}$$

where N^{obs} represents the total number of four-cluster events in the data sample after imposing the event selection, and μ represents the purity of $K_L \to \pi^0\pi^0$ for the data sample. The purity was estimated as

$$\mu = \frac{A_{K_L\to\pi^0\pi^0} \cdot \mathcal{B}(K_L \to \pi^0\pi^0)}{\sum_i (A_i \cdot \mathcal{B}_i)}. \tag{6.8}$$

The denominator in Equation 6.8 is a sum of products of the acceptance and the branching ratio for a decay mode i considered in the analysis. The acceptance was estimated as a fraction of the number of events that passed all the selection criteria to the total number of events generated by the MC simulation for each decay mode . In addition to the $K_L \to \pi^0\pi^0$ sample, we also estimated the K_L yield using the $K_L \to 3\pi^0$ and $K_L \to 2\gamma$ samples that were reconstructed from six-cluster and two-cluster events, respectively. This allowed us to crosscheck the consistency of the K_L yield estimates among the three decay modes.

6.2.1.1 Selection Criteria for the Normalization Modes

We imposed event selections (cuts) to the reconstructed samples in order to purify events of interest. For the three normalization decay modes, we determined selection criteria based on veto information and kinematic features of each decay. To ensure that there are no extra particles other than photons hitting CSI, we applied various veto cuts that are summarized in Table 6.1. The criteria on the veto cuts were the same as the ones used for the $K_L \to \pi^0\nu\bar{\nu}$ analysis except for the absence of veto on UCV, as will be described in Section 6.2.2.

The kinematic cuts are summarized in Table 6.2. The kinematic-cut variables were calculated using information from CSI, and each of them is detailed below.

- Trigger timing

  The photon clusters should be created in CSI at the coincident timing. Thus, we impose a cut with the average cluster timing ($\overline{T}_{\text{clus}}$) defined as

  $$\overline{T}_{\text{clus}} = \frac{\sum_{i=1}^{N_\gamma} t^i_{\text{clus}}}{N_\gamma}, \tag{6.9}$$

  where N_γ is the number of photon clusters and t^i_{clus} is the cluster timing of i-th photon cluster. The average cluster timing was required to be within ±15 ns around the nominal timing of CSI.

- Total energy (E_{total})

  Total energy of photon clusters was required to be larger than 650 MeV so that an effect of the CSIEt trigger with the threshold of 550 MeV can be negligible.

- Photon energy (E_γ)

  The photon energy, which was obtained from the cluster energy with corrections described in Section 4.2.2.3, was required to be larger than 50 MeV to ensure the quality of photon reconstruction.

- Photon position (x, y)

  The photon hit position was required to be within the fiducial region of CSI such that $\max(|x|, |y|) \geq 150$ mm and $\sqrt{x^2 + y^2} \leq 850$ mm were satisfied. This allows to reject events with electromagnetic shower leakage through inner and out boundaries of CSI.

- Two-photon distance (d)

  The distance between two photon clusters for all the possible pairs were required to be larger than 150 mm to ensure that electromagnetic showers are well separated.

Table 6.1: Summary of the veto cuts. For each detector, the deposited energy corresponding to a hit detected within the veto window was required to be less than the threshold.

Subdetector for veto	Energy threshold	Width of veto window
FB	1 MeV	51 ns
FB (wide window)[a]	3.2 MeV	170 ns
NCC (common readout)	1 MeV	40 ns
NCC (common readout, wide window)[a]	3.2 MeV	100 ns
NCC (individual readout)	10 MeV	10 ns
Hinemos	1 MeV	60 ns
MB	1 MeV	40 ns
IB	1 MeV	50 ns
MBCV	0.5 MeV	60 ns
IBCV	0.5 MeV	60 ns
CV	0.2 MeV	20 ns
CV (wide window)[a]	0.4 MeV	150 ns
CSI (isolated-hit crystal)	see Section 4.3.1	
CSI (extra cluster)	see Section 4.3.1	
OEV	1 MeV	20 ns
LCV	0.6 MeV	30 ns
CC03	3 MeV	60 ns
CC04, CC05, CC06 (CsI crystal)	3 MeV	30 ns
CC04, CC05, CC06 (plastic scintillator)	1 MeV	30 ns
DCV	5 MeV	60 ns
newBHCV[b]	221 eV	25 ns
BHPV[c]	2.5 p.e.	15 ns
BHGC	2.5 p.e.	15 ns

[a] The veto with the wide window was applied only if the χ^2_{FFT} value exceeded a given threshold. See Section 4.3.2.4 and Refs. [105, 49].

[b] The veto on newBHCV required hits in two out of three layers. The energy threshold shown here is for each layer.

[c] The veto on BHPV required the number of consecutive modules with hits to be three or more.

- $\Delta T_{\mathrm{vtx}}^{K_L}$

  The timing difference between $T_{\mathrm{vtx}}^{K_L}$ and the vertex time of each photon was required to be smaller than 3 ns to reject accidental photon hits.

- $Z_{\mathrm{vtx}}^{K_L}$

  The reconstructed z-vertex position was required to be within the decay volume of the KOTO detector as $3000 \leq Z_{\mathrm{vtx}}^{K_L} \leq 5000$ mm.

- K_L transverse momentum ($P_t^{K_L}$)

  The transverse momentum the reconstructed K_L was required to be smaller than 50 MeV/c. Since incident K_L direction was assumed to be parallel to the beam axis, this ensured that there were no missing particles in the final states of the normalization-mode decays.

- K_L mass (M_{K_L})

  The invariant mass of the reconstructed K_L was required to be within ±15 MeV/c^2 of the nominal K_L mass of 497.614 MeV/c^2 [1]. This cut was used to eliminate contamination of $K_L \to 3\pi^0$ decays in the $K_L \to \pi^0\pi^0$ analysis, and contamination of events with mis-combination in the $K_L \to \pi^0\pi^0$ and $K_L \to 3\pi^0$ analyses. In the $K_L \to 2\gamma$ analysis, events were reconstructed assuming the K_L mass for the invariant mass of the two photons. Thus, this cut was not used.

- χ_z^2

  χ_z^2 (defined in Section 4.2.3) was required to be smaller than 20 for $K_L \to 3\pi^0$ and $K_L \to \pi^0\pi^0$ to ensure the consistency among the vertex z-positions of π^0.

- ΔZ_{vtx}

  ΔZ_{vtx} (defined in Section 4.2.3) was required to be smaller than 400 mm for $K_L \to 3\pi^0$ and $K_L \to \pi^0\pi^0$ for the same purpose as the χ_z^2 cut.

- π^0 mass (M_{π^0})

  The invariant mass of the reconstructed π^0 was required to be within ±10(6) MeV/c^2 of the nominal π^0 mass of 134.9766 MeV/c^2 [1] for $K_L \to 3\pi^0$ ($K_L \to \pi^0\pi^0$). This cut was used to reduce events with the mis-combination of π^0.

- K_L position at beam-exit (X_{exit}, Y_{exit})

  The reconstructed K_L position at the beam-exit was required to be within $100 \times 100\,\mathrm{mm}^2$. If all the final-state particles hit CSI, the COE radius tends to be around the beam center. This cut was used to ensure there were no missing particles for the $K_L \to \pi^0\pi^0$ analysis. The position at the beam-exit $\boldsymbol{R}_{\mathrm{exit}} = (X_{\mathrm{exit}}, Y_{\mathrm{exit}})$ was calculated as

$$\boldsymbol{R}_{\mathrm{exit}} = \frac{Z_{\mathrm{exit}} - Z_{\mathrm{target}}}{Z_{\mathrm{CSI}} - Z_{\mathrm{target}}} \cdot \boldsymbol{R}_{\mathrm{COE}}, \tag{6.10}$$

  where Z_{exit}, Z_{target}, and Z_{CSI} are the z-positions of the beam-exit, the production target, and the upstream surface of CSI, respectively.

Table 6.2: Summary of the cuts on CSI-related variables. The top eight cuts in the table were imposed on all the three reconstructed samples while the bottom five cuts were imposed on the $K_L \to 3\pi^0$ sample and/or the $K_L \to \pi^0\pi^0$ sample.

Cut variable	Requirement for each reconstructed sample		
	$K_L \to 3\pi^0$	$K_L \to \pi^0\pi^0$	$K_L \to 2\gamma$
Trigger timing[a]	$\leq \pm 15\,\mathrm{ns}$		
Total energy (E_{total})[a]	$E_{\mathrm{total}} \geq 650\,\mathrm{MeV}$		
Photon energy (E_γ)	$E_\gamma \geq 50\,\mathrm{MeV}$		
Photon position (x, y)[a]	$\max(\lvert x\rvert, \lvert y\rvert) \geq 150\,\mathrm{mm}$ $\sqrt{x^2+y^2} \leq 850\,\mathrm{mm}$		
Two-photon distance (d)	$d \geq 150\,\mathrm{mm}$		
$\Delta T_{\mathrm{vtx}}^{K_L}$	$\Delta T_{\mathrm{vtx}}^{K_L} \leq 3\,\mathrm{ns}$		
$Z_{\mathrm{vtx}}^{K_L}$	$3000 \leq Z_{\mathrm{vtx}}^{K_L} \leq 5000\,\mathrm{mm}$		
K_L transverse momentum ($P_t^{K_L}$)	$P_t^{K_L} \leq 50\,\mathrm{MeV}/c$		
K_L mass	$\leq 15\,\mathrm{MeV}/c^2$	$\leq 15\,\mathrm{MeV}/c^2$	–
χ_z^2	$\chi_z^2 < 20$	$\chi_z^2 < 20$	–
ΔZ_{vtx}	$\Delta Z_{\mathrm{vtx}} \leq 400\,\mathrm{mm}$	$\Delta Z_{\mathrm{vtx}} \leq 400\,\mathrm{mm}$	–
π^0 mass	$\leq 10\,\mathrm{MeV}/c^2$	$\leq 6\,\mathrm{MeV}/c^2$	–
K_L position at beam exit	–	$\max(\lvert X_{\mathrm{exit}}\rvert, \lvert Y_{\mathrm{exit}}\rvert) \leq 50\,\mathrm{mm}$	–

[a] The same cut was used for the $K_L \to \pi^0 \nu \bar{\nu}$ analysis described in Section 6.2.2.1.

6.2.1.2 Distributions of Kinematic Variables

Figures 6.1 and 6.2 show distributions of kinematic-cut variables used for the $K_L \to \pi^0\pi^0$ sample. Each figure shows the distribution of the $K_L \to \pi^0\pi^0$ sample after imposing all the selection criteria except for the cut shown in the figure. In the reconstructed $K_L \to \pi^0\pi^0$ sample, the contamination of the $K_L \to 3\pi^0$ decay exists. The $K_L \to 3\pi^0$ decays can make four clusters in CSI with the extra two photons being missed in veto detectors, or two or more photons being fused into other clusters in CSI. The $K_L \to 3\pi^0$ contribution was significantly reduced by the cut with the reconstructed K_L mass shown in Figure 6.1a. The slight deviation seen in the tail of the K_L mass peak was not understood yet but treated as a systematic uncertainty on SES described in Section 6.2.4.5. After imposing all the cuts, the contamination of the $K_L \to 3\pi^0$ decay was about 3% in the $K_L \to \pi^0\pi^0$ sample. Most of the distributions show good agreement between the data and MC samples. The distribution of $\Delta T_{\mathrm{vtx}}^{K_L}$ shown in Figure 6.1f does not agree between the data and MC samples. Although this implies that the CSI timing response in the MC simulation was not fully understood, it did not make a large impact on the systematic uncertainty on SES by using a loose threshold of 3 ns, as described in Section 6.2.4.5.

Figure 6.3 shows distributions of kinematic-cut variables used for the reconstructed $K_L \to 3\pi^0$ sample. In the reconstructed $K_L \to 3\pi^0$ sample, the requirement for the number of clusters in CSI eliminates other K_L decays contaminating this sample. Thus, the purity of the $K_L \to 3\pi^0$ was kept at nearly 100%. The distribution of $\Delta T_{\mathrm{vtx}}^{K_L}$ shown in Figure 6.3f shows inconsistency similar to the one seen in the $K_L \to \pi^0\pi^0$ sample, which did not make an effect on the SES. The tail component in the distribution of the K_L mass can come from the mis-measurement of the π^0 kinematics due

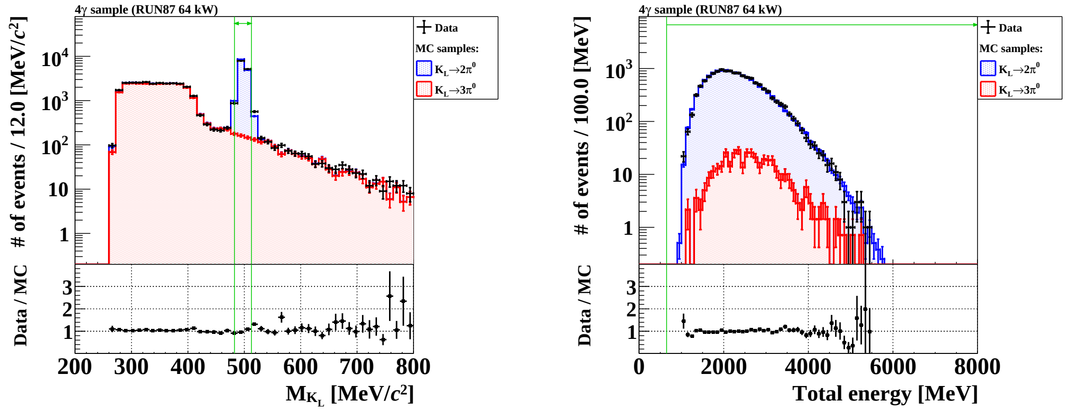

(a) Reconstructed K_L mass (b) Total energy

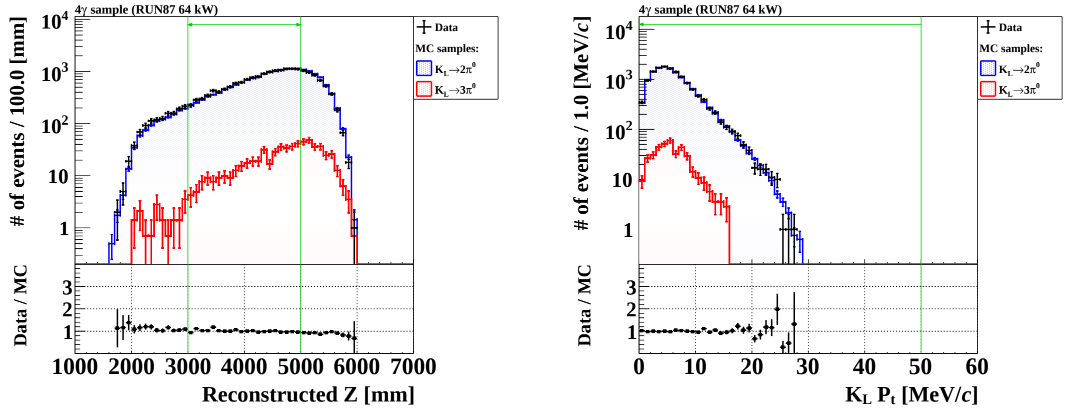

(c) Reconstructed Z_{vtx} (d) Reconstructed K_L P_t

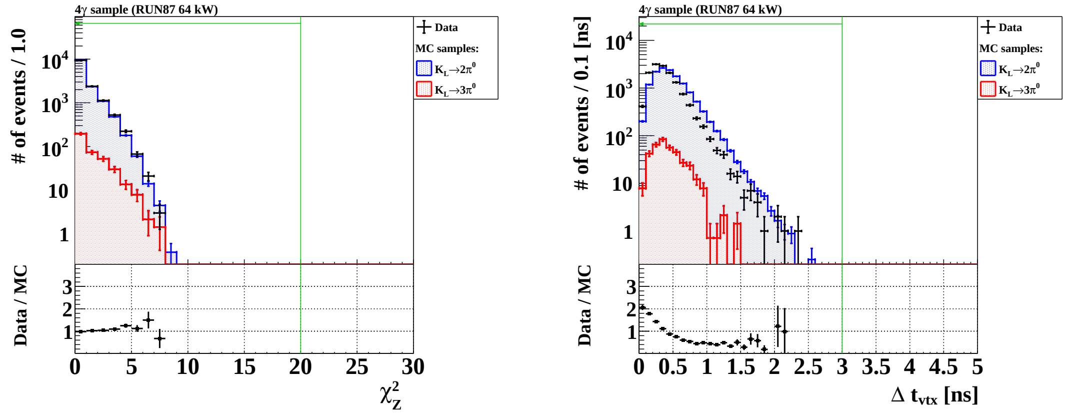

(e) χ^2_z (f) $\Delta T^{K_L}_{\mathrm{vtx}}$

Figure 6.1: Distributions of kinematic-cut variables used for the reconstructed $K_L \to \pi^0\pi^0$ sample. For each distribution, all the cuts except for the cut shown in each figure were imposed. The green line indicates the threshold for each cut.

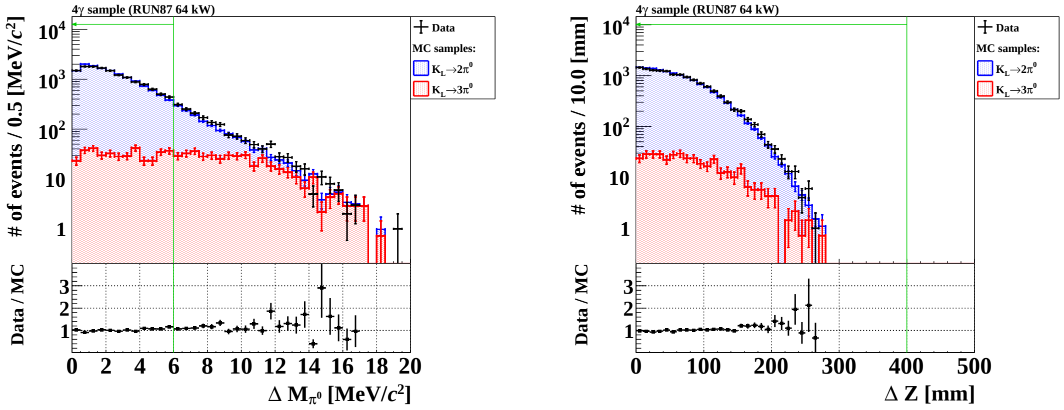

(a) Maximum $|\Delta M_{\pi^0}|$ (b) ΔZ_{vtx}

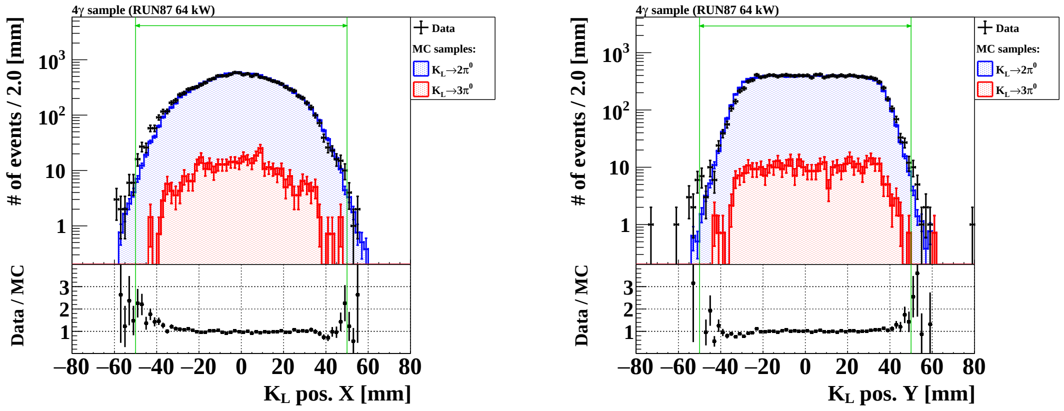

(c) K_L x-position at beam exit (d) K_L y-position at beam exit

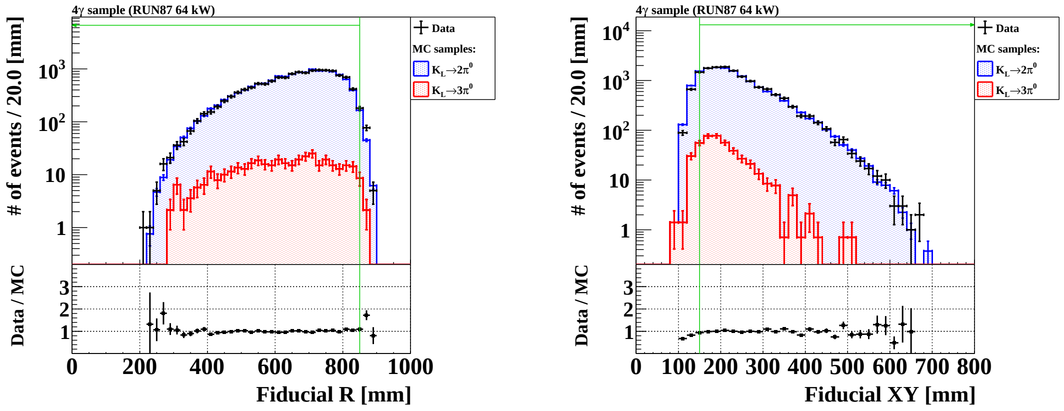

(e) Photon hit position (outer R) (f) Photon hit position (inner xy)

Figure 6.2: Distributions of kinematic-cut variables used for the reconstructed $K_L \to \pi^0\pi^0$ sample. For each distribution, all the cuts except for the cut shown in each figure were imposed. The green line indicates the threshold for each cut.

to incorrect combinations of $\pi^0 \to 2\gamma$. The edge at the lower K_L mass region is determined by the three times the π^0 mass for the $K_L \to 3\pi^0$ reconstruction.

Figure 6.4 shows distributions of kinematic-cut variables used for the reconstructed $K_L \to 2\gamma$ sample. The discrepancy in the distribution of $\Delta T^{K_L}_{\mathrm{vtx}}$ was observed in the $K_L \to 2\gamma$ sample as is the case with the $K_L \to \pi^0\pi^0$ and $K_L \to 3\pi^0$ samples. This did not have an effect on the *SES* estimation. Other distributions show good agreement.

6.2.1.3 Results of the K_L Yield Estimation

Table 6.3 summarizes the results of the K_L yield estimation with the $K_L \to \pi^0\pi^0$ sample. The K_L yield divided by the corresponding POT is referred to as the K_L flux ($F_{K_L} = N_{K_L}/\mathrm{POT}$), and is also shown in the table. The results of the normalization-mode analysis for the $K_L \to 3\pi^0$ and $K_L \to 2\gamma$ samples are summarized in Appendix C.

Table 6.3: Summary of the K_L yield estimation with the $K_L \to \pi^0\pi^0$ sample. $A_{K_L\to\pi^0\pi^0}$, μ, p_{norm}, $N^{\mathrm{obs}}_{K_L\to\pi^0\pi^0}$, N_{K_L}, and F_{K_L} represent the acceptance of $K_L \to \pi^0\pi^0$ decays, the purity of $K_L \to \pi^0\pi^0$ decays, the prescale factor in the normalization trigger, the number of events observed in the reconstructed $K_L \to \pi^0\pi^0$ sample, the K_L yield at the beam exit, and the K_L flux, respectively.

Period	$A_{K_L\to\pi^0\pi^0}$	μ	p_{norm}	$N^{\mathrm{obs}}_{K_L\to\pi^0\pi^0}$	N_{K_L}	F_{K_L} [/(2 × 10^{14} POT)][a]
Period-0	1.15×10^{-4}	0.97	30	2639	7.70×10^{11}	$(4.27\pm0.09)\times10^{7}$
Period-1	2.94×10^{-4}	0.97	2	2150	1.64×10^{10}	$(4.78\pm0.12)\times10^{7}$
Period-2	2.65×10^{-4}	0.97	3	1899	2.41×10^{10}	$(4.51\pm0.12)\times10^{7}$
Period-3	2.07×10^{-4}	0.97	5	1104	2.99×10^{10}	$(4.69\pm0.16)\times10^{7}$
Period-4	1.48×10^{-4}	0.98	10	920	7.10×10^{10}	$(4.63\pm0.16)\times10^{7}$
Period-5	1.29×10^{-4}	0.97	20	2565	4.48×10^{11}	$(4.27\pm0.09)\times10^{7}$
Period-6	1.31×10^{-4}	0.97	20	528	9.03×10^{10}	$(3.86\pm0.18)\times10^{7}$
Period-7	1.23×10^{-4}	0.95	30	137	3.66×10^{10}	$(4.21\pm0.37)\times10^{7}$
Period-8	1.20×10^{-4}	0.97	30	541	1.52×10^{11}	$(4.00\pm0.18)\times10^{7}$
Period-9	1.11×10^{-4}	0.97	30	2408	7.31×10^{11}	$(4.06\pm0.09)\times10^{7}$
Period-10	1.06×10^{-4}	0.97	30	13779	4.39×10^{12}	$(4.12\pm0.04)\times10^{7}$
Total				28670	6.76×10^{12}	$(4.14\pm0.03)\times10^{7}$

[a] 2 × 10^{14} is the design value of POT per spill.

Figure 6.5 shows the comparison of the K_L flux among the three normalization modes. The maximum flux deviation of 3.6% was observed between $K_L \to \pi^0\pi^0$ and $K_L \to 3\pi^0$. This inconsistency was considered as a systematic uncertainty on *SES*, as will be described in Section 6.2.4.

6.2.2 Signal Acceptance of $K_L \to \pi^0\nu\bar{\nu}$

The signal acceptance for $K_L \to \pi^0\nu\bar{\nu}$ was mainly estimated with the MC simulation. The signal acceptance was estimated as a fraction of the number of events that passed all the selection criteria to the total number of $K_L \to \pi^0\nu\bar{\nu}$ events generated by the MC simulation. As mentioned

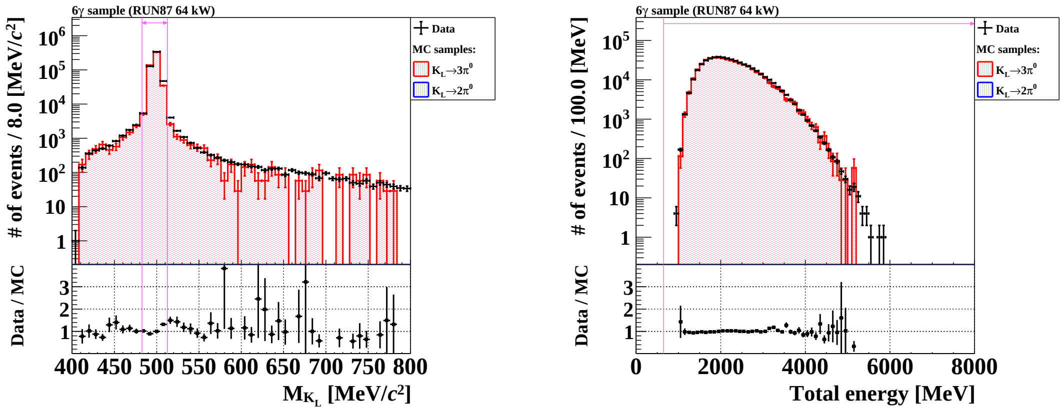

(a) Reconstructed K_L mass (b) Total energy

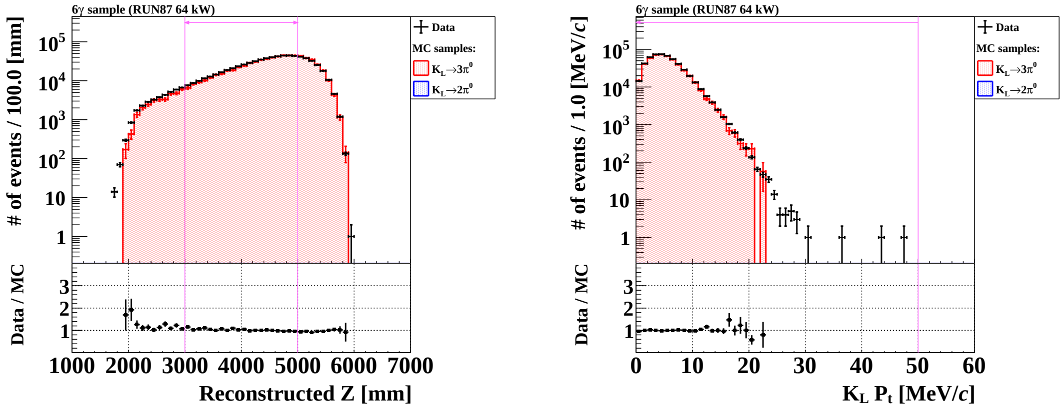

(c) Reconstructed Z_{vtx} (d) Reconstructed K_L P_t

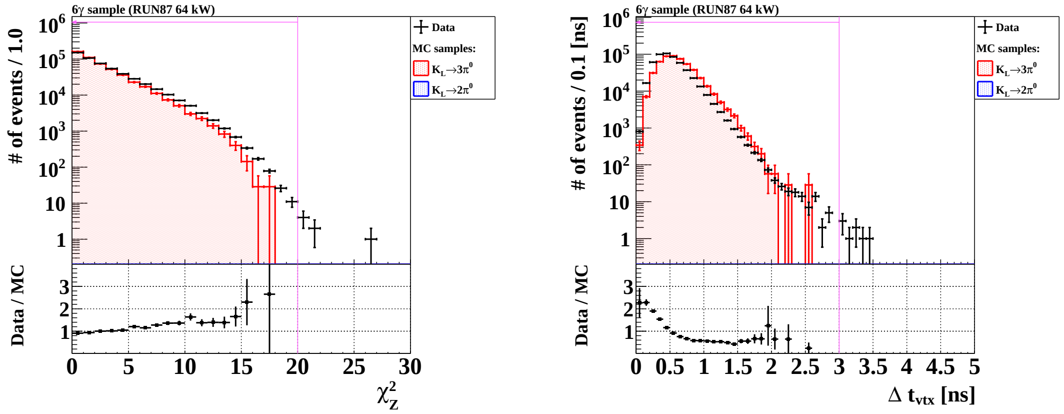

(e) χ^2_z (f) $\Delta T^{K_L}_{\text{vtx}}$

Figure 6.3: Distributions of kinematic-cut variables used for the reconstructed $K_L \to 3\pi^0$ sample. For each distribution, all the cuts except for the cut shown in each figure were imposed. The pink line indicates the threshold for each cut.

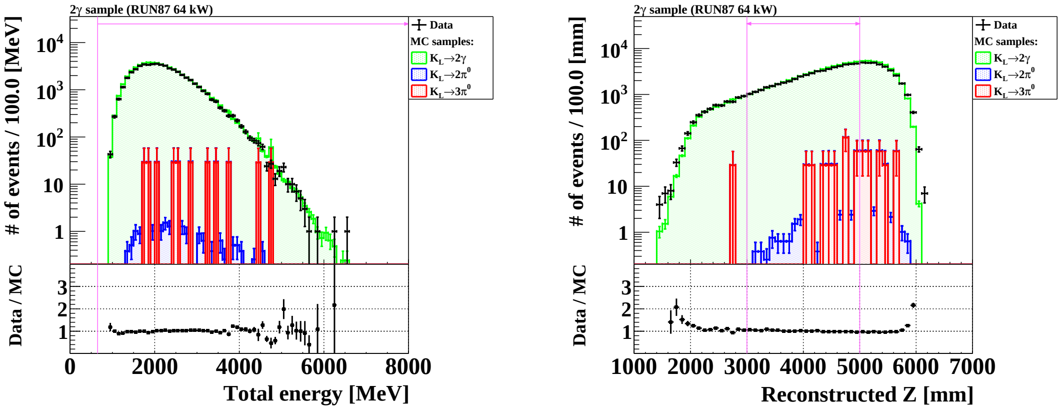

(a) Total energy

(b) Reconstructed Z_{vtx}

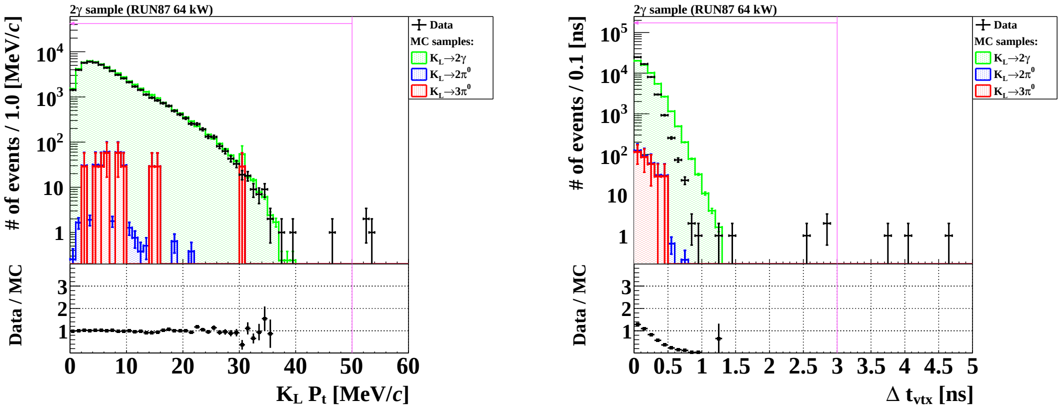

(c) Reconstructed K_L P_t

(d) $\Delta T_{\mathrm{vtx}}^{K_L}$

Figure 6.4: Distributions of kinematic-cut variables used for the reconstructed $K_L \rightarrow 2\gamma$ sample. For each distribution, all the cuts except for the cut shown in each figure were imposed. The pink line indicates the threshold for each cut.

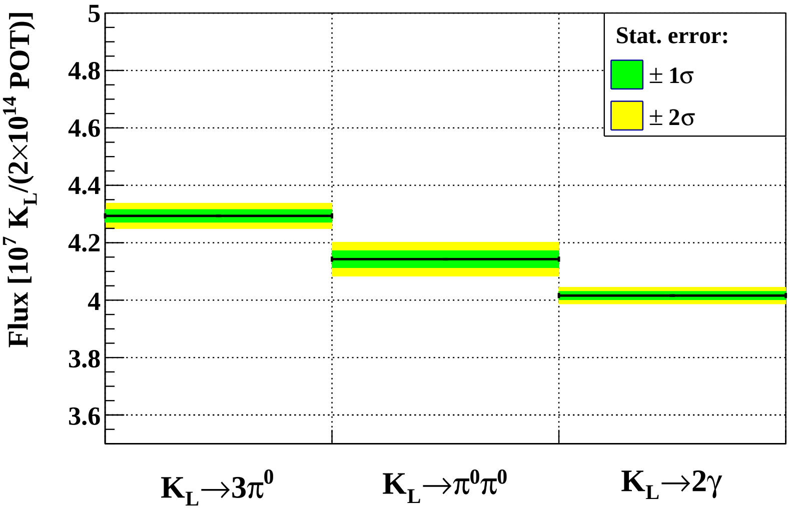

Figure 6.5: K_L flux estimated with three normalization modes using the data from the whole periods. The black lines represent the central value. The green and yellow bands represent 1σ and 2σ statistical errors, respectively.

in Chapter 5, the accidental activities in UCV were estimated in a data-driven evaluation. The acceptance of the cut with the both-end readout method for CSI was also estimated using data.

6.2.2.1 Selection Criteria for $K_L \to \pi^0 \nu \bar{\nu}$

The event selection for $K_L \to \pi^0 \nu \bar{\nu}$ consists of the several categories: trigger-related cuts, photon selection, kinematic cuts, veto cuts, shape-related cuts, ΔT_{CSI}. All the cuts are summarized in Table 6.5.

Trigger-Related Cuts

The $K_L \to \pi^0 \nu \bar{\nu}$ sample was collected by the physics trigger described in Section 3.2.1.1. To be insensitive to the online trigger effect, the following cuts were imposed.

- Total energy (E_{total})

  The total deposited energy in CSI was required to be larger than 650 MeV. As is the case with the normalization mode analysis described in Section 6.2.1.1, the effect of the CSIEt trigger was removed with this cut.

- Trigger timing

  The trigger timing cut was also imposed with the same criterion as the normalization mode analysis described in Section 6.2.1.1. The average cluster timing was required to be within ±15 ns around the nominal timing.

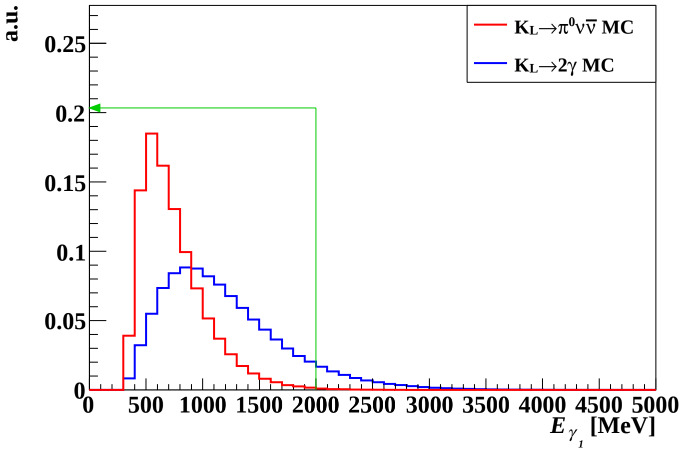

Figure 6.6: Distributions of the larger photon energy (E_{γ_1}) of the two photons for the $K_L \to \pi^0 \nu \bar{\nu}$ and $K_L \to 2\gamma$ MC events. The green arrow indicates the accepted region.

Photon Selection

The photon selection ensures the quality of photon clusters. The following cuts were imposed.

- Photon energy (E_γ)

  The photon energy was required to be larger than 100 MeV to ensure the photon reconstruction. The energy was also required to be smaller than 2000 MeV to avoid events with unusually energetic photons. The upper limit is also effective to reduce the $K_L \to 2\gamma$ decays in which the initial K_L energy is fully exploited by the final-state photons only, as shown in Figure 6.6.

- Photon position (x, y)

  The photon hit position on the CSI surface was required to be within the fiducial region to fully contain electromagnetic showers. The cut criteria, $\max(|x|, |y|) \geq 150$ mm and $\sqrt{x^2 + y^2} \leq 850$ mm, were imposed.

Kinematic Cuts

Kinematic cuts consist of the reconstructed π^0 information and various cut-variables dedicated to the background reduction.

- Signal region ($Z_{\rm vtx}$, P_t)

  We defined the signal region as $130 < P_t < 250$ MeV/c and $3200 < Z_{\rm vtx} < 5000$ mm, and required events to be in it. The cut definition was changed from the one used in the 2016–2018 analysis, and will be detailed in Section 6.2.2.2.

- Projection angle ($\theta_{\rm proj}$)

The angle between the two photons projected onto the plane perpendicular to the beam axis is called the projection angle. The projection angle was required to be smaller than 150°. This cut is effective to reduce the $K_L \to 2\gamma$ background, as shown in Figure 6.7.

- Cluster distance (d_{clus})

  The distance between the positions of the two clusters on the CSI surface is called the cluster distance. The cluster distance was required to be larger than 300 mm to ensure two clusters that were well-separated from each other.

- COE radius (R_{COE})

  The radius of the COE position on the CSI surface was required to be larger than 200 mm. Since the π^0 from $K_L \to \pi^0\nu\bar{\nu}$ decays into two photons with finite transverse momentum, the distance between the COE position and the center of CSI tends to be large.

- ΔT_{vtx}

  The vertex timing difference between two photon hits was required to be smaller than 1 ns. This cut ensured that the two photons originated from the same π^0 decay. This cut is effective to reduce the hadron-cluster background, in which the secondary neutron interaction in CSI is caused by the primary hit from the beam-halo neutron, as shown in Figure 6.8a.

- $E_\gamma \cdot \theta_\gamma$

  The product of the photon energy (E_γ) and the photon incident angle (θ_γ)[1] was required to be larger than 2500 MeV · deg. This cut reduces the $K_L \to \pi^0\pi^0$ background, particularly in the case where a π^0 is reconstructed from the two photons from different π^0's in $K_L \to \pi^0\pi^0$. This kind of mis-combination events are referred to as the odd-pairing events, and will be further explained in Section 6.3.1.

- Energy ratio ($E_{\gamma_2}/E_{\gamma_1}$)

  The ratio of the two photon energies, $E_{\gamma_2}/E_{\gamma_1}$ (where $E_{\gamma_1} > E_{\gamma_2}$), was required to be larger than 0.2. This cut is effective to reduce the hadron-cluster background, as shown in Figure 6.8b. This cut is also effective to reduce the $K_L \to \pi^0\pi^0$ background with the odd-pairing.

- π^0-kinematics cuts (P_t/P_z-Z_{vtx}, E_{π^0}-Z_{vtx})

  The $\pi^0 \to 2\gamma$ like events were selected based on the kinematic variables of the reconstructed π^0: z-vertex position (Z_{vtx}), transverse momentum (P_t), longitudinal momentum (P_z), and energy (E_{π^0}). The cut boundaries are defined on the planes of P_t/P_z-Z_{vtx} and E_{π^0}-Z_{vtx}.

- Beam-halo $K_L \to 2\gamma$ Fisher discriminant

  The beam-halo $K_L \to 2\gamma$ decay was one of the major background events in the 2016–2018 data analysis. In order to suppress this background, two different cuts were developed for this analysis[2]. One of the cuts is the multivariate classification using the Toolkit for MultiVariate data Analysis with ROOT (TMVA)[129]. The other cut is based on the likelihood ratio evaluating the consistency of the shower shape. The latter cut is described in the later part of this section.

---

[1] Polar angle of the photon direction with respect to the beam axis.

[2] These cuts were developed by Y. Noichi [128].

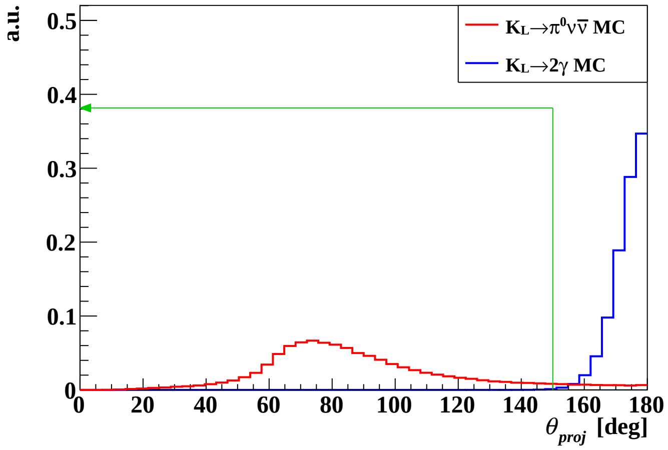

Figure 6.7: Distributions of the projection angle (θ_{proj}) for the $K_L \to \pi^0 \nu \bar{\nu}$ and $K_L \to 2\gamma$ MC events. The green arrow indicates the accepted region.

TMVA provides a machine-learning interface where one can perform training with dedicated samples to extract features of the signal and the background. In the $K_L \to \pi^0 \nu \bar{\nu}$ analysis, we used the classification algorithm called Fisher Discriminant (FD)[130][3]. For the inputs of the training, we used the following kinematic variables:

- Photon energy (both photons with the larger and smaller energy)
- Cluster distance
- Projection angle
- Total energy
- Reconstructed π^0 P_t
- Reconstructed π^0 Z_{vtx}
- COE radius (R_{COE})
- Incident polar angles of photons (both photons with the larger and smaller energy)

These variables implied differences in their distributions between the signal and the background, as shown in Figures 6.10 and 6.11.

After the training, the FD output based on the above variables was obtained. Events can be classified depending on the FD output value. In our case, signal-like events give the FD output value close to one. The FD output was also tested with a different sample (test sample) to check for overtraining. No significant discrepancy between the training and test samples was found. For the $K_L \to \pi^0 \nu \bar{\nu}$ selection, we required the FD output to be larger than -0.3. Detailed studies on the beam-halo $K_L \to 2\gamma$ FD cut are available in Ref. [128].

Since the performance of the FD cut mentioned above only relied on the MC simulation, the validation of the cut was further checked with data. We investigated the reproducibility of

---

[3] As described in Ref.[128], the FD classification resulted in the better separation between the $K_L \to \pi^0 \nu \bar{\nu}$ signal and the beam-halo $K_L \to 2\gamma$background than other methods, such as Boosted Decision Tree (BDT) and Gradient BDT.

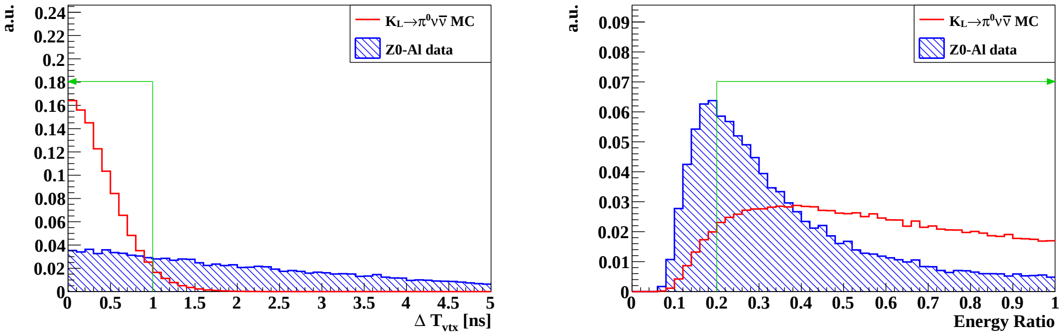

(a) ΔT_{vtx}

(b) Energy ratio

Figure 6.8: Distributions of ΔT_{vtx} and the energy ratio for the $K_L \to \pi^0 \nu \bar{\nu}$ MC simulation and the neutron sample collected in the Z0-Al run. The green arrow in each figure indicates the accepted region.

the FD output using the $K_L \to 3\pi^0$ and $K_L \to 2\gamma$ samples from the beam-core K_L due to the statistical limitation of the beam-halo $K_L \to 2\gamma$ sample. For the $K_L \to 3\pi^0$ sample, we selected one $\pi^0(\to 2\gamma)$ with the largest energy out of three π^0's in each event. Figure 6.12, shows the distributions of the FD output for the $K_L \to \pi^0 \nu \bar{\nu}$ and the beam-halo $K_L \to 2\gamma$ MC samples, and the validation samples.

- $K_L \to \pi^0 \pi^0$ neural network cut

  A new cut to reduce the $K_L \to \pi^0 \pi^0$ background events was introduced to this analysis[4]. The cut was developed using a neural network (NN) with inputs of kinematic variables, such as reconstructed π^0 P_t, Z_{vtx}, R_{COE}, photon energy (E_γ), photon energy ratio ($E_{\gamma_2}/E_{\gamma_1}$), etc. For the training of signal and background samples, the $K_L \to \pi^0 \nu \bar{\nu}$ signal MC sample and the $K_L \to \pi^0 \pi^0$ background MC sample under loose veto selection were used, respectively. By requiring the output of the NN to be greater than 0.3, we reduced the background while keeping the signal acceptance of 90%. In terms of the background reduction, details are described in Section 6.3.1.

Veto Cuts

We applied the veto cuts used in the normalization mode analysis described in Section 6.2.1.1. In addition, we imposed the veto cut with UCV for the $K_L \to \pi^0 \nu \bar{\nu}$ event selection to reduce the $K^\pm$ background events according to the criteria shown in Table 6.4. As described in Chapter 5, we did not use the simulation-based information for UCV. Instead, we evaluated the signal acceptance of the veto cut (veto acceptance) of UCV using data so that the realistic contribution can be reproduced. We used the $K_L \to 3\pi^0$ sample in which all the six photons hit CSI. The large branching ratio of $K_L \to 3\pi^0$ ($\simeq$ 20%) helped us collect the high-statistics data, and the requirement on the number of clusters in CSI eliminated background events for the six-cluster sample, as already seen in Section 6.2.1.

---

[4] This cut was developed by J. Redeker.

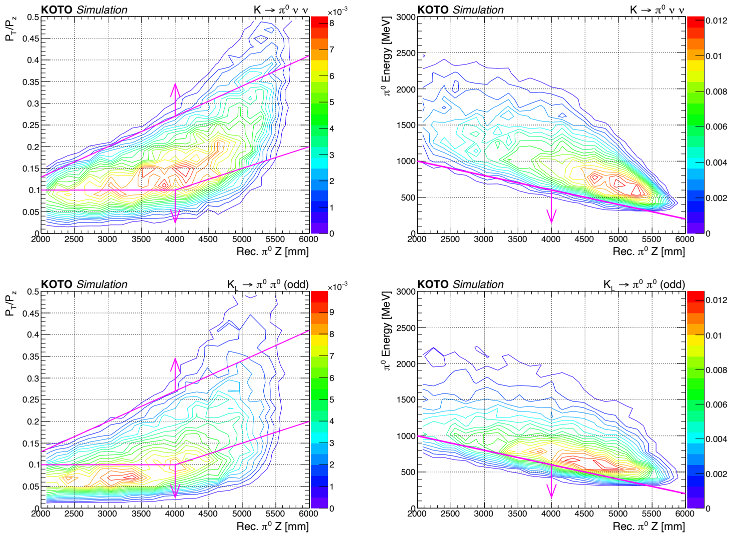

Figure 6.9: Distributions of P_t/P_z-$Z_{\rm vtx}$ (left) and E_{π^0}-$Z_{\rm vtx}$ (right). The top (bottom) row shows distributions of $K_L \to \pi^0\nu\bar{\nu}$ ($K_L \to \pi^0\pi^0$ odd-pairing) MC events The regions indicated by pink arrows were discarded. The area of each histogram is normalized to unity. The figure is quoted from Ref. [49].

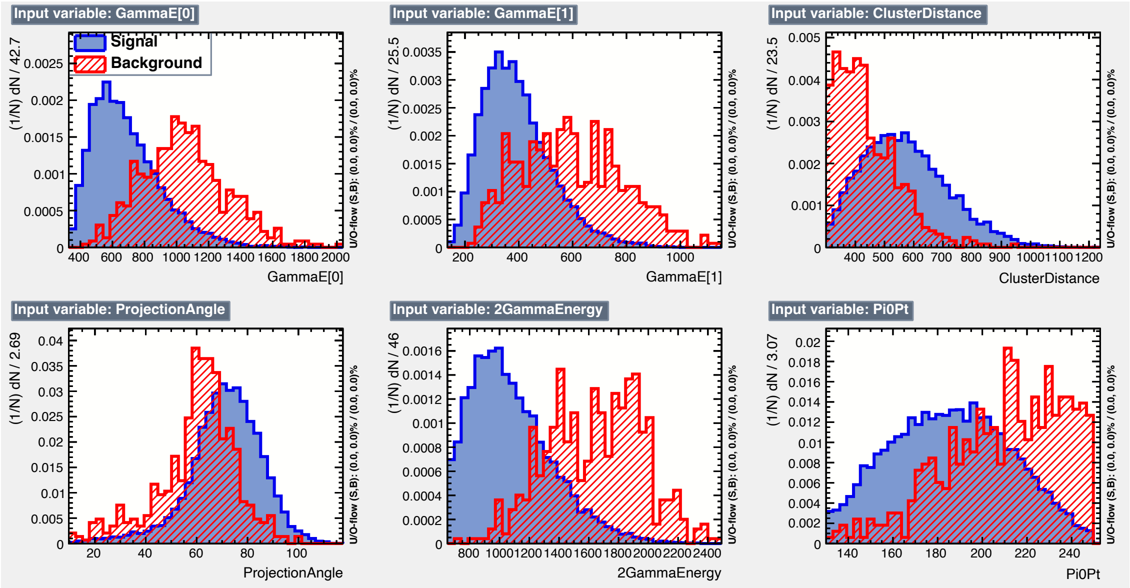

Figure 6.10: Distributions of kinematic variables for the input of the multivariate analysis. The blue and red distributions show the $K_L \to \pi^0\nu\bar{\nu}$ signal MC events and the beam-halo $K_L \to 2\gamma$ background MC events, respectively. In the top row, the smaller photon energy (left), larger photon energy (center), and cluster distance (right) are shown. In the bottom row, the projection angle (left), total energy (center), and π^0 P_t (right) are shown. The figure is quoted from Ref. [128].

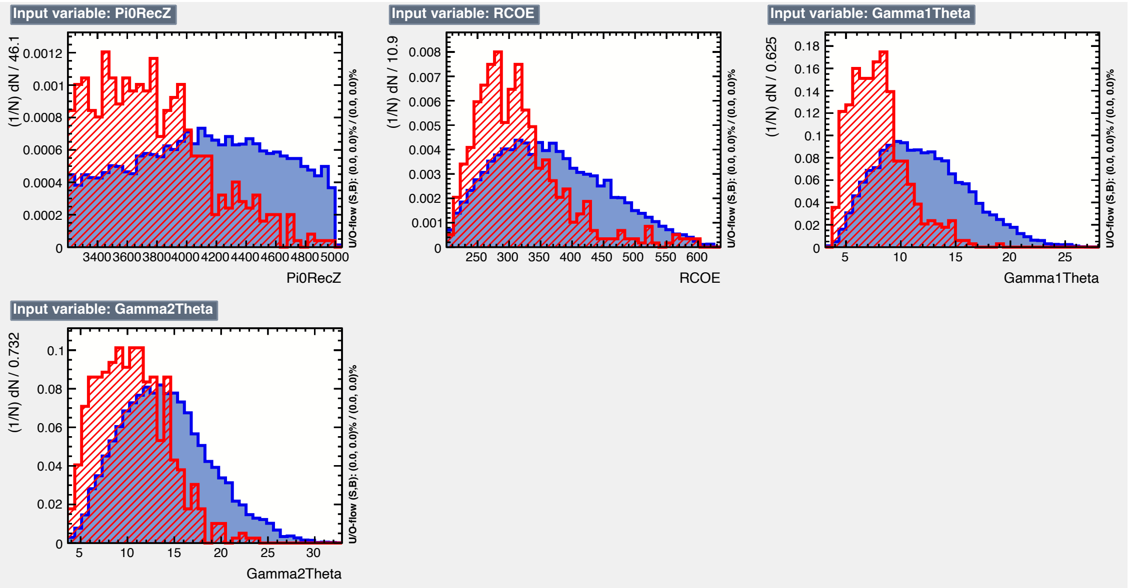

Figure 6.11: Distributions of kinematic variables for the input of the multivariate analysis. The blue and red distributions show the $K_L \to \pi^0 \nu \bar{\nu}$ signal MC events and the beam-halo $K_L \to 2\gamma$ background MC events, respectively. In the top row, π^0 Z_{vtx} (left), R_{COE} (center), incident polar angle of a photon with the larger energy (right) are shown. In the bottom row, the incident polar angle of a photon with the smaller energy is shown. The figure is quoted from Ref. [128].

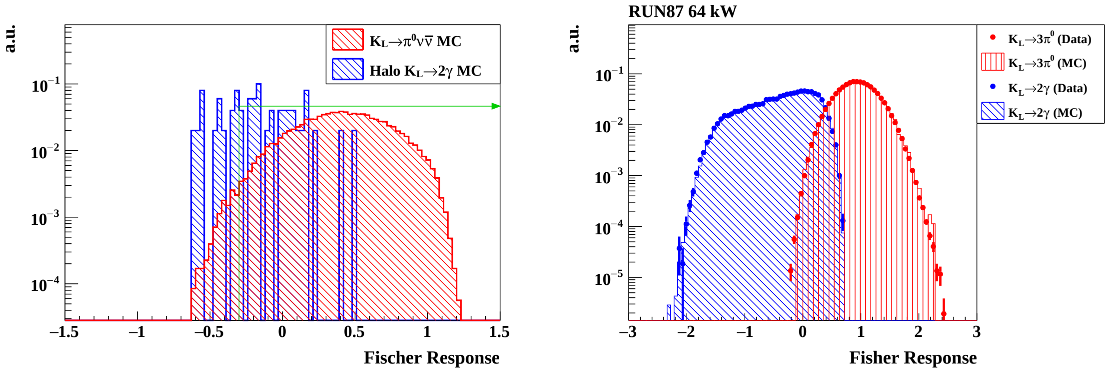

Figure 6.12: Distributions of the beam-halo $K_L \to 2\gamma$ FD output. The left figure shows the distributions of the $K_L \to \pi^0 \nu \bar{\nu}$ MC and the the beam-halo $K_L \to 2\gamma$ MC samples after applying all the cuts except for the signal region cut, $K_L \to \pi^0 \pi^0$ NN cut, and the beam-halo $K_L \to 2\gamma$ cuts including the FD cut. The green arrow indicates the accepted region for $K_L \to \pi^0 \nu \bar{\nu}$ events. The right figure shows the distributions of the validation samples: the $K_L \to 3\pi^0$ sample and the beam-core $K_L \to 2\gamma$ sample. In the validation samples, the distributions of the data are reproduced by the MC samples.

Table 6.4: Criteria of the veto cut with UCV. The threshold is equivalent to 0.4 times the most probable value in the energy deposition of $K^{\pm}$ events.

Subdetector for veto	Energy threshold	Width of veto window
UCV	$0.088 \times 0.4\,\mathrm{MeV}$	20 ns

Figure 6.13 shows the distribution of the energy deposition in UCV for six-cluster events collected by the minimum-bias trigger. Most of the events distribute in the low energy region. The fraction of events below the energy threshold corresponds to the veto acceptance for UCV. Since the accidental loss[5] depended on the beam power, the loss varied across different run periods. In addition, as the accumulation of POT went on, the radiation damage on MPPCs used for UCV increased. Thus, the increased amount of noise further contributed to the accidental loss, as shown in Figure 6.14. The MPPCs used for UCV were once replaced with new ones in the middle of the period-10 in order to keep the veto acceptance at the acceptable level for the rest of the run periods. Figure 6.15 shows the veto acceptance of UCV for each run period after considering the correlation with other veto detectors. The overall acceptance of $(96.17 \pm 0.25)\%$ was obtained by weighting the veto acceptance with the K_L yield in each period. The error originated from the statistics of the $K_L \to 3\pi^0$ sample used for the evaluation. Appendix D.3 gives further details on the accidental activities in UCV.

---

[5] The accidental loss is approximately equal to 1-(veto acceptance).

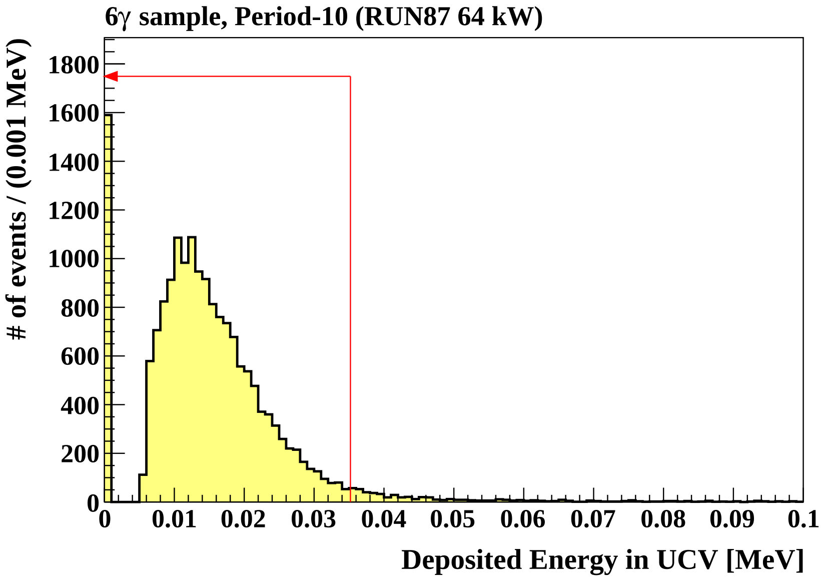

Figure 6.13: Distribution of the energy deposition in UCV for six-cluster events after imposing all the $K_L \to 3\pi^0$ selection. The red arrow indicates the accepted region for the $K_L \to \pi^0 \nu\bar{\nu}$ selection. Events below the threshold were accepted after imposing the veto on UCV. The maximum peak in each waveform of UCV was found for the peak height over a detection threshold. That made a sharp edge around 0.005 MeV. The selection of the maximum peak height made the peak structure in the distribution around 0.01 MeV. The events in the leftmost bin correspond to the case where no hits were detected within the veto window and the initialization value of zero was assigned.

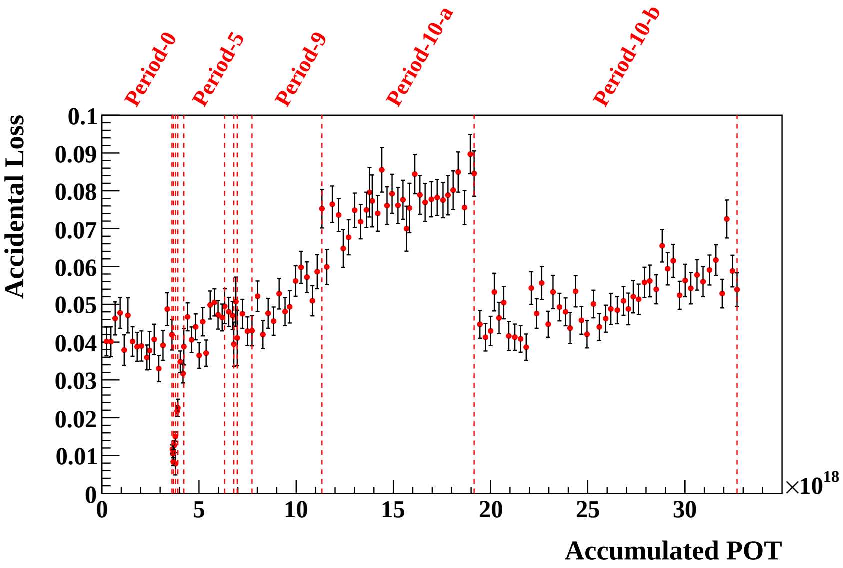

Figure 6.14: Transition of the accidental loss of UCV estimated with the 6-cluster sample. The red dashed lines indicate the different run periods. In this figure, the period-10 is subdivided into period-10-a and period10-b. The MPPCs for UCV were replaced between these two periods. The sudden drop of the loss around 4×10^{18} POT corresponds to the period where the accelerator was operated with the low beam power after the trouble with the electrostatic septum.

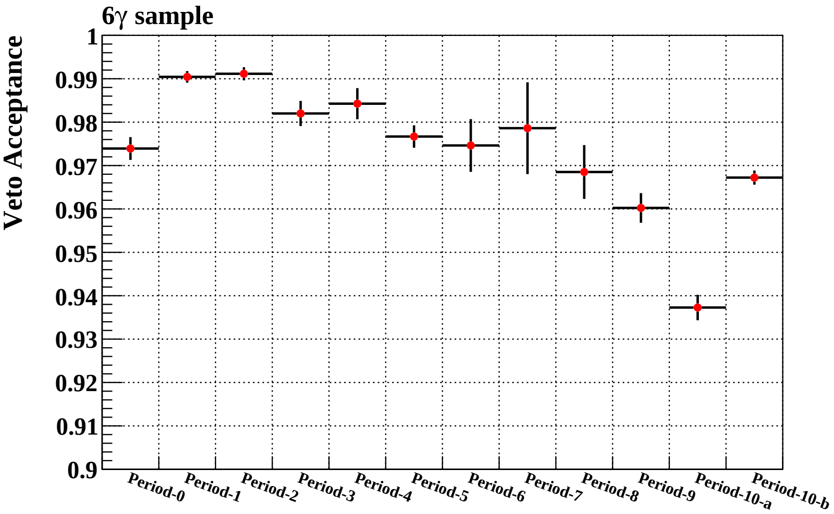

Figure 6.15: Veto acceptance of UCV for each period. As in the case of Figure 6.14, the period-10 is subdivided into period-10-a and period10-b.

Shape-Related Cuts

The shape information from waveforms and electromagnetic showers in CSI is the key to the identification of photon clusters from $K_L \to \pi^0 \nu \bar{\nu}$. The shape-related cuts described below played an important role to suppress the hadron-cluster background.

- Cluster size (n_{cryst})

  The cluster size, n_{cryst}, is defined as the number of crystals associated with each cluster. We required n_{cryst} to be larger than five. Photon clusters tend to have a larger cluster size than neutron clusters. Thus, this cut is effective to reduce the hadron-cluster background. Figure 6.16a shows the distribution of the cluster size for the $K_L \to \pi^0 \nu \bar{\nu}$ MC simulation and the neutron sample collected in the Z0-Al run.

- Cluster RMS (RMS_{clus})

  The cluster RMS is defined as

$$RMS_{\text{clus}} = \sqrt{\frac{\sum_i^{n_{\text{cryst}}} e_i r_i^2}{\sum_i^{n_{\text{cryst}}} e_i}}, \tag{6.11}$$

  where e_i and r_I are the deposited energy in i-th crystal and the distance of i-th crystal from the cluster position. The cluster RMS was required to be larger than 10 mm. Figure 6.16b shows the distribution of the cluster RMS for the $K_L \to \pi^0 \nu \bar{\nu}$ MC simulation and the neutron sample collected in the Z0-Al run.

- Cluster shape discrimination

  - CSD-had

    We used the Cluster Shape Discrimination (CSD) cut to suppress the hadron-cluster background. Historically, there were two different methods of CSD: the shape-χ^2 (χ^2_{shape}) cut and the CSD cut using a neural network (CSD$_{\text{NN}}$). These cuts were used in the 2015 data analysis [50]. In the 2016–2018 data analysis, a new CSD method based on a Convolutional Neural Network (CNN) was introduced[6]. This cut is referred to as CSD-had in this thesis. For the CNN inputs, the two-dimensional map of the cluster energy and timing on CSI, reconstructed incident angle, and χ^2_{shape} that is described below were used. Examples of the energy and timing distributions on CSI for photon and neutron clusters can be seen in Figure 6.17. The variable χ^2_{shape} was calculated to evaluate the consistency of shower shapes with a typical shape of photon clusters. The χ^2_{shape} was defined as

$$\chi^2_{\text{shape}} = \frac{1}{N} \sum_{i=1}^{N} \left(\frac{e_i/E_\gamma - \mu_i}{\sigma_i} \right), \tag{6.12}$$

    where the index i denotes the i-th crystal in the cluster, e_i is the deposited energy in each crystal, and E_γ is the photon energy. The parameters μ_i and σ_i are the mean value and standard deviation of e_i/E_γ, respectively. These were determined from the template made by MC simulations. The summation in Equation 6.12 was performed over N crystals with deposited energies, which were located in the region of 27 × 27 crystals

---

[6] This cut was developed by Y.-C. Tung.

centered around the one with the maximum energy deposition. Detailed studies on the χ^2_{shape} method are available in Ref. [81]. Using all these input variables, the CSD-had was trained with $K_L \to \pi^0 \nu \bar{\nu}$ MC sample for photon clusters and with Z0-Al data for neutron clusters. For the $K_L \to \pi^0 \nu \bar{\nu}$ selection, we required the CSD-had output to be larger than 0.99. Figure 6.16c shows the distribution of the CSD-had output for the $K_L \to \pi^0 \nu \bar{\nu}$ MC simulation and the neutron sample collected in the Z0-Al run. Details of the CSD-had cut are available in Ref. [131].

- CSD-η

  The CSD cut dedicated to the suppression of the CV-η background was named CSD-η[7]. This cut was introduced in 2016–2018 data analysis. As input information, the cluster energy and timing patterns in CSI, and the reconstructed incident angle were used. For the training of signal and background samples, the $K_L \to \pi^0 \nu \bar{\nu}$ signal MC sample and the CV-η background MC sample were used, respectively. For the $K_L \to \pi^0 \nu \bar{\nu}$ selection, we required the CSD-η output to be larger than 0.91. Figure 6.16d shows the distribution of the CSD-η output for the $K_L \to \pi^0 \nu \bar{\nu}$ MC simulation and the neutron sample collected in the Z0-Al run.

- χ^2_θ

  The χ^2_θ cut was introduced from the 2015 data analysis [83]. This cut evaluates the consistency of the incident polar angle of the photon. The incident photon angle was evaluated with the π^0 reconstruction method and the neural network (NN) regression method, separately. The NN regression methods uses the energy distribution, the radial position, and the azimuthal angle of the cluster for the input information.The agreement between the two methods was quantified as

$$\chi^2_\theta = \frac{(\theta_{\text{rec}} - \theta_{\text{NN}})^2}{\sigma^2_{\theta_{\text{NN}}}}, \tag{6.13}$$

  where θ_{rec} (θ_{NN}) is the angle obtained from the π^0 reconstruction method (NN regression method) and $\sigma^2_{\theta_{\text{NN}}}$ is the resolution of the θ_{NN} angle. Figure 6.16e shows the distribution of χ^2_θ output for the $K_L \to \pi^0 \nu \bar{\nu}$ MC simulation and the neutron sample collected in the Z0-Al run.

---

[7] This cut was developed by Q. S. Lin.

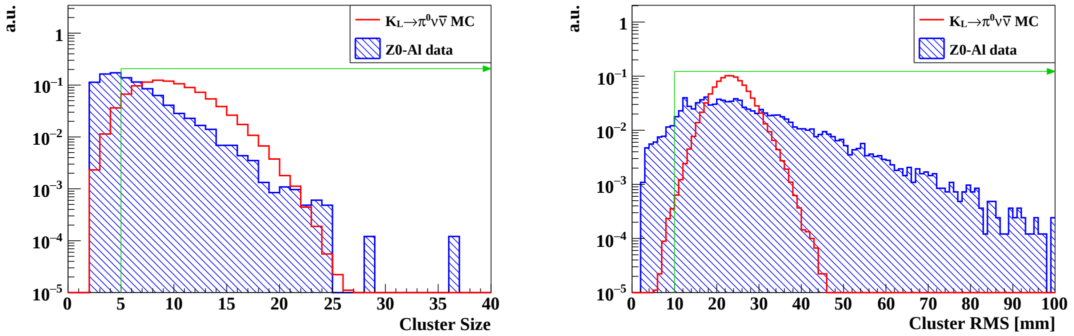

(a) Cluster size

(b) Cluster RMS

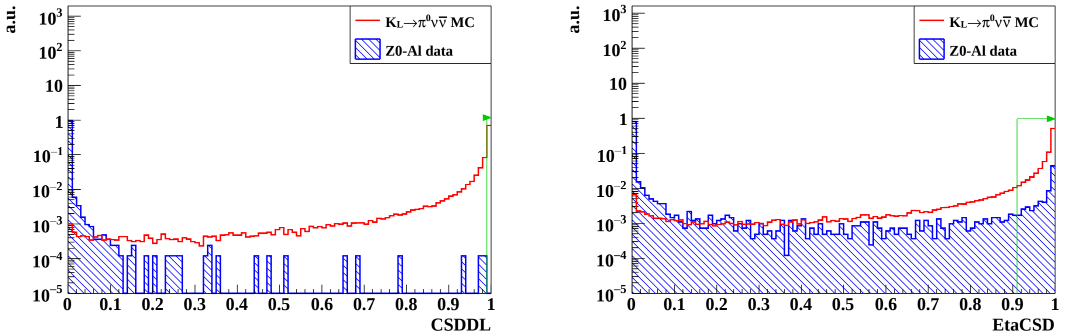

(c) CSD-had

(d) CSD-η

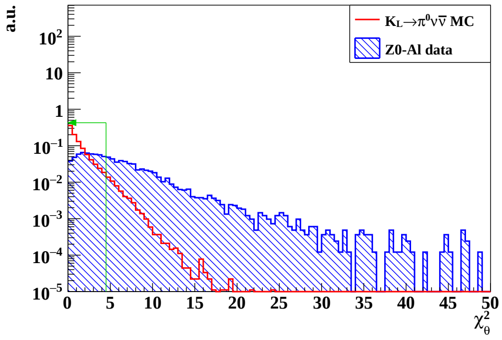

(e) χ^2_θ

Figure 6.16: Distributions of the cluster size, the cluster RMS, the CSD-had output, the CSD-η output, and χ^2_θ for the $K_L \to \pi^0 \nu \bar{\nu}$ MC simulation and the neutron sample collected in the Z0-Al run. The green arrow in each figure indicates the accepted region.

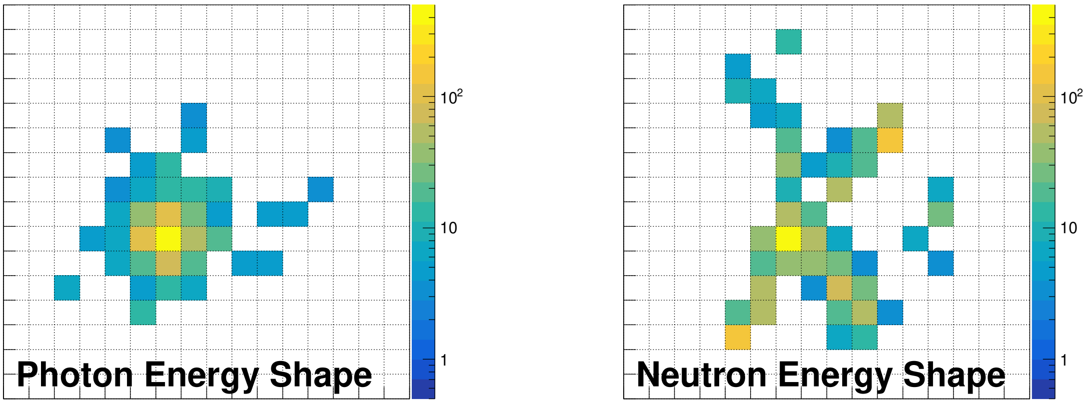

(a) Photon energy

(b) Neutron energy

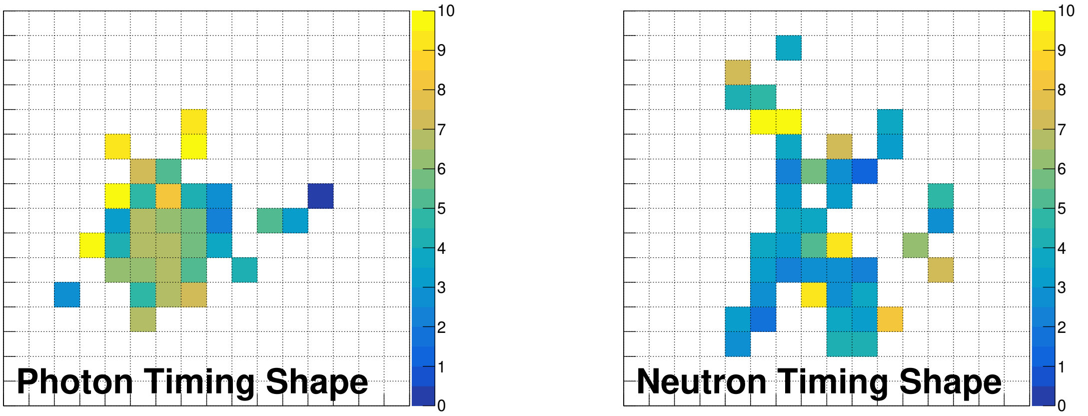

(c) Photon timing

(d) Neutron timing

Figure 6.17: Examples of the energy and timing shapes of a photon cluster from the MC simulation (left) and a neutron cluster from data (right). The color represents the deposited energy in MeV and the timing in ns. Typically, photon clusters are more circular and symmetric in shapes. The figure is quoted from Ref. [131].

- Beam-halo $K_L \to 2\gamma$ likelihood ratio

  The likelihood-ratio cut is another method introduced to the $K_L \to \pi^0 \nu \bar{\nu}$ analysis to suppress the beam-halo $K_L \to 2\gamma$ background [128]. The $K_L \to \pi^0 \nu \bar{\nu}$ signal decays are assumed to occur on the beam axis, while the beam-halo $K_L \to 2\gamma$ decays occur away from the beam axis. This should cause a difference in the shower shape though two clusters were made by photon hits in both cases. In order to judge which assumption is more likely to match with each event, we calculated the χ^2_{shape} value defined in Equation 6.12 with both assumptions for the event reconstruction.

  For the assumption of the beam-halo $K_L \to 2\gamma$ background, we took a similar approach to the case of the (beam-core) $K_L \to 2\gamma$ decay described in Section 4.2.3. We assumed the K_L mass for the invariant mass of the final-state two photons. We calculated the x-y position of the decay vertex using the COE position, $\boldsymbol{R}_{\mathrm{COE}}(= X_{\mathrm{COE}}, Y_{\mathrm{COE}})$, and the z-position of the reconstructed K_L vertex ($Z^{K_L}_{\mathrm{vtx}}$). We used the z-position of the 2nd collimator instead of the T1 target position because the beam-halo K_L's originated from the collimator region. The x-y position of the K_L decay vertex, $\boldsymbol{R}^{K_L}_{\mathrm{vtx}}$ $(= X^{K_L}_{\mathrm{vtx}}, Y^{K_L}_{\mathrm{vtx}})$, was thus approximately estimated as

  $$\boldsymbol{R}^{K_L}_{\mathrm{vtx}} = \frac{Z^{K_L}_{\mathrm{vtx}} - Z_{\mathrm{coll}}}{Z_{\mathrm{CSI}} - Z_{\mathrm{coll}}} \cdot \boldsymbol{R}_{\mathrm{COE}}, \tag{6.14}$$

  where Z_{coll} $(= -6000\,\mathrm{mm})$ is the z-position of the top part of the downstream end of the 2nd collimator.

  The likelihood was defined using the probability-density function of the χ^2_{shape} distribution as

  $$L_i = \frac{x_i^{k_i/2-1} e^{-x_i/2}}{2^{k_i/2}\Gamma\left(\frac{k_i}{2}\right)}, \tag{6.15}$$

  where x_i and k_i denote χ^2_{shape} and n_{cryst} for i-th cluster, respectively, The function $\Gamma(k_i/2)$ denotes the gamma function defined as

  $$\Gamma(z) = \int_0^\infty t^{z-1} e^{-t} dt, \quad \mathrm{Re}(z) > 0. \tag{6.16}$$

  The likelihood gives a value close to one if the assumption is realistic for the event. As studied in Ref.[128], there is no strong correlation of the likelihood between the two photon clusters. Therefore, the likelihood for the two-cluster events was defined as

  $$L = L_1 \times L_2, \tag{6.17}$$

  where L_1 (L_2) represents the likelihood of the cluster with the larger (smaller) energy.

  Finally, the likelihood ratio (LR) was defined as

  $$LR = \frac{L_{\mathrm{sig}}}{L_{\mathrm{sig}} + L_{\mathrm{bg}}}, \tag{6.18}$$

  where L_{sig} (L_{bg}) denotes the likelihood given by Equation 6.17 with the signal (background) assumption. The LR gives a value close to one (zero) if the event is likely to come from the signal (background). For the $K_L \to \pi^0 \nu \bar{\nu}$ selection, we required the LR

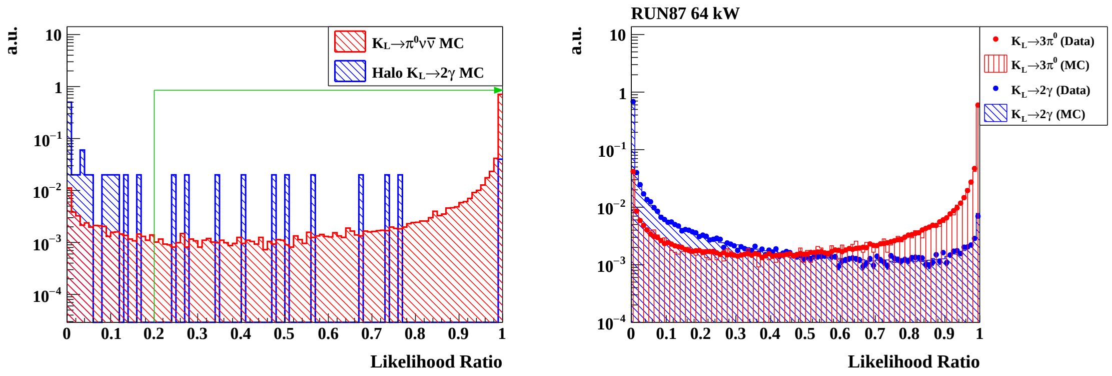

Figure 6.18: Distributions of the beam-halo $K_L \to 2\gamma$ LR. The left figure shows the distributions of the $K_L \to \pi^0 \nu \bar{\nu}$ MC and the beam-halo $K_L \to 2\gamma$ MC samples after applying all the cuts except for the signal region cut, $K_L \to \pi^0 \pi^0$ NN cut, and the beam-halo $K_L \to 2\gamma$ cuts including the LR cut. The green arrow indicates the accepted region for $K_L \to \pi^0 \nu \bar{\nu}$ events. The right figure shows the distributions of the validation samples: the $K_L \to 3\pi^0$ sample and the beam-core $K_L \to 2\gamma$ sample. In the validation samples, the distributions of the data are reproduced by the MC samples.

to be larger than 0.2. Detailed studies on the beam-halo $K_L \to 2\gamma$ LR cut are available in Ref. [128].

As is the case with the FD cut, the validation of the LR cut was checked with the data samples. Figure 6.18, shows the distributions of the LR for the $K_L \to \pi^0 \nu \bar{\nu}$ and the beam-halo $K_L \to 2\gamma$ MC samples, and the validation samples.

- Pulse shape discrimination

  We also discriminated between photon clusters and hadron clusters on the basis of the output pulse shape obtained in each CSI channel. The pulse shape difference appears in the tail region of waveforms, as shown in Figure 6.19. We can utilize this feature for further suppression of the hadron-cluster background. This Pulse Shape Discrimination (PSD) cut[8] was introduced in the 2016–2018 data analysis. The PSD is based on a fast Fourier transform (FFT) applied to each waveform.

  A discrete Fourier transform (DFT) was applied to $N_s (= 28)$ ADC samples around the peak of a pulse in each waveform[9]. The DFT was calculated as

$$X_k = \sum_{n=0}^{N_s-1} \mathcal{H}^n \exp\left(-\frac{i2\pi k}{N_s} n\right), \tag{6.19}$$

  where X_k is the complex number representing the amplitude and its phase at the frequency of $2\pi k / N_s$, $\mathcal{H}^n$ represents the height of the ADC value from the baseline at the n-th sample among the 28 samples. The amplitudes of X_k ($\mathcal{A}_k = |X_k|$) for the lowest five frequency components were used to make templates for both photon and neutron samples, as shown in Figure 6.19. To judge how likely a given cluster is to be a photon (γ) or neutron (n) cluster,

---

[8] This cut was developed by J. Li and Y.-C. Tung.

[9] The 28 samples were selected such that the 10-th sample out of them corresponded to the peak of the pulse.

we calculated the the likelihood for each cluster ($\mathcal{L}^{\gamma\,(n)}_{\mathrm{crystal}}$) defined as

$$\mathcal{L}^{\gamma\,(n)}_{\mathrm{crystal}} = \prod_{k=0}^{k<5} \frac{1}{\sqrt{2\pi}\sigma_k^{\gamma\,(n)}} \exp\left[-\frac{1}{2}\left(\frac{\mathcal{A}_k - \bar{\mathcal{A}}_k^{\gamma\,(n)}}{\sigma_k^{\gamma\,(n)}}\right)^2\right], \tag{6.20}$$

where $\bar{\mathcal{A}}_k^{\gamma\,(n)}$ and $\sigma_k^{\gamma\,(n)}$ are the template Fourier amplitude and its standard deviation for the photon or neutron cluster. The likelihood for each cluster was then given as

$$\mathcal{L}^{\gamma\,(n)}_{\mathrm{cluster}} = \prod_{j}^{N_c} \mathcal{L}^{\gamma\,(n)}_{\mathrm{crystal}\,(j)}, \tag{6.21}$$

where N_c is the number of crystals contained in the cluster. The likelihood ratio ($\mathcal{R}$) was defined as

$$\mathcal{R} = \frac{\mathcal{L}^{\gamma}_{\mathrm{cluster}}}{\mathcal{L}^{\gamma}_{\mathrm{cluster}} + \mathcal{L}^{n}_{\mathrm{cluster}}}, \tag{6.22}$$

where a cluster with the $\mathcal{R}$ value closer to one implies a more photon-like cluster. For the final cut variable (PSD-FFT), the smaller one of the $\mathcal{R}$ values from the two clusters was used. We required the PSD-FFT value to be larger than 0.1 for the $K_L \to \pi^0\nu\bar{\nu}$ selection. Figure 6.20a shows the PSD-FFT distribution in the photon sample from $K_L \to \pi^0\pi^0$ decays and the neutron sample from the Z0-Al run.

The signal acceptance of this cut was estimated using a photon sample from $K_L \to \pi^0\pi^0$ and $K_L \to 3\pi^0$ decays[10]. As described in the next paragraph, the signal acceptance of the cut using the both-end readout method for CSI was estimated together to take the correlation between the cuts into account.

Details of the PSD cut are available in Ref. [131].

CSI Both-End Readout Cut (ΔT_{CSI} Cut)

As described in Section 2.5.1, the both-end readout method for CSI was newly introduced to this analysis to further suppress the hadron-cluster background[11]. As already described in Section 2.5.1, the key to the photon-neutron separation is the depth information of hits in the crystal, which can be obtained from the timing difference between the upstream photo sensors (MPPC) and downstream photo sensors (PMT). The timing difference (ΔT_{CSI}) was defined as

$$\Delta T_{\mathrm{CSI}} = T_{\mathrm{MPPC}} - T_{\mathrm{PMT}}, \tag{6.23}$$

where T_{PMT} is the timing measured by PMTs, which is equivalent to the cluster timing defined in Equation 4.7, and T_{MPPC} is the timing measured by MPPCs. T_{MPPC} was defined as

$$T_{\mathrm{MPPC}} = \frac{\sum_i e_i t_i}{\sum_i e_i}, \tag{6.24}$$

where e_i and t_i denote the energy and timing measured by i-th MPPC channel included in a cluster, respectively. We calculated ΔT_{CSI} for both two clusters and selected the one giving the larger ΔT_{CSI} value as a cut variable. Detailed studies on the ΔT_{CSI} cut are available in Ref.[94].

---

[10] The data-driven evaluation was adopted because waveforms in CSI were poorly reproduced in the MC simulation.

[11] The development of this cut was based on the past studies on the upgrade of CSI and the performance evaluation [90, 91, 92, 93, 94].

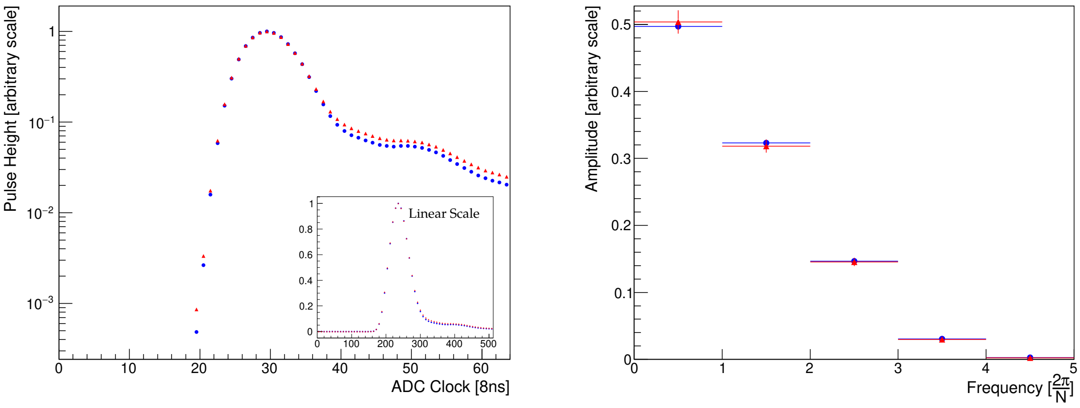

Figure 6.19: Algorithm of the PSD cut. The left figure shows the average waveform of photon samples (blue dots) and neutron samples (red triangles) for the CSI channel 1013. The photon samples and the neutron samples were obtained from the $K_L \to 3\pi^0$ events and the control sample collected in the Z0-Al run, respectively. The neutron-induced cluster shows the longer tail component. The right figure shows the lowest five frequency components of the templates of photon (blue dots) and neutron (red triangles) waveforms for the same CSI channel. The figures are quoted from Ref. [131].

We required the ΔT_{CSI} to be smaller than 32.2 ns for the $K_L \to \pi^0\nu\bar{\nu}$ selection. Figure 6.20b shows the ΔT_{CSI} distribution in the photon sample from $K_L \to \pi^0\pi^0$ decays and the neutron sample from the Z0-Al run. As shown in Figure 6.21, the both photon clusters distribute around the small ΔT_{CSI} region, and the primary (secondary) hadron cluster distributes around the small (large) ΔT_{CSI} region. Thus, the cut with the larger ΔT_{CSI} of the two clusters gives more effective separation.

The combined signal acceptance of the ΔT_{CSI} cut, the PSD cut, and the CSD-had cut was evaluated using the photon sample collected from $K_L \to \pi^0\pi^0$ and $K_L \to 3\pi^0$ decays[12]. This evaluation was performed by another collaborator[13]. A weight factor, $w(E,\ \theta)$, as a function of the photon energy (E) and the incident polar angle of the photon (θ) was obtained by calculating the survival probability of the each cluster. The photon energy and the photon incident angle distributions for the $K_L \to \pi^0\nu\bar{\nu}$, $K_L \to \pi^0\pi^0$, and $K_L \to 3\pi^0$ decays are different due to their kinematical features, as shown in Figure 6.22. The signal acceptance of each event was then given as a product of $w(E,\ \theta)$ for two clusters. We chose a set of thresholds for the PSD cut and the ΔT_{CSI} cut such that the combined signal acceptance was kept at 75%.

---

[12] As is the case with the PSD cut, the waveform simulation for the ΔT_{CSI} cut was not reliable enough, and thus the acceptance was evaluated with the data-driven analysis.

[13] This was evaluated by Y.-C. Tung.

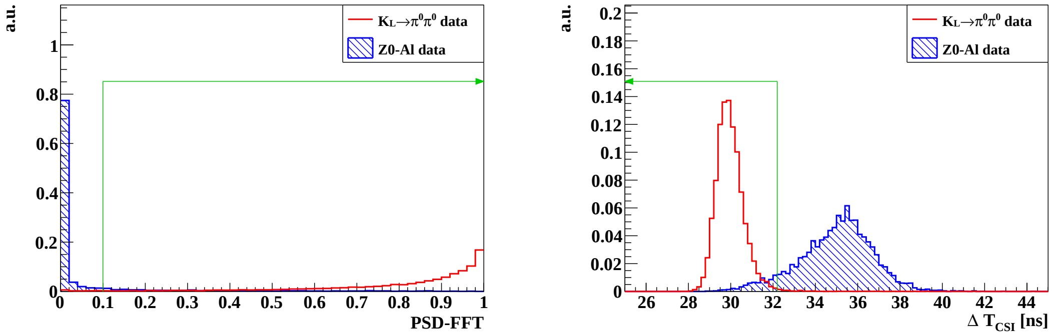

(a) PSD-FFT

(b) ΔT_{CSI}

Figure 6.20: Distributions of PSD-FFT and ΔT_{CSI} in the $\pi^0 \to 2\gamma$ events collected from the $K_L \to \pi^0\pi^0$ sample and the neutron events collected in the Z0-Al run. The green arrow in each figure indicates the accepted region.

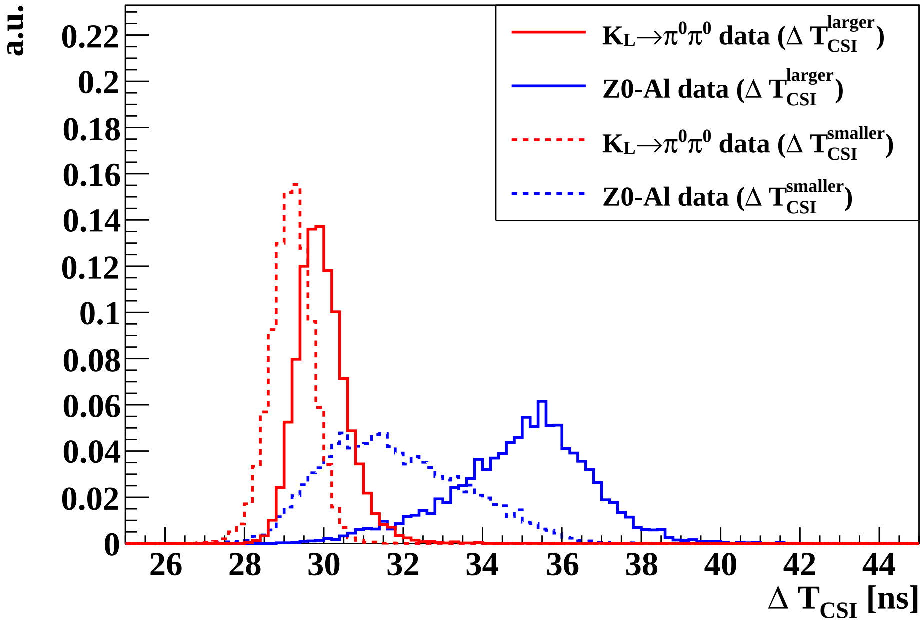

Figure 6.21: Distributions of ΔT_{CSI} in the $\pi^0 \to 2\gamma$ events collected from the $K_L \to \pi^0\pi^0$ sample and the neutron events collected in the Z0-Al run. The red solid (dashed) line shows the larger (smaller) ΔT_{CSI} distribution in the photon sample, and the blue solid (dashed) line shows the larger (smaller) ΔT_{CSI} distribution in the neutron sample. The neutron sample shows the significant difference between the larger and smaller ΔT_{CSI} distributions while the photon sample shows the relatively similar distribution.

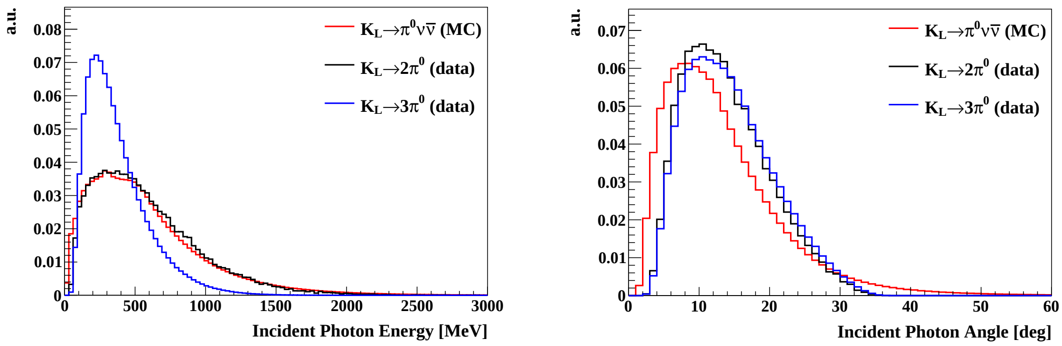

(a) Incident photon energy

(b) Incident photon angle

Figure 6.22: Distributions of the incident photon energy and angle in the $K_L \to \pi^0 \nu \bar{\nu}$ MC sample and the $K_L \to \pi^0 \pi^0$ and $K_L \to 3\pi^0$ samples.

6.2.2.2 Signal Region

Figure 6.23 shows the two-dimensional plane of P_t versus Z_{vtx} for the $K_L \to \pi^0 \nu \bar{\nu}$ MC events after imposing all the other selection criteria except for the signal region cut. To increase the signal acceptance, we extended the signal region from the one used in the 2016–2018 data analysis, as shown in Figure 6.24. In the 2016–2018 data analysis, the $K_L \to \pi^+ \pi^- \pi^0$ background was reduced by excluding the right bottom corner in the signal region defined as

$$P_t < \left(\frac{1}{35\,\text{mm}} (Z_{\text{vtx}} - 4000\,\text{mm}) + 130 \right) \text{MeV}/c \qquad (4000 < Z_{\text{vtx}} < 5000\,\text{mm}). \tag{6.25}$$

In the 2021 data analysis, we suppressed the $K_L \to \pi^+ \pi^- \pi^0$ background by DCV, and thus we included the right bottom corner of the signal region. This increased the signal acceptance by 1% compared to the case using the signal region used for the previous analysis.

6.2.2.3 Signal Acceptance Loss due to Trigger Effects

In addition to the cuts described in Section 6.2.2.1, we further considered the possible signal loss due to the online trigger effect. In the level-1 trigger, we required CSIEt to be larger than 550 MeV. Although the total energy in CSI was required to be larger than 650 MeV to eliminate the CSIEt effect in the MC simulation, still there was a chance that the trigger-induced loss existed. We evaluated this effect using data collected with a lower CSIEt threshold, and estimated the extra loss to be less than 0.3%. Details are described in Appendix E. In the case of the normalization mode analysis, this loss was assumed to be negligible because the total energy deposition by $K_L \to \pi^0 \pi^0$ decays is relatively higher than the CSIEt threshold, as shown in Figure 6.1b.

Although the number of clusters determined by the offline clustering algorithm described in Section 4.2.1 was required to be exactly two for both the data and $K_L \to \pi^0 \nu \bar{\nu}$ MC samples, the possible loss due to the cluster-finding algorithm in the level-2 trigger can exist. In the MC simulation, the online cluster-finding algorithm was also implemented to reflect this trigger bias. We thus required the number of online clusters ($n_{\text{clus}}^{\text{online}}$) predicted in the $K_L \to \pi^0 \nu \bar{\nu}$ MC simulation to be two. Figure 6.25 shows the distribution of $n_{\text{clus}}^{\text{online}}$ for the $K_L \to \pi^0 \nu \bar{\nu}$ MC events

Table 6.5: Summary of the event selection for $K_L \to \pi^0\nu\bar{\nu}$.

Category	Cut variable	Criteria
Trigger-related cuts	Total energy ($E_{\rm total}$)	$E_{\rm total} \geq 650\,\rm MeV$
	Trigger timing	$\leq \pm 15\,\rm ns$
Photon selection	Photon energy (E_γ)	$100 \leq E_\gamma \leq 2000\,\rm MeV$
	Photon position (x, y)	$\max(\lvert x\rvert, \lvert y\rvert) \geq 150\,\rm mm$ $\sqrt{x^2+y^2} \leq 850\,\rm mm$
Kinematic cuts	Signal region ($Z_{\rm vtx}$)	$3200 < Z_{\rm vtx} < 5000\,\rm mm$[b]
	Signal region (P_t)	$130 < P_t < 250\,{\rm MeV}/c$[b]
	Projection angle ($\theta_{\rm proj}$)	$\theta_{\rm proj} \leq 150\,\rm deg$
	Cluster distance ($d_{\rm clus}$)	$d_{\rm clus} \geq 300\,\rm mm$
	COE radius ($R_{\rm COE}$)	$R_{\rm COE} \geq 200\,\rm mm$
	$\Delta T_{\rm vtx}$	$\Delta T_{\rm vtx} \leq 1\,\rm ns$
	$E_\gamma \cdot \theta_\gamma$	$E_\gamma \cdot \theta_\gamma \geq 2500\,\rm MeV \cdot deg$
	Energy ratio ($E_{\gamma_2}/E_{\gamma_1}$)	$E_{\gamma_2}/E_{\gamma_1} \geq 0.2$
	P_t/P_z-$Z_{\rm vtx}$, E_{π^0}-$Z_{\rm vtx}$	see Figure 6.9
	Beam-halo $K_L \to 2\gamma$ FD	> -0.3[a]
	$K_L \to \pi^0\pi^0$ NN	> 0.3[a]
Veto cuts	Cut set in Table 6.1[c]	
	UCV (described in this section and Section 6.3.6.2)[a]	
Shape-related cuts	Cluster size ($n_{\rm cryst}$)	$n_{\rm cryst} \geq 5$
	Cluster RMS ($RMS_{\rm clus}$)	$RMS_{\rm clus} \geq 10$
	CSD-had	> 0.99[b]
	CSD-η	> 0.91
	χ^2_θ	$\chi^2_\theta < 4.5$
	PSD-FFT	> 0.1[b]
	Beam-halo $K_L \to 2\gamma$ LR	> 0.2[a]
CSI both-end readout cut	$\Delta T_{\rm CSI}$	$\Delta T_{\rm CSI} < 32.2\,\rm ns$[a]

[a] New cuts introduced in this analysis.

[b] Cuts used in the 2016–2018 analysis with different criteria.

[c] All the cut criteria are the same as the 2016–2018 analysis except for the vetoes on DCV and the NCC individual readout channels.

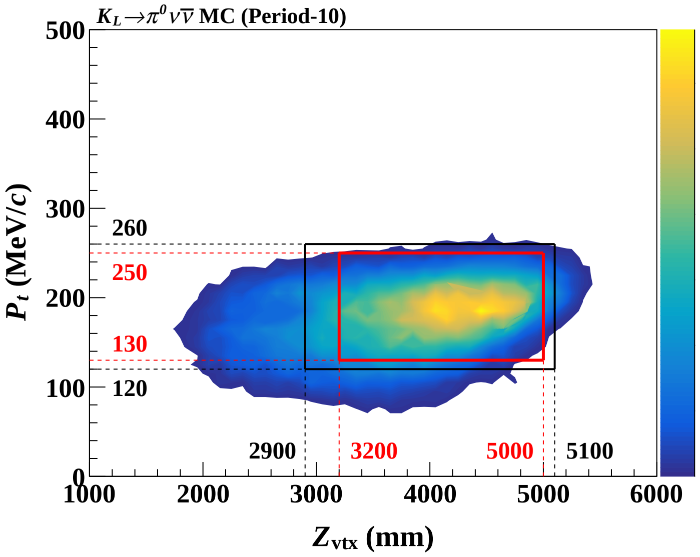

Figure 6.23: Contour plot for the reconstructed π^0 transverse momentum (P_t) versus π^0 decay vertex position ($Z_{\rm vtx}$) of $K_L \to \pi^0 \nu \bar{\nu}$ MC events after imposing all the other $K_L \to \pi^0 \nu \bar{\nu}$ selection criteria. The red (black) box shows the signal (blind) region.

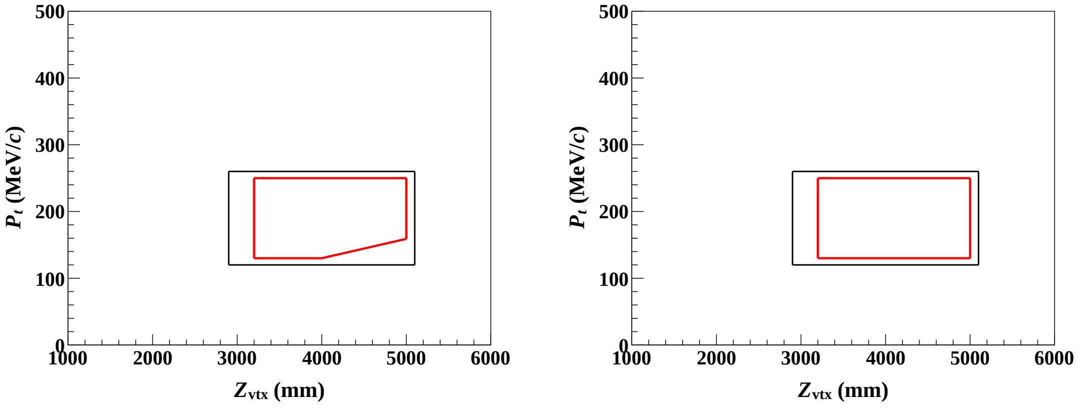

(a) Signal region for the 2016–2018 data analysis.

(b) Signal region for the 2021 data analysis.

Figure 6.24: Extension of the signal region on the plane of P_t versus $Z_{\rm vtx}$. The red (black) boundary shows the signal (blind) region.

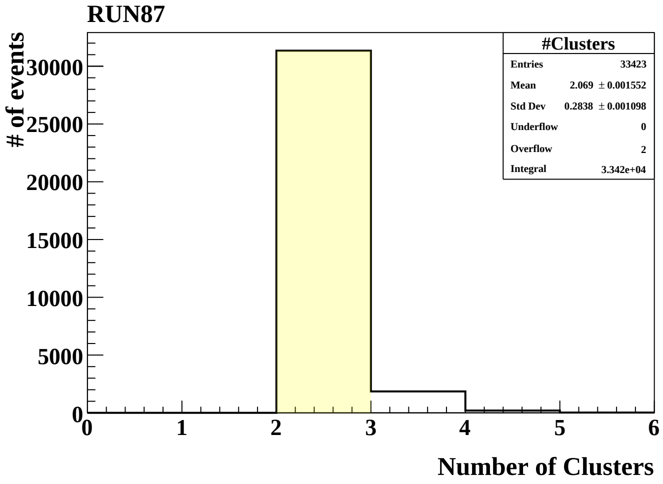

Figure 6.25: Distribution of $N_{\mathrm{clus}}^{\mathrm{online}}$ for the $K_L \to \pi^0\nu\bar{\nu}$ MC simulation. The yellow region was selected to estimate the signal acceptance.

after imposing all the selection criteria. As can be seen, there were small number of events with $n_{\mathrm{clus}}^{\mathrm{online}}$ not equal to two. The additional loss by the requirement for $n_{\mathrm{clus}}^{\mathrm{online}}$ to be two was estimated to be 6%. The cause of this loss was dominated by the incorrect cabling for the channels used for the online-clustering[14]. An effect on the systematic uncertainty on the sensitivity will be described in Section 6.2.4.2.

6.2.2.4 Results of the Signal Acceptance Estimation

After imposing all the selection criteria, the signal acceptance (A_{sig}) was estimated as

$$A_{\mathrm{sig}} = \frac{N^{\mathrm{rem}}_{K_L\to\pi^0\nu\bar{\nu}}}{N^{\mathrm{gen}}_{K_L\to\pi^0\nu\bar{\nu}}} \cdot \epsilon_{\mathrm{UCV}} \cdot \epsilon_{\mathrm{trig}}, \tag{6.26}$$

where N^{gen} is the number of generated $K_L \to \pi^0\nu\bar{\nu}$ MC events and N^{rem} is the number of $K_L \to \pi^0\nu\bar{\nu}$ MC events that remained after applying all the selection criteria for $K_L \to \pi^0\nu\bar{\nu}$. The signal acceptance includes the K_L decay probability of 3.34% for $3200 < Z_{\mathrm{vtx}} < 5000\,\mathrm{mm}$. The factors ϵ_{UCV} and ϵ_{trig} are the signal acceptance of the UCV veto cut estimated in Section 6.2.2.1 and the signal acceptance originating from the loss due to the online trigger requirements explained in Section 6.2.2.3.

Figure 6.26 shows the signal acceptance at each cut stage. The main difference among the periods arose from the veto cuts, which were affected by the beam power. The higher beam power gave the smaller acceptance because the accidental loss became larger. The acceptance of the veto cuts (A_{veto}) can be expressed as

$$A_{\mathrm{veto}} = (1 - L_{\mathrm{a}}) \cdot (1 - L_{\mathrm{b}}), \tag{6.27}$$

where L_{a} and L_{b} are the amount of the accidental loss and the backsplash loss, respectively. For instance, in the period-10, the acceptance loss by the veto cuts (i.e., $1 - A_{\mathrm{veto}}$) was 84%. The

---

[14] This was found later in the analysis stage. In the MC simulation, this incorrect channel mapping was reflected.

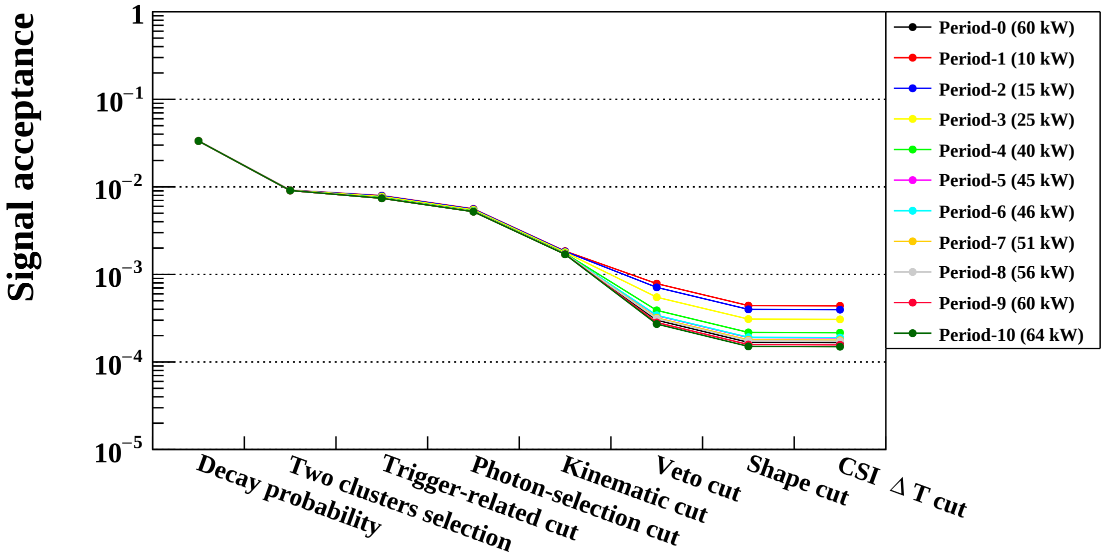

Figure 6.26: Acceptance change with the event selection. The difference in the signal acceptance among various periods was caused by the veto cuts whose acceptance was dependent on the beam power.

backsplash loss can also be estimated using the $K_L \to \pi^0 \nu \bar{\nu}$ signal MC sample without applying accidental overlay. Assuming there was no backsplash loss at UCV, the acceptance loss due to the veto cuts for the $K_L \to \pi^0 \nu \bar{\nu}$ signal MC sample without the accidental overlay should only originate from the backsplash loss. For the period-10, such loss was estimated to be $L_\mathrm{b} = 43\%$, and the accidental loss was then estimated using Equation 6.27 to be $L_\mathrm{a} = 72\%$. The values of the signal acceptance evaluated at each cut stage are available in Appendix F.

6.2.3 Single Event Sensitivity

With the K_L yield and the signal acceptance obtained from each data-taking period, the overall SES for the 2021 data was calculated as

$$\begin{aligned} SES &= \frac{1}{\sum_{i=0}^{10}(1/SES_i)} \\ &= \frac{1}{\sum_{i=0}^{10}(N^i_{K_L} \cdot A^i_{\mathrm{sig}})} \\ &= (9.31 \pm 0.06_{\mathrm{stat}}) \times 10^{-10}, \end{aligned} \tag{6.28}$$

where the index i for summation runs from period-0 to period-10, and SES_i, $N^i_{K_L}$, and A^i_{sig} represent the single event sensitivity, the K_L yield, and the signal acceptance obtained from each period. The uncertainty came from the statistics of the $K_L \to \pi^0 \pi^0$ sample in the normalization-mode analysis. The sensitivity was improved by a factor of 1.4 compared to the 2015 data analysis, but was worse than the 2016–2018 data analysis by a factor of 0.8.

Table 6.6: Summary of the estimation of the single event sensitivity. The table shows the beam power, the K_L yield at the beam exit (N_{K_L}), the signal acceptance for $K_L \to \pi^0\nu\bar{\nu}$ (A_{sig}), and the single event sensitivity (SES) for each run period. In the bottom row, N_{K_L} shows the total K_L yield, A_{sig} shows the signal acceptance weighted by N_{K_L} obtained from each period, and SES shows the single event sensitivity for the total run periods calculated by Equation 6.28.

Period	Beam power	N_{K_L}	A_{sig}	SES
Period-0	60 kW	7.70×10^{11}	1.66×10^{-4}	7.80×10^{-9}
Period-1	10 kW	1.64×10^{10}	4.37×10^{-4}	1.40×10^{-7}
Period-2	15 kW	2.41×10^{10}	3.96×10^{-4}	1.05×10^{-7}
Period-3	25 kW	2.99×10^{10}	3.07×10^{-4}	1.09×10^{-7}
Period-4	40 kW	7.10×10^{10}	2.16×10^{-4}	6.52×10^{-8}
Period-5	45 kW	4.48×10^{11}	1.88×10^{-4}	1.18×10^{-8}
Period-6	46 kW	9.03×10^{10}	1.90×10^{-4}	5.83×10^{-8}
Period-7	51 kW	3.66×10^{10}	1.77×10^{-4}	1.54×10^{-7}
Period-8	56 kW	1.52×10^{11}	1.73×10^{-4}	3.81×10^{-8}
Period-9	60 kW	7.31×10^{11}	1.57×10^{-4}	8.72×10^{-9}
Period-10	64 kW	4.39×10^{12}	1.49×10^{-4}	1.52×10^{-9}
Total		6.76×10^{12}	1.59×10^{-4}	9.31×10^{-10}

6.2.4 Systematic Uncertainty of Single Event Sensitivity

Next, we studied systematic uncertainties on the estimated SES. As already seen, SES was given as Equation 6.5, and the possible sources of uncertainties should lie in A_{sig}, $A_{K_L\to\pi^0\pi^0}$, $N_{K_L\to\pi^0\pi^0}$, and $\mathcal{B}(K_L \to \pi^0\pi^0)$. The uncertainty from $N_{K_L\to\pi^0\pi^0}$ was assigned as a statistical uncertainty, as mentioned in Section 6.2.3. The uncertainty of 0.69% on $\mathcal{B}(K_L \to \pi^0\pi^0)$ quoted from Ref. [1] was assigned as a systematic uncertainty on SES. Additionally, the discrepancy of 3.6% in the K_L flux among three normalization modes obtained in Section 6.2.1.3 was also assigned as a systematic uncertainty.

For A_{sig} and $A_{K_L\to\pi^0\pi^0}$, the systematic uncertainties were evaluated by investigating the reproducibility of each cut acceptance between the data and MC samples. The ratio between the two, $A_{K_L\to\pi^0\pi^0}/A_{\mathrm{sig}}$, enables cancellation of part of the uncertainties because some of the selection criteria for the $K_L \to \pi^0\nu\bar{\nu}$ and $K_L \to \pi^0\pi^0$ analyses are the same. The acceptances for $K_L \to \pi^0\nu\bar{\nu}$ can be factorized as

$$A_{\mathrm{sig}} = A^{\mathrm{sig}}_{\mathrm{geom}} \cdot A^{\mathrm{sig}}_{\mathrm{trig}} \cdot A^{\mathrm{sig}}_{\mathrm{photon}} \cdot A^{\mathrm{sig}}_{\mathrm{kine}} \cdot A^{\mathrm{sig}}_{\mathrm{veto}} \cdot A^{\mathrm{sig}}_{\mathrm{shape}} \cdot A^{\mathrm{sig}}_{\Delta T_{\mathrm{CSI}}}, \tag{6.29}$$

where $A^{\mathrm{sig}}_{\mathrm{geom}}$ is the geometrical acceptance of two photons in the final state hitting CSI, and $A^{\mathrm{sig}}_{\mathrm{trig}}$, $A^{\mathrm{sig}}_{\mathrm{photon}}$, $A^{\mathrm{sig}}_{\mathrm{kine}}$, $A^{\mathrm{sig}}_{\mathrm{veto}}$, $A^{\mathrm{sig}}_{\mathrm{shape}}$, and $A^{\mathrm{sig}}_{\Delta T_{\mathrm{CSI}}}$ are the acceptances of the trigger-related cuts, photon selection, kinematic cuts, veto cuts, shape-related cuts, and ΔT_{CSI} cut, respectively. Likewise, the acceptance of $K_L \to \pi^0\pi^0$ in the normalization-mode analysis can be factorized as

$$A_{K_L\to\pi^0\pi^0} = A^{K_L\to\pi^0\pi^0}_{\mathrm{geom}} \cdot A^{K_L\to\pi^0\pi^0}_{\mathrm{trig}} \cdot A^{K_L\to\pi^0\pi^0}_{\mathrm{photon}} \cdot A^{K_L\to\pi^0\pi^0}_{\mathrm{kine}} \cdot A^{K_L\to\pi^0\pi^0}_{\mathrm{veto}}, \tag{6.30}$$

where $A^{K_L\to\pi^0\pi^0}_{\mathrm{geom}}$ is the geometrical acceptance of four photons in the final state hitting CSI, and

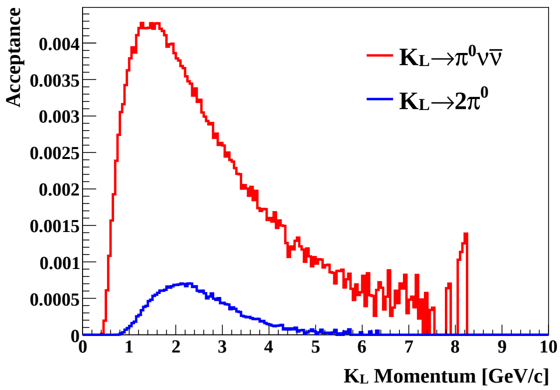

Figure 6.27: Geometrical acceptances of $K_L \to \pi^0\nu\bar{\nu}$ and $K_L \to \pi^0\pi^0$ as a function of the K_L momentum.

$A_{\mathrm{trig}}^{K_L\to\pi^0\pi^0}$, $A_{\mathrm{photon}}^{K_L\to\pi^0\pi^0}$, $A_{\mathrm{kine}}^{K_L\to\pi^0\pi^0}$, and $A_{\mathrm{veto}}^{K_L\to\pi^0\pi^0}$ are the acceptances of the trigger-related cuts, photon selection, kinematic cuts, veto cuts, respectively.

The uncertainty from each source is described from the following section.

6.2.4.1 Uncertainty from K_L Momentum

$K_L \to \pi^0\nu\bar{\nu}$ and $K_L \to \pi^0\pi^0$ decays generated photons in the final states, and we detected all of them at CSI to collect candidate events. We thus defined the geometrical acceptance as a fraction of K_L decays where all the final-state photons hit CSI to the total K_L decays occurring in the region of $3200 < z < 5000$ mm. Since the decay vertex and the photon momentum depend on the incident K_L momentum, the uncertainty on the geometrical acceptance should depend on how well Equation 5.1 models the K_L momentum with respect to the real data. Figure 6.27 shows the geometrical acceptances as a function of the K_L momentum.

We thus evaluated the uncertainty on the geometrical acceptance by varying parameters for the K_L momentum spectrum. The parameter vector $\boldsymbol{a}_0 = (\mu, \sigma_0, A, S)$ was obtained in the past measurement as already explained in Section 5.2.1. We varied the parameters around $\boldsymbol{a}_0$ with Gaussian considering the correlation between the parameters using the variance-covariance matrix defined in Ref.[68]. We calculated the acceptance ratio defined as

$$R_{\mathrm{geom}}(\boldsymbol{a}) = \frac{A_{\mathrm{geom}}^{K_L\to\pi^0\pi^0}(\boldsymbol{a})}{A_{\mathrm{geom}}^{\mathrm{sig}}(\boldsymbol{a})}, \tag{6.31}$$

where $\boldsymbol{a}$ is the vector with varied parameters. Figure 6.28 shows the distribution of the relative deviation of the acceptance ratio defined as

$$\frac{R_{\mathrm{geom}}(\boldsymbol{a}) - R_{\mathrm{geom}}(\boldsymbol{a}_0)}{R_{\mathrm{geom}}(\boldsymbol{a}_0)}. \tag{6.32}$$

We took the 68.27% range of the distribution as the systematic uncertainty induced from the K_L momentum spectrum, which resulted in the uncertainty of 0.98%.

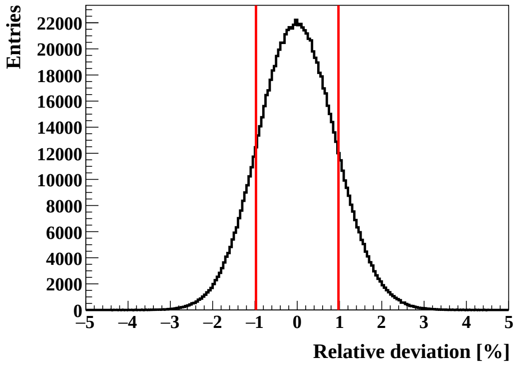

Figure 6.28: Relative deviation of the acceptance ratio obtained from 10^6 trials for $\boldsymbol{a}$. The region within the red lines represents the 68.27% region.

6.2.4.2 Uncertainty from Trigger-Related Cuts

The trigger system was designed to collect target samples with as higher efficiency as possible. Systematic uncertainties on SES was considered based on the acceptance loss induced from the trigger effect. We used the physics trigger and the normalization trigger to collect the $K_L \to \pi^0 \nu \bar{\nu}$ sample and the $K_L \to \pi^0 \pi^0$ sample, respectively. We considered the effect of the online cluster-finding algorithm in the level-2 trigger system. The requirement on the number of clusters in the level-2 trigger ($n_{\text{clus}}^{\text{online}}$) was included in the physics trigger but not in the normalization trigger. As described in Section 6.2.2.3, the acceptance loss due to trigger effect was estimated by the $K_L \to \pi^0 \nu \bar{\nu}$ MC simulation. To evaluate the systematic uncertainty, we used the $K_L \to 2\gamma$ sample collected by the normalization trigger as a control sample for the two-cluster events, and investigated the reproducibility of the MC simulation. We defined the efficiency of the cluster number requirement as

$$\epsilon_{n_{\text{clus}}^{\text{online}}} = \frac{N_{K_L \to 2\gamma}^{n_{\text{clus}}^{\text{online}}=2}}{N_{K_L \to 2\gamma}}, \tag{6.33}$$

where $N_{K_L \to 2\gamma}$ represents the number of $K_L \to 2\gamma$ events after imposing all the $K_L \to 2\gamma$ selection criteria, and $N_{K_L \to 2\gamma}^{n_{\text{clus}}^{\text{online}}=2}$ represents the number of $K_L \to 2\gamma$ events after further requiring $n_{\text{clus}}^{\text{online}}$ to be two. Note that the number, $n_{\text{clus}}^{\text{online}}$, was not required in the normalization trigger but recorded in each event for data. We evaluated the efficiency for both the data and MC samples, and considered the consistency between them. The discrepancy between the data and MC samples was given as

$$\Delta = \left| \frac{\epsilon_{n_{\text{clus}}^{\text{online}}}^{\text{MC}}}{\epsilon_{n_{\text{clus}}^{\text{online}}}^{\text{data}}} - 1 \right|, \tag{6.34}$$

where $\epsilon_{n_{\text{clus}}^{\text{online}}}^{\text{data}}$ and $\epsilon_{n_{\text{clus}}^{\text{online}}}^{\text{MC}}$ represent the efficiency for the data and MC samples, respectively. The systematic uncertainty was estimated to be 1.9% by weighting Δ obtained from each period with the K_L yield.

6.2.4.3 Uncertainty from Photon Selection

The uncertainty from the photon selection was evaluated using $\pi^0 \to 2\gamma$ events as a control sample extracted from the $K_L \to \pi^0\pi^0$ sample where the photon selection cuts were excluded. The acceptance of each cut was defined as

$$A_i = \frac{N_{\pi^0 \to 2\gamma}}{N^i_{\pi^0 \to 2\gamma}}, \tag{6.35}$$

where $N_{\pi^0 \to 2\gamma}$ and $N^i_{\pi^0 \to 2\gamma}$ represent the number of π^0 events after imposing all the cuts to be evaluated and the number of π^0 events after imposing all the cuts except for an i-th cut, respectively. The discrepancy between the data and MC samples for the i-th cut was given as

$$\Delta_i = \left| \frac{A_i^{\mathrm{MC}}}{A_i^{\mathrm{data}}} - 1 \right|, \tag{6.36}$$

where A_i^{data} and A_i^{MC} represent the acceptance of the i-th cut for the data and MC samples, respectively. The total discrepancy was obtained by summing the discrepancies for all the photon selection cuts in quadrature. The systematic uncertainty was estimated to be 0.81% by weighting the discrepancy obtained from each period with the K_L yield.

Figure 6.29 shows the acceptance of each cut.

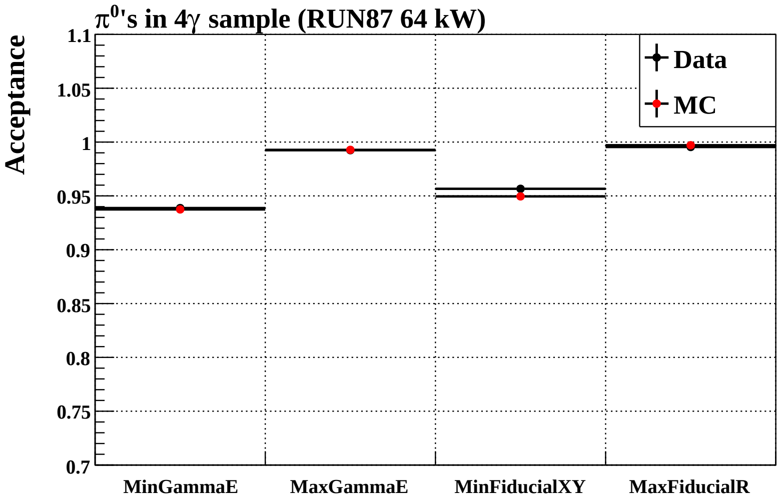

Figure 6.29: Acceptances of the photon selection cuts for $K_L \to \pi^0\nu\bar{\nu}$ in the π^0 events.

6.2.4.4 Uncertainty from Kinematic Cuts for $K_L \to \pi^0\nu\bar{\nu}$

The kinematic cuts used for $K_L \to \pi^0\nu\bar{\nu}$ and $K_L \to \pi^0\pi^0$ were different. Thus these were evaluated separately in this section and the next section. The uncertainty from the kinematic cuts for $K_L \to \pi^0\nu\bar{\nu}$ was evaluated using $\pi^0 \to 2\gamma$ events as a control sample extracted from the $K_L \to \pi^0\pi^0$ sample. Each π^0 was reconstructed again from the two photons based on the procedure[15] described in Section 4.2.2. We evaluated the acceptance and discrepancy of an i-th cut, and the total discrepancy, following the same procedure described in Section 6.2.4.3. The systematic uncertainty was estimated to be 3.5% by weighting the discrepancy obtained from each period with the K_L yield. Figure 6.30 shows the acceptance of each cut.

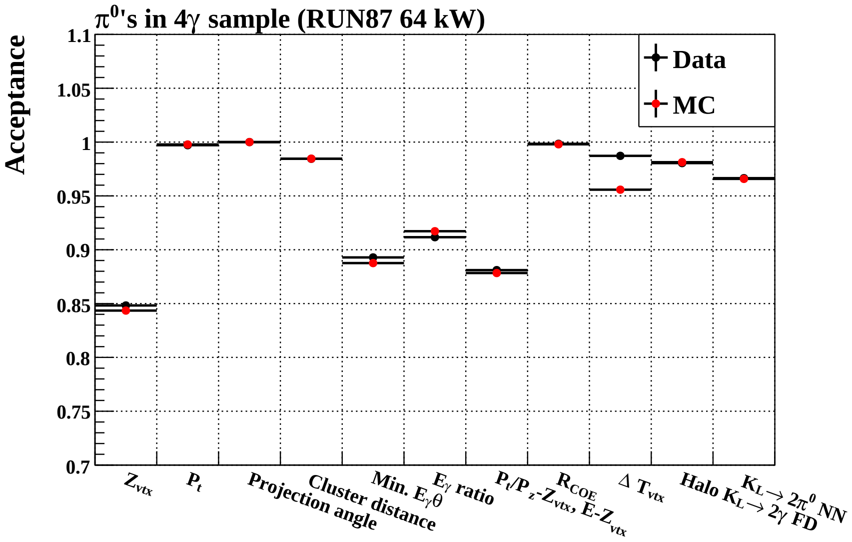

Figure 6.30: Acceptances of the kinematic cuts for $K_L \to \pi^0\nu\bar{\nu}$ in the π^0 events.

6.2.4.5 Uncertainty from Kinematic Cuts for $K_L \to \pi^0\pi^0$

The uncertainty from the kinematic cuts for $K_L \to \pi^0\pi^0$ was evaluated using the $K_L \to \pi^0\pi^0$ sample. We evaluated the acceptance and discrepancy of an i-th cut, and the total discrepancy, following the same procedure described in Section 6.2.4.3. The systematic uncertainty was estimated to be 4.6% by weighting the discrepancy obtained from each period with the K_L yield. Figure 6.31 shows the acceptance of each cut.

6.2.4.6 Uncertainty from Veto Cuts

The veto cuts used for the $K_L \to \pi^0\nu\bar{\nu}$ and $K_L \to \pi^0\pi^0$ are the same except for the additional veto on UCV for the $K_L \to \pi^0\nu\bar{\nu}$ selection. Thus, error cancellations between the two modes are expected by evaluating the uncertainty on the acceptance ratio, $A_{\text{veto}}^{K_L\to\pi^0\pi^0}/A_{\text{veto}}^{\text{sig}}$. Since all the final-state photons were required to hit CSI for the both decays, reproducibility of accidental activities were considered for the systematic uncertainty. First, we investigated the veto cuts other than UCV.

We used the $K_L \to 2\gamma$ sample[16] and the $K_L \to \pi^0\pi^0$ sample as control samples to evaluate the uncertainty. For the evaluation of the systematic uncertainty of $K_L \to \pi^0\nu\bar{\nu}$, we calculated the

---

[15] The vertex position was assumed to be on the beam axis.

[16] We used the $K_L \to 2\gamma$ sample as a control sample for $K_L \to \pi^0\nu\bar{\nu}$ because there was no data sample for $K_L \to \pi^0\nu\bar{\nu}$. Instead, the $K_L \to 2\gamma$ decay provided the events with only two clusters in CSI, just like the signal case.

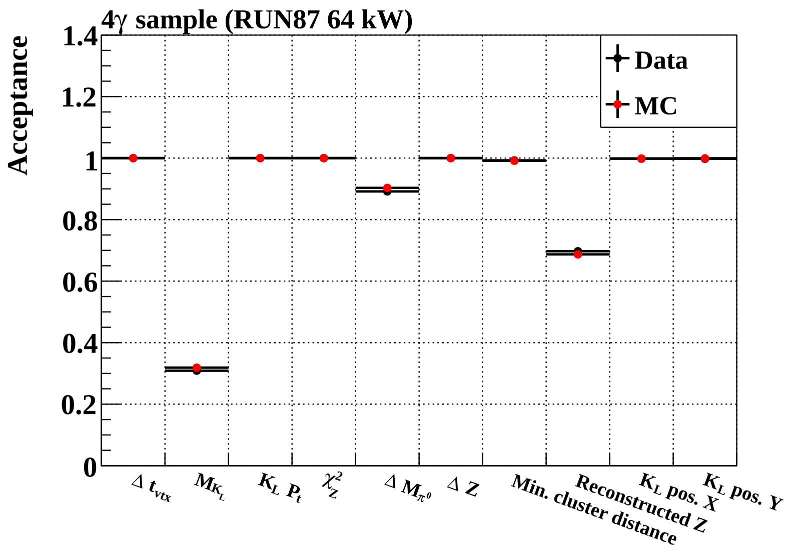

Figure 6.31: Acceptances of the kinematic cuts for $K_L \to \pi^0\pi^0$ in the π^0 events.

acceptance of an i-th veto cut for the data and MC samples with $K_L \to 2\gamma$ events defined as

$$A^i_{K_L\to 2\gamma \text{ data(MC)}} = \frac{N_{K_L\to 2\gamma \text{ data(MC)}}}{N^i_{K_L\to 2\gamma \text{ data(MC)}}}, \tag{6.37}$$

where $N_{K_L\to 2\gamma \text{ data(MC)}}$ and $N^i_{K_L\to 2\gamma \text{ data(MC)}}$ represent the number of $K_L \to 2\gamma$ events after imposing all the veto cuts to be evaluated and the number of $K_L \to 2\gamma$ events after imposing all the cuts except for the i-th veto cut, respectively. In the same way, we calculated the acceptance of an i-th veto cut for the data and MC samples for $K_L \to \pi^0\pi^0$ defined as

$$A^i_{K_L\to \pi^0\pi^0 \text{ data(MC)}} = \frac{N_{K_L\to \pi^0\pi^0 \text{ data(MC)}}}{N^i_{K_L\to \pi^0\pi^0 \text{ data(MC)}}}, \tag{6.38}$$

where the definitions of the numerator and the denominator are the same as Equation 6.37 with the decay mode replaced. We then calculated a double ratio for the i-th veto cut defined as

$$DR_i = \frac{A^i_{K_L\to\pi^0\pi^0 \text{ MC}}/A^i_{K_L\to\pi^0\pi^0 \text{ data}}}{A^i_{K_L\to 2\gamma \text{ MC}}/A^i_{K_L\to 2\gamma \text{ data}}}. \tag{6.39}$$

The discrepancy for the i-th veto cut between the data and MC samples as well as between $K_L \to 2\gamma$ and $K_L \to \pi^0\pi^0$ were evaluated as

$$\Delta_i = |DR_i - 1|. \tag{6.40}$$

Figure 6.32 shows the acceptance and the double ratio for each veto cut.

For the veto cut with UCV, we took the statistical error of the signal acceptance estimated with the $K_L \to 3\pi^0$ sample in Section 6.2.2.1 for the systematic uncertainty. The total uncertainty was obtained by summing the uncertainties for all the veto cuts in quadrature. The systematic uncertainty was estimated to be 3.3% by weighting the uncertainty obtained from each period with the K_L yield.

6.2.4.7 Uncertainty from Shape-Related Cuts

The uncertainty from the shape-related cuts for $K_L \to \pi^0 \nu \bar{\nu}$ was evaluated using the same sample used in Section 6.2.4.4. We evaluated the acceptance and discrepancy of an i-th cut, and the total discrepancy, following the same procedure described in Section 6.2.4.3. The systematic uncertainty was estimated to be 4.1% by weighting the discrepancy obtained from each period with the K_L yield. Figure 6.33 shows the acceptance of each cut. The main discrepancy came from the cluster shape discrimination cut.

6.2.4.8 Uncertainty from ΔT_{CSI} Cut

The uncertainty from the ΔT_{CSI} cut was evaluated using the same sample used in Section 6.2.4.4. We evaluated the acceptance and discrepancy of the ΔT_{CSI} cut, following the same procedure described in Section 6.2.4.3. The systematic uncertainty was estimated to be 0.22% by weighting the discrepancy obtained from each period with the K_L yield. Figure 6.34 shows the distribution of ΔT_{CSI}.

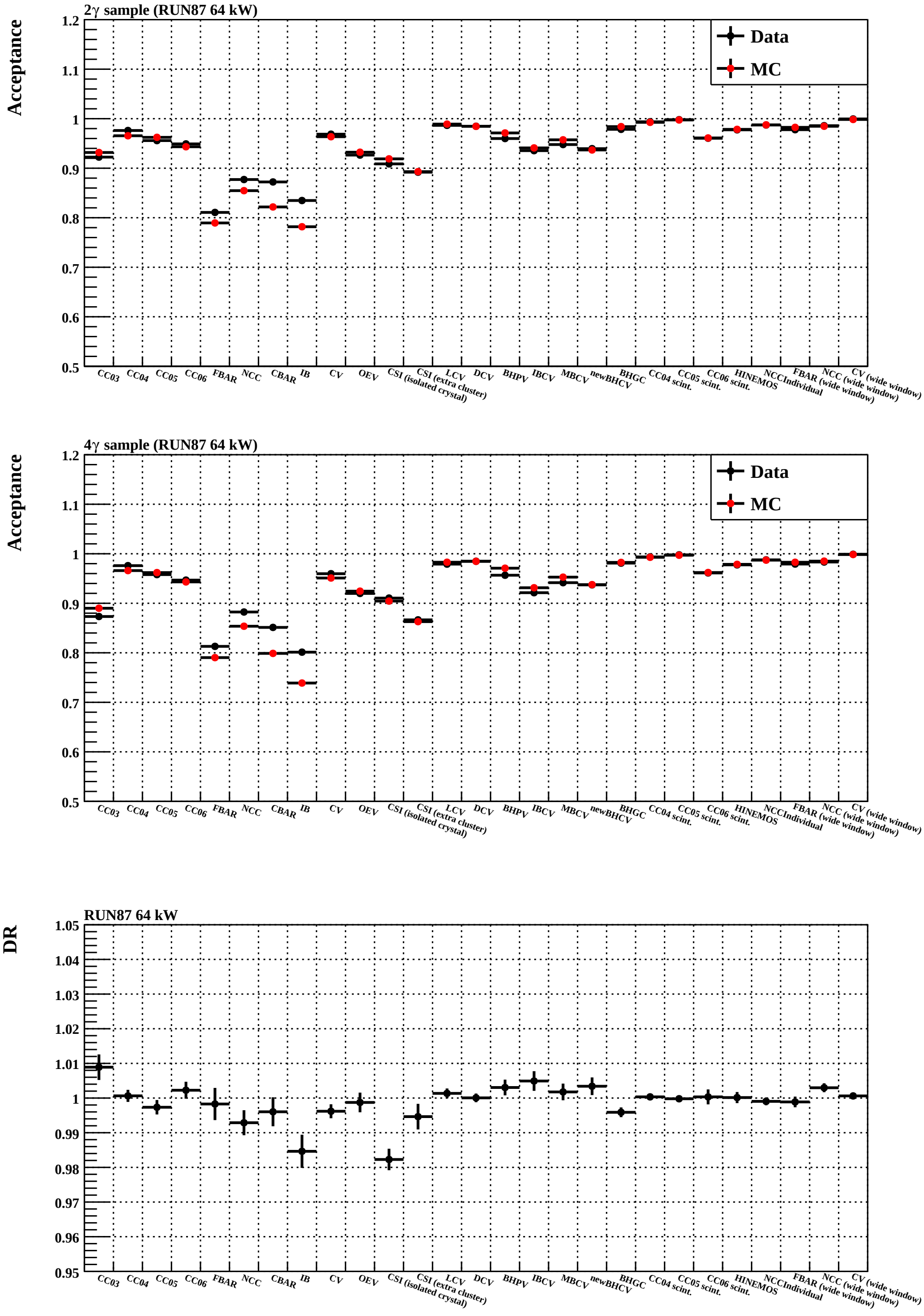

Figure 6.32: Acceptance of each veto cut for the $K_L \rightarrow 2\gamma$ sample (top) and the $K_L \rightarrow \pi^0\pi^0$ sample (middle), and the double ratio (bottom).

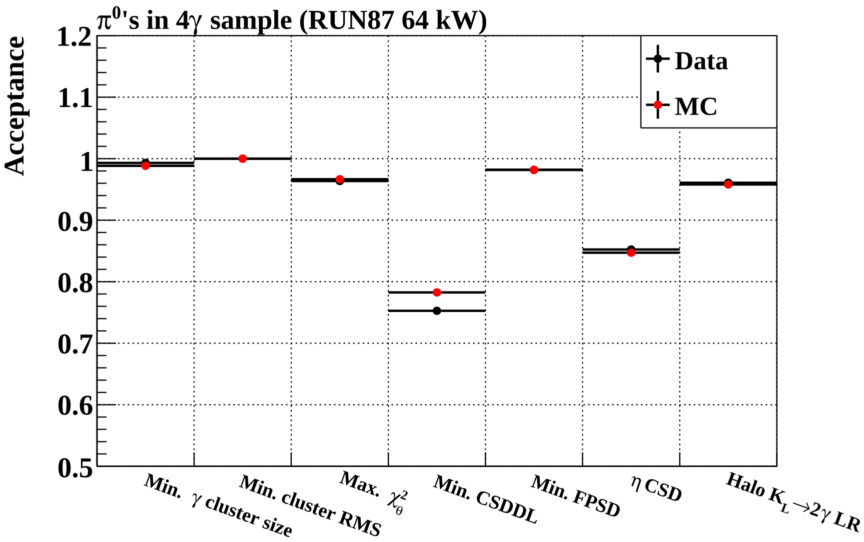

Figure 6.33: Acceptances of the shape-related cuts in the π^0 events.

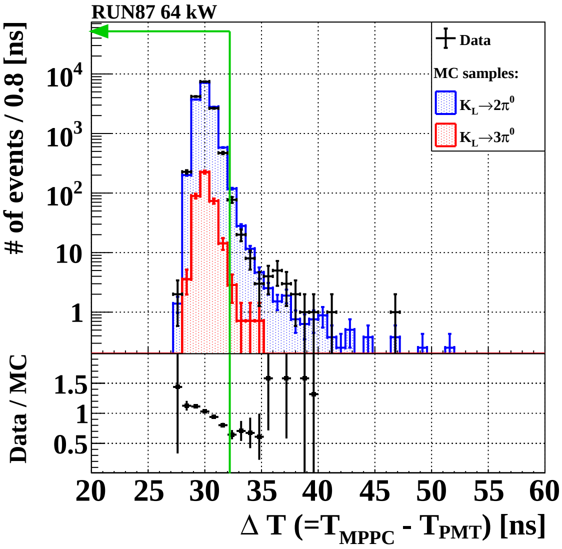

Figure 6.34: Distribution of ΔT_{CSI} in the π^0 events. The green arrow indicates the accepted region for $K_L \to \pi^0\nu\bar{\nu}$.

6.2.4.9 Summary of the Systematic Uncertainties

The results of the systematic uncertainties are summarized in Table 6.7. The total systematic uncertainty was estimated to be 9.0% by summing all the uncertainties in quadrature. According to this estimate, the single event sensitivity with uncertainties was determined to be

$$\begin{aligned} SES &= (9.31 \pm 0.06_{\mathrm{stat}} \pm 0.83_{\mathrm{syst}}) \times 10^{-10} \\ &= (9.31 \pm 0.84) \times 10^{-10}. \end{aligned} \tag{6.41}$$

Table 6.7: Relative systematic uncertainties on the single event sensitivity.

Source	Uncertainty [%]
Kinematic cuts for $K_L \to \pi^0\pi^0$	4.6
Shape-related cuts	4.1
Normalization modes inconsistency	3.6
Kinematic cuts for $K_L \to \pi^0\nu\bar{\nu}$	3.5
Veto cuts	3.3
Trigger effect	1.9
Photon selection	0.81
K_L momentum spectrum	0.98
ΔT_{CSI} cut	0.22
$K_L \to \pi^0\pi^0$ branching ratio	0.69
Total	9.0

6.3 Background Estimation

As introduced in Section 2.1.2, the background for the $K_L \to \pi^0\nu\bar{\nu}$ search was categorized into K_L decays, $K^\pm$ decays, and neutron-induced events. Table 6.8 summarizes the numbers of background events expected in the signal region. We estimated the total number of background events to be $0.252 \pm 0.055|_{\mathrm{stat}}{}^{+0.052}_{-0.067}|_{\mathrm{syst}}$ in the signal region. Figure 6.35 shows the number of estimated background events in each region. The distribution of events in data before unblinding the signal region is also shown in the same figure. The following sections describe the background evaluation for each source.

Table 6.8: Summary of background estimation. The second (third) numbers represent the statistical uncertainties (systematic uncertainties).

Source		Number of events
$K^\pm$		$0.042 \pm 0.014\ ^{+0.004}_{-0.028}$
K_L	$K_L \to 2\gamma$ (beam-halo)	$0.045 \pm 0.010 \pm 0.006$
	$K_L \to \pi^0\pi^0$	$0.059 \pm 0.022\ ^{+0.050}_{-0.059}$
Neutron	Hadron-cluster	$0.024 \pm 0.004 \pm 0.006$
	CV-η	$0.023 \pm 0.010 \pm 0.005$
	Upstream-π^0	$0.060 \pm 0.046 \pm 0.007$
Total		$0.252 \pm 0.055\ ^{+0.052}_{-0.067}$

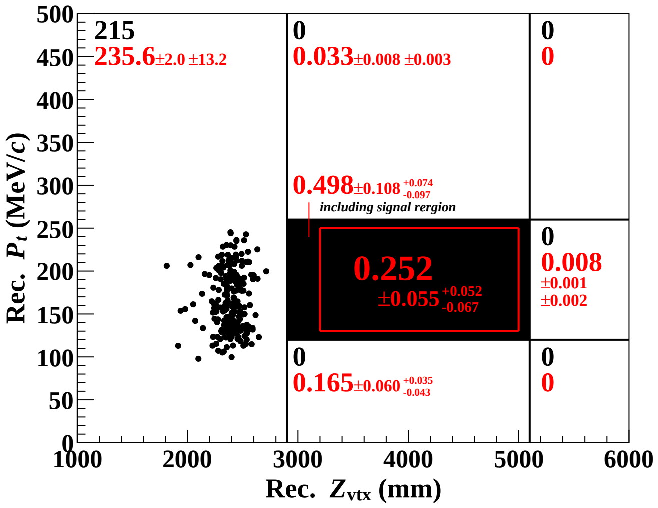

Figure 6.35: Reconstructed π^0 transverse momentum (P_t) versus π^0 decay vertex position (Z_{vtx}) for events after imposing the $K_L \to \pi^0\nu\bar{\nu}$ selection criteria in the 2021 data analysis. The region surrounded by red lines is the signal region. The black dots represent observed events. The black italic (red regular) numbers indicate the number of observed (background) events for different regions. The first and second errors represent the statistical and systematic errors, respectively.

6.3.1 $K_L \to \pi^0\pi^0$ Background

The $K_L \to \pi^0\pi^0$ decay becomes a background source when extra two photons in the final state are not detected by any veto detectors. The mechanism of the $K_L \to \pi^0\pi^0$ background is categorized into three types: even-pairing, odd-pairing, and fusion. The even-pairing represents the correct pairing of the two photons from the same π^0 for the $\pi^0 \to 2\gamma$ reconstruction. The odd-pairing, on the other hand, represents the incorrect pairing of two photons from the different π^0's. The fusion-type event is caused when two or more photons are merged into a single cluster due to the proximity of their cluster positions.

The number of $K_L \to \pi^0\pi^0$ background events was evaluated with the MC simulation. With the K_L yield obtained in Section 6.2.1, the number of MC events was normalized to be equivalent to the data.

6.3.1.1 Event Property

Figure 6.36 shows P_t versus Z_{vtx} for the $K_L \to \pi^0\pi^0$ MC events after imposing the $K_L \to \pi^0\nu\bar{\nu}$ selection criteria except for the signal region cuts. The $K_L \to \pi^0\pi^0$ NN cut reduced the number of background events in the signal region by 20%. After imposing the $K_L \to \pi^0\pi^0$ NN cut, the number of $K_L \to \pi^0\pi^0$ background events expected in the signal region was $0.049 \pm 0.018_{\text{stat}}$. There are eight MC events that remained in the signal region, which was dominated by the even-pairing type, as shown in Table 6.9. After looking into the events, it was revealed that most of the events were associated with a photonuclear reaction in veto detectors. Since a part of the incident photon energy was missed due to the photonuclear reaction, it induced inefficiency in the photon veto detectors.

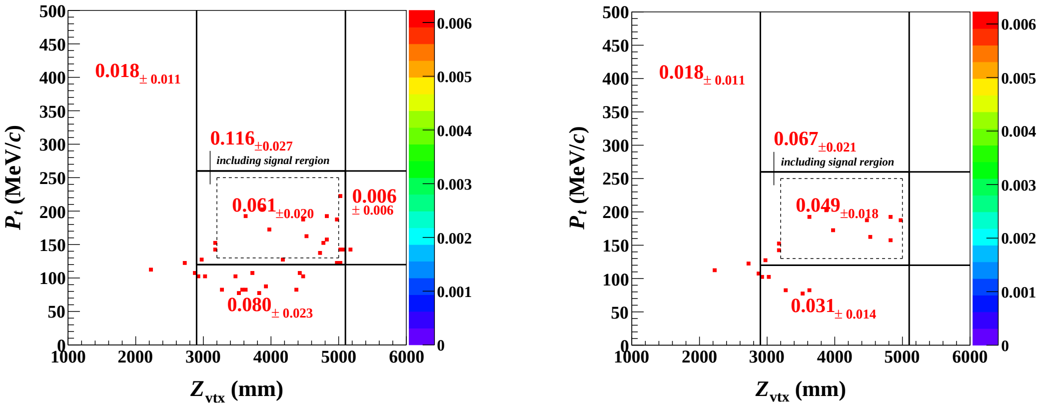

Figure 6.36: Reconstructed π^0 transverse momentum (P_t) versus π^0 decay vertex position (Z_{vtx}) for $K_L \to \pi^0\pi^0$ MC events. The left (right) figure shows distribution before (after) applying the $K_L \to \pi^0\pi^0$ NN cut.

Table 6.9: Property of the $K_L \to \pi^0\pi^0$ MC events remaining in the signal region. Photonuclear reactions were observed in all the events except for the one with the event ID of 5.

Event ID	(Z_{vtx}, P_t)	Event type	Extra 2γ destination (Incident γ energy)
0	(3642 mm, 192 MeV/c)	even-pairing	IB (348 MeV) BHPV (168 MeV)
1	(3852 mm, 202 MeV/c)	even-pairing	CSI (510 MeV)[a] FB (10 MeV)
2	(3962 mm, 174 MeV/c)	even-pairing	CSI (425 MeV)[b] MB (12 MeV)
3	(4472 mm, 189 MeV/c)	even-pairing	CSI (418 MeV)[a] MB (15 MeV)
4	(4508 mm, 163 MeV/c)	even-pairing	CSI (361 MeV)[a] FB (15 MeV)
5	(4832 mm, 158 MeV/c)	even-pairing	BHPV (4483 MeV) IB (3 MeV)
6	(4847 mm, 194 MeV/c)	even-pairing	MB (239 MeV) BHPV (154 MeV)
7	(4967 mm, 190 MeV/c)	fusion	CV (283 MeV) CSI[c]

[a] Photon hitting the cover (CFRP ring) for CSI.

[b] Photon hitting the iron cylinder for CSI.

[c] Photon fused into one of the clusters in CSI.

6.3.1.2 Inefficiency of Photon Veto Detectors

Since the number of background events highly relied on the photon detection inefficiency of the veto detectors, an accurate evaluation of the inefficiency was critical. Thus, a new method to evaluate the inefficiency of the photon veto detectors was proposed. This evaluation was performed by another collaborator[17].

Although we did not collect a sample dedicated to this study, the data collected by the normalization trigger and the minimum bias trigger were available. We thus utilized events in which five out of six photons in the final state of the $K_L \to 3\pi^0$ decay hit CSI (5γ sample). The vertex was reconstructed with the $K_L \to \pi^0\pi^0$ reconstruction method using four out of five photons hitting CSI. Figure 6.37 illustrates a schematic view of the 5γ sample collection using $K_L \to 3\pi^0$ decays. Momenta of all the five photons including the one that was not used for the vertex reconstruction were then determined. The remaining photon (missing photon) momentum was reconstructed under kinematical constraints on the K_L transverse momentum, the K_L vertex position, the invariant mass of the missing photon and the photon not used in the $K_L \to \pi^0\pi^0$ reconstruction, and the invariant mass of the six photons including the missing photon. Inefficiency was defined as a ratio of the number of events with deposited energy smaller than a given threshold for each detector to the total number of events with a missing photon hitting the veto detector. The difference in the inefficiency between the data and MC samples was evaluated for FB, IB, MB, and BHPV, as shown in Table 6.10. We considered the obtained differences as correction factors to estimate the number of $K_L \to \pi^0\pi^0$ background events.

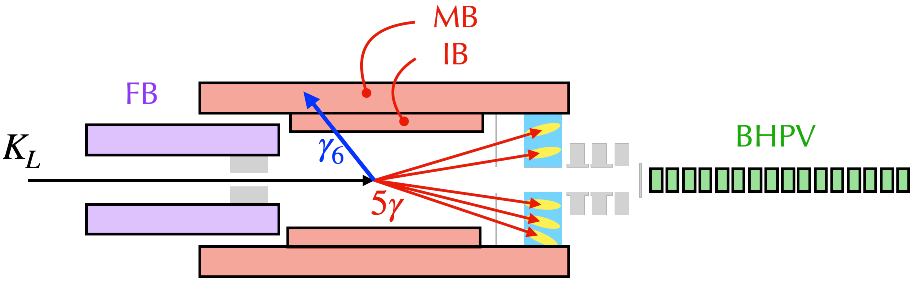

Figure 6.37: Schematic illustration of the inefficiency evaluation using the 5γ control sample. Events in which five photons from the $K_L \to 3\pi^0$ decays hit CSI are collected. In this figure, a missing photon (γ_6) hitting the barrel veto detectors (MB and IB) is used as an incident photon to estimate the inefficiency.

6.3.1.3 Number of $K_L \to \pi^0\pi^0$ Background Events

By applying the correction factors for the inefficiency of the photon veto detectors, the number of $K_L \to \pi^0\pi^0$ background events was estimated to be $0.059 \pm 0.022|_{\text{stat}}{}^{+0.050}_{-0.059}|_{\text{syst}}$. Figure 6.38 shows P_t versus Z_{vtx} for the $K_L \to \pi^0\pi^0$ MC events after imposing the $K_L \to \pi^0\nu\bar{\nu}$ selection criteria except for the signal region cuts and applying the correction factors. The systematic error was induced from the uncertainty on the correction factors. They suffered from the statistical limitations of both the data and MC samples, and thus resulted in the error of almost 100%.

---

[17] This was evaluated by K. Shiomi

Table 6.10: Correction factors on the photon detection efficiencies used in the $K_L \to \pi^0\pi^0$ background estimation.

Detector	Difference of the inefficiency between data and MC (Data/MC)
FB	1.42 ± 0.13
IB+MB for high energy photon[a]	$0.77^{+0.85}_{-0.77}$
IB+MB for low energy photon[a]	1.10 ± 0.10
BHPV	$1.50^{+0.42}_{-0.51}$

[a] The photon detection inefficiency for IB and MB was evaluated together while the inefficiency was separately evaluated for high energy photons and low energy photons. The reconstructed energy of the missing photon is required to be larger than 200 MeV or less than 50 MeV for the high energy photon or low energy photon, respectively. The statistical uncertainties on the 5γ events are taken into account.

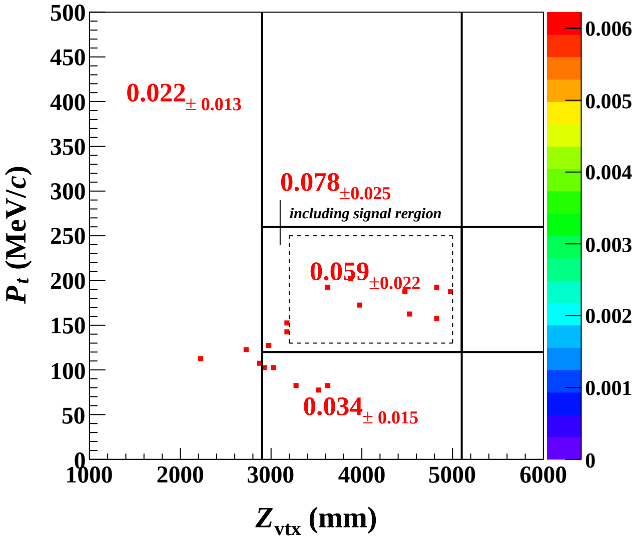

Figure 6.38: Reconstructed π^0 transverse momentum (P_t) versus π^0 decay vertex position ($Z_{\rm vtx}$) for $K_L \to \pi^0\pi^0$ MC events after imposing all the other $K_L \to \pi^0\nu\bar{\nu}$ selection criteria. In this figure, the error shown for each number is the statistical error.

6.3.2 Beam-Halo $K_L \to 2\gamma$ Background

The beam-halo $K_L \to 2\gamma$ background was caused by the beam-halo K_L that decays away from the beam axis. The wrong assumptions of the mass of the parent particle and the decay vertex position make the reconstructed P_t large enough to be in the signal region. It was revealed in the 2016–2018 data analysis that the flux of the beam-halo K_L originating from the scattering at the collimators in the KL beamline was underestimated if just relying on the prediction by the beam-line simulation [105, 128]. In the 2021 data analysis, the upstream in-beam detector, UCV, was also a non-negligible scattering source although we managed to keep its thickness as small as possible. We refer to the contribution of the K_L originating from the collimator simply as the halo K_L and to the one from UCV as the scattered K_L. This background was mainly studied by another collaborator[18].

6.3.2.1 Beam-Halo K_L Flux

The beam-halo K_L flux was studied using the reconstructed $K_L \to 3\pi^0$ sample. The data was collected with the $K_L \to 3\pi^0$ trigger described in Section 3.2.1.6. The MC sample for the halo K_L was generated using the beam-line seed while the MC sample for the scattered K_L was generated by collecting K_L's scattered at UCV after shooting K_L's with the beam-core K_L seed. For both the data and MC samples, the veto cuts with FB, CV, NCC, MB, IB, CC03, CC04, CC05, CC06, and OEV were imposed. The kinematic cuts with $\Delta T^{K_L}_{\mathrm{vtx}}$, M_{K_L}, and the minimum E_γ were also imposed with the same criteria as the normalization-mode analysis described in Section 6.2. The halo K_L and the scattered K_L can be represented with the large R_{COE} value, as shown in Figure 6.39. The region of $R_{\mathrm{COE}} > 200\,\mathrm{mm}$ was further selected to evaluate the beam-halo K_L flux. To reconcile the difference in the K_L yield between the data and MC samples, the data-to-MC ratio was obtained as correction factors for the halo K_L and the scattered K_L fluxes by fitting the R_{COE} distribution with two free parameters. The correction factors for the halo K_L and the scattered K_L were determined to be 5.74 and 1.54, respectively. Figure 6.40 shows the R_{COE} distribution after applying the correction factors.

---

[18] This was evaluated by K. Shiomi

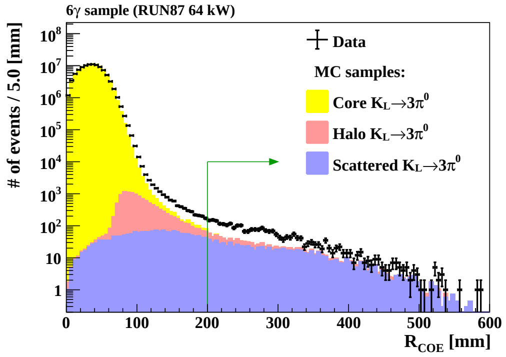

Figure 6.39: Distribution of R_{COE} for the reconstructed $K_L \longrightarrow 3\pi^0$ sample. The halo and scattered $K_L \longrightarrow 3\pi^0$ MC samples were normalized with the K_L yield the and halo-to-core K_L flux ratio in the beam-line simulation. The tail region shows that the data was imperfectly reproduced by the MC simulation. The green arrow represents the region used to evaluate the flux of the halo and scattered K_L components.

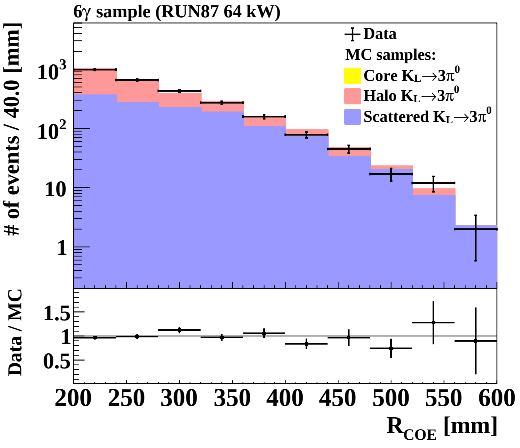

Figure 6.40: Distribution of R_{COE} in the region over 200 mm for the reconstructed $K_L \longrightarrow 3\pi^0$ sample. The correction factors for the halo and scattered K_L fluxes were applied to the MC samples.

6.3.2.2 Number of Beam-Halo $K_L \to 2\gamma$ Background Events

As already described in Section 6.2.2.1, the LR cut and the FD cut were developed to reduce the beam-halo $K_L \to 2\gamma$ background events. Figure 6.41 shows P_t versus Z_{vtx} for the halo $K_L \to 2\gamma$ and the scattered $K_L \to 2\gamma$ MC events after imposing the $K_L \to \pi^0 \nu \bar{\nu}$ selection criteria except for the signal region cuts. The two new cuts successfully reduced the number of beam-halo $K_L \to 2\gamma$ background events by a factor of eight. In total, the number of background events was estimated to be $0.045 \pm 0.010_{\text{stat}} \pm 0.006_{\text{syst}}$.

The systematic uncertainty originated from the flux correction factors, the beam-halo $K_L \to 2\gamma$ LR cut, and the FD cut. The correction factors for the halo and scattered K_L fluxes were further evaluated by excluding one of the cuts used in the event selection for the (beam-halo) $K_L \to 3\pi^0$ decays described in the previous section. The deviation of the correction factors from the results estimated with all the selection criteria was taken into account as a systematic uncertainty. The acceptances of the beam-halo $K_L \to 2\gamma$ cuts were evaluated using the beam-core $K_L \to 2\gamma$ events to study the systematic uncertainty. The beam-halo $K_L \to 2\gamma$ events were emulated by shifting the measured hit positions of the two photons in the radial direction for the beam-core $K_L \to 2\gamma$ events. The shifting distance was determined such that the R_{COE} value obtained from the shifted two photons followed the R_{COE} distribution of the beam-halo $K_L \to 2\gamma$ events. The acceptances of the LR cut and FD cut were evaluated for the data and MC samples. The discrepancy in the cut acceptance between the data and MC samples was assigned as a systematic uncertainty.

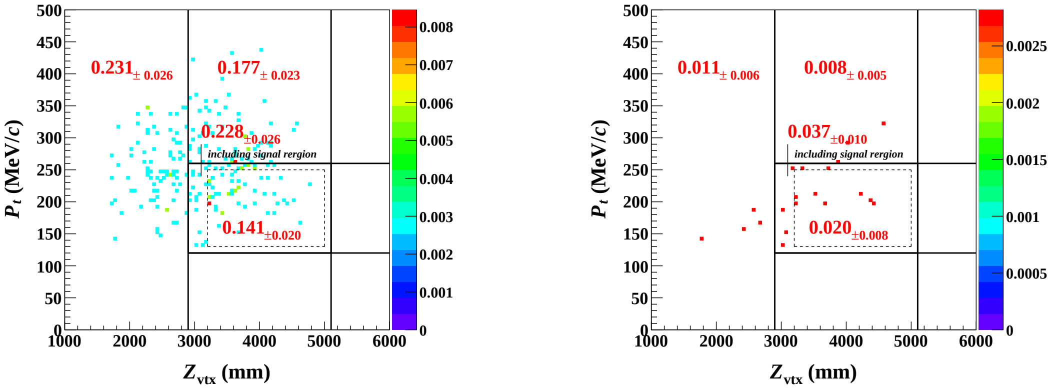

(a) Halo $K_L \to 2\gamma$ MC simulation before applying the beam-halo $K_L \to 2\gamma$ LR and FD cuts

(b) Halo $K_L \to 2\gamma$ MC simulation after applying the beam-halo $K_L \to 2\gamma$ LR and FD cuts

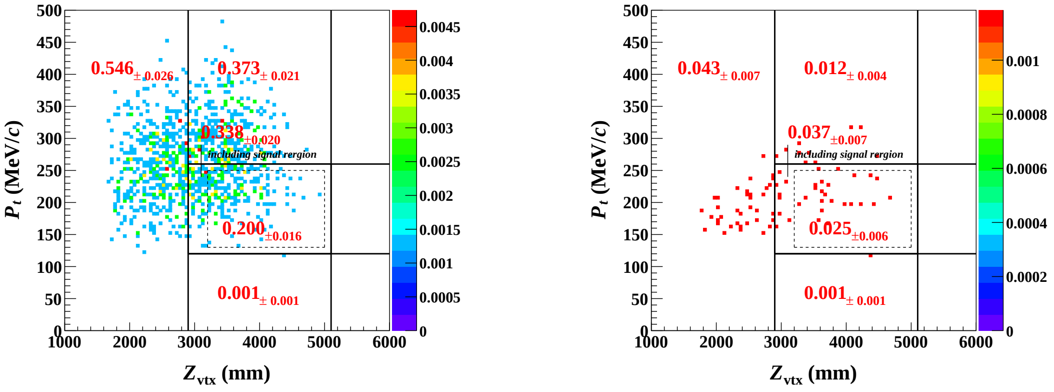

(c) Scattered $K_L \to 2\gamma$ MC simulation before applying the beam-halo $K_L \to 2\gamma$ LR and FD cuts

(d) Scattered $K_L \to 2\gamma$ MC simulation after applying the beam-halo $K_L \to 2\gamma$ LR and FD cuts

Figure 6.41: Reconstructed π^0 transverse momentum (P_t) versus π^0 decay vertex position (Z_{vtx}) for the halo $K_L \to 2\gamma$ and the scattered $K_L \to 2\gamma$ MC events. The background yield was normalized with the K_L flux and the correction factors. In this figure, the error shown for each number represents the statistical error.

6.3.3 Hadron-Cluster Background

The hadron-cluster background was caused by beam-halo neutrons directly hitting CSI. The cluster created by the incident neutron emits a secondary neutron creating another cluster in CSI. The number of hadron-cluster background events was estimated by another collaborator[19]. The hadron-cluster background was studied with the neutron control sample collected in the Z0-Al run.

The sideband region defined as $120 < P_t < 500\,\mathrm{MeV}/c$ and $2900 < Z_{\mathrm{vtx}} < 6000\,\mathrm{mm}$ except for the blind region was used to select neutron events. Figures 6.42 and 6.43 show the distribution of kinematic cuts and the shape-related cuts for the physics data sample and the control sample before applying the shape-related cuts except for the cuts with the cluster size and the cluster RMS. Under the loose $K_L \to \pi^0 \nu\bar{\nu}$ selection without including the cuts for the neutron suppression, such as the CSD-had cut, the PSD cut, and the ΔT_{CSI} cut, events in the physics data are dominated by the neutron events. In order to normalize the number of background events predicted from the neutron control sample, we used events in the sideband region under the loose selection. The photon selection cuts, the kinematic cuts and the veto cuts were imposed with loose condition, and the χ^2_θ cut and the CSD-η cut were further imposed. Figure 6.44 shows P_t versus Z_{vtx} for the physics data sample and the control sample under the loose selection.

The Z0-Al events in the sideband region and in the blind region under the loose condition were also used to study the background reduction capability by the three neutron cuts. The reduction factor of each cut was obtained for each cluster. The number of background events was estimated as $\alpha \cdot \left(\sum_i^n w_1^i \cdot w_2^i\right)$, where α is the normalization factor between the Z0-Al data and the physics data, $w^i_{1(2)}$ is the reduction factor for each cluster in the i-th event, and n is the number of events in the Z0-Al data after applying all the cuts except for the three neutron cuts. When multiplying the weight factors, the veto cuts were still applied with loose thresholds to keep the high statistics data for reliable evaluation. These cuts were applied with the tight threshold after the weight factors were multiplied.

With the normalization factor of $\alpha = 2.72$, the number of background events was estimated to be $0.024 \pm 0.004_{\mathrm{stat}} \pm 0.006_{\mathrm{syst}}$. The statistical uncertainty originated from the events remaining in the signal region from the Z0-Al data. The systematic uncertainty was evaluated by considering the normalization method and the acceptances of the three neutron cuts. For the normalization method, we calculated the ratio defined as $R_{\mathrm{phys\ (Z0)}} = N^{SR}_{\mathrm{phys\ (Z0)}}/N^{SB}_{\mathrm{phys\ (Z0)}}$, where $N^{SR}_{\mathrm{phys\ (Z0)}}$ is the number of events in the signal region from the physics data (Z0-Al data) and $N^{SB}_{\mathrm{phys\ (Z0)}}$ is the number of events in the sideband region from the physics data (Z0-Al data). The ratio was evaluated for the both physics data and the Z0-Al data by imposing the neutron cuts with the inverse condition[20] to enhance the neutron events[21]. The relative difference in the ratio between the physics data and the Z0-Al data was assigned as a systematic uncertainty. For the cut acceptance, we calculated the acceptance of one of the three cuts by imposing the other two neutron cuts with the inverse condition. The relative difference in the cut acceptance between the physics data and the Z0-Al data was taken into account as a systematic uncertainty. The total systematic uncertainty

---

[19] This was evaluated by Y.-C. Tung

[20] The inverse condition means that the accepted region and the rejected region in the $K_L \to \pi^0 \nu\bar{\nu}$ selection are swapped. For instance, the inverse condition of the CSD-had cut means that we require CSD-had<0.99, instead of CSD-had>0.99.

[21] Note that the events in the signal region after the $K_L \to \pi^0 \nu\bar{\nu}$ selection in the physics data were not unveiled at this stage because the inverse neutron cuts allowed us to examine the different parameter space.

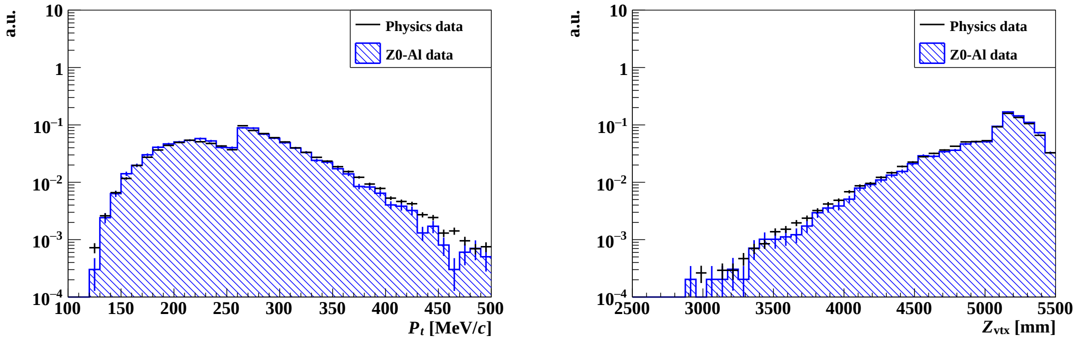

(a) P_t

(b) Z_{vtx}

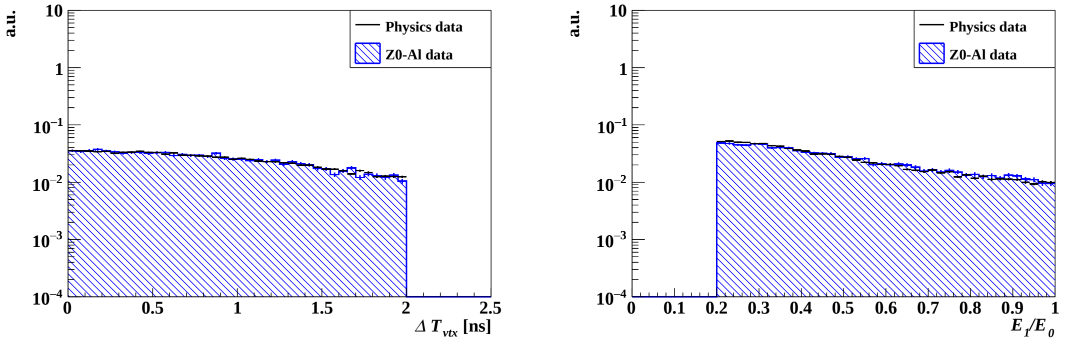

(c) ΔT_{vtx}

(d) Energy ratio

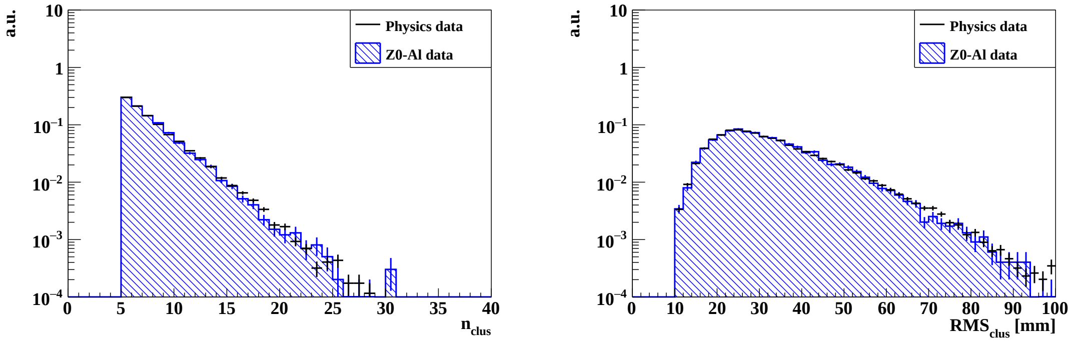

(e) Cluster size

(f) Cluster RMS

Figure 6.42: Distribution of the variables for the kinematic cuts and the shape-related cuts for the events in the sideband region in the physics run and the Z0-Al run. Each histogram is normalized to its area. The sharp edge seen in the distributions of P_t and Z_{vtx} are due to the exclusion of the events in the blind region.

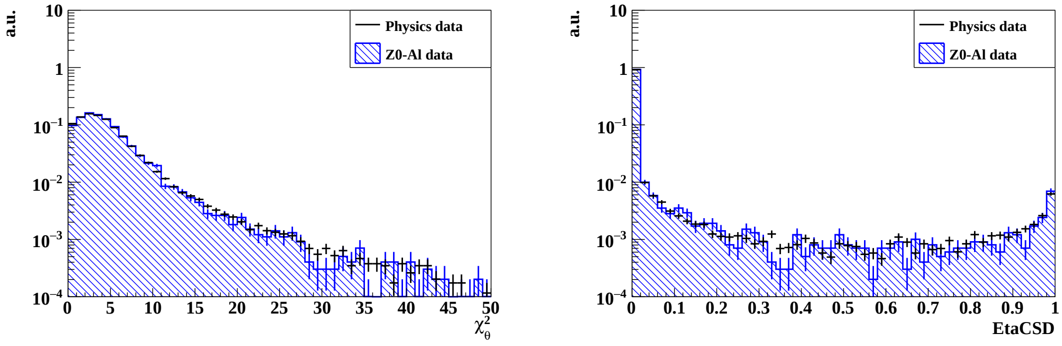

(a) χ^2_θ

(b) CSD-η

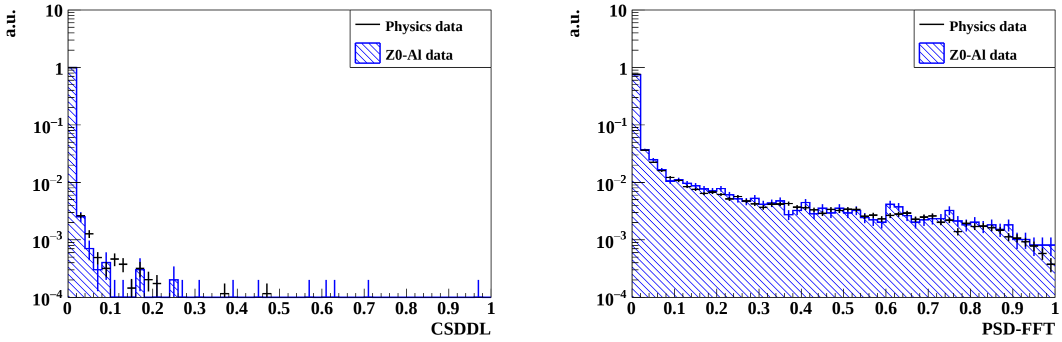

(c) CSD-had

(d) PSD-FFT

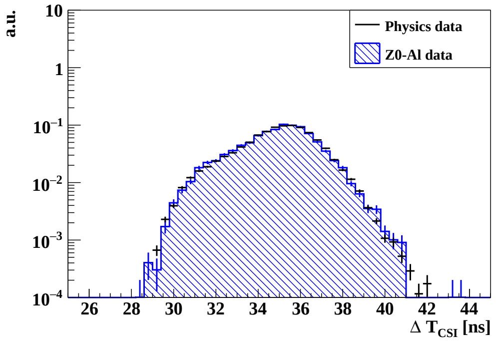

(e) ΔT_{CSI}

Figure 6.43: Distribution of the variables for the shape-related cuts and the ΔT_{CSI} cut for the events in the sideband region in the physics run and the Z0-Al run. Each histogram is normalized to its area.

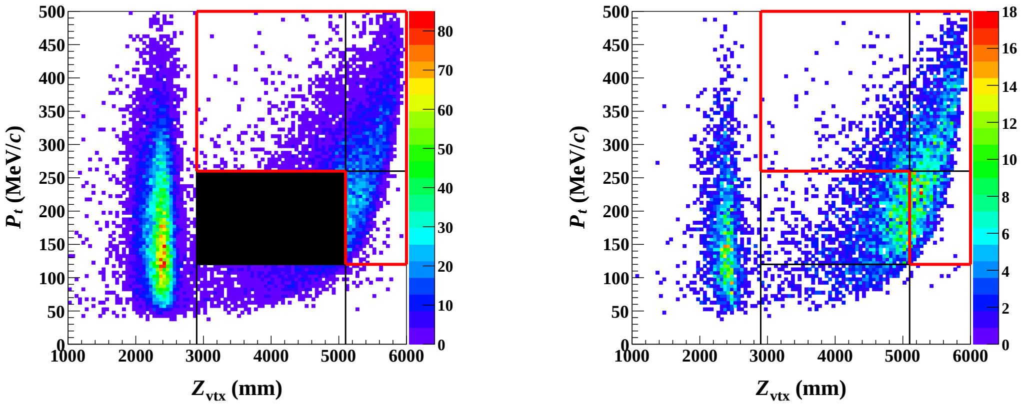

(a) Physics run

(b) Z0-Al run

Figure 6.44: Reconstructed π^0 transverse momentum (P_t) versus π^0 decay vertex position (Z_{vtx}) for the neutron events in the physics run and the Z0-Al run. The region surrounded by the red lines indicate the sideband region used for the normalization.

was obtained by summing the differences in the normalization method and the weight factors of the three neutron cuts in quadrature.

6.3.4 Upstream-π^0 Background

As described in Section 2.1.2.2, the upstream-π^0 background was caused by beam-halo neutrons hitting the upstream veto detector, NCC. The beam-halo neutron interacted with NCC and produced a π^0 decaying into two photons. The reconstructed Z_{vtx} of such events is localized in the upstream region corresponding to the location of NCC. As illustrated in Figure 6.45, some events can be shifted into the signal region when photonuclear reactions occur in CSI. If secondary neutral particles such as neutrons are emitted in the photonuclear reaction, they carry away a part of the incident photon energy. The mis-measurement of the photon energy can push Z_{vtx} downstream according to Equation 2.3. The number of upstream-π^0 background events was estimated by another collaborator[22].

The upstream-π^0 background was evaluated with the MC simulation for the beam-halo neutrons. The number of events in the region of $Z_{\mathrm{vtx}} < 2900\,\mathrm{mm}$ under loose selection criteria was used to normalize the MC simulation. The uncertainty with regard to the photonuclear reaction can lie in the background estimation for the upstream-π^0 events. Therefore, the probability of the energy mis-measurement in CSI was further evaluated using $K_L \to 3\pi^0$ decays in the 2021 data analysis. The events associated with photonuclear reactions were enhanced by requiring the invariant mass of the six photons ($M_{6\gamma}$) to be $|M_{6\gamma} - M_{K_L}| > 15\,\mathrm{MeV}/c^2$, where M_{K_L} is the nominal K_L mass. In addition, the COE radius was required to be $100 < R_{\mathrm{COE}} < 200\,\mathrm{mm}$. The remaining number of reconstructed $K_L \to 3\pi^0$ events in the data sample was found to be 2.64 times larger than that in the MC sample, and this difference was considered as a correction factor

---

[22] This was evaluated by K. Shiomi

in the background estimation.

The number of upstream-π^0 background events was estimated to be $0.060 \pm 0.046_{\mathrm{stat}} \pm 0.007_{\mathrm{syst}}$. The systematic uncertainty originated from the statistical error of the correction factor and the dependence of the data-to-MC normalization factor on the event selection. Figure 6.46 shows P_t versus Z_{vtx} after imposing all the selection criteria for $K_L \to \pi^0 \nu \bar{\nu}$ and the correction factor for the probability of the energy mis-measurement.

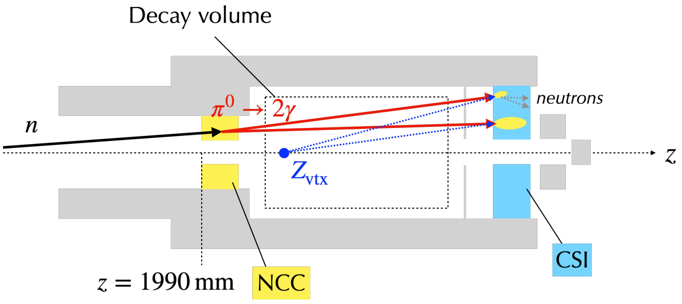

Figure 6.45: Mechanism of the upstream-π^0 background. Secondary particles such as neutrons generated in the photonuclear reaction can take away a part of the photon energy. The blue point represents the reconstructed vertex position.

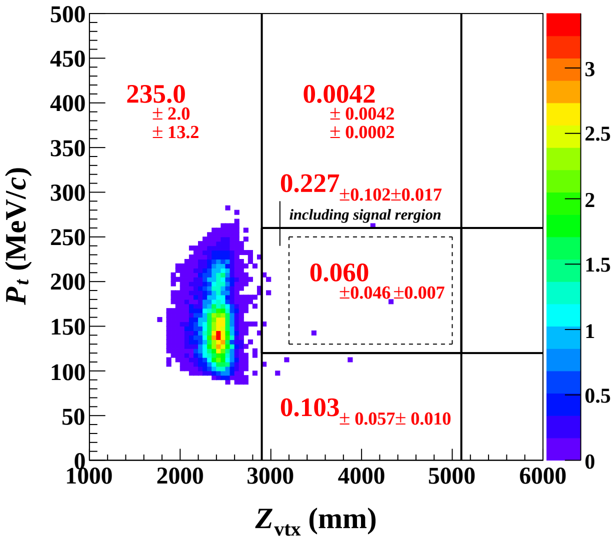

Figure 6.46: Reconstructed π^0 transverse momentum (P_t) versus π^0 decay vertex position (Z_{vtx}) for the upstream-π^0 MC events after imposing all the other $K_L \to \pi^0 \nu \bar{\nu}$ selection criteria. In this figure, the first (second) error shown for each number is the statistical (systematic) error.

6.3.5 CV-η Background

The CV-η background was caused by beam-halo neutrons hitting CV, as described in Section 2.1.2.2. An η particle produced in CV decays into two photons hitting CSI, leaving no energy deposition in other veto detectors. As illustrated in Figure 6.47, the reconstructed Z_{vtx} was pushed upstream due to the wrong mass assumption of the parent particle, according to Equation 2.3. This number of background events was estimated by another collaborator[23].

The background was evaluated by using the MC simulation for the beam-halo neutrons. The number of background events in the MC simulation was normalized to data using events in the downstream region of $Z_{\text{vtx}} > 5100$ mm under loose kinematic selection. In this region, events were dominated by the π^0 production in CV.

The number of CV-η background events was estimated to be $0.023 \pm 0.010_{\text{stat}} \pm 0.005_{\text{syst}}$. The systematic uncertainty was evaluated by investigating the production ratio of η to π^0. The special run described in Section 3.2.2.3 was performed in 2019 to take a control sample for the η and π^0 productions in CV. By comparing the number of events for η and π^0 candidates between the data and MC samples, the uncertainty on the normalization factor was evaluated. Figure 6.48 shows P_t versus Z_{vtx} after imposing all the selection criteria for $K_L \to \pi^0\nu\bar{\nu}$.

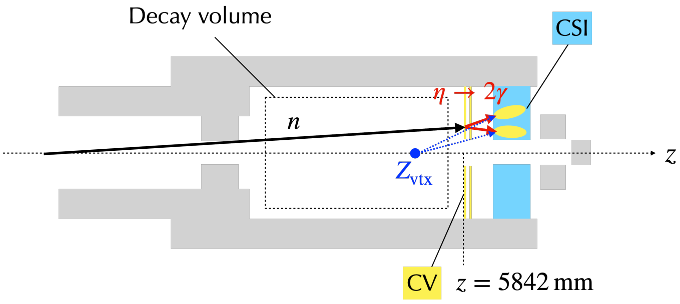

Figure 6.47: Mechanism of the CV-η background. The blue point represents the reconstructed vertex position.

---

[23] This was evaluated by K. Shiomi

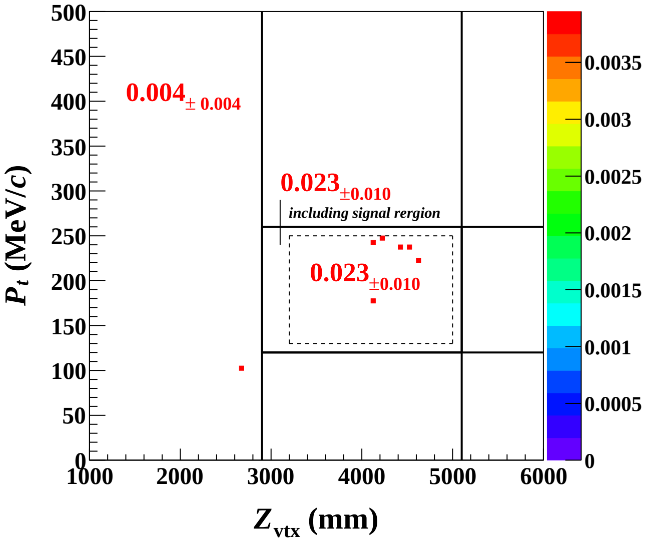

Figure 6.48: Reconstructed π^0 transverse momentum (P_t) versus π^0 decay vertex position ($Z_{\rm vtx}$) for the CV-η MC events after imposing all the other $K_L \to \pi^0 \nu \bar{\nu}$ selection criteria. In this figure, the error shown for each number is the statistical error.

6.3.6 $K^\pm$ Decay Background

The $K^\pm$ decay was the most dominant background source in the 2016–2018 data analysis. As described in Section 2.1.2.2, the $K^\pm$ background originates from the generation of $K^\pm$'s at the downstream collimator in the KL beamline. The number of background events was evaluated using the MC simulation with the beam-line seed for the incident $K^\pm$. The $K^\pm$ that is likely to be a background source should decay in the decay volume in the KOTO detector after passing through the beam hole at NCC. The $K^\pm$ momentum of such events gets filtered to have a peak around 1.5 GeV/c, as shown in Figure 6.49. Considering the normalization of the $K^\pm$ yield and the $K^\pm$ detection inefficiency of UCV, the background evaluation was performed in the following steps:

1. Estimation of the flux ratio of $K^\pm$ to K_L
2. Estimation of the $K^\pm$ detection inefficiency of UCV
3. Estimation of the number of $K^\pm$ decay background events in the signal region

The $K^\pm$ flux as well as the inefficiency of UCV were studied using the $K^\pm$ sample collected with the $K^\pm \to \pi^\pm \pi^0$ trigger and the less-biassed $K^\pm$ trigger during the period-10. In the following section, the evaluation of each quantity is described.

6.3.6.1 Flux of the $K^\pm$

The flux of $K^\pm$ was measured using $K^\pm \to \pi^\pm \pi^0$ decays because this decay mode is a simple two-body decay, which made it easier to reconstruct candidate events. In addition, the branching

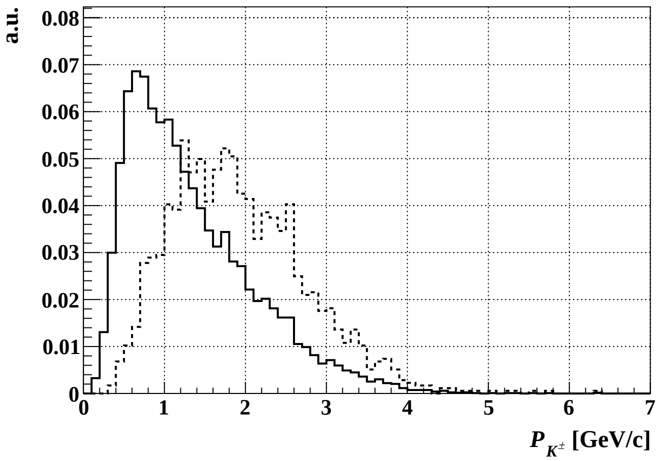

Figure 6.49: $K^\pm$ momentum spectrum predicted by the beam-line seed. The solid line shows the histogram of the incident $K^\pm$ momentum. The dashed line shows the histogram of the $K^\pm$ momentum after requiring the x-y position of the $K^\pm$ trajectory extrapolated to the position of NCC to be geometrically inside the beam hole region. Each histogram is normalized with its area.

ratio of $K^\pm \to \pi^\pm\pi^0$ is relatively large among major $K^\pm$ decays, as shown in Table 6.11, which helped to collect events with large statistics. We collected $K^\pm \to \pi^\pm\pi^0$ signals in which a $\pi^\pm$ and two photons from the π^0 decay created three clusters in CSI. We reconstructed $K^\pm \to \pi^\pm\pi^0$ decays as follows.

$K^\pm \to \pi^\pm\pi^0$ Reconstruction

The following reconstruction method was applied to all the three combinations of the clusters for a $\pi^\pm$ and two photons. A $\pi^0 \to 2\gamma$ decay was reconstructed with the procedure used for $K_L \to \pi^0\nu\bar{\nu}$, and the $K^\pm$ vertex was assumed to be the same as the π^0 vertex position. Since the deposited energy of a $\pi^\pm$ in CSI can be poorly measured, we assumed the momentum balance between π^0 and $\pi^\pm$ in the transverse direction, and used the hit position of the $\pi^\pm$ to determine the $\pi^\pm$ direction. The transverse momentum of the $\pi^\pm$ ($P_t^{\pi^\pm} = (P_x^{\pi^\pm}, P_y^{\pi^\pm})$) was given as

$$P_x^{\pi^\pm} = -P_x^{\pi^0}, \tag{6.42}$$

$$P_y^{\pi^\pm} = -P_y^{\pi^0}, \tag{6.43}$$

where $P_x^{\pi^0}$ ($P_y^{\pi^0}$) is the $x(y)$-component of the the π^0 momentum. The angle of the $\pi^\pm$ direction with respect to the beam axis ($\theta_{\pi^\pm}$) can be determined based on the π^0 vertex position and the $\pi^\pm$ hit position. Thus, the magnitude of the $\pi^\pm$ momentum was calculated as

$$\left|P^{\pi^\pm}\right| = \frac{\left|P_t^{\pi^\pm}\right|}{\sin\theta_{\pi^\pm}}. \tag{6.44}$$

Using $\left|P^{\pi^\pm}\right|$ and the $\pi^\pm$ direction, all the momenta of the $\pi^\pm$ can be reconstructed. Accordingly, the invariant mass of the π^0-$\pi^\pm$ system that is equivalent to the reconstructed $K^\pm$ mass was obtained from the momenta of the π^0 and the $\pi^\pm$ with an additional assumption of the constant $\pi^\pm$ mass

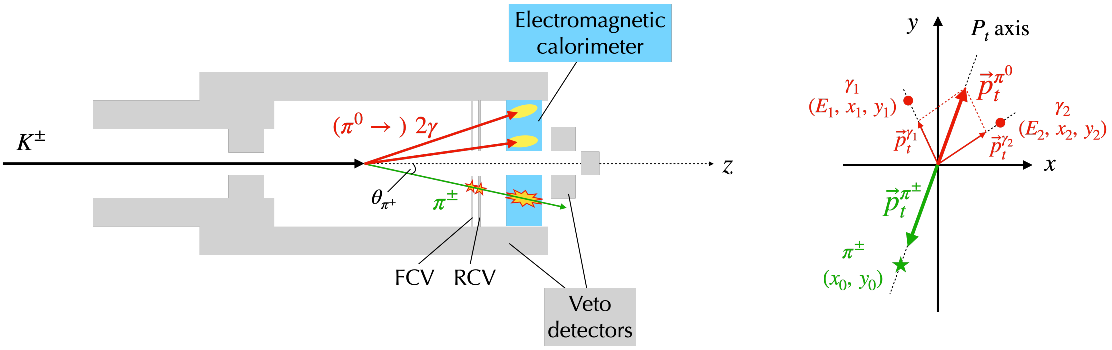

Figure 6.50: Schematic illustration of the $K^{\pm} \rightarrow \pi^{\pm}\pi^0$ reconstruction. The left figure shows the $K^{\pm} \rightarrow \pi^{\pm}\pi^0$ decay with the KOTO detector from the direction perpendicular to the z-axis. The right figure shows the $K^{\pm} \rightarrow \pi^{\pm}\pi^0$ decay projected on the x-y plane. For the $\pi^{\pm}$ candidate cluster, we only used the information of the hit position.

(139.57 MeV/c^2) quoted from Ref. [1]. To select one of the cluster combinations, the χ^2_{shape} value described in Section 6.2.2.1 was calculated for the three clusters. The combination giving the smallest sum of the χ^2_{shape} values for two photon candidates was selected in the $K^{\pm} \rightarrow \pi^{\pm}\pi^0$ reconstruction. Figure 6.50 shows the schematic explanation of the reconstruction method for $K^{\pm} \rightarrow \pi^{\pm}\pi^0$.

Table 6.11: Main decay modes of $K^{\pm}$ and their branching ratios [1].

Decay mode	Branching ratio
$K^{\pm} \rightarrow \mu^{\pm}\nu_{\mu}$	$(63.56 \pm 0.11)\%$
$K^{\pm} \rightarrow \pi^{\pm}\pi^0$	$(20.67 \pm 0.08)\%$
$K^{\pm} \rightarrow \pi^{\pm}\pi^{\pm}\pi^{\mp}$	$(5.583 \pm 0.024)\%$
$K^{\pm} \rightarrow \pi^0 e^{\pm}\nu_e$	$(5.07 \pm 0.04)\%$
$K^{\pm} \rightarrow \pi^0\mu^{\pm}\nu_{\mu}$	$(3.352 \pm 0.034)\%$
$K^{\pm} \rightarrow \pi^{\pm}\pi^0\pi^0$	$(1.760 \pm 0.023)\%$

Event Selection

The event selection for the $K^{\pm} \rightarrow \pi^{\pm}\pi^0$ decay was based on the strategy to purify $K^{\pm} \rightarrow \pi^{\pm}\pi^0$ signals while keeping the enough statistics by relaxing some of the selection criteria in comparison with the $K_L \rightarrow \pi^0\nu\bar{\nu}$ selection. As preliminary selections to eliminate the trigger biases and to suppress events with extra particles, we applied selections on the total energy in CSI, the charged-particle track (CV-matching)[24], and the veto. For the veto cuts, we used selection criteria with a loose condition summarized in Appendix G.1. As for the selection with CV, we required the deposited energy to be greater than 0.3 MeV instead of using it as a veto detector.

---

[24] In this algorithm, a charged-particle track was evaluated by counting the number of hits in each CV layer with the deposited energy grater than 0.2 MeV. The number of hits in both FCV and RCV was required to be one. In addition, the position of the hit module in each CV layer was required to match with the track determined from the vertex position and the $\pi^{\pm}$ candidate cluster position in CSI.

To enhance events from the $K^\pm \to \pi^\pm \pi^0$ decay in the three-cluster sample, we further imposed the selection criteria shown in Table 6.12. The photon selection cuts aimed to collect events with two photon-like hits out of three clusters. We applied cuts on the photon hit positions, the vertex timing difference (ΔT_{vtx}), the cluster sizes (n_{cryst}) of the two photon candidate clusters, χ^2_{shape}, and CSD_{NN}, all of which were explained in Section 6.2.2.1. Since we assumed that the remaining cluster was made by a $\pi^\pm$, we required the deposited energy in CSI for a $\pi^\pm$ candidate cluster ($E_{\pi^\pm}$) to be the MIP-like energy deposition by imposing $200 < E_{\pi^\pm} < 400\,\text{MeV}$. Moreover, kinematical features of the $K^\pm \to \pi^\pm \pi^0$ decay were utilized to extract the signal events. The azimuthal angle between the $\pi^\pm$ and π^0 momenta projected onto the x-y plane ($\phi_{\pi^\pm\pi^0}$) was required to be larger than 140° to achieve the back-to-back configuration for $\pi^\pm\pi^0$ in the $K^\pm$-rest frame. The vertex timing difference between the $\pi^\pm$ and the π^0 ($\delta T_{\pi^\pm\pi^0}$) was required to be $-3 < \delta T_{\pi^\pm\pi^0} < 2\,\text{ns}$ to ensure the coincident hit timings of the two. The Z_{vtx} and P_t of the reconstructed π^0 were required to be $2000 < Z_{\text{vtx}} < 5250\,\text{mm}$ and $P_t > 80\,\text{MeV}/c$, respectively. The requirement on Z_{vtx} was loosened compared with the $K_L \to \pi^0 \nu \bar{\nu}$ selection in order to increase the statistics of the $K^\pm$ sample. Finally, the invariant mass of the reconstructed $K^\pm$ ($M_{K^\pm}$) was required to be $440 < M_{K^\pm} < 600\,\text{MeV}/c^2$ to ensure that the events originated from $K^\pm$ decays.

The three-cluster sample under loose selection criteria was dominated by the $K_L \to \pi^+\pi^-\pi^0$ decay. The majority of $K_L \to \pi^+\pi^-\pi^0$ events made three clusters in CSI with one $\pi^\pm$ and two photons from the π^0 decay. The remaining $\pi^\pm$ escaped through the beam hole to the downstream region. Figure 6.51 shows the distribution of the reconstructed $K^\pm$ mass in the three-cluster sample collected with the less-biassed $K^\pm$ trigger. Most of the events are from $K_L \to \pi^+\pi^-\pi^0$ and concentrated in the smaller mass region than the nominal $K^\pm$ mass due to the missing $\pi^\pm$. The number of events in the MC simulation for each K_L decay mode was normalized to the K_L yield obtained from the $K_L \to \pi^+\pi^-\pi^0$ decays under the loose selection.

On top of the kinematic cuts described above, we further imposed cuts with the downstream veto detectors to reduce the $K_L \to \pi^+\pi^-\pi^0$ contribution. We applied the veto cuts on CC04, CC05, DCV, newBHCV, and BHPV with almost the same criteria used for the $K_L \to \pi^0 \nu \bar{\nu}$ selection[25]. Figures 6.52 and 6.53 show distributions of cut variables listed in Table 6.12 for the data sample collected with the $K^\pm \to \pi^\pm \pi^0$ trigger and the MC samples. For each distribution, events were selected with all the cuts for $K^\pm \to \pi^\pm \pi^0$ except for the cut shown in each figure. As shown in Figure 6.53a, the $K^\pm$ candidate events around the nominal $K^\pm$ mass are dominated by the $K^\pm \to \pi^\pm \pi^0$ signal as well as other $K^\pm$ decays of $K^\pm \to \pi^0 \mu^\pm \nu_\mu$ and $K^\pm \to \pi^0 e^\pm \nu_e$. There was 1.3% of K_L contamination in the $K^\pm$ candidate events. The majority of such K_L events originated from $K_L \to \pi^0 \pi^0$ decays. In the small $M_{K^\pm}$ region, there was a discrepancy between the data and MC samples. This discrepancy was not fully understood. This can have an impact on the possible contamination in the $K^\pm$ sample, as will be described in Section 6.3.6.3.

$K^\pm$ Flux Measurement

We collected 2912 $K^\pm$ candidate events with 2.13×10^{19} POT from the data. The $K^\pm$ yield at the beam exit ($N_{K^\pm}$) was calculated using the three $K^\pm$ decay modes, $K^\pm \to \pi^\pm \pi^0$, $K^\pm \to \pi^0 \mu^\pm \nu_\mu$, and $K^\pm \to \pi^0 e^\pm \nu_e$, as

$$N_{K^\pm} = \frac{N^{\text{obs}} \cdot (1 - \mu_{K_L})}{\sum_{i=1}^{3} (A_i \cdot \mathcal{B}_i)}, \tag{6.45}$$

---

[25] The energy threshold for DCV was set to 4 MeV instead of 5 MeV.

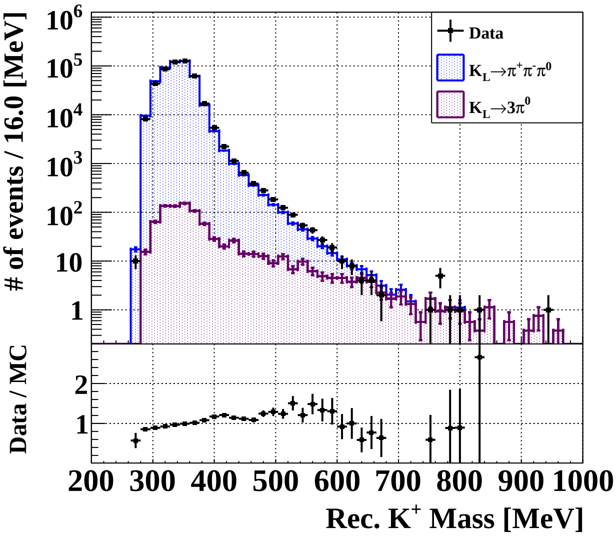

Figure 6.51: Distribution of the reconstructed $K^{\pm}$ mass in the three-cluster sample under the loose selection. For this distribution, all the loose veto cuts and the kinematic cuts except for the cuts with $E_{\pi^{\pm}}$, Z_{vtx}, P_t, and $M_{K^{\pm}}$ were imposed. The histogram of the MC simulation is normalized to the area.

Table 6.12: Kinematic selection for $K^{\pm} \rightarrow \pi^{\pm}\pi^{0}$.

Category	Cut variable	Criteria
Photon selection	Hit position (x, y)	$\max(\lvert x\rvert, \lvert y\rvert) \geq 150\,\text{mm}$
	Vertex timing difference (ΔT_{vtx})	$\Delta T_{\text{vtx}} \leq 1.5\,\text{ns}$
	Cluster size (n_{cryst})	$n_{\text{cryst}}^{\gamma_1}$ $(n_{\text{cryst}}^{\gamma_2}) \geq 5$ (4)[a]
	χ^2_{shape}	$\chi^2_{\text{shape}} > 10$
	CSD_{NN}	CSD_{NN} output > 0.8
$\pi^{\pm}$ selection	$\pi^{\pm}$ energy deposition ($E_{\pi^{\pm}}$)	$200 < E_{\pi^{\pm}} < 400\,\text{MeV}$
$K^{\pm} \rightarrow \pi^{\pm}\pi^{0}$ selection	$\pi^{\pm}$-π^{0} angle ($\phi_{\pi^{\pm}\pi^{0}}$)	$\phi_{\pi^{\pm}\pi^{0}} > 140^{\circ}$
	$\pi^{\pm}$-π^{0} timing difference ($\delta T_{\pi^{\pm}\pi^{0}}$)	$-3 < \delta T_{\pi^{\pm}\pi^{0}} < 2\,\text{ns}$
	Reconstructed π^{0} Z_{vtx}	$2000 < Z_{\text{vtx}} < 5250\,\text{mm}$
	Reconstructed π^{0} P_t	$P_t > 80\,\text{MeV}/c$
	Reconstructed $K^{\pm}$ mass ($M_{K^{\pm}}$)	$440 < M_{K^{\pm}} < 600\,\text{MeV}/c^2$

[a] γ_1 and γ_2 are defined as the two photons where the energy of γ_1 is larger than that of γ_2. $n_{\text{cryst}}^{\gamma_1}$ $(n_{\text{cryst}}^{\gamma_2})$ represents the the cluster size of γ_1 (γ_2).

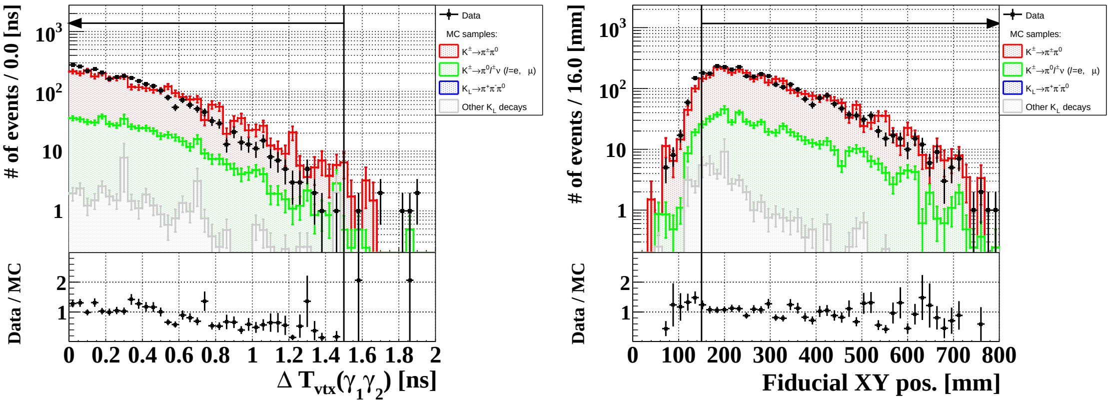

(a) Vertex timing difference (ΔT_{vtx})

(b) Hit position ($\max(|x|, |y|)$)

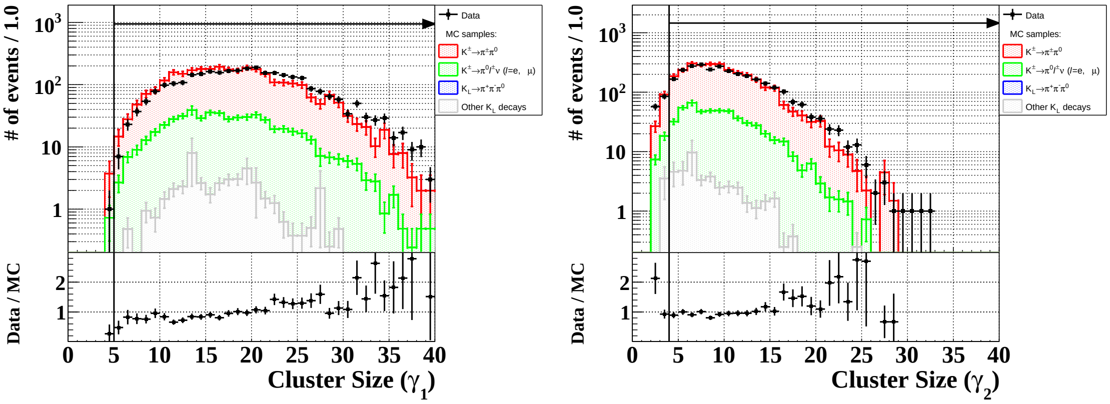

(c) Cluster size of γ_1 ($n^{\gamma 1}_{\mathrm{cryst}}$)

(d) Cluster size of γ_2 ($n^{\gamma 2}_{\mathrm{cryst}}$)

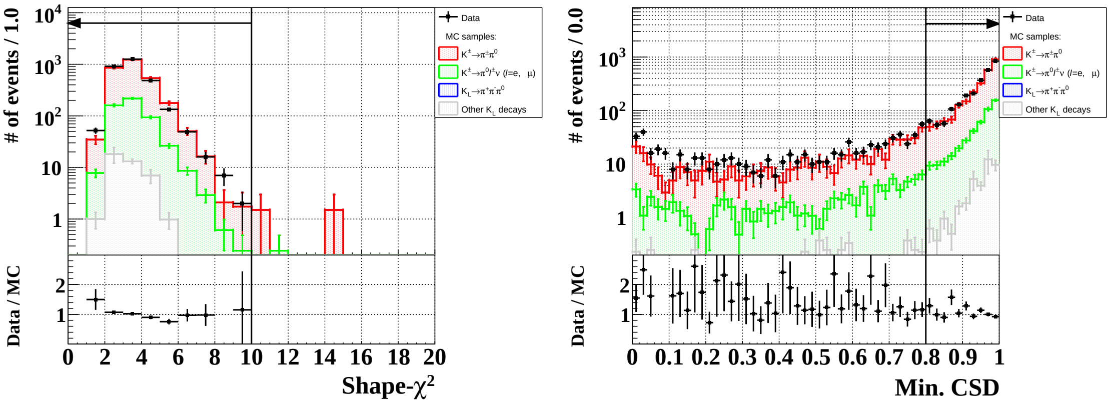

(e) χ^2_{shape}

(f) $\mathrm{CSD}_{\mathrm{NN}}$

Figure 6.52: Distributions of kinematic-cut variables used for the three-cluster $K^\pm$ sample. For each distribution, all the cuts for $K^\pm \to \pi^\pm \pi^0$ signals except for the cut shown in each figure were imposed. The MC samples for $K^\pm$ decays were normalized with the measured $K^\pm$ flux. The black arrow in each figure indicates the accepted region.

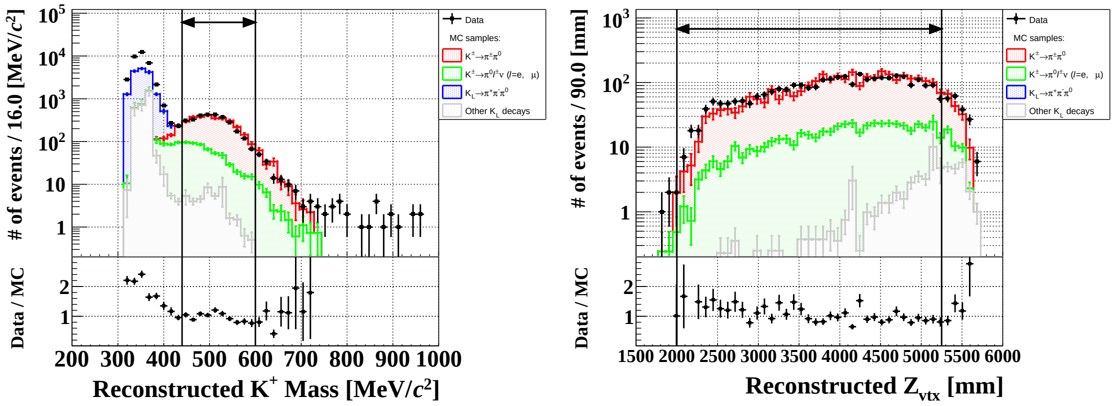

(a) Reconstructed $K^{\pm}$ mass (b) Reconstructed Z_{vtx}

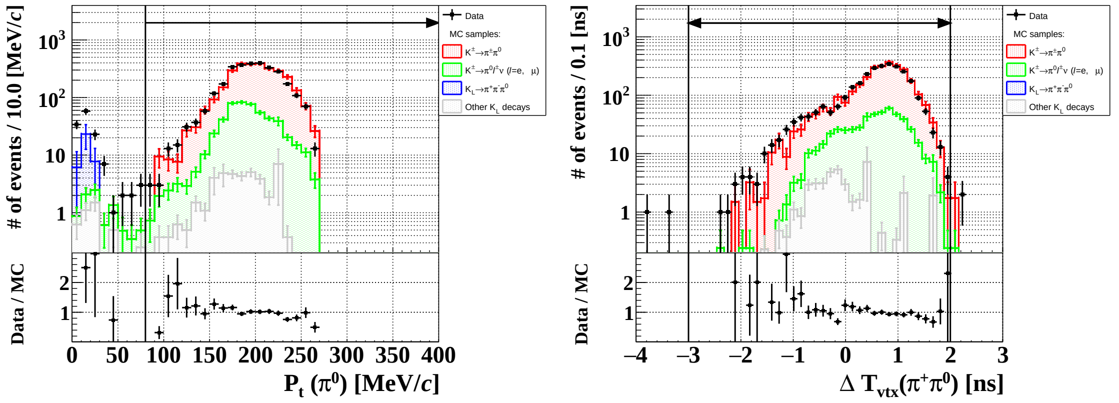

(c) Reconstructed π^0 P_t (d) $\pi^{\pm}$-π^0 timing difference ($\delta T_{\pi^{\pm}\pi^0}$)

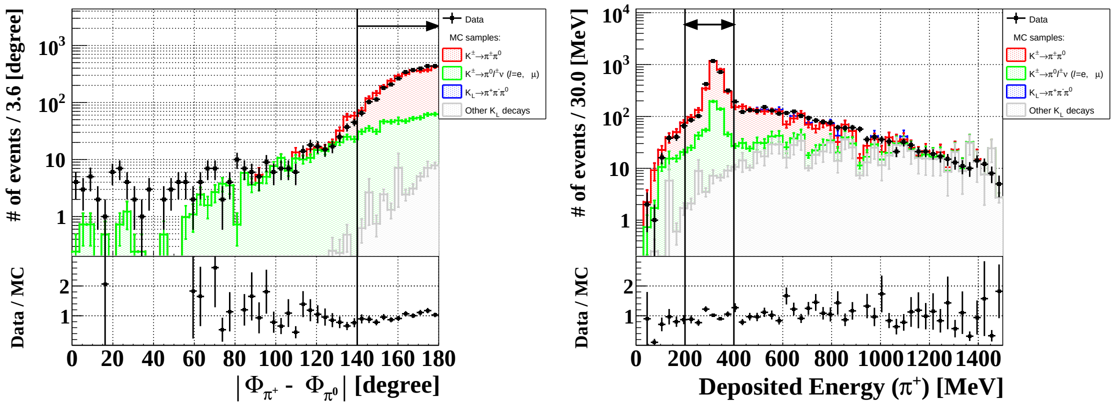

(e) $\pi^{\pm}$-π^0 angle ($\phi_{\pi^{\pm}\pi^0}$) (f) Deposited energy of a $\pi^{\pm}$ cluster

Figure 6.53: Distributions of kinematic-cut variables used for the three-cluster $K^{\pm}$ sample. For each distribution, all the cuts for $K^{\pm} \to \pi^{\pm}\pi^0$ signals except for the cut shown in each figure were imposed. The MC samples for $K^{\pm}$ decays were normalized with the measured $K^{\pm}$ flux. The black arrow in each figure indicates the accepted region.

where N^{obs} represents the number of events observed in the data, and the index i stands for the $K^\pm$ decay modes. Accordingly, A_i and $\mathcal{B}_i$ represent the acceptance and the branching ratio for the i-th mode, respectively. The acceptance was estimated by the MC simulation. The factor $\mu_{K_L}(= 1.3\%)$ represents the contamination of the K_L decays, which was estimated by the MC simulation and the measured K_L flux.

The $K^\pm$ flux ($F_{K^\pm} = N_{K^\pm}/\text{POT}$) was estimated to be

$$F_{K^\pm} = (1.36 \pm 0.04) \times 10^3 \,[/(2 \times 10^{14}\ \text{POT})], \tag{6.46}$$

where the uncertainty originated from the statistics of the data and the MC samples. This result subsequently derived the $K^\pm$-to-K_L flux ratio ($R_{K^\pm/K_L}$) as

$$R_{K^\pm/K_L} = \frac{F_{K^\pm}}{F_{K_L}} = (3.30 \pm 0.10) \times 10^{-5}, \tag{6.47}$$

where F_{K_L} is the result of the K_L flux measurement described in Section 6.2.1 using the data from the period-10. The result was used to normalize the number of $K^\pm$ background events generated by the MC simulation for the $K_L \to \pi^0\nu\bar{\nu}$ analysis, which will be described in Section 6.3.6.4.

6.3.6.2 Inefficiency of UCV

We evaluated the $K^\pm$ detection inefficiency of UCV using the $K^\pm$ sample. We defined the inefficiency as a ratio of the number of events with deposited energy below the threshold to the total number of $K^\pm$ events. Figure 6.54 shows the energy and timing distributions of UCV for the $K^\pm$ sample. We found that there were 8.8% of events below the energy threshold. We further made the following corrections:

- Subtraction of the contamination of the K_L decays
- Correction of the fake hits due to accidental activities

As described in the previous section, the K_L decays contaminated the $K^\pm$ sample by 1.3%. Therefore, this contribution should be subtracted. Additionally, the accidental activities in UCV can make a contribution to the energy deposition greater than the threshold even when the energy deposition by $K^\pm$'s is below the threshold. The inefficiency of UCV (w^{UCV}) was estimated as

$$w^{\text{UCV}} = \frac{f - \mu_{K_L}}{1 - \mu_{K_L}} \cdot \frac{1}{1 - L}, \tag{6.48}$$

where $f(= 8.8\%)$ is the fraction of events below the energy threshold in Figure 6.54 and $L(= 4.3\%)$ is the accidental loss of UCV. The accidental loss was evaluated under the veto conditions used for the $K^\pm \to \pi^\pm\pi^0$ selection. The resulting inefficiency was estimated to be $(7.84 \pm 0.60) \times 10^{-2}$, where the uncertainty is the statistical error.

6.3.6.3 Systematic Uncertainties

We evaluated systematic uncertainties on the $K^\pm$ flux and the inefficiency of UCV.

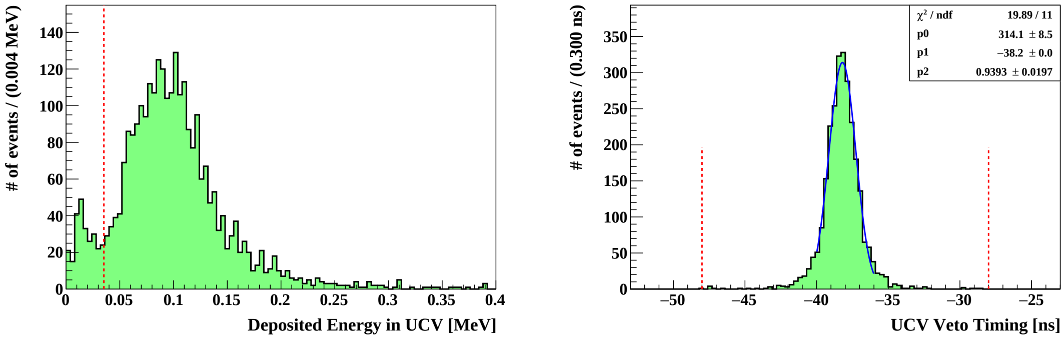

Figure 6.54: Distributions of the deposited energy (left) and the veto timing (right) of UCV for the $K^{\pm}$ data sample after applying all the selection criteria. In the left figure, the red dashed line indicates the energy threshold. In the right figure, events with the energy deposition greater than the energy threshold are shown. The two red dashed lines indicate the boundaries of the 20-ns-wide veto window. The blue curve shows the fitting by the Gaussian function with the mean (standard deviation) denoted as p1 (p2).

Uncertainties from the Contamination

First, we investigated possible unknown contamination in the $K^{\pm}$ sample. As seen in Figure 6.53a, the discrepancy between the data and MC samples in the three-cluster events implied that there was a contribution that we did not fully understand with the MC simulation. If that existed in the region around the nominal $K^{\pm}$ mass as well, it should introduce systematic uncertainties on the $K^{\pm}$ flux and the inefficiency of UCV. To evaluate such effects, we studied the $K^{\pm}$ events by using the data collected in the special run for UCV described in Section 3.2.3.2. This data-taking was conducted with the beam power of 10 kW.

Figures 6.55 and 6.56 show distributions of kinematic cuts for the data collected in the special run. In this study, we considered only the $K^{\pm}$ decays for the MC simulation. The good agreement between the data and MC samples ensured that the events were dominated by $K^{\pm}$ decays. Although the reproducibility of timing distributions seen in Figures 6.55a and 6.56d is not perfect, as also seen in the normalization-mode analysis in Section 6.2.1, this does not have an impact on the estimation of the $K^{\pm}$ flux and the inefficiency. Although the deviation seen in the tail region of the distribution in Figure 6.56f may imply possible other contributions, events in that region were not selected and thus had no impact on the $K^{\pm}$ candidate events. In the special run, the number of remaining events after applying all the $K^{\pm} \to \pi^{\pm}\pi^{0}$ selection was 21468 events with 5.70×10^{15} POT. In comparison with the $K^{\pm}$ sample collected in the physics run described in the previous sections, 275 times more $K^{\pm}$ candidate events were collected with the same amount of POT. Figure 6.56a shows the distribution of the reconstructed $K^{\pm}$ mass. The distribution was well reproduced by the contribution of the $K^{\pm}$ decays only.

Figure 6.57 shows the distribution of the deposited energy in UCV for the $K^{\pm}$ data sample collected in the special run. The fraction of the events below the energy threshold was 2.9%, which is about three times smaller than that obtained in the physics run. In the $K^{\pm} \to \pi^{\pm}\pi^{0}$ event selection described in the previous section, we did not include any requirement for UCV. To investigate the unidentified contamination, we further imposed the veto cut with UCV on the

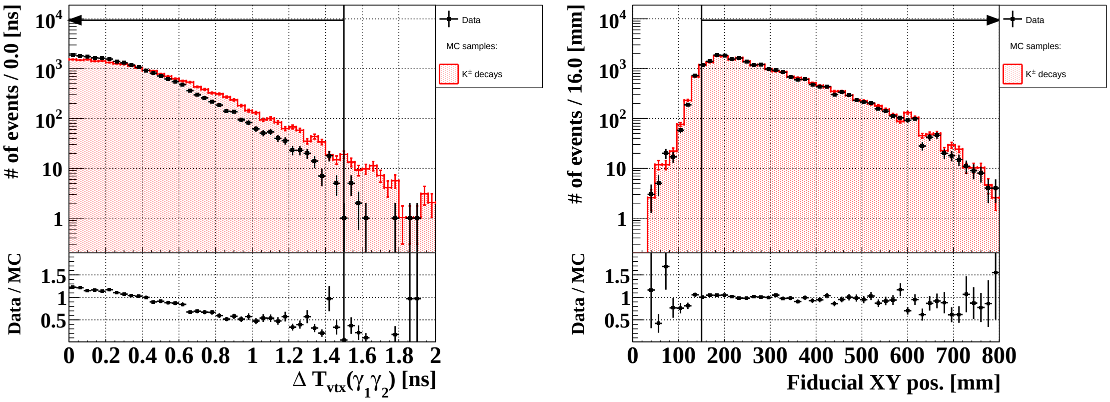

(a) Vertex timing difference (ΔT_{vtx})

(b) Hit position ($\max(|x|, |y|)$)

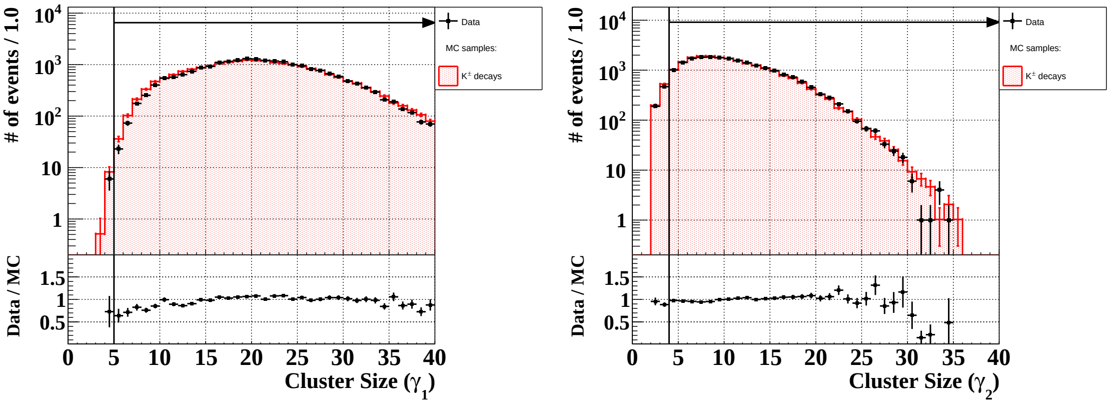

(c) Cluster size of γ_1 ($n^{\gamma_1}_{\mathrm{cryst}}$)

(d) Cluster size of γ_2 ($n^{\gamma_2}_{\mathrm{cryst}}$)

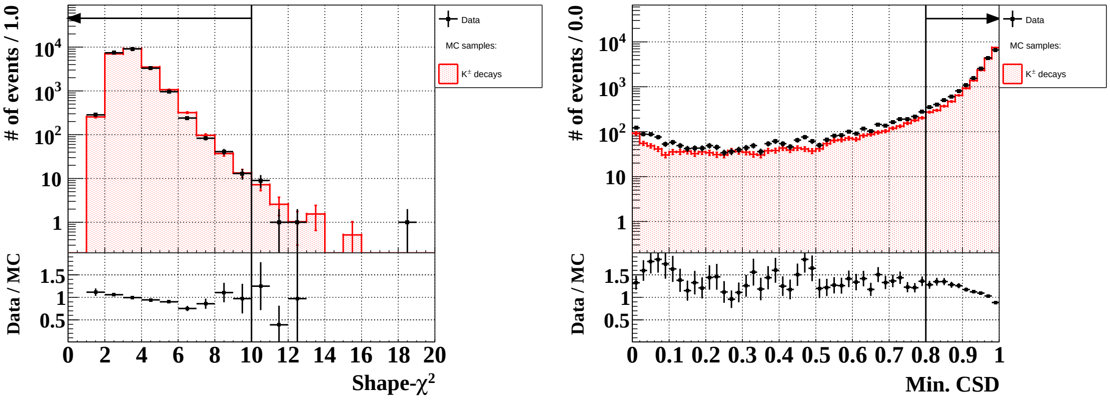

(e) χ^2_{shape}

(f) $\mathrm{CSD}_{\mathrm{NN}}$

Figure 6.55: Distributions of kinematic-cut variables used for the three-cluster $K^{\pm}$ sample collected in the special run. For each distribution, all the cuts for $K^{\pm} \to \pi^{\pm}\pi^0$ signals except for the cut shown in each figure were imposed. The red histogram shows MC simulation that contains all the $K^{\pm}$ decay modes. The black arrow in each figure indicates the accepted region.

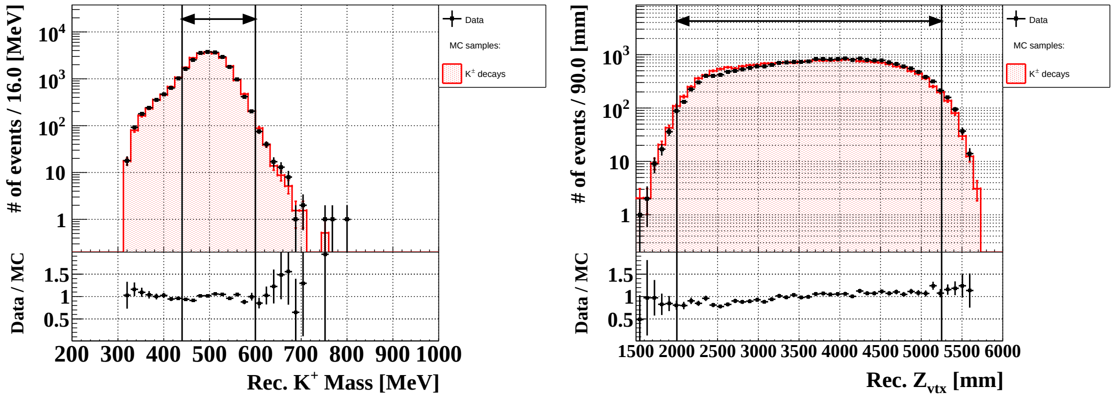

(a) Reconstructed $K^{\pm}$ mass

(b) Reconstructed Z_{vtx}

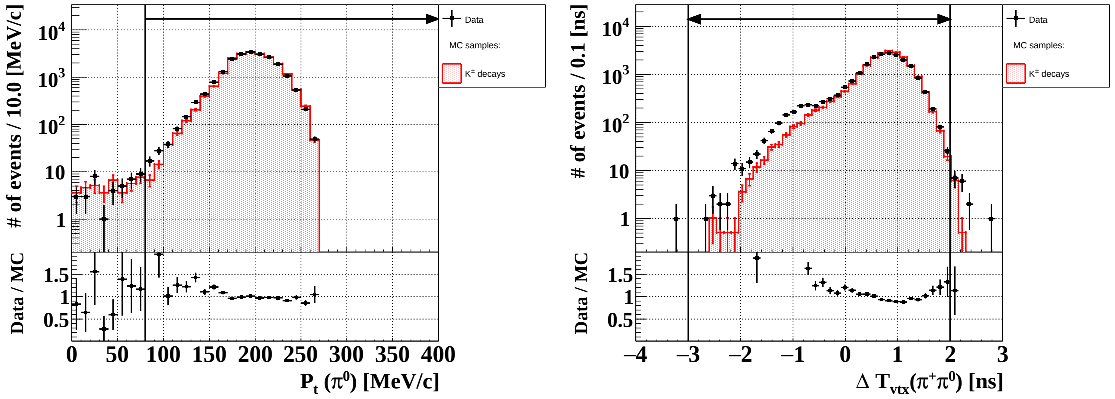

(c) Reconstructed π^0 P_t

(d) $\pi^{\pm}$-π^0 timing difference ($\delta T_{\pi^{\pm}\pi^0}$)

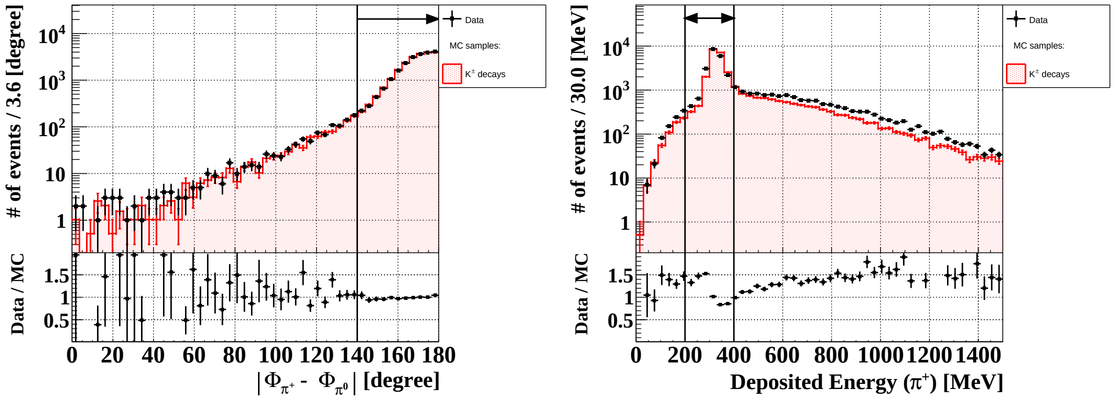

(e) $\pi^{\pm}$-π^0 angle ($\phi_{\pi^{\pm}\pi^0}$)

(f) Deposited energy of a $\pi^{\pm}$ cluster

Figure 6.56: Distributions of kinematic-cut variables used for the three-cluster $K^{\pm}$ sample collected in the special run. For each distribution, all the cuts for $K^{\pm} \rightarrow \pi^{\pm}\pi^0$ signals except for the cut shown in each figure were imposed. The red histogram shows the MC simulation that contains all the $K^{\pm}$ decay modes. The black arrow in each figure indicates the accepted region.

$K^\pm$ sample. Figure 6.58 compares the distribution of $M_{K^\pm}$ before and after imposing the veto cut with UCV. The fraction of the events below the threshold has a dependence on $M_{K^\pm}$ in the data obtained in the physics run while it is almost uniform in the data obtained in the special run. Other kinematic variables for the same comparison are available in Appendix G.4. To estimate the contamination in the data obtained in the physics run numerically, we subtracted the number of events below the threshold in the special run from that in the physics run under the assumption that all the events in the special run originated from $K^\pm$ decays. The subtraction was based on the M_{K_L} distribution. The data obtained in the special run was normalized to the data obtained in the physics run using the events around $M_{K^\pm}$ peak region. After enhancing the $K^\pm$ events by requiring the deposited energy in UCV to be greater than the energy threshold, the normalization factor was determined. Figure 6.59 shows the $M_{K^\pm}$ distributions for the data after imposing the veto cut with UCV and applying the normalization factor to the special run. After the subtraction, the residual number of events in the accepted region for $K^\pm \to \pi^\pm\pi^0$ resulted in the contamination of 6.4% for the total number of 2912 candidate events in the data obtained in the physics run[26]. Hereinafter, the contamination estimated in the above procedure is denoted as μ.

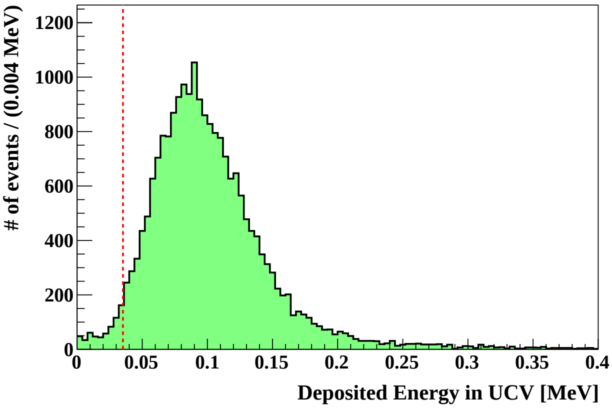

Figure 6.57: Distribution of the deposited energy in UCV for the $K^\pm$ data sample after applying all the selection criteria in the special run. The red dashed line indicates the energy threshold.

We calculated the relative deviation of the $K^\pm$ flux defined as

$$\frac{F_{K^\pm}(\mu) - F_{K^\pm}(\mu_{K_L})}{F_{K^\pm}(\mu_{K_L})}, \tag{6.49}$$

where $F_{K^\pm}(\mu_{K_L})$ and $F_{K^\pm}(\mu)$ are the $K^\pm$ flux results calculated with the contamination of μ_{K_L} and μ, respectively. Equation 6.49 resulted in the deviation of −5.3% , and we assigned it to the systematic uncertainty on the $K^\pm$ flux.

In the same way, we considered the relative deviation of the inefficiency defined as

$$\frac{w^{\mathrm{UCV}}(\mu) - w^{\mathrm{UCV}}(\mu_{K_L})}{w^{\mathrm{UCV}}(\mu_{K_L})}, \tag{6.50}$$

where $w^{\mathrm{UCV}}(\mu_{K_L})$ and $w^{\mathrm{UCV}}(\mu)$ are the inefficiency results calculated with the contamination of μ_{K_L} and μ, respectively. Equation 6.50 resulted in the deviation of −65% , and we assigned it to the systematic uncertainty on the inefficiency of UCV.

---

[26] The known K_L contamination predicted by the MC simulation was assumed to be included in this 6.4%

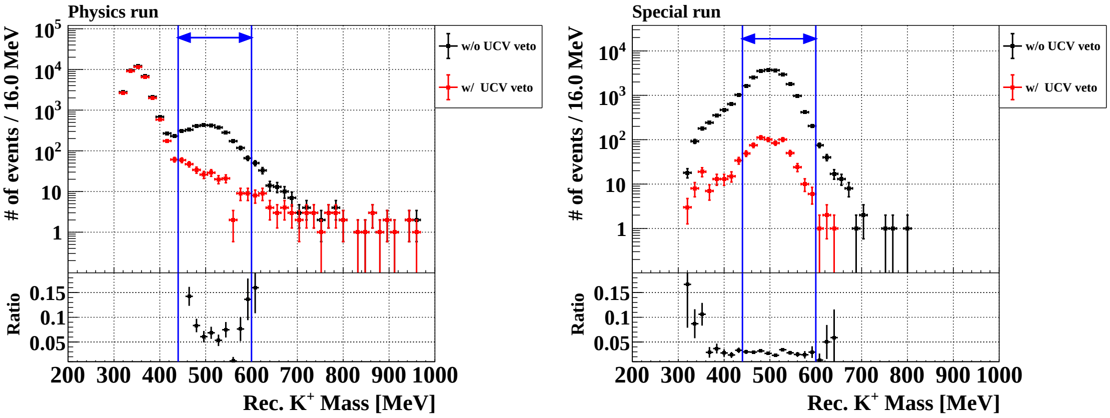

(a) Physics run

(b) Special run

Figure 6.58: Distributions of $M_{K^{\pm}}$ for the $K^{\pm}$ data sample after applying all the selection criteria except for Z_{vtx}. The black (red) histogram shows the events before (after) imposing the veto cut with UCV. The ratio shown in the bottom pad represents the red histogram divided by the black histogram, which corresponds to the fraction of the events below the energy threshold of UCV. The blue arrow in each figure indicates the accepted region for the $K^{\pm} \rightarrow \pi^{\pm}\pi^{0}$ signal.

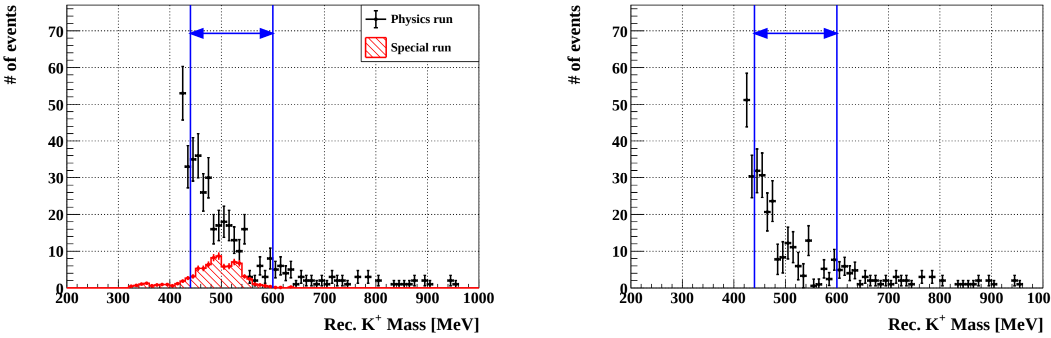

Figure 6.59: Distributions of $M_{K^{\pm}}$ for the $K^{\pm}$ data sample after applying veto cut with UCV and all the selection criteria except for Z_{vtx}. The left figure compares the distributions of the data obtained from the physics run and the special run. The large contribution in the small $M_{K^{\pm}}$ region in the physics run is outside the range of the y-axis. The right figure shows the remaining events after subtracting the contribution of the special run from that of the physics run. The blue arrow in each figure indicates the accepted region for the $K^{\pm} \rightarrow \pi^{\pm}\pi^{0}$ signal.

Uncertainties from the Cut Acceptances

Next, we investifated the consistency of the acceptance estimated with the MC simulation and the data sample. We considered the acceptances of the kinematic cuts and the downstream veto cuts used in the event selection for $K^\pm \to \pi^\pm \pi^0$. The acceptance of an i-th cut was evaluated as

$$A_i = \frac{N^{\mathrm{all}}}{N^i}, \tag{6.51}$$

where N^{all} is the number of three-cluster events after applying all the cuts and N^i is the number of three-cluster events after applying all the cuts except for the i-th cut. For the cut with the reconstructed $K^\pm$ mass, there was the large discrepancy in the small mass region between the data and MC samples, as already seen in Figure 6.53a. Since the dominant contribution in this region is the K_L decay background according to the MC simulation, the observed discrepancy does not represent the inconsistency for the $K^\pm$ signal events. To reduce the background, the reconstructed $K^\pm$ mass over 380 MeV/c^2 was required as a preselection to evaluate the acceptance. The relative deviation of the acceptance for the i-th cut was then calculated as

$$\Delta_i = \left| \frac{A_i^{\mathrm{MC}} - A_i^{\mathrm{data}}}{A_i^{\mathrm{data}}} \right|, \tag{6.52}$$

where A_i^{data} and A_i^{MC} are the acceptance of the i-th cut evaluated with the data and MC samples, respectively. By summing the deviations from the cuts in quadrature, the total deviation was estimated to be $^{+8.5}_{-8.9}$%. We assigned it to the systematic uncertainty on the $K^\pm$ flux.

Uncertainties from the Accidental Loss

The inefficiency of UCV was calculated using Equation 6.48. The statistical uncertainty on the veto efficiency of UCV was considered as a systematic uncertainty on the inefficiency. As mentioned in Section 6.3.6.2, the accidental loss of UCV was calculated under the veto conditions for the $K^\pm \to \pi^\pm \pi^0$ selection. The corresponding veto acceptance was (95.7 ± 0.1)%. The uncertainty of 0.1% was assigned to the systematic uncertainty on the inefficiency of UCV.

Summary of the $K^\pm$ Flux and Inefficiency

All the uncertainties taken into account, the $K^\pm$-to-K_L flux ratio and the inefficiency of UCV were estimated to be

$$R_{K^\pm/K_L} = \left(3.30^{+0.30}_{-0.36}\right) \times 10^{-5}, \tag{6.53}$$

$$w^{\mathrm{UCV}} = \left(7.84^{+0.60}_{-5.16}\right) \times 10^{-2}. \tag{6.54}$$

6.3.6.4 Number of $K^\pm$ Background Events

The number of $K^\pm$ background events was estimated with the MC simulation. By normalizing the number of events in the MC simulation with the $K^\pm$-to-K_L flux ratio and multiplying w^{UCV} as a reduction factor, the number of $K^\pm$ decay background events was estimated to be $0.042 \pm 0.014|_{\mathrm{stat}}{}^{+0.004}_{-0.028}|_{\mathrm{syst}}$. The systematic uncertainty originated from the sources studied in the previous section. Figure 6.60 shows the distribution of P_t versus Z_{vtx} of the $K^\pm$ MC events after imposing all the other selection criteria. In the 2021 data analysis, we reduced the number of $K^{\pm}$ background events using UCV by a factor of 13 ($\simeq 1/w^{\text{UCV}}$), and controlled the number of $K^{\pm}$ background events to be less than 0.1.

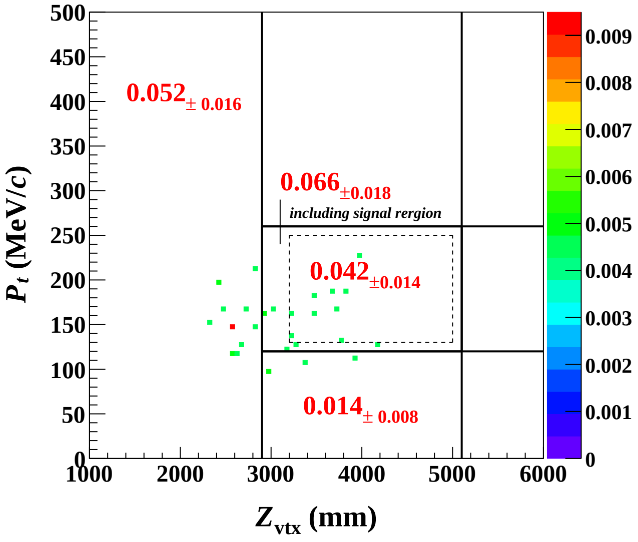

Figure 6.60: Reconstructed π^0 transverse momentum (P_t) versus π^0 decay vertex position (Z_{vtx}) for $K^{\pm}$ MC events after imposing all the other $K_L \to \pi^0 \nu \bar{\nu}$ selection criteria and the reduction factor from the inefficiency of UCV. In this figure, the error shown for each number is the statistical error.

6.4 Result of the $K_L \to \pi^0 \nu \bar{\nu}$ Search

After we determined the selection criteria for $K_L \to \pi^0 \nu \bar{\nu}$ events and estimated the expected number of background events, we unblinded the masked region. As shown in Figure 6.61, no events were observed in the signal region. To extract an upper limit on the branching ratio, we treated the observed events[27] as signals and did not consider the background contribution. Assuming the Poisson statistics with the systematic uncertainty taken into account [132], we set an upper limit on the branching ratio for $K_L \to \pi^0 \nu \bar{\nu}$ at the 90% C.L. as

$$\begin{aligned}\mathcal{B}(K_L \to \pi^0 \nu \bar{\nu}) &< 2.30 \times \left[1 + \frac{1 - \sqrt{1 - 2.30^2 \times \sigma_{SES}^2}}{2.30} \right] \times SES \\ &= 2.2 \times 10^{-9},\end{aligned} \tag{6.55}$$

where $\sigma_{SES}(= 9.0\%)$ is the total relative uncertainty on SES from Equation 6.41. This result has improved the previous limit [65] obtained from the 2015 data in KOTO by a factor of 1.4, and is the most stringent upper limit at present. A case with the background contribution included is discussed in Section 7.3.

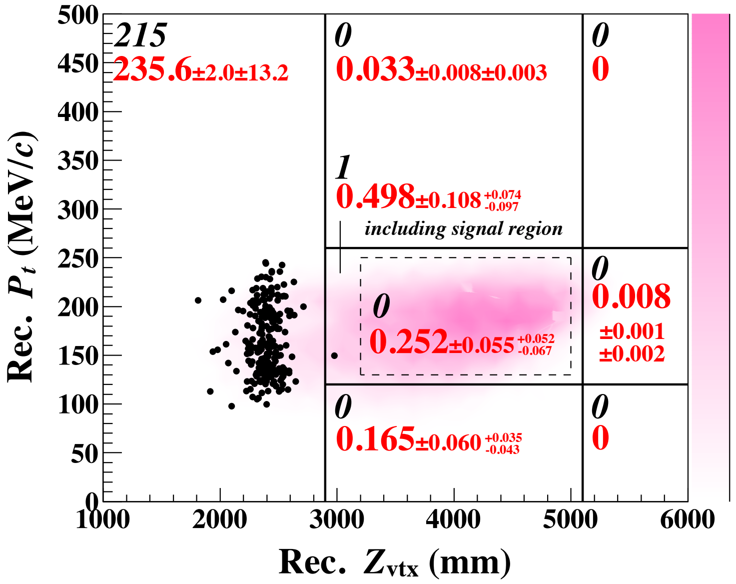

Figure 6.61: Reconstructed π^0 transverse momentum (P_t) versus π^0 decay vertex position (Z_{vtx}) for events after imposing the $K_L \to \pi^0 \nu \bar{\nu}$ selection criteria in the 2021 data analysis. The region surrounded by dashed lines is the signal region. The black dots represent observed events, and the shaded contour indicates the $K_L \to \pi^0 \nu \bar{\nu}$ distribution from the MC simulation. The black italic (red regular) numbers indicate the number of observed (background) events for different regions. The figure is quoted from Ref. [65].

---

[27] Null events in this case.

6.5 Analysis of the $K_L \to \pi^0 X^0$ Search

This section describes the analysis of the $K_L \to \pi^0 X^0$ search with the same dataset used for the $K_L \to \pi^0 \nu\bar{\nu}$ search.

6.5.1 Signal Acceptance and Single Event Sensitivity

We assumed that X^0 is an invisible boson which does not decay. We considered the X^0 mass (m_{X^0}) at various points from 1 MeV/c^2 to 260 MeV/c^2. By simulating $K_L \to \pi^0 X^0$ decays, we estimated the signal acceptance for each m_{X^0} assumption. Figure 6.62 shows the signal acceptance of $K_L \to \pi^0 X^0$ as a function of m_{X^0}. Since the larger X^0 mass restricts the reconstructed π^0 P_t, the signal acceptance for the heavy X^0 is relatively lower. Figure 6.63 shows the distributions of P_t versus Z_{vtx} for $m_{X^0} = 135$ MeV/c^2 and $m_{X^0} = 260$ MeV/c^2.

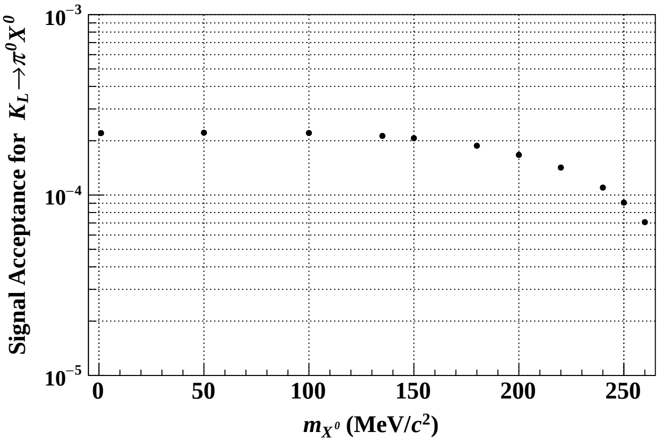

Figure 6.62: Signal acceptance for $K_L \to \pi^0 X^0$ decays with the various m_{X^0} assumptions.

6.5.2 Results

The SES of the $K_L \to \pi^0 X^0$ search was calculated for various m_{X^0}. The systematic uncertainty on SES was assumed to be the same value obtained in the $K_L \to \pi^0 \nu\bar{\nu}$ search. Figure 6.64 shows SES and the obtained upper limits on the branching ratio for $K_L \to \pi^0 X^0$. For X^0 with its mass of the π^0 mass $\simeq$ 135 MeV/c^2, we obtained the upper limit on the branching ratio as

$$\mathcal{B}(K_L \to \pi^0 X^0) < 1.6 \times 10^{-9} \quad (90\% \text{ C.L.}). \tag{6.56}$$

The previous best limit obtained by the KOTO experiment using the data collected in 2015 was 2.4×10^{-9} at the 90% C.L. for the same X^0 mass [50].

As described in Section 1.2.4, the upper limit on the branching ratio for $K^+ \to \pi^+ X^0$ was set by NA62 around the π^0 mass region. The upper limit is about 1.0×10^{-9} at the 90% C.L., which is read from Figure 1.9. Thus, an indirect limit on $\mathcal{B}(K_L \to \pi^0 X^0)$ from the Grossman-Nir bound

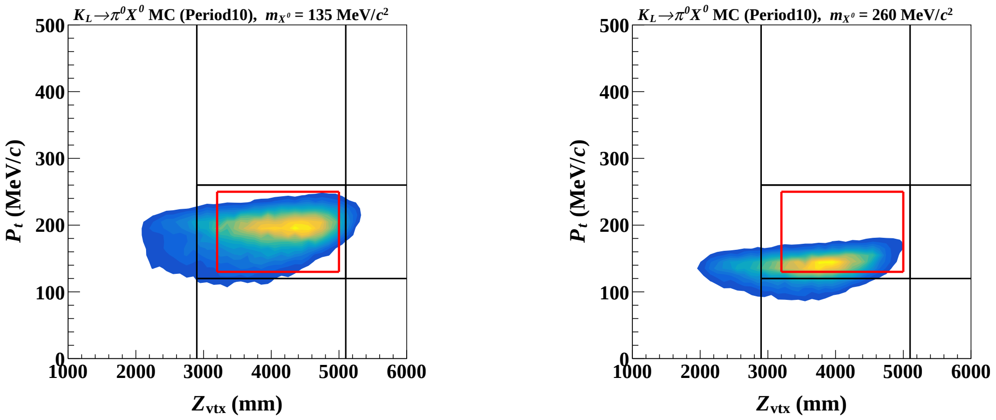

(a) m_{X^0} = 135 MeV/c^2

(b) m_{X^0} = 260 MeV/c^2

Figure 6.63: Reconstructed π^0 transverse momentum (P_t) versus π^0 decay vertex position ($Z_{\rm vtx}$) for $K_L \to \pi^0 X^0$ MC events after imposing all the other $K_L \to \pi^0 X^0$ selection criteria. The red line shows the signal region. Since the signal region was optimized for $K_L \to \pi^0\nu\bar{\nu}$ decays, the signal acceptance of $K_L \to \pi^0 X^0$ depends on the mass of X^0.

is around 4.3×10^{-9}, which is still larger than the limit obtained in Equation 6.56. The result obtained in this analysis has therefore improved the previous best limit by a factor of 1.4.

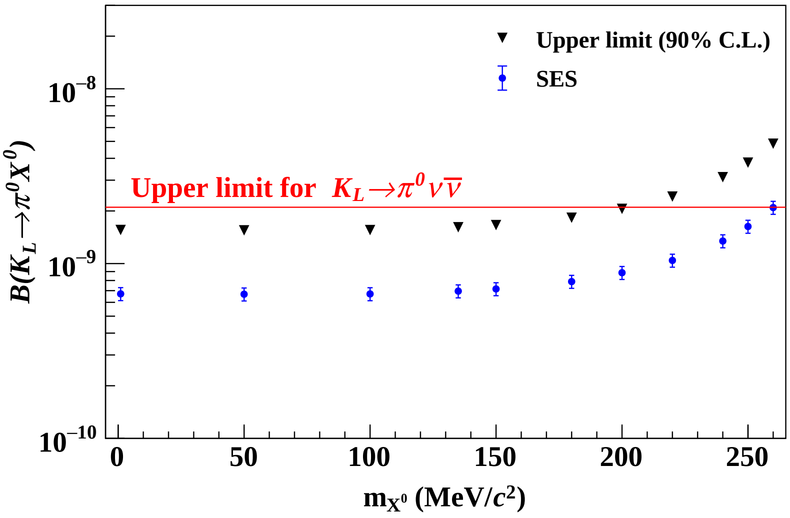

Figure 6.64: *SES* and the upper limits at 90% C.L. on the branching ratio for $K_L \to \pi^0 X^0$. The red line indicates the upper limit on $\mathcal{B}(K_L \to \pi^0 \nu \bar{\nu})$ obtained in Section 6.4.

Chapter 7

Discussion

7.1 Interpretation of the Results

The background evaluation in the 2021 data analysis explains the number of observed events with the higher probability compared to the previous results. In the 2021 data analysis, the probability of observing no events with the estimated number of background events is 78% according to the Poisson statistics. In the case of the 2016–2018 data analysis, the probability of observing three events or more with the estimated number of background events of 1.22 ± 0.26 was 13% [61].

Figure 7.1 shows the current constraints on $\mathcal{B}(K_L \to \pi^0 \nu \bar{\nu})$ and $\mathcal{B}(K^+ \to \pi^+ \nu \bar{\nu})$. The new upper limit obtained by this work is still above the current Grossman-Nir bound calculated from the latest measurement of $\mathcal{B}(K^+ \to \pi^+ \nu \bar{\nu})$ by the NA62 experiment. As described in Section 1.2.3, some NP models consider the deviation of $\mathcal{B}(K_L \to \pi^0 \nu \bar{\nu})$ from the SM prediction even if it is higher than the Grossman-Nir bound. Although such models were not excluded yet, the region allowed for $\mathcal{B}(K_L \to \pi^0 \nu \bar{\nu})$ was constrained up to 2.2×10^{-9} at the 90% C.L. by the result of this work.

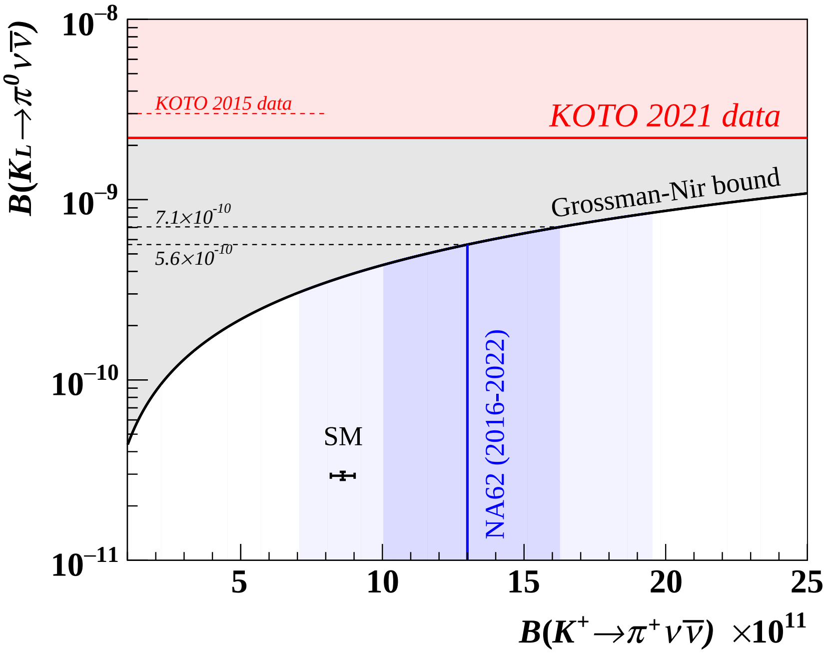

Figure 7.1: Global status of the current constraints on $\mathcal{B}(K^+ \to \pi^+\nu\bar{\nu})$ and $\mathcal{B}(K^+ \to \pi^+\nu\bar{\nu})$. The red region was excluded at the 90% C.L. by this work. The red dashed line indicates the previous upper limit on $\mathcal{B}(K_L \to \pi^0\nu\bar{\nu})$ obtained by the KOTO experiment using the 2015 data [50]. The blue region shows the latest measurement of $\mathcal{B}(K^+ \to \pi^+\nu\bar{\nu})$ by the NA62 experiment [17]. The blue line is the central value of the measurement and the dark blue (light blue) region is the 1σ (2σ) range. The black point is the SM prediction quoted from Ref. [10]. The black line corresponds to the Grossman-Nir bound.

7.2 Comparison with the 2016–2018 Data Analysis

In this section, the difference between the 2021 data analysis and the 2016–2018 data analysis is discussed.

7.2.1 Single Event Sensitivity

As already described, the SES value obtained in the 2021 data analysis was larger than that in the 2016–2018 data analysis. Table 7.1 shows the comparison of the accumulated number of POT, K_L yield, K_L flux, signal acceptance, and single event sensitivity. In 2021, we accumulated about 7% more amount of POT than that in 2016–2018. The K_L yield is almost the same between the two datasets since the K_L flux was reduced by about 10%. This is due to the difference of the T1 target replaced in 2019. As described in Section 2.3, the new T1 target has a 0.3-mm gap at the center to allow for the thermal expansion, which led to the reduction of the flux. The difference in the signal acceptance is 20%, and it caused the difference in the SES.

Table 7.2 and Figure 7.2 show the comparison of the signal acceptance at each cut stage. For the 2016–2018 data analysis, the signal acceptance for the RUN79 period with the beam power

Table 7.1: Comparison of the single event sensitivity and other quantities between the 2016–2018 data analysis [105] and the 2021 analysis.

	2016–2018 data	2021 data
POT	3.05×10^{19}	3.26×10^{19}
K_L yield	6.83×10^{12}	6.76×10^{12}
K_L flux	$4.54 \times 10^{7}/(2 \times 10^{14}$ POT)	$4.14 \times 10^{7}/(2 \times 10^{14}$ POT)
Signal acceptance	2.0×10^{-4}	1.6×10^{-4}
SES	7.20×10^{-10}	9.31×10^{-10}

Table 7.2: Comparison of the signal acceptance between the 2016–2018 data analysis [105] and the 2021 data analysis. The signal acceptance shown in the table corresponds to the acceptance after adding the cuts in each category.

	2016–2018 data (RUN79, 51 kW)	2021 data (RUN87, 64 kW)
Decay probability	3.34×10^{-2}	3.34×10^{-2}
Two-cluster selection	9.11×10^{-3}	9.09×10^{-3}
Trigger-related cuts	5.83×10^{-3}	5.19×10^{-3}
Photon selection cuts	4.58×10^{-3}	4.13×10^{-3}
Kinematic cuts	2.13×10^{-3}	1.83×10^{-3}
Veto cuts	3.83×10^{-4}	2.87×10^{-4}
Shape-related cuts	1.90×10^{-4}	1.51×10^{-4}
ΔT_{CSI} cut	–	1.49×10^{-4}

of 51 kW was used [105][1], and for the 2021 data analysis, the signal acceptance for the period-10, RUN87 with the beam power of 64 kW, was used. In the 2016–2018 data-taking, the COE radius cut was used as a part of the event selection at the trigger stage. The COE radius cut was thus included in the category of the trigger-related cut for this comparison[2]. The signal acceptance loss mainly due to the incorrect cabling described in Section 6.2.2.3 was also included in the category of the trigger-related cut, which caused about 10% difference in the signal acceptance.

The kinematic cuts, veto cuts, and shape-related cuts also caused the difference in the signal acceptance. We added the beam-halo $K_L \to 2\gamma$ cut and the $K_L \to \pi^0\pi^0$ NN cut to the kinematic cuts in the 2021 data analysis, which resulted in about 5% difference. At the veto cut stage, another loss of 13% exists. The difference of the acceptance in the veto cuts was affected by the beam power, the beam-spill structure, and the additional veto cuts. For the shape-related cut, the selection criteria on the CSD-had cut and the PSD cuts were loosened to recover the signal acceptance. This change contributed to the increase in the signal acceptance by 6%.

---

[1] The values are quoted from Ref. [105] and from errata shared internally.

[2] The COE radius cut is included in the category of the kinematic cuts in Figure 6.26 and in Table 6.6

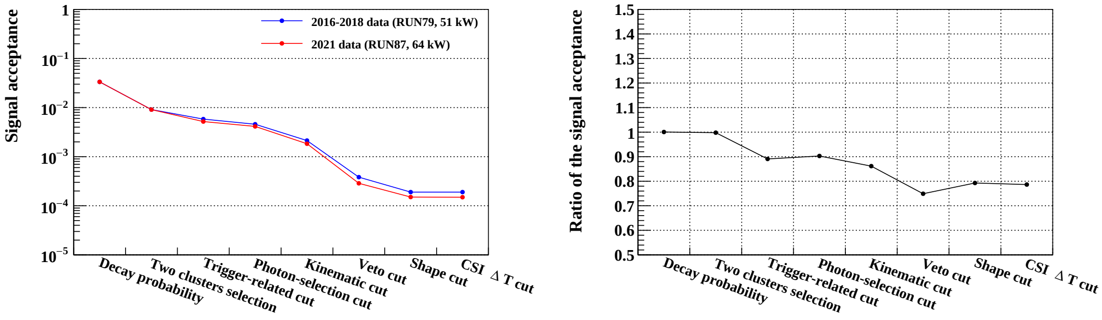

Figure 7.2: Comparison of the signal acceptance change at each cut stage. In the left figure, the blue (red) line shows the signal acceptance in the 2016–2018 (2021) data analysis. In the right figure, the ratio of the signal acceptance at each cut stage in the 2021 data analysis to that in the 2016–2018 data analysis is shown.

Table 7.3: Comparison of the background level between the 2016–2018 and 2021 datasets.

	2016–2018 data	2021 data
$K^{\pm}$	$(6.3 \pm 1.9) \times 10^{-10}$	$(3.9^{+1.4}_{-2.9}) \times 10^{-11}$
$K_L \to 2\gamma$ (beam-halo)	$(1.9 \pm 5.3) \times 10^{-10}$	$(4.2 \pm 1.1) \times 10^{-11}$
$K_L \to \pi^0\pi^0$	$< 5.8 \times 10^{-11}$[a]	$(5.5^{+5.1}_{-5.9}) \times 10^{-11}$
Hadron-cluster	$(1.2 \pm 0.2) \times 10^{-11}$	$(2.2 \pm 0.7) \times 10^{-11}$
CV-η	$(2.2 \pm 0.7) \times 10^{-11}$	$(2.1 \pm 1.1) \times 10^{-11}$
Upstream-π^0	$(2.2 \pm 2.2) \times 10^{-11}$	$(5.6 \pm 4.4) \times 10^{-11}$
Total	$(8.8 \pm 2.0) \times 1.0^{-10}$	$(2.3^{+0.7}_{-0.8}) \times 10^{-10}$

[a] Upper limit at the 90% C.L.

7.2.2 Background Level

For the background contribution in the two analyses, we considered a background level (BGL) defined as the number of expected background events in the signal region multiplied by SES[3]. Table 7.3 shows the BGL for each source. The BGL of the $K^{\pm}$ background and the beam-halo $K_L \to 2\gamma$ background was reduced thanks to UCV and the cuts with the beam-halo $K_L \to 2\gamma$ LR and FD methods. The beam-halo $K_L \to 2\gamma$ background includes the effect of the scattering at UCV, which increased the beam-halo K_L flux by a factor of about 2. The increase in the BGL of the hadron-cluster background was due to the effect of the scattering at UCV and the different selection criteria for the neutron cuts. We introduced the ΔT_{CSI} cut to improve the background rejection power, but loosened the thresholds of the CSD-had cut and the PSD cut after optimization. As a result, the BGL of the total background contribution was reduced by a factor of 4 compared to the 2016–2018 data analysis.

---

[3] The signal (S) to background (B) ratio can be therefore expressed as $S/B = (\mathcal{B}(K_L \to \pi^0\nu\bar{\nu})/SES)/N_{\mathrm{BG}} = \mathcal{B}(K_L \to \pi^0\nu\bar{\nu})/\mathrm{BGL}$, where N_{BG} is the expected number of background events.

7.3 Impact of the Background Reduction on the Upper Limit

As described in Section 6.4, we did not consider the background contribution to extract the upper limit on the branching ratio for $K_L \to \pi^0 \nu \bar{\nu}$. In this section, we discuss the upper limit by considering the background and the impact of suppressing background events, particularly, the $K^{\pm}$ background.

According to Ref. [133], a method to construct a certain range of confidence interval based on likelihood ratios was proposed. Hereinafter, this method is referred to as the Feldman-Cousins (F-C) method. Table 7.4 shows the upper limit obtained in Section 6.4 without considering the background contribution and the upper limit obtained by the Feldman-Cousins method with the expected number of background events of 0.252. The uncertainty on the background estimate is not included in the following discussion. The upper limit obtained by the F-C method is smaller than the one obtained in Section 6.4 by 10%. This difference comes from the fact that the observed zero events were explained by both the signal and the background contributions. The background contribution was therefore subtracted to obtain the upper limit on the signal events.

Table 7.4: Upper limit on the branching ratio for $K_L \to \pi^0 \nu \bar{\nu}$. The Poisson limit shown in the first row corresponds to the result obtained in Section 6.4. The F-C limit shown in the second row corresponds to the limit obtained by the F-C method with the background contribution of 0.252 events taken into account.

	Upper limit at the 90% C.L.
Poisson limit	2.2×10^{-9}
F-C limit with the background	2.0×10^{-9}

Next, we consider a case where the $K^{\pm}$ background was not suppressed by UCV in order to discuss the impact of the background reduction. If excluding the veto cut with UCV from the $K_L \to \pi^0 \nu \bar{\nu}$ event selection, the expected number of $K^{\pm}$ background events was 0.56 ± 0.19, where the uncertainty represents only the statistical error. The absence of the UCV veto cut can increase the other background events since the accidental loss of UCV does not come into effect. The effect, however, is only 4% according to the estimation described in Section 6.2.2.1. Therefore, we only consider the increase in the $K^{\pm}$ background events. Under this assumption, the total expected number of background events rises up to 0.77. The single event sensitivity without applying UCV veto cut is $(8.96 \pm 0.06) \times 10^{-10}$.

For the future sensitivity, we consider $SES = 1.0 \times 10^{-10}$, which is a benchmark sensitivity in KOTO experiment[4]. For the background contribution, we consider the following two cases:

(A) $SES = 1.0 \times 10^{-10}$ with the reduction of the $K^{\pm}$ background by UCV

(B) $SES = 1.0 \times 10^{-10}$ without the reduction of the $K^{\pm}$ background by UCV

In the case A, the expected number of background events can be estimated by scaling the result of the 2021 data analysis as $0.252 \times (9.31 \times 10^{-10})/(1.0 \times 10^{-10}) = 2.3$. In the same way, the expected

---

[4] At this sensitivity, the SM signal contribution is still about 0.3 events, and not included in the calculation of the probability in the following discussion.

number of background events in the case B can be estimated as $0.77\times(8.96\times10^{-10})/(1.0\times10^{-10}) = 6.9$.

Tables 7.5 and 7.6 show the estimated upper limits for the numbers of observed events (N_{obs}) from 0 to 10. Based on the probability and the corresponding upper limit for each N_{obs}, one can calculate the expected value of the upper limit. For the Poisson limit and the F-C limit with the background contribution considered, we denote the expected values as $\overline{UL}^{\mathrm{A}}_{\mathrm{Poi}}$ and $\overline{UL}^{\mathrm{A}}_{\mathrm{FC}}$, respectively. We then obtained

$$\overline{UL}^{\mathrm{A}}_{\mathrm{Poi}} = 5.7\times10^{-10}, \tag{7.1}$$

$$\overline{UL}^{\mathrm{A}}_{\mathrm{FC}} = 4.1\times10^{-10}. \tag{7.2}$$

In the same way, we estimated the expected values, $\overline{UL}^{\mathrm{B}}_{\mathrm{Poi}}$ and $\overline{UL}^{\mathrm{B}}_{\mathrm{FC}}$, for the case B, as

$$\overline{UL}^{\mathrm{B}}_{\mathrm{Poi}} = 1.2\times10^{-9}, \tag{7.3}$$

$$\overline{UL}^{\mathrm{B}}_{\mathrm{FC}} = 5.8\times10^{-10}. \tag{7.4}$$

The background subtraction considered in the F-C limit gives the 30% (50%) smaller expected value of the upper limit at the 90% C.L. for the case A (B). In addition, if comparing the case A and B, we estimated the 50% (30%) smaller expected value of the Poisson limit (F-C limit). From these comparisons, it is suggested that the background subtraction becomes more crucial at this level of sensitivity. Moreover, the reduction of the $K^{\pm}$ background also has a significant impact on the obtained upper limit even with the background subtraction.

Table 7.5: Upper limits at the 90% C.L. depending on the number of observed events (N_{obs}) from 0 to 10 in the case A. The upper limit shown in the rightmost column considers 2.3 events as the background contribution. The probability was calculated as the Poisson probability of observing N_{obs} events with the 2.3 events expected.

N_{obs}	Probability	Poisson limit	F-C limit with the background
0	9.6%	2.3×10^{-10}	9.2×10^{-11}
1	22.5%	3.9×10^{-10}	2.3×10^{-10}
2	26.3%	5.3×10^{-10}	3.6×10^{-10}
3	20.1%	6.7×10^{-10}	5.1×10^{-10}
4	12.1%	8.0×10^{-10}	6.3×10^{-10}
5	5.7%	9.3×10^{-10}	7.6×10^{-10}
6	2.2%	1.1×10^{-9}	9.1×10^{-10}
7	0.7%	1.2×10^{-9}	1.0×10^{-9}
8	0.2%	1.3×10^{-9}	1.2×10^{-9}
9	0.6%	1.4×10^{-9}	1.3×10^{-9}
10	0.1%	1.5×10^{-9}	1.4×10^{-9}

Table 7.6: Upper limits at the 90% C.L. depending on the number of observed events ($N_{\rm obs}$) from 0 to 10 in the case B. The upper limit shown in the rightmost column considers 6.9 events as the background contribution. The probability was calculated as the Poisson probability of observing $N_{\rm obs}$ events with the 6.9 events expected.

$N_{\rm obs}$	Probability	Poisson limit	F-C limit with the background
0	0.1%	2.3×10^{-10}	6.7×10^{-11}
1	0.7%	3.9×10^{-10}	7.4×10^{-11}
2	2.4%	5.3×10^{-10}	1.1×10^{-10}
3	5.4%	6.7×10^{-10}	1.6×10^{-10}
4	9.4%	8.0×10^{-10}	2.2×10^{-10}
5	13.0%	9.3×10^{-10}	3.3×10^{-10}
6	15.1%	1.1×10^{-9}	4.6×10^{-10}
7	14.9%	1.2×10^{-9}	5.6×10^{-10}
8	12.9%	1.3×10^{-9}	7.1×10^{-10}
9	9.9%	1.4×10^{-9}	8.4×10^{-10}
10	6.9%	1.5×10^{-9}	9.6×10^{-10}

7.4 Prospect

7.4.1 Background Reduction and Evaluation

Figure 7.3 shows the summary of the background estimations in the 2021 data analysis. The expected number of signal events predicted in the SM is also shown in the same figure. The largest and the second largest background sources are the upstream-π^0 and the $K_L \to \pi^0\pi^0$ decay, which also have the large statistical and systematic uncertainties, respectively. The single event sensitivity achieved in the 2021 analysis is approximately 30 times above the SM sensitivity ($\simeq 3 \times 10^{-11}$). This implies that the number of expected background events at the SM sensitivity would be around 7.8 events if simply extrapolating from the results of this work[5]. In order to further reduce and accurately estimate the background events, the following measures have been taken.

- $K^\pm$ background
  - A new upstream charged veto detector to reduce the $K^\pm$ background events was developed using a 0.2 mm-thick scintillator film and 12 μm-thick aluminized mylar films [134]. As shown in Figure 7.4, we aim to collect photons that are not trapped inside the scintillator film. This is because the light yield from the scintillation photons propagating inside the scintillator is highly reduced due to reflections in the thin film. In order to improve the radiation tolerance, we used PMTs for the light collection. The detector is equipped with its dedicated trigger counters so that we can calibrate the detector and measure the inefficiency using them. After we uninstalled UCV used in the 2021 data analysis, this "new UCV" was installed in the spring of 2023. The new UCV was first operated with beam in the summer of 2023. Figure 7.5 shows the performance

---

[5] $0.252 \times 9.31 \times 10^{-10}/(3 \times 10^{-11}) \simeq 7.8$

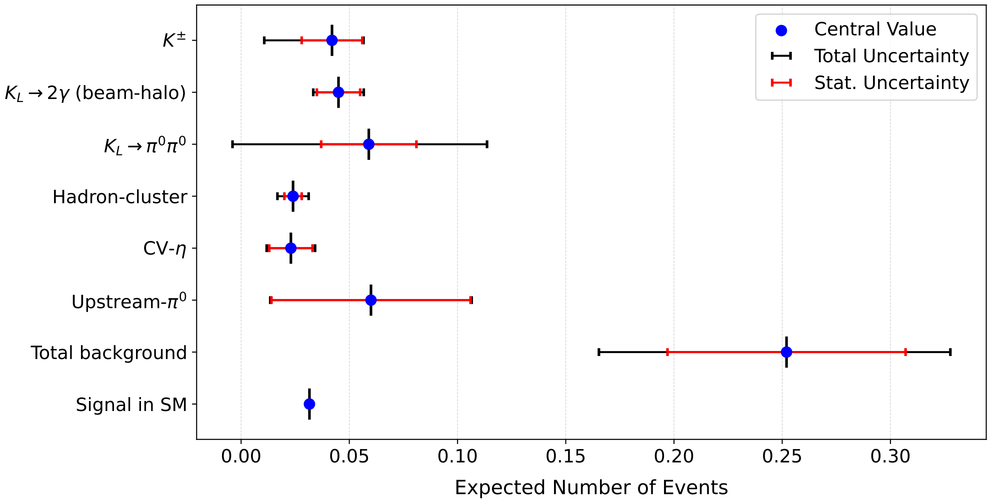

Figure 7.3: Expected numbers of background events and the signal events predicted in the SM at the single event sensitivity in the 2021 data analysis. The red (black) error bar shows the statistical uncertainty (quadratic sum of statistical and systematic uncertainties) on the estimated number of background events. The label “Total background” represents the sum of all the numbers of background events. The label “Signal in SM” represents the number of SM signals calculated as $\mathcal{B}(K_L \to \pi^0\nu\bar{\nu})_{\mathrm{SM}}/SES$, where SES is the single event sensitivity achieved in the 2021 data analysis and $\mathcal{B}(K_L \to \pi^0\nu\bar{\nu})_{\mathrm{SM}}$ is the SM prediction of the branching ratio for $K_L \to \pi^0\nu\bar{\nu}$.

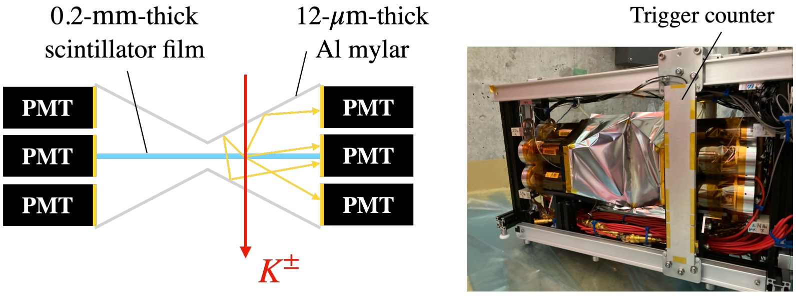

Figure 7.4: New detector to suppress the $K^{\pm}$ background events. The detector was developed with a 0.2 mm-thick scintillator film and 12 μm-thick aluminized mylar films. The left figure shows the schematic top view of the detector. The right picture shows the entire view of the detector with a trigger counter.

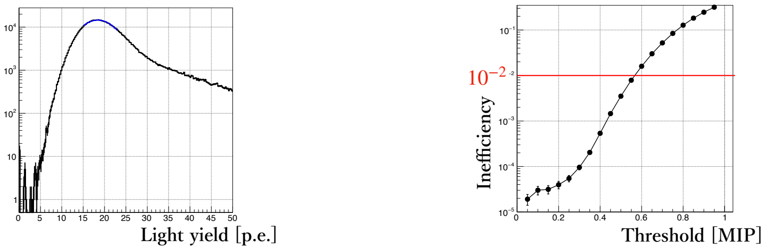

Figure 7.5: Performance of the new detector. The left figure shows the light output of the detector. The photoelectron yield corresponding to the MIP peak was estimated to be 18.5 p.e. based on the data collected in the plug-closed run. The right figure shows the inefficiency as a function of the detection threshold. The figures are quoted from Ref. [134].

of the detector using data collected at J-PARC in 2024. The inefficiency of 5×10^{-4} was estimated to be 5×10^{-4}, which gives a reduction factor of over 10^3. The smaller material thickness also mitigates the enhancement of the background events induced from beam-halo particles, such as the hadron-cluster background and the beam-halo $K_L \to 2\gamma$ background.

- A more straightforward way to eliminate the $K^{\pm}$ background is put a magnet at the downstream side of the collimator so that charged particles can be swept away before they enter the KOTO detector. We thus installed a permanent magnet at the downstream end of the second collimator[6]. The magnet has a length of 540 mm along the beam axis and has the maximum field strength of 0.9 T. The magnet is expected to reduce the $K^{\pm}$ background events by an order of magnitude.

- $K_L \to \pi^0\pi^0$ background
  - The $K_L \to \pi^0\pi^0$ decay was estimated to be the second largest background background source in the 2021 data analysis. We suffered from the lack of statistics of the 5γ control sample to evaluate the photon veto inefficiency. After the data-taking in 2021,

---

[6] This was not realized before the data-taking in 2021 since it required optimization of the geometry and the strength of the magnetic field in advance. It also took a time to prepare the magnet.

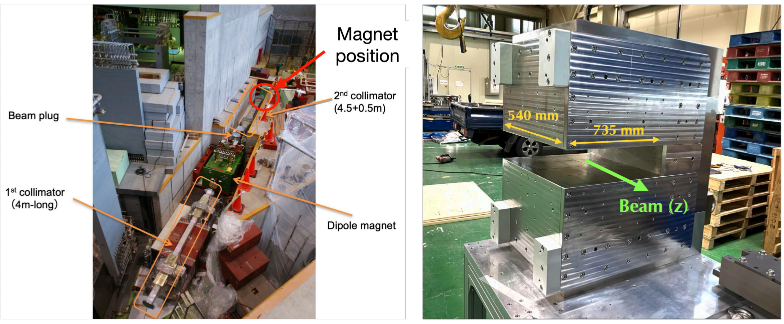

Figure 7.6: Photographs of the second magnet. The left picture shows the location of the second magnet. The top part of the picture corresponds to the downstream side of the beam line. The right picture shows the entire view of the second magnet.

we introduced a new trigger system dedicated to the collection of a 5γ sample. The upgraded DAQ system allowed for the faster accumulation of the control sample [136, 137].

Chapter 8

Conclusions

This thesis reported the search for the $K_L \to \pi^0 \nu \bar{\nu}$ decay at the J-PARC KOTO experiment using the data collected in 2021. After we found the two major background events from the $K^\pm$ decay and the beam-halo $K_L \to 2\gamma$ decay, we installed a charged-particle detector, UCV, to reject the $K^\pm$ background and developed new analysis methods to suppress the beam-halo $K_L \to 2\gamma$ background. With a single event sensitivity of $(9.31 \pm 0.06_{\mathrm{stat}} \pm 0.83_{\mathrm{syst}}) \times 10^{-10}$, we estimated the total number of backgroud events to be $0.252 \pm 0.055|_{\mathrm{stat}}{}^{+0.052}_{-0.067}|_{\mathrm{syst}}$.

Including the upgrades of the other detectors and the improvements in analysis methods, we observed no events in the signal region, and obtained the best upper limit on the branching ratio for the $K_L \to \pi^0 \nu \bar{\nu}$ decay as

$$\mathcal{B}(K_L \to \pi^0 \nu \bar{\nu}) < 2.2 \times 10^{-9} \quad (90\%\ \mathrm{C.L.}). \tag{8.1}$$

This result improved the previous upper limit by a factor of 1.4. Additionally, the search for the $K_L \to \pi^0 X^0$ decay with various X^0 mass assumptions was performed. For the X^0 mass of $135\,\mathrm{MeV}/c^2$, we obtained the best upper limit as

$$\mathcal{B}(K_L \to \pi^0 X^0) < 1.6 \times 10^{-9} \quad (90\%\ \mathrm{C.L.}), \tag{8.2}$$

which also improved the previous limit by a factor of 1.4. These upper limits further constrained the allowed region for branching ratios of $K_L \to \pi^0 \nu \bar{\nu}$ and $K_L \to \pi^0 X^0$ predicted in NP models.

In this study, the author made a main contribution to the development, installation, and performance evaluation of UCV. The author evaluated the $K^\pm$ background and suppressed the number of expected events by a factor of 13 using UCV. The evaluation of the single event sensitivity and the systematic uncertainties were performed by the author with other collaborators. The background level in this analysis was reduced by a factor of 4 compared to the previous analysis of the 2016–2018 data.

Appendices

A Uncertainties on $\mathcal{B}(K_L \to \pi^0 \nu \bar{\nu})$ in the SM

The uncertainties on $\mathcal{B}(K^+ \to \pi^+ \nu \bar{\nu})$ and $\mathcal{B}(K_L \to \pi^0 \nu \bar{\nu})$ in the SM prediction are summarized in Refs.[13, 12]. The branching ratios can be formalized as

$$\mathcal{B}(K^+ \to \pi^+ \nu \bar{\nu}) = \kappa_+ (1 + \Delta_{\mathrm{EM}}) \cdot \left[\left(\frac{\mathrm{Im}\lambda_t}{\lambda^5} X(x_t) \right)^2 + \left(\frac{\mathrm{Re}\lambda_c}{\lambda} P_c(X) + \frac{\mathrm{Re}\lambda_t}{\lambda^5} X(x_t) \right)^2 \right], \tag{A.1}$$

$$\mathcal{B}(K_L \to \pi^0 \nu \bar{\nu}) = \kappa_L \cdot \left(\frac{\mathrm{Im}\lambda_t}{\lambda^5} X(x_t) \right)^2, \tag{A.2}$$

$$\tag{A.3}$$

where $x_t = m_t^2/M_W^2$, $\lambda = |V_{us}|$, $\lambda_i = V_{is}^* V_{id}$. κ_+ and κ_L summarize the remaining factors for $\mathcal{B}(K^+ \to \pi^+ \nu \bar{\nu})$ and $\mathcal{B}(K_L \to \pi^0 \nu \bar{\nu})$, respectively. Δ_{EM} is the electromagnetic radiative correction from photon exchanges. $X(m_t)$ and $P_c(X)$ are the loop functions for the top and charm quark contributions. The remaining factors such as the relevant hadronic matrix elements are summarized in κ_+ and κ_L, which are given as

$$\kappa_+ = (5.173 \pm 0.025) \cdot 10^{-11} \left[\frac{\lambda}{0.225} \right]^8, \tag{A.4}$$

$$\kappa_L = (2.231 \pm 0.013) \cdot 10^{-10} \left[\frac{\lambda}{0.225} \right]^8. \tag{A.5}$$

Figure A.1 shows the error budgets of the prediction of $\mathcal{B}(K^+ \to \pi^+ \nu \bar{\nu})$ and $\mathcal{B}(K_L \to \pi^0 \nu \bar{\nu})$ in the SM. The main source of the uncertainty in both cases lies in the choice of numerical values for the CKM parameters.

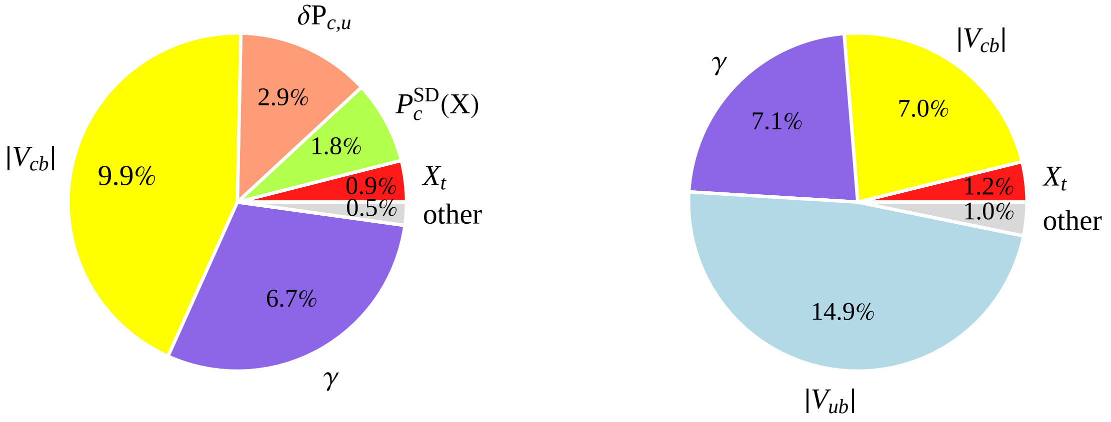

Figure A.1: Error budgets for $\mathcal{B}(K^+ \to \pi^+\nu\bar{\nu})$ (left) and $\mathcal{B}(K_L \to \pi^0\nu\bar{\nu})$ (right) in the SM prediction. V_{ub} and V_{cb} are the CKM matrix elements. γ is the angle defined in the unitarity triangle, as shown in Figure 1.2. $P_c^{\rm SD}(X)$ and $\delta P_{c,u}$ represent the short-distance and long-distance contributions in $P_c(X)$, respectively. The remaining parameters, which each contribute an error of less than 1%, are grouped into the “other" category. The figure is quoted from Ref.[12].

B Reconstruction of Veto Information

This section give additional explanations on the reconstruction procedures of the veto information.

B.1 OEV, LCV, Collar Counters, and Downstream Detectors

This section explains the procedures of OEV, LCV, the collar counters and the downstream detectors shown in Figure B.2. The module-timing with both-ended readout channels for CC04, CC05, CC06, DCV, BHPV, and BHGC were given as the mean of those timings. The module-timing of the CC03 module with two PMTs for the readout was also obtained as the mean of them. The correction for TOF using Equation 4.27 works well for downstream beam hole detectors because the distance D can be approximately given as $Z_{\rm det} - Z_{\rm vtx}$, where $Z_{\rm det}$ is the z-position of each detector module. In this case, the module-veto-timing can be approximated from Equation 4.27 as

$$
\begin{aligned}
t_{\rm mod}^{\rm veto} &= t_{\rm mod} - T_{\rm vtx} - D/c \\
&\approx t_{\rm mod} - \left(T_{\rm CSI} - \left(\frac{Z_{\rm CSI} - Z_{\rm vtx}}{c}\right)\right) - \left(\frac{Z_{\rm det} - Z_{\rm vtx}}{c}\right) \\
&= t_{\rm mod} - T_{\rm CSI} - \left(\frac{Z_{\rm CSI} - Z_{\rm det}}{c}\right),
\end{aligned}
\tag{B.6}
$$

where the reconstructed quantity, $Z_{\rm vtx}$, can be canceled assuming $T_{\rm vtx} \approx T_{\rm CSI} - (Z_{\rm CSI} - Z_{\rm vtx})/c$. For the energy calculation of BHPV and BHGC, the number of photons corresponding to the deposited energy was calculated. The veto on BHPV requires the number of modules with coincident hits across consecutive modules to be three or more. To calculate the coincident-hit timing, the TOF correction was performed with reference to the z-position of the most upstream module, and not exactly using Equation B.6.

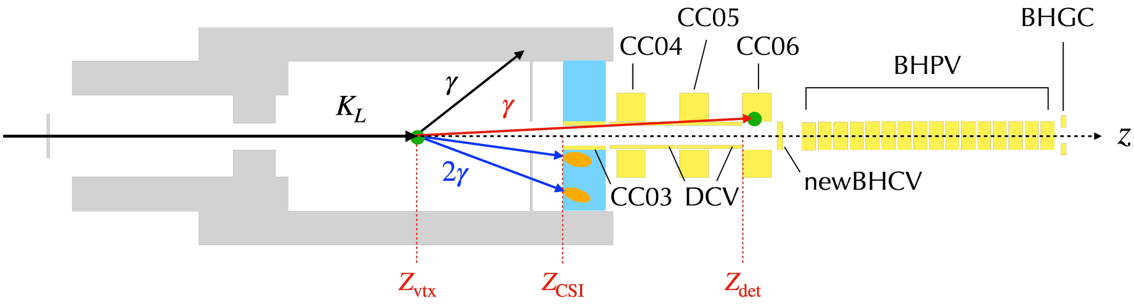

Figure B.2: Schematic view of the downstream veto detectors. In this figure, the $K_L \to \pi^0\pi^0$ decay is illustrated. The distance between two green points, D, is approximately equal to $Z_{\rm det} - Z_{\rm vtx}$.

Detailed explanation on the reconstruction strategy can be found in Refs. [68, 83].

B.2 MB and IB

The barrel detectors with the both-ended readout require special treatment. The module-timing was calculated as

$$t_{\rm mod} = \frac{t_u + t_d}{2}, \tag{B.7}$$

where t_u and t_d are the timing measured by the upstream and downstream channels, respectively. The hit position in the direction of the z-axis can then be given as

$$z_{\rm hit} = \frac{v_{\rm prop} \cdot (t_u - t_d)}{2} + z_{\rm center}, \tag{B.8}$$

where $v_{\rm prop} = 168.1\,(181.0)\,\text{mm/ns}$ is the propagation velocity of light in MB (IB) and $z_{\rm center} = 4105\,(4332.5)\,\text{mm}$ is the center position of MB (IB). in order to avoid the effect of the wrong vertex reconstruction, we used the distance L shown in Figure B.3 instead of D. The distance L can be given as

$$L = \sqrt{(z_{\rm hit} - Z_{\rm vtx})^2 + R^2}, \tag{B.9}$$

where $R = 1018\,(758.6)\,\text{mm}$ is the inner radius of IB (MB).

$$\begin{aligned} t_{\rm mod}^{\rm veto} &= t_{\rm mod} - T_{\rm vtx} - D/c \\ &= t_{\rm mod} - T_{\rm CSI} - L/c \end{aligned} \tag{B.10}$$

For the barrel detectors, the hit position can be obtained with Equation B.8, and thus the module-energy ($E_{\rm mod}$) that is calculated as a sum of the energy measured at the both ends was also corrected with the light attenuation as

$$E_{\rm mod} = \frac{e_u}{\exp\left(\frac{-(z_{\rm hit} - z_{\rm center})}{\Lambda + \alpha(z_{\rm hit} - z_{\rm center})}\right)} + \frac{e_d}{\exp\left(\frac{(z_{\rm hit} - z_{\rm center})}{\Lambda - \alpha(z_{\rm hit} - z_{\rm center})}\right)}, \tag{B.11}$$

where e_u and e_d are the energy measured by upstream and downstream channels, respectively, and Λ and α are the attenuation parameters.

Detailed explanation on the reconstruction strategy for these detectors can be found in Refs. [105, 49].

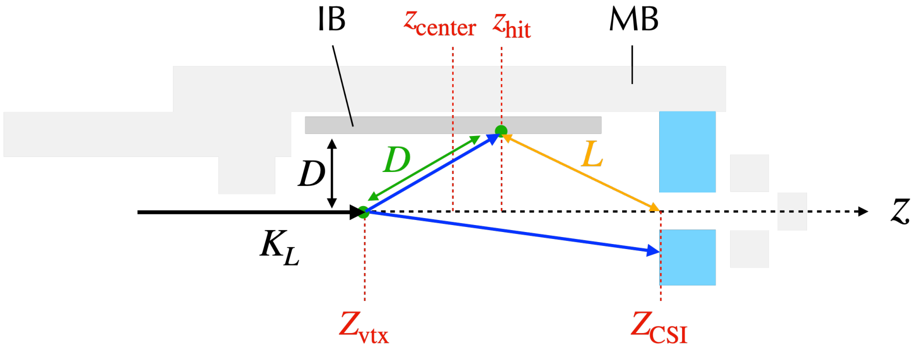

Figure B.3: Schematic explanation of the calculation for the module-veto-timing. In this figure, a photon hit to IB is illustrated. The blue arrows represent two photons.

B.3 Other Detectors

Detailed explanation on the reconstruction strategy for other detectors can be found in Refs. [68, 105, 49].

C Normalization-Mode Analysis with $K_L \to 3\pi^0$ and $K_L \to 2\gamma$

Figure C.1 and C.2 summarize the results of the K_L yield estimations with the $K_L \to 3\pi^0$ and $K_L \to 2\gamma$ samples, respectively. The analysis procedure is the same as the case with the $K_L \to \pi^0\pi^0$ sample, as described in Section 6.2.1. $A_{K_L\to 3\pi^0}$ ($A_{K_L\to 2\gamma}$) represents the acceptance for $K_L \to 3\pi^0$ ($K_L \to 2\gamma$) decays in each sample.

Table C.1: Summary of the K_L yield estimation with the $K_L \to 3\pi^0$ sample.

Period	$A_{K_L\to 3\pi^0}$	μ	p_{norm}	$N^{\mathrm{obs}}_{K_L\to 3\pi^0}$	N_{K_L}	F_{K_L} [/(2 × 10^{14} POT)]
Period-0	1.15×10^{-4}	1.00	30	100423	7.99×10^{11}	$(4.44\pm0.03)\times10^{7}$
Period-1	2.94×10^{-4}	1.00	2	83828	1.76×10^{10}	$(5.15\pm0.06)\times10^{7}$
Period-2	2.65×10^{-4}	1.00	3	76456	2.62×10^{10}	$(4.92\pm0.05)\times10^{7}$
Period-3	2.07×10^{-4}	1.00	5	43046	3.21×10^{10}	$(5.03\pm0.07)\times10^{7}$
Period-4	1.48×10^{-4}	1.00	10	34304	7.00×10^{10}	$(4.56\pm0.07)\times10^{7}$
Period-5	1.29×10^{-4}	1.00	20	98533	4.65×10^{11}	$(4.42\pm0.03)\times10^{7}$
Period-6	1.31×10^{-4}	1.00	20	20735	9.59×10^{10}	$(4.10\pm0.07)\times10^{7}$
Period-7	1.23×10^{-4}	1.00	30	5147	3.76×10^{10}	$(4.33\pm0.09)\times10^{7}$
Period-8	1.20×10^{-4}	1.00	30	21935	1.68×10^{11}	$(4.41\pm0.08)\times10^{7}$
Period-9	1.11×10^{-4}	1.00	30	93544	7.79×10^{11}	$(4.33\pm0.03)\times10^{7}$
Period-10	1.06×10^{-4}	1.00	30	518743	4.52×10^{12}	$(4.24\pm0.03)\times10^{7}$
Total				1096694	7.01×10^{12}	$(4.29\pm0.02)\times10^{7}$

Table C.2: Summary of the K_L yield estimation with the $K_L \to 2\gamma$ sample.

Period	$A_{K_L\to 2\gamma}$	μ	p_{norm}	$N^{\mathrm{obs}}_{K_L\to 2\gamma}$	N_{K_L}	F_{K_L} [/(2 × 10^{14} POT)]
Period-0	1.15×10^{-4}	1.00	30	10585	7.62×10^{11}	$(4.23\pm0.04)\times10^{7}$
Period-1	2.94×10^{-4}	0.99	2	8751	1.64×10^{10}	$(4.80\pm0.05)\times10^{7}$
Period-2	2.65×10^{-4}	1.00	3	7870	2.46×10^{10}	$(4.62\pm0.05)\times10^{7}$
Period-3	2.07×10^{-4}	1.00	5	4439	2.97×10^{10}	$(4.66\pm0.07)\times10^{7}$
Period-4	1.48×10^{-4}	0.99	10	3578	6.66×10^{10}	$(4.34\pm0.08)\times10^{7}$
Period-5	1.29×10^{-4}	1.00	20	10062	4.31×10^{11}	$(4.11\pm0.04)\times10^{7}$
Period-6	1.31×10^{-4}	1.00	20	2186	9.28×10^{10}	$(3.96\pm0.09)\times10^{7}$
Period-7	1.23×10^{-4}	1.00	30	534	3.65×10^{10}	$(4.20\pm0.18)\times10^{7}$
Period-8	1.20×10^{-4}	0.99	30	2355	1.62×10^{11}	$(4.24\pm0.09)\times10^{7}$
Period-9	1.11×10^{-4}	1.00	30	9743	7.29×10^{11}	$(4.05\pm0.04)\times10^{7}$
Period-10	1.06×10^{-4}	0.99	30	53790	4.20×10^{12}	$(3.94\pm0.02)\times10^{7}$
Total				113893	6.55×10^{12}	$(4.02\pm0.01)\times10^{7}$

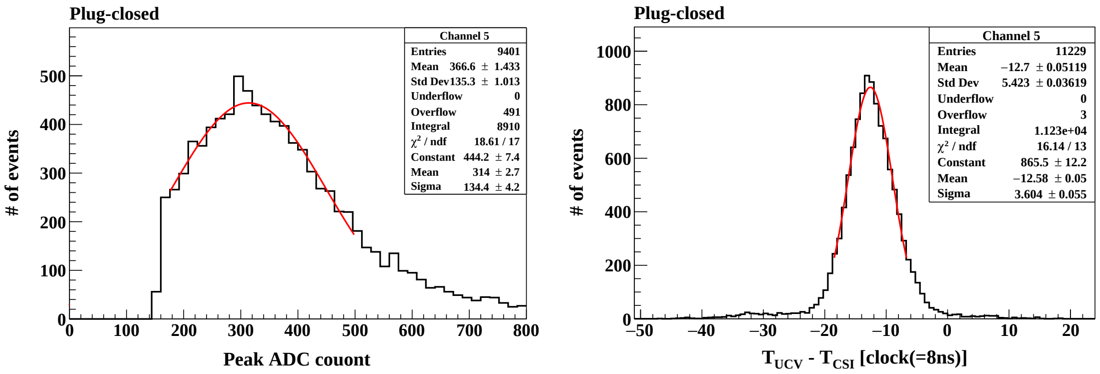

Figure D.4: Example of the calibration for UCV. The left figure shows the distribution of the ADC counts of the maximum peak height from the baseline. The distribution was cut around 150 ADC counts to obtain the clear peak structure around the most probable value. The Gaussian fit around the most probable value gave the ADC counts corresponding to the energy calibration constant. The right figure shows the distribution of the timing difference between UCV and CSI. For CSI, the total ADC counts was required to be greater than a given threshold to ensure the minimum energy deposition.

D Calibration and Basic Performance of UCV

D.1 Calibration for UCV

The calibration for UCV was performed using the plug-closed data. As described in Section 3.2.2.2, the plug-closed run provides charged pions and muons. Thus, the minimum-ionization-particle (MIP) peak can be observed in the distribution of deposited energy. We converted the ADC counts corresponding to the MIP peak to the deposited energy obtained from the GEANT4 simulation. The timing adjustment among 12 channels can also be done by measuring the timing difference between UCV and CSI. Figure D.4 shows an example of the distributions of peak ADC counts and the timing difference. The calibration data was taken about once per week to monitor the detector stability.

D.2 Light Yield

The light yield for the MIP events detected in UCV was also measured. We collected data for UCV by flashing LED with its intensity tuned to be low enough so that the ADC counts equivalent to a few photoelectrons (p.e.) can be observed. Figure D.5 shows the distribution of the ADC counts obtained from the LED data. By taking the difference in the ADC counts between the 1 p.e. peak and the 2 p.e. peak, we estimated the single-p.e.-equivalent ADC counts for each channel. The resulting light yield corresponding to the MIP peak is shown in Figure D.6. On average, the light of 12 p.e. was obtained.

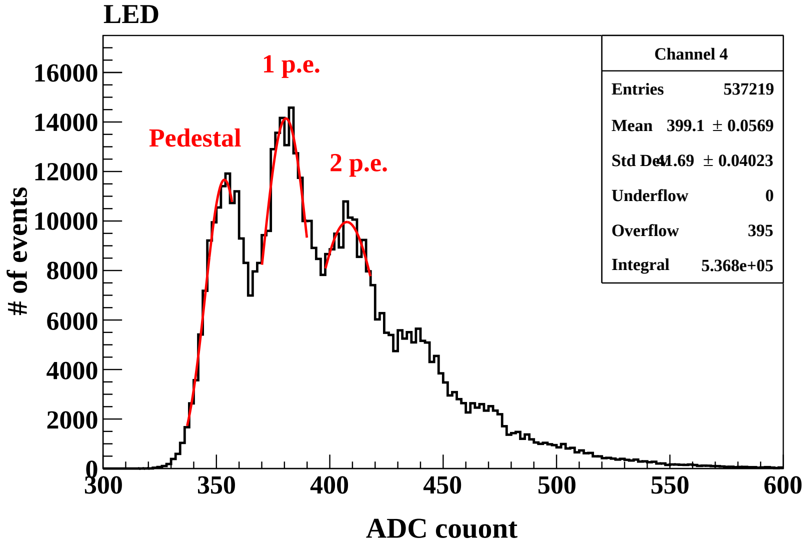

Figure D.5: Example of the distribution of the peak ADC counts of UCV in the LED data. Each peak in the histogram was fitted with a Gaussian function.

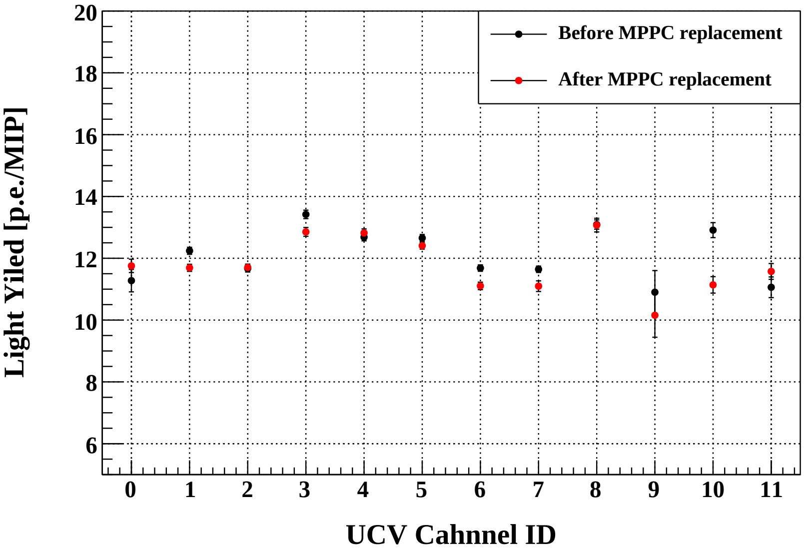

Figure D.6: Light yield obtained in UCV.

D.3 Accidental Activity in UCV

This section gives further details on the accidental activity in UCV.

D.3.1 Sources of Accidental Activities

The accidental hits in UCV arose from the contributions of beam particles and noise activity. While the veto acceptance of UCV was evaluated using the $K_L \to 3\pi^0$ data, the accidental activities can also be monitored with the data collected by random triggers, such as the TMON trigger and the clock trigger. As described in Section 3.2.1.7, such events were recorded during physics runs. Since events collected by the TMON trigger reflects both noise and beam-induced activity including effect of the spill structure of the beam[1], one can obtain the rate of accidental hits during the beam operation. On the other hand, events collected by the clock trigger does also provide the contribution from beam particles as well as noise activities, but it does not reflect the effect of the spill structure.

Figure D.7 shows the rate of UCV calculated using the random trigger data[2]. The red points show the rate calculated with events collected by the TMON trigger. The blue points show the rate obtained by subtracting the noise-induced contribution from the red points. The noise rate was calculated using events collected by the clock trigger, further selecting the off-spill region shown in Figure D.8 in order to exclude the beam contribution. The blue points therefore represent the beam contribution. The overall structure of the rate change follows the transition of the accidental loss shown in Figure 6.14 because the rate can be related with the loss, as seen in Equation 4.29. The beam contribution was approximately 2 MHz except for the period with the lower beam power. The noise rate, on the other hand, was changing in time. It was a negligible level at the beginning of the first period or right after replacing MPPCs on June 9th in 2021, but reached the similar rate of the beam contribution right before replacing MPPCs.

D.3.2 Hit Rate and Beam Profile

The TMON-triggered data gave further information of the accidental activity in UCV. Figure D.9 shows the distribution of the hit rate for each readout channel of UCV. Although the effective rate for the detector was around 2 MHz for beam particles, as described in Section D.3.1, the rate for each channel (single count rate) of UCV had the dependence on the vertical position. The maximum rate was approximately 0.4 MHz at the center. The shpae of the distribution represents the profile of the beam particles contributing to the accidental hits.

D.3.3 Correlation with Other Veto Detectors

As described in Section 6.2.2, the veto acceptance was estimated using the $K_L \to 3\pi^0$ data collected by the minimum-bias trigger. In order to estimate the signal acceptance of UCV exclusively, we

---

[1] It is known that the beam has non-flat time structure during a spill. This is because the current ripple in the MR power supplies changes the instantaneous rate of the beam particles. This beam structure results in the larger accidental loss.

[2] In this rate calculation, if multiples hits were observed across the channels in an event, they were defined as one hit to represent the rate for the detector.

[1] The beam was delivered to another branch of beam line in the HEF with 8 GeV, and we did not collect data during this period.

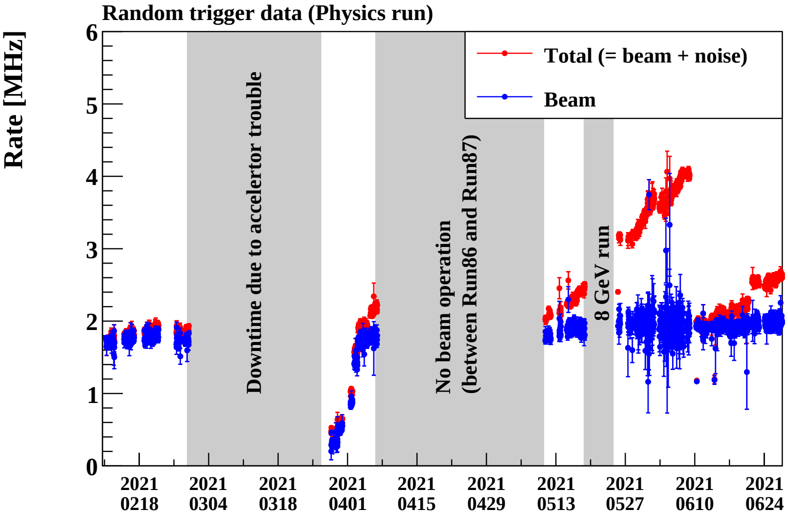

Figure D.7: Count rate of the accidental activities in UCV. The red (blue) points show the rate of the total contribution (beam contribution). The three shaded regions show the major non-beam periods: downtime due to the accelerator trouble (left), the period without the beam operation (center), and the period under the special beam configuration¹ (right), respectively.

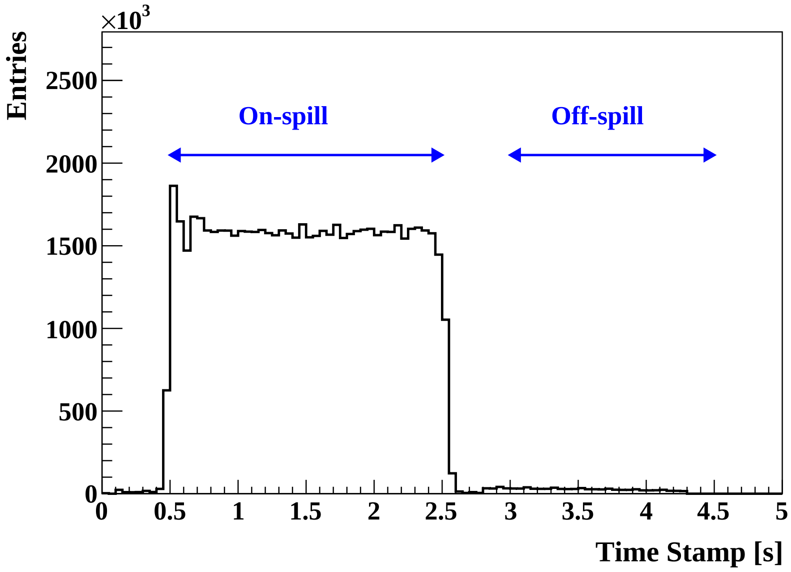

Figure D.8: Distribution of the event timing in a spill. Within a spill repetition cycle, the beam particles were delivered for 2 s in the "on-spill" region.

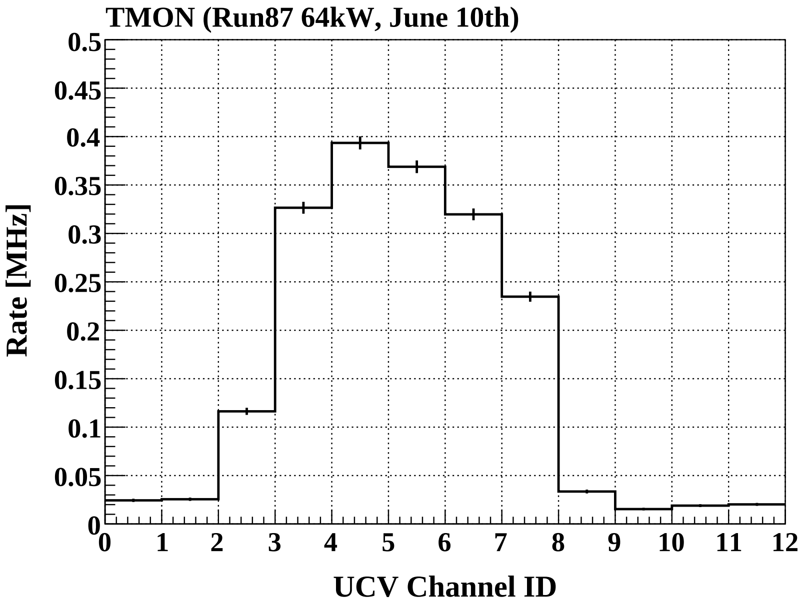

Figure D.9: Single count rate and the hit profile of UCV for the TMON data with the beam power of 64 kW. For this figure, deposited engyer for each channel was required to be greater than 0.5 tiems the energy deposition at the MIP peak obtained in Section D.1. Note that the vertical center of UCV corresponds to the channel ID 4, as shown in Figure 2.30. Channel 9, 10, and 11 cover the outer region.

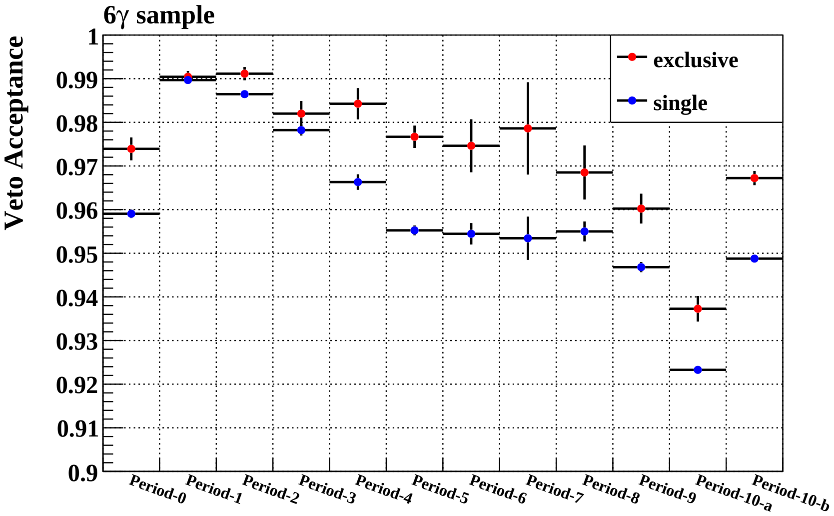

Figure D.10: Comparison of the veto acceptance of UCV under the different conditions of other veto detectors. The red (blue) markers show the exclusive (single) veto acceptance.

imposed the selection criteria described in Section 6.2.1.1 including all the other veto cuts on the $K_L \to 3\pi^0$ sample. Thus, the effect of accidental hits that correlated between UCV and other detectors, if any, was excluded from this estimate. Since veto acceptances of the other detectors relied on the MC simulation with the accidental overlay, we avoided from overestimating the signal acceptance for $K_L \to \pi^0\nu\bar{\nu}$ by evaluating the veto acceptance of UCV as an exclusive contribution. In this section, we refer to such acceptance as the exclusive veto acceptance. In case that any contributions of accidental hits regardless of the correlation with other detectors are included, we refer to it as the single veto acceptance.

Figure D.10 shows the comparison of the veto acceptance of UCV between the exclusive veto acceptance and the single veto acceptance. There was about 1 to 2% difference between them. Note that, although the single veto acceptance was estimated without including other veto cuts in the event selection, the $K_L \to 3\pi^0$ event purity was still about 100%. Figure D.11 explains the correlation of the veto acceptance of UCV with other veto detectors. By adding one of the veto cuts to the $K_L \to 3\pi^0$ selection, one can observe the difference in the veto acceptance of UCV. If veto cuts on upstream detectors, such as FB and NCC, or downstream beam-hole detectors, BHPV and newBHCV, are included, the single veto acceptance of UCV is raised up. This implies that the difference observed in Figure D.10 originated from accidental activities coincident with these detectors.

D.3.4 Effect of the Backsplash Loss

If a backsplash effect affected the veto acceptance of UCV, there is a chance that such a contribution was overestimated. This is because the veto acceptance was evaluated using the $K_L \to 3\pi^0$ sample where more number of photon clusters than the $K_L \to \pi^0\nu\bar{\nu}$ case would give the large backsplash loss. In order to investigate a possible dependence on the number of clusters in CSI, the veto acceptance of UCV was crosschecked with the $K_L \to \pi^0\pi^0$ and $K_L \to 2\gamma$ samples as well as the

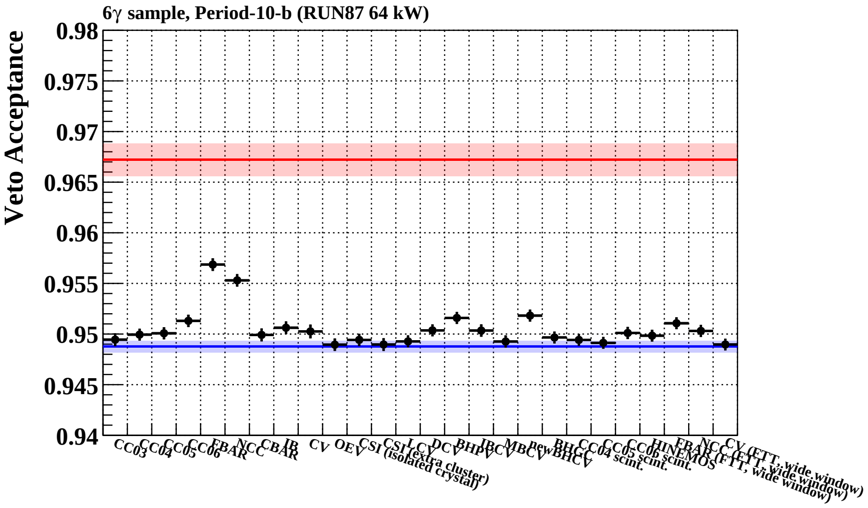

Figure D.11: Dependence of the single veto acceptance of UCV on other detectors. Each detector written in the horizontal axis was included in the event selection for the $K_L \to 3\pi^0$ sample. The red (blue) line corresponds the exclusive (single) veto acceptance and the band shown in the same color represents the 1σ error.

$K_L \to 3\pi^0$ sample. For this check, the events collected by the normalization trigger were used to secure the large statistics. As shown in Figure D.12, there was no significant discrepancy among the three samples. To further study the effect of the backsplash loss on UCV, the MC simulation might be helpful.

D.3.5 Timing Distribution of UCV in the $K_L \to 3\pi^0$ Sample

The energy deposition in UCV was calculated as the maximum peak height within the veto window of 20 ns. The veto timing for events with the deposited energy larger than the threshold distributes within that range. Although the $K_L \to 3\pi^0$ sample used to estimate the veto acceptance of UCV showed the contribution of accidental hits, its timing distribution did not have the flat structure. Figure D.13 shows the distribution of the veto timing of UCV. The periodic structure observed in the distribution corresponds to the effect of the transverse RF signal applied with a frequency of about 47 MHz. This RF signal was deliberately applied to suppress the spill structure of the beam induced from the current ripple in the MR power supplies. The same structure can also be observed in other beam-hole detectors, such as BHPV and BHGC [118, 68].

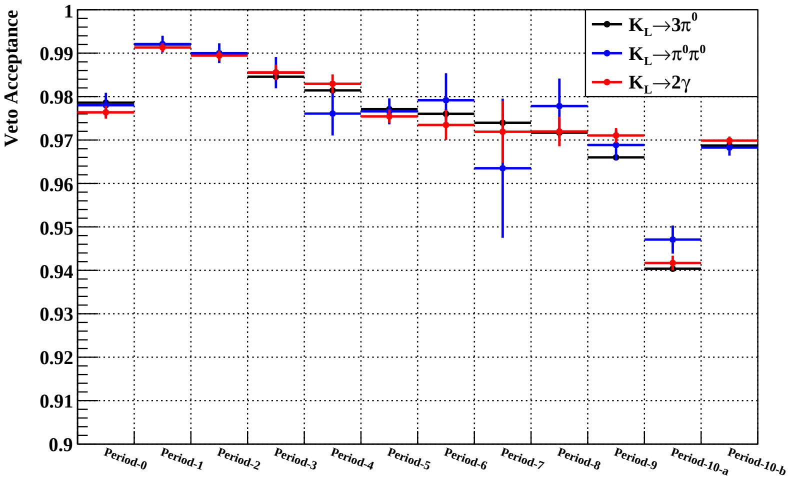

Figure D.12: Comparison of the exclusive veto acceptance of UCV among three normalization decay modes. The black, blue, and red points correspond to the veto acceptance estimated with the $K_L \to 3\pi^0$ (6-cluster), $K_L \to \pi^0\pi^0$ (4-cluster), and $K_L \to 2\gamma$ (2-cluster) samples, respectively.

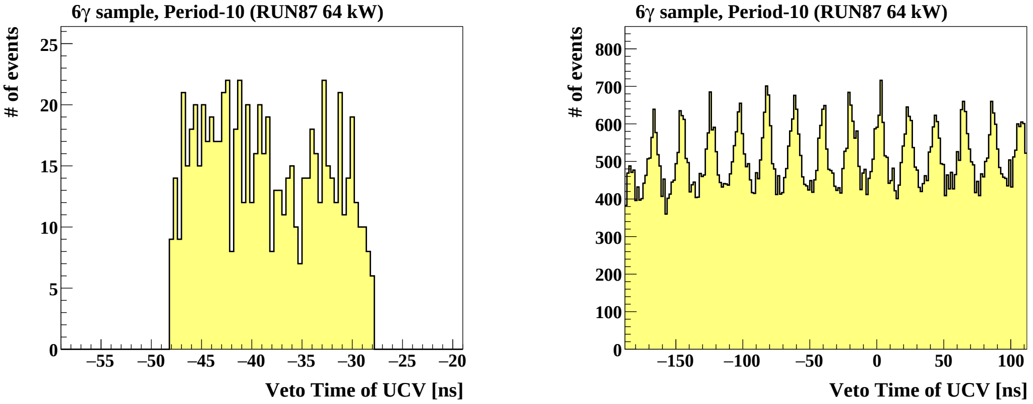

Figure D.13: Distribution of the veto timing of UCV. The left figure shows the distribution of the veto timing for the $K_L \to 3\pi^0$ sample after requiring the deposited energy to be larger than the threshold. The right figure shows the distribution of the veto timing. As is the case in the left figure, hits in UCV were required. The deposited energy was, however, calculated without the constraint of the 20 ns time window to see the broader timing range. To increase the statistics, the events collected by the normalization trigger are shown in the right figure.

E Acceptance Loss due to CSIEt in Level-1 Trigger

The loss of the signal acceptance induced from the CSIEt requirement in the level-1 trigger was evaluated using the special run taken with the lower CSIEt threshold. The standard CSIEt threshold was set to 550 MeV while the lower threshold was set to 200 MeV. Figure E.14 shows the distributions of total energy (E_{total}) in CSI and the efficiency. The efficiency was fitted with the function defined as

$$\epsilon_{Et}(E_{\mathrm{total}}) = \frac{1}{1 + \exp\left\{-(E_{\mathrm{total}} - p_0)/p_1\right\}}, \tag{E.12}$$

where p_0 and p_1 are the fitting parameters. By applying the obtained function to the $K_L \to \pi^0 \nu \bar{\nu}$ MC simulation as a weight factor, we estimated the loss was less than 0.3%.

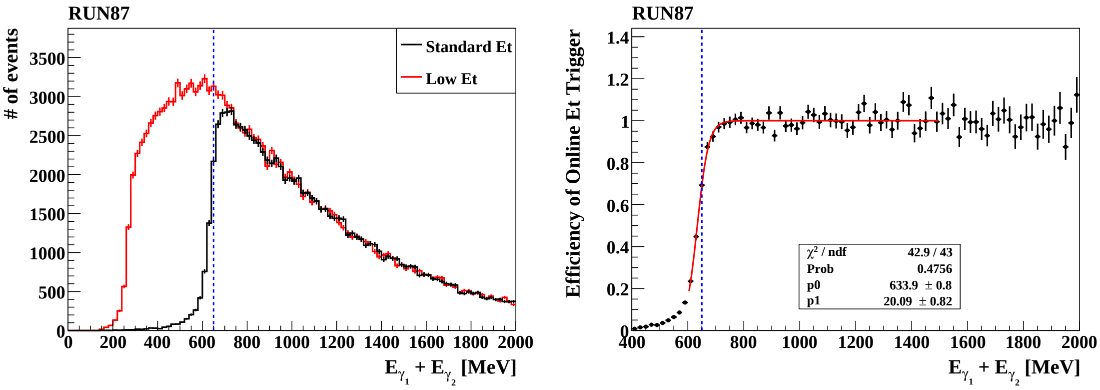

Figure E.14: The effect of the CSIEt trigger. The left figure shows the distribution of the total energy. The black (red) histogram shows the events collected with the standard (lower) CSIEt threshold. The right figure shows the efficiency of the CSIEt trigger. The red curve shows the fitted function. In each figure, the blue dashed line indicates the total energy threshold at 650 MeV in the offline analysis.

F Signal Acceptance for $K_L \to \pi^0 \nu \bar{\nu}$

This section summarizes the breakdown of the signal acceptance for $K_L \to \pi^0 \nu \bar{\nu}$. Table F.3 shows the signal acceptance at each cut stage.

$A^{\mathrm{sig}}_{\mathrm{geom}}$ is the geometrical acceptance of two photons in the final state hitting CSI, and $A^{\mathrm{sig}}_{\mathrm{trig}}$, $A^{\mathrm{sig}}_{\mathrm{photon}}$, $A^{\mathrm{sig}}_{\mathrm{kine}}$, $A^{\mathrm{sig}}_{\mathrm{veto}}$, $A^{\mathrm{sig}}_{\mathrm{shape}}$, and $A^{\mathrm{sig}}_{\Delta T_{\mathrm{CSI}}}$ are the acceptances of the trigger-related cuts, photon selection, kinematic cuts, veto cuts, shape-related cuts, and ΔT_{CSI} cut

Table F.3: Summary of the estimation of the signal acceptance for $K_L \to \pi^0 \nu \bar{\nu}$. The table shows the beam power, the K_L decay probability (P_{decay}), the acceptances after adding the two-cluster selection, the trigger-related cuts, the photon-selection, the kinematic cuts, the veto cuts, the shape-related cuts, and the ΔT_{CSI} cut, which are denoted as A_{2clus}, A_{trig}, A_{photon}, A_{kine}, A_{veto}, A_{shape}, $A_{\Delta T_{\mathrm{CSI}}}$, respectively. The value shown in parenthesis represents the each cut acceptance relative to the previous cut stage.

Period	Beam power	P_{decay}	A_{2clus}	A_{trig}	A_{photon}	A_{kine}	A_{veto}	A_{shape}	$A_{\Delta T_{\mathrm{CSI}}}$
Period-0	60 kW	3.34×10^{-2}	9.09×10^{-3}	7.42×10^{-3}	5.22×10^{-3}	1.85×10^{-3}	3.19×10^{-4}	1.68×10^{-4}	1.66×10^{-4}
		(3.34%)	(27.2%)	(81.8%)	(70.3%)	(35.4%)	(17.2%)	(52.6%)	(99.2%)
Period-1	10 kW	3.34×10^{-2}	9.18×10^{-3}	7.95×10^{-3}	5.61×10^{-3}	2.00×10^{-3}	8.32×10^{-4}	4.41×10^{-4}	4.37×10^{-4}
		(3.34%)	(27.5%)	(86.6%)	(70.5%)	(35.6%)	(41.7%)	(53.0%)	(99.2%)
Period-2	15 kW	3.34×10^{-2}	9.17×10^{-3}	7.89×10^{-3}	5.56×10^{-3}	1.98×10^{-3}	7.53×10^{-4}	3.99×10^{-4}	3.96×10^{-4}
		(3.34%)	(27.4%)	(86.0%)	(70.5%)	(35.6%)	(38.0%)	(53.0%)	(99.2%)
Period-3	25 kW	3.34×10^{-2}	9.15×10^{-3}	7.75×10^{-3}	5.46×10^{-3}	1.94×10^{-3}	5.83×10^{-4}	3.09×10^{-4}	3.07×10^{-4}
		(3.34%)	(27.4%)	(84.7%)	(70.5%)	(35.5%)	(30.0%)	(53.0%)	(99.2%)
Period-4	40 kW	3.34×10^{-2}	9.11×10^{-3}	7.55×10^{-3}	5.32×10^{-3}	1.88×10^{-3}	4.12×10^{-4}	2.18×10^{-4}	2.16×10^{-4}
		(3.34%)	(27.3%)	(82.9%)	(70.4%)	(35.4%)	(21.9%)	(52.8%)	(99.2%)
Period-5	45 kW	3.34×10^{-2}	9.08×10^{-3}	7.43×10^{-3}	5.23×10^{-3}	1.85×10^{-3}	3.58×10^{-4}	1.90×10^{-4}	1.88×10^{-4}
		(3.34%)	(27.2%)	(81.8%)	(70.4%)	(35.3%)	(19.4%)	(53.0%)	(99.2%)
Period-6	46 kW	3.34×10^{-2}	9.09×10^{-3}	7.44×10^{-3}	5.24×10^{-3}	1.85×10^{-3}	3.62×10^{-4}	1.92×10^{-4}	1.90×10^{-4}
		(3.34%)	(27.2%)	(81.9%)	(70.4%)	(35.3%)	(19.6%)	(53.0%)	(99.1%)
Period-7	51 kW	3.34×10^{-2}	9.09×10^{-3}	7.41×10^{-3}	5.22×10^{-3}	1.84×10^{-3}	3.38×10^{-4}	1.79×10^{-4}	1.77×10^{-4}
		(3.34%)	(27.2%)	(81.6%)	(70.4%)	(35.2%)	(18.4%)	(52.9%)	(99.1%)
Period-8	56 kW	3.34×10^{-2}	9.11×10^{-3}	7.47×10^{-3}	5.26×10^{-3}	1.85×10^{-3}	3.30×10^{-4}	1.74×10^{-4}	1.73×10^{-4}
		(3.34%)	(27.3%)	(81.9%)	(70.4%)	(35.2%)	(18.4%)	(52.9%)	(99.1%)
Period-9	60 kW	3.34×10^{-2}	9.09×10^{-3}	7.41×10^{-3}	5.22×10^{-3}	1.84×10^{-3}	3.00×10^{-4}	1.58×10^{-4}	1.57×10^{-4}
		(3.34%)	(27.2%)	(81.5%)	(70.4%)	(35.3%)	(16.3%)	(52.8%)	(99.2%)
Period-10	64 kW	3.34×10^{-2}	9.09×10^{-3}	7.40×10^{-3}	5.20×10^{-3}	1.84×10^{-3}	2.87×10^{-4}	1.51×10^{-4}	1.49×10^{-4}
		(3.34%)	(27.2%)	(81.4%)	(70.3%)	(35.3%)	(15.6%)	(52.5%)	(99.2%)

G Analysis for the $K^{\pm} \to \pi^{\pm}\pi^{0}$ Decay

This section gives supplemental information on the analysis discussed in Section 6.3.6.

G.1 Loose Veto Selection for $K^{\pm} \to \pi^{\pm}\pi^{0}$

Table G.4 shows the loose selection criteria with veto detectors for $K^{\pm} \to \pi^{\pm}\pi^{0}$. Some of the veto detectors were used with a higher energy threshold than the one used for the normalization-mode analysis and the $K_L \to \pi^0\nu\bar{\nu}$ analysis described in Section 6.2.1.1. In the final selection for $K^{\pm} \to \pi^{\pm}\pi^{0}$, veto cuts with the other downstream detectors were also imposed to eliminate the $K_L \to \pi^+\pi^-\pi^0$ contribution.

Table G.4: Summary of the veto cuts. For each detector, the deposited energy corresponding to a hit detected within the veto window was required to be less than the threshold.

Subdetector for veto	Energy threshold	Width of veto window
FB	5 MeV	20 ns
NCC (common readout)	1 MeV	40 ns
Hinemos	1 MeV	60 ns
MB	5 MeV	40 ns
IB	1 MeV	50 ns
MBCV	0.5 MeV	60 ns
IBCV	0.5 MeV	60 ns
CSI (isolated-hit crystal)[b]	see Section 4.3.1	
CSI (extra cluster)	see Section 4.3.1	
OEV	2 MeV	20 ns
LCV	0.6 MeV	30 ns
CC03	3 MeV	60 ns
CC06 (CsI crystal)	3 MeV	30 ns
CC06 (plastic scintillator)	1 MeV	30 ns

[a] Cut with the standard condition defined in Equation 4.24 was used.

G.2 Accidental Loss of UCV in the Special Run

The beam condition during the special run is significantly different from the physics run. Since the sweeping magnet was turned off to enhance charged particles, detector hit rate increased. We evaluated the inefficiency of UCV using the $K^{\pm}$ sample collected in the special run with the beam power of 10 kW. For the correction for the inefficiency described in Section 6.3.6.2, we used the $K_L \to 3\pi^0$ data collected during the special run. In general, the veto acceptance (= 1 - accidental loss) has correlations with other veto detectors, as discussed in Appendix D.3.3. Thus, we evaluated the veto acceptance of UCV after applying all the other veto cuts in the $K_L \to \pi^0\nu\bar{\nu}$ analysis. However, we did not have the enough statistics of the $K_L \to 3\pi^0$ sample collected in the special run. Therefore, the veto acceptance of UCV during the special run was evaluated as the single veto acceptance (see Appendix D.3.3) to increase the statistics. The veto acceptance of UCV was estimated to be (85.1 ± 4.4)%, which is equivalent to the accidental loss of 15%. Figure G.15 shows the distribution of the deposited energy in UCV.

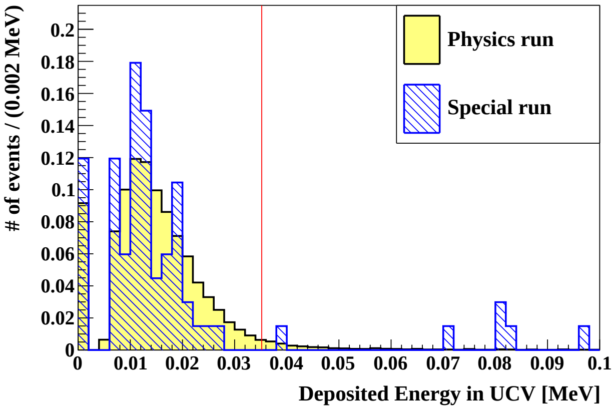

Figure G.15: Distribution of the deposited energy in UCV for the $K_L \to 3\pi^0$ data sample. The yellow (blue) histogram shows the events collected in the physics run (special run). The red line indicates the energy threshold.

G.3 $K^{\pm}$ Momentum Distribution in the Three-Cluster Events

Figure G.16 shows the $K^{\pm}$ momentum distribution after applying all the selection criteria. The distributions for the data obtained in the physics run and the special run are not completely the same. This is because the $K^{\pm}$'s in the special run should come directly from the T1 target and result in the harder momentum than the that in the physics run.

G.4 Distributions of Kinematic Variables with the Veto on UCV

Figure G.17 shows the correlation between $M_{K^{\pm}}$ and Z_{vtx} for the $K^{\pm}$ data sample collected in the physics run and the special run.

Figures G.18 and G.19 shows the comparison of the variables used in the kinematic cuts for the three-cluster data sample collected in the physics run before and after imposing the veto cut with UCV. The distributions for the data sample collected in the special run are shown in Figures G.20 and G.21.

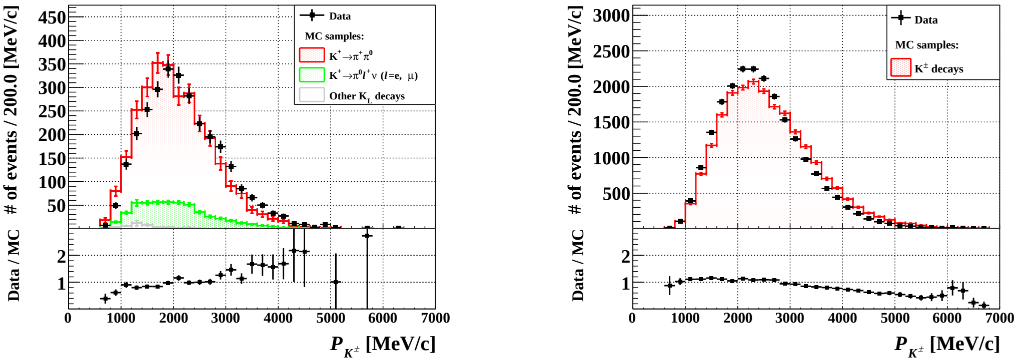

(a) Physics run

(b) Special run

Figure G.16: Distributions of the reconstructed $K^{\pm}$ momentum for the $K^{\pm}$ sample after applying all the selection criteria.

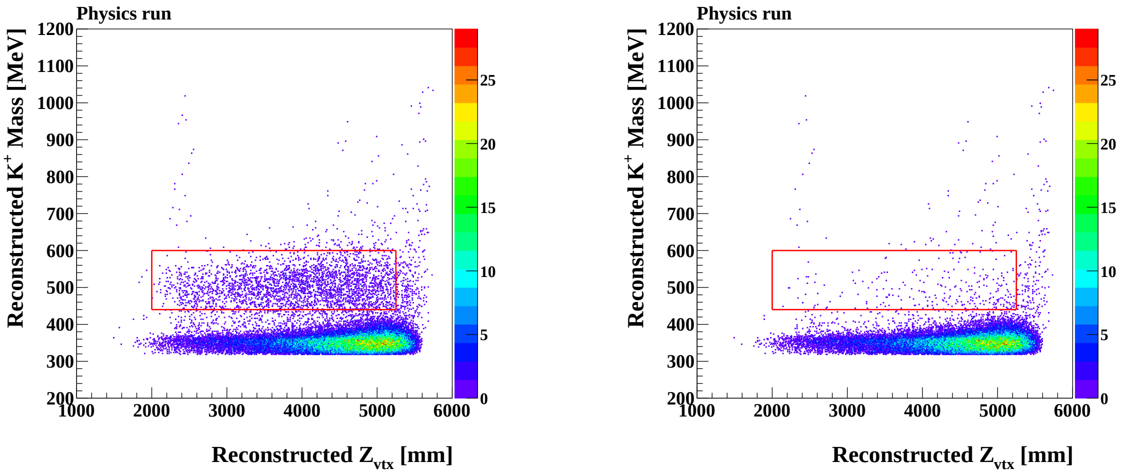

(a) Physics run

(b) Physics run with no energy deposition in UCV

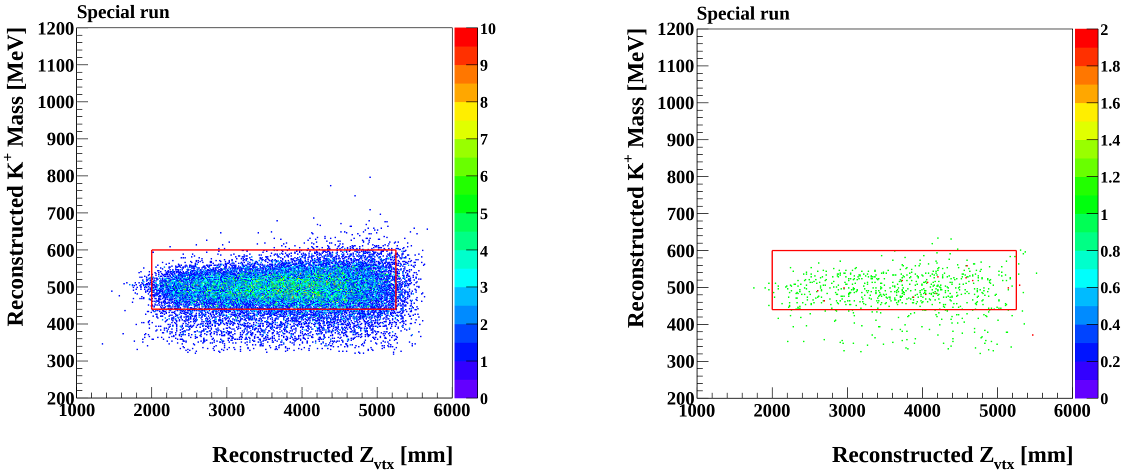

(c) Special run

(d) Special run with no energy deposition in UCV

Figure G.17: Distributions of $M_{K^{\pm}}$ versus Z_{vtx} for the $K^{\pm}$ data sample after applying all the selection criteria except for Z_{vtx} and $M_{K^{\pm}}$. In the right figures, the veto cut with UCV was further imposed. The red box indicates the accepted region for the $K^{\pm} \to \pi^{\pm}\pi^{0}$ signal. The smaller $M_{K^{\pm}}$ region in the physics run is dominated by the K_L decays.

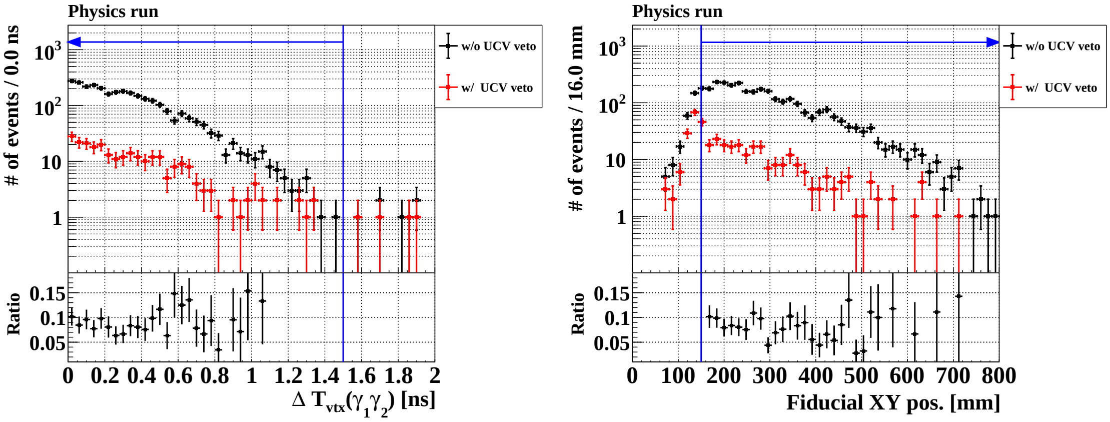

(a) Vertex timing difference (ΔT_{vtx})

(b) Hit position ($\max(|x|, |y|)$)

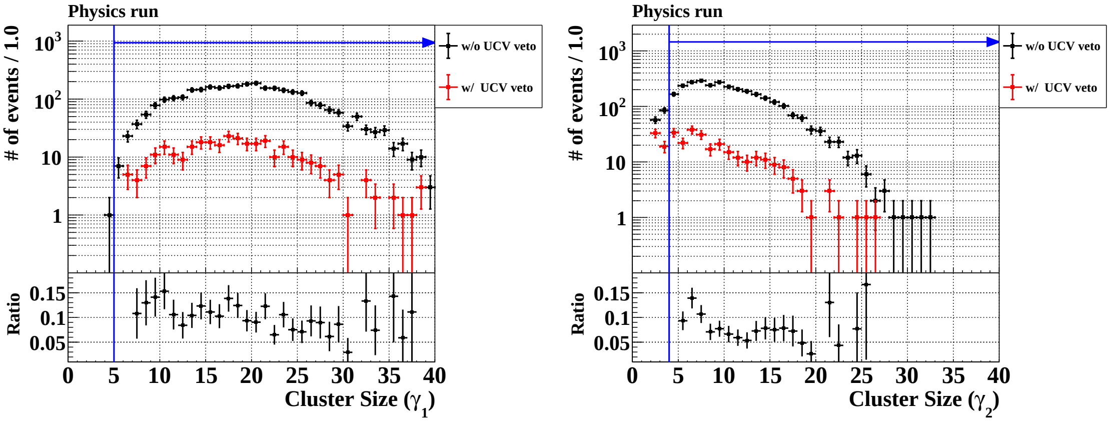

(c) Cluster size of γ_1 ($n_{\mathrm{cryst}}^{\gamma 1}$)

(d) Cluster size of γ_2 ($n_{\mathrm{cryst}}^{\gamma 2}$)

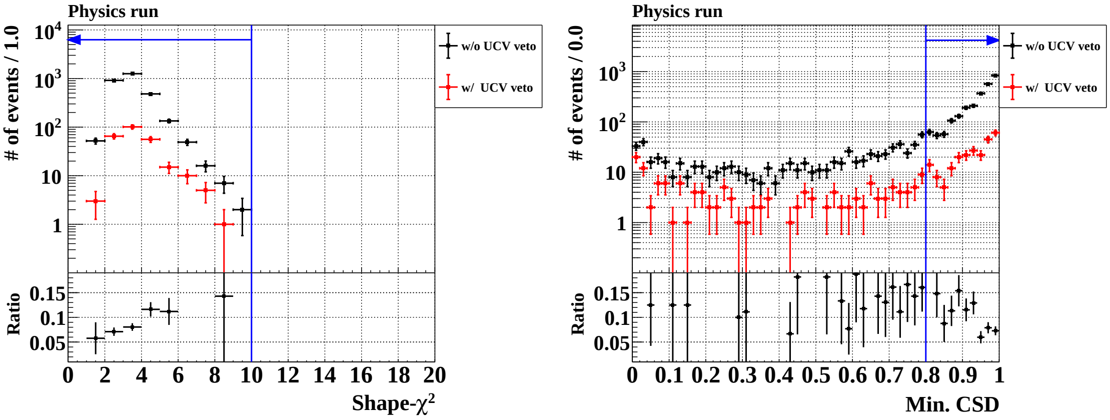

(e) χ^2_{shape}

(f) $\mathrm{CSD}_{\mathrm{NN}}$

Figure G.18: Distributions of $M_{K^\pm}$ for the $K^\pm$ data sample obtain in the physics run after applying all the selection criteria except for the one shown in each figure. The black (red) histogram shows the events before (after) imposing the veto cut with UCV. The blue arrow in each figure indicates the accepted region for the $K^\pm \to \pi^\pm \pi^0$ signal.

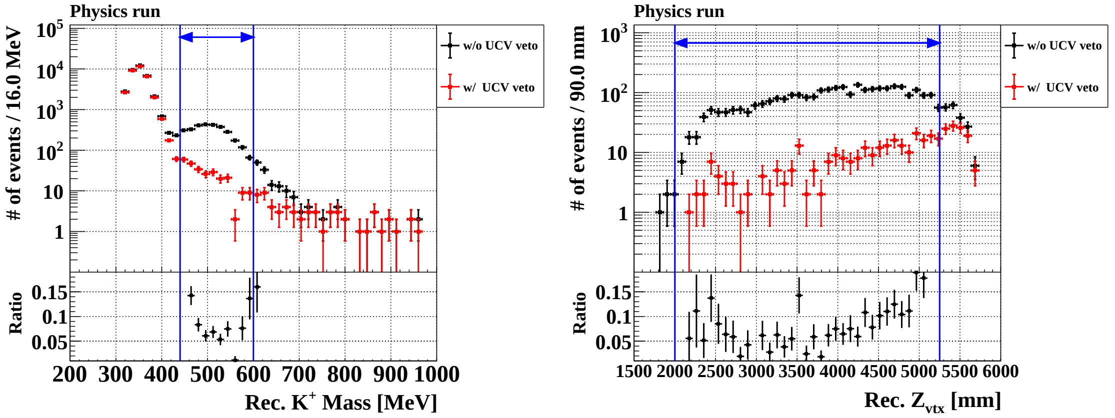

(a) Reconstructed $K^{\pm}$ mass (b) Reconstructed Z_{vtx}

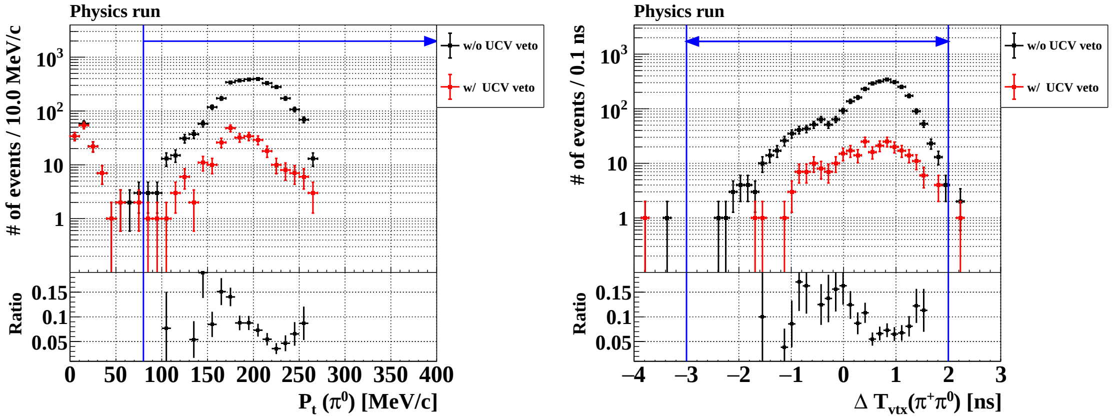

(c) Reconstructed π^{0} P_t (d) $\pi^{\pm}$-π^{0} timing difference ($\delta T_{\pi^{\pm}\pi^{0}}$)

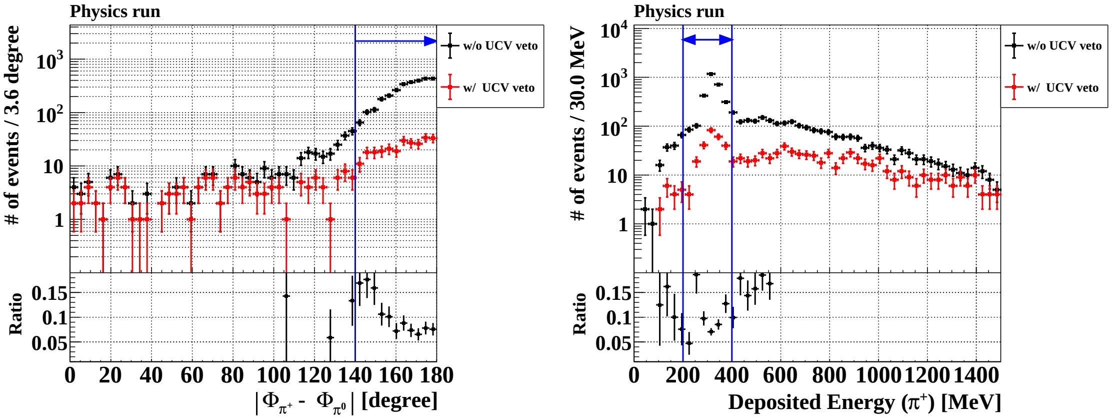

(e) $\pi^{\pm}$-π^{0} angle ($\phi_{\pi^{\pm}\pi^{0}}$) (f) Deposited energy of a $\pi^{\pm}$ cluster

Figure G.19: Distributions of $M_{K^{\pm}}$ for the $K^{\pm}$ data sample obtain in the physics run after applying all the selection criteria except for the one shown in each figure. The black (red) histogram shows the events before (after) imposing the veto cut with UCV. The blue arrow in each figure indicates the accepted region for the $K^{\pm} \to \pi^{\pm}\pi^{0}$ signal.

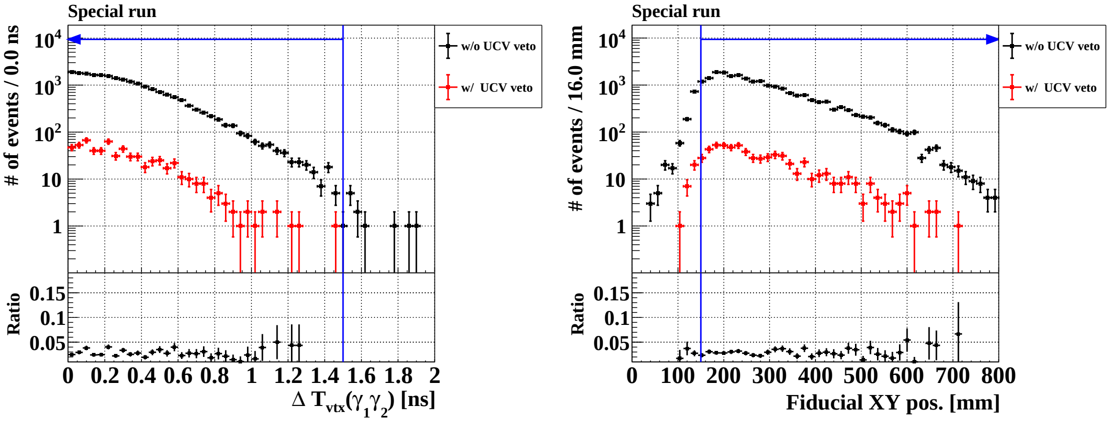

(a) Vertex timing difference (ΔT_{vtx})

(b) Hit position ($\max(|x|, |y|)$)

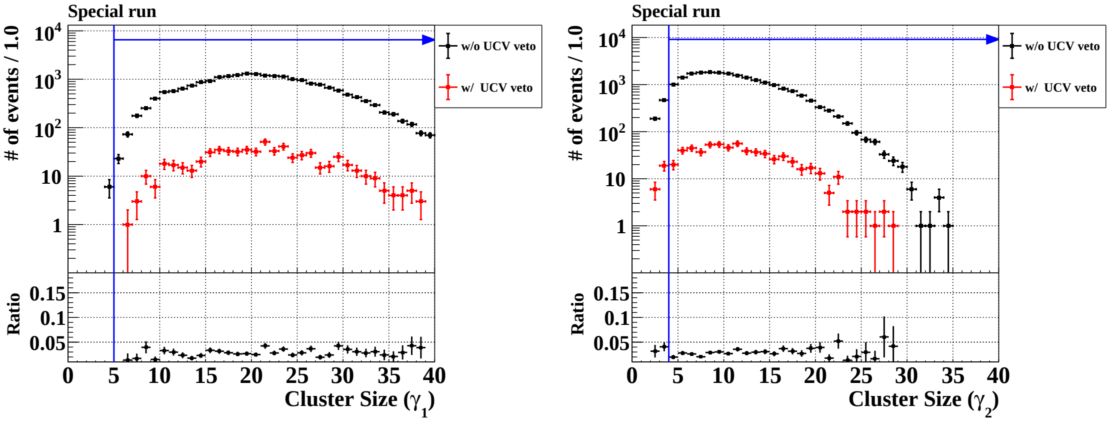

(c) Cluster size of γ_1 ($n_{\mathrm{cryst}}^{\gamma 1}$)

(d) Cluster size of γ_2 ($n_{\mathrm{cryst}}^{\gamma 2}$)

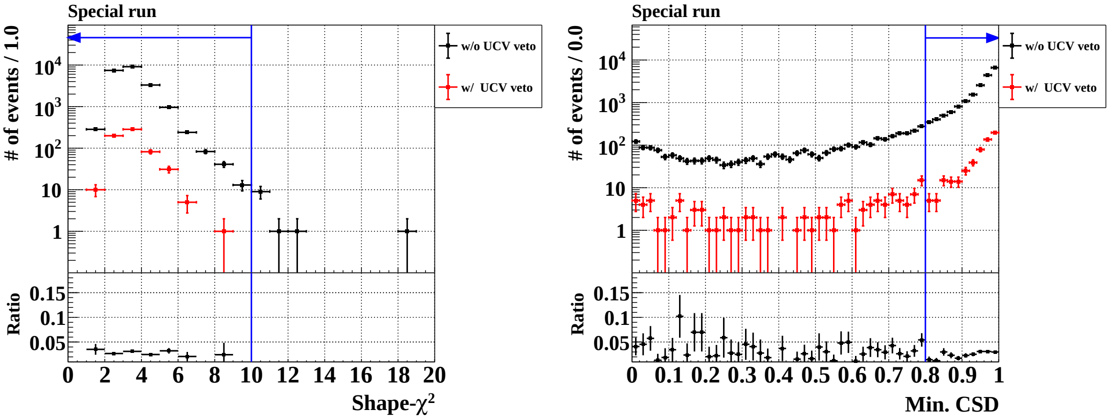

(e) χ^2_{shape}

(f) $\mathrm{CSD}_{\mathrm{NN}}$

Figure G.20: Distributions of $M_{K^{\pm}}$ for the $K^{\pm}$ data sample obtain in the special run after applying all the selection criteria except for the one shown in each figure. The black (red) histogram shows the events before (after) imposing the veto cut with UCV. The blue arrow in each figure indicates the accepted region for the $K^{\pm} \to \pi^{\pm}\pi^{0}$ signal.

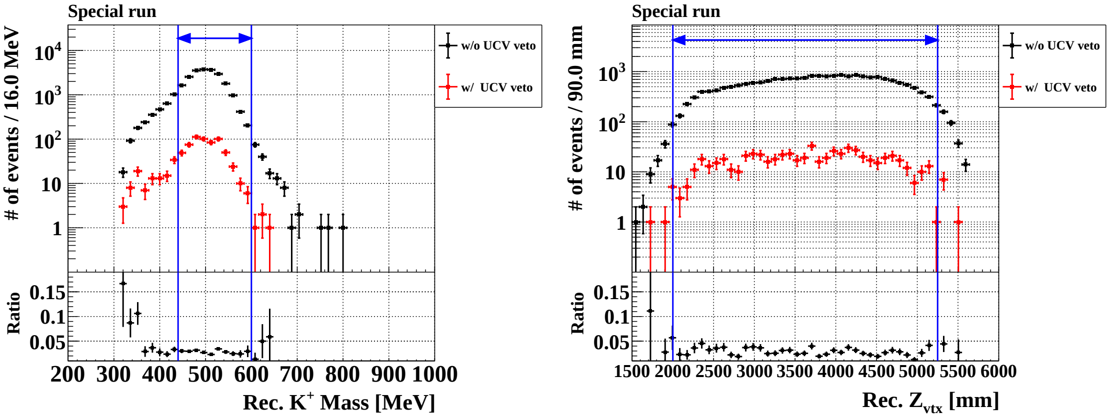

(a) Reconstructed $K^{\pm}$ mass (b) Reconstructed Z_{vtx}

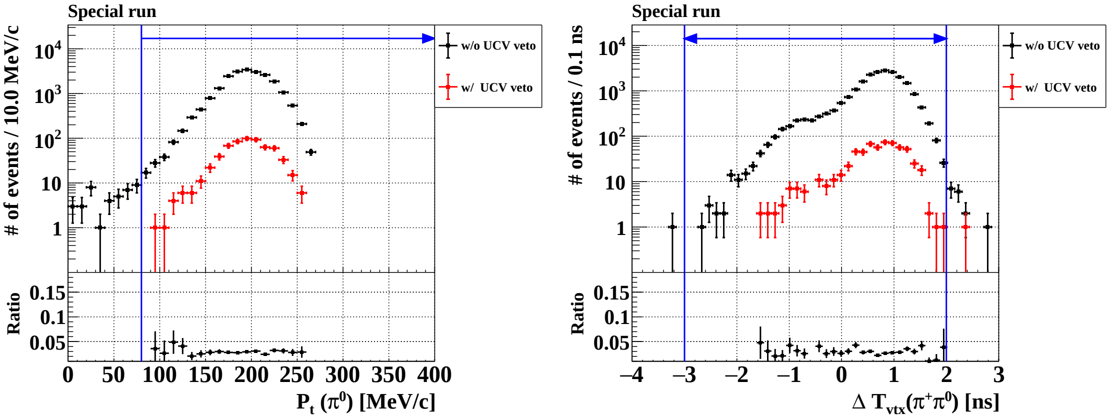

(c) Reconstructed π^{0} P_t (d) $\pi^{\pm}$-π^{0} timing difference ($\delta T_{\pi^{\pm}\pi^{0}}$)

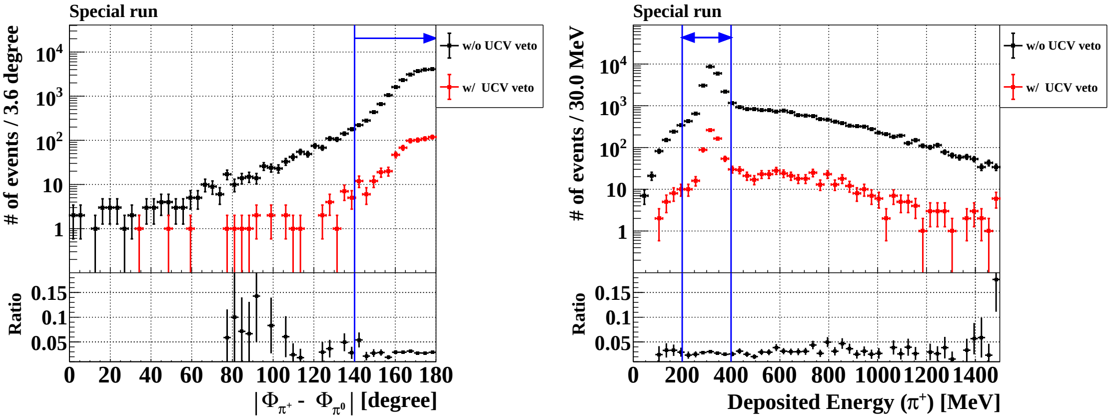

(e) $\pi^{\pm}$-π^{0} angle ($\phi_{\pi^{\pm}\pi^{0}}$) (f) Deposited energy of a $\pi^{\pm}$ cluster

Figure G.21: Distributions of $M_{K^{\pm}}$ for the $K^{\pm}$ data sample obtain in the special run after applying all the selection criteria except for the one shown in each figure. The black (red) histogram shows the events before (after) imposing the veto cut with UCV. The blue arrow in each figure indicates the accepted region for the $K^{\pm} \to \pi^{\pm}\pi^{0}$ signal.

References

[1] S. Navas *et al*. (Aug 2024). `doi:10.1103/PhysRevD.110.030001`, [link].
URL https://link.aps.org/doi/10.1103/PhysRevD.110.030001

[2] N. Aghanim *et al*., Astronomy & Astrophysics 641 (2020) A6. `doi:10.1051/0004-6361/201833910`, [link].
URL http://dx.doi.org/10.1051/0004-6361/201833910

[3] A. J. Buras *et al*., J. High Energy Phys. 2014 (11). `doi:10.1007/jhep11(2014)121`, [link].
URL http://dx.doi.org/10.1007/JHEP11(2014)121

[4] J. H. Christenson *et al*., Phys. Rev. Lett. 13 (1964) 138–140. `doi:10.1103/PhysRevLett.13.138`, [link].
URL https://link.aps.org/doi/10.1103/PhysRevLett.13.138

[5] N. Cabibbo, Phys. Rev. Lett. 10 (1963) 531–533. `doi:10.1103/PhysRevLett.10.531`, [link].
URL https://link.aps.org/doi/10.1103/PhysRevLett.10.531

[6] M. Kobayashi, T. Maskawa, Prog. Theor. Exp. Phys. 49 (2) (1973) 652–657. `doi:10.1143/PTP.49.652`, [link].
URL https://doi.org/10.1143/PTP.49.652

[7] L. Wolfenstein, Phys. Rev. Lett. 51 (1983) 1945–1947. `doi:10.1103/PhysRevLett.51.1945`, [link].
URL https://link.aps.org/doi/10.1103/PhysRevLett.51.1945

[8] V. Cirigliano *et al*., Rev. Mod. Phys. 84 (2012) 399–447. `doi:10.1103/RevModPhys.84.399`, [link].
URL https://link.aps.org/doi/10.1103/RevModPhys.84.399

[9] S. L. Glashow, J. Iliopoulos, L. Maiani, Phys. Rev. D 2 (1970) 1285–1292. `doi:10.1103/PhysRevD.2.1285`, [link].
URL https://link.aps.org/doi/10.1103/PhysRevD.2.1285

[10] A. J. Buras, Eur. Phys. J. C 83 (66). `doi:10.1140/epjc/s10052-023-11222-6`, [link].
URL https://doi.org/10.1140/epjc/s10052-023-11222-6

[11] F. Mescia, C. Smith, Phys. Rev. D 76 (2007) 034017. `doi:10.1103/PhysRevD.76.034017`, [link].
URL https://link.aps.org/doi/10.1103/PhysRevD.76.034017

[12] A. J. Buras *et al.*, J. High Energy Phys. 2015 (11). `doi:10.1007/jhep11(2015)033`, [link].
URL http://dx.doi.org/10.1007/JHEP11(2015)033

[13] J. Brod, M. Gorbahn, E. Stamou, PoS BEAUTY2020 (2021) 056. `arXiv:2105.02868`, `doi:10.22323/1.391.0056`.

[14] Y. Grossman, Y. Nir, Physics Letters B 398 (1) (1997) 163–168. `doi:https://doi.org/10.1016/S0370-2693(97)00210-4`, [link].
URL https://www.sciencedirect.com/science/article/pii/S0370269397002104

[15] W. J. Marciano, Z. Parsa, Phys. Rev. D 53 (1996) R1–R5. `doi:10.1103/PhysRevD.53.R1`, [link].
URL https://link.aps.org/doi/10.1103/PhysRevD.53.R1

[16] A. V. Artamonov *et al.*, Phys. Rev. D 79 (2009) 092004. `doi:10.1103/PhysRevD.79.092004`, [link].
URL https://link.aps.org/doi/10.1103/PhysRevD.79.092004

[17] E. Cortina Gil *et al.*, Journal of High Energy Physics 2025 (2). `doi:10.1007/jhep02(2025)191`, [link].
URL http://dx.doi.org/10.1007/JHEP02(2025)191

[18] A. J. Buras, D. Buttazzo, R. Knegjens, J. High Energy Phys. 2015 (166). `doi:10.1007/JHEP11(2015)166`, [link].
URL https://doi.org/10.1007/JHEP11(2015)166

[19] A. J. Buras, J. Girrbach, Reports on Progress in Physics 77 (8) (2014) 086201. `doi:10.1088/0034-4885/77/8/086201`, [link].
URL https://dx.doi.org/10.1088/0034-4885/77/8/086201

[20] J. Aebischer, A. J. Buras, J. Kumar, J. High Energy Phys. 2020 (12). `doi:10.1007/jhep12(2020)097`, [link].
URL http://dx.doi.org/10.1007/JHEP12(2020)097

[21] G. D'Ambrosio *et al.*, Nuclear Physics B 645 (1) (2002) 155–187. `doi:https://doi.org/10.1016/S0550-3213(02)00836-2`, [link].
URL https://www.sciencedirect.com/science/article/pii/S0550321302008362

[22] C. Bobeth *et al.*, Nuclear Physics B 726 (1) (2005) 252–274. `doi:https://doi.org/10.1016/j.nuclphysb.2005.06.035`, [link].
URL https://www.sciencedirect.com/science/article/pii/S0550321305004931

[23] G. Isidori *et al.*, J. High Energy Phys. 2006 (08) (2006) 064. `doi:10.1088/1126-6708/2006/08/064`, [link].
URL https://dx.doi.org/10.1088/1126-6708/2006/08/064

[24] M. Blanke *et al.*, J. High Energy Phys. 2007 (01) (2007) 066. `doi:10.1088/1126-6708/2007/01/066`, [link].
URL https://dx.doi.org/10.1088/1126-6708/2007/01/066

[25] M. Blanke *et al.*, Acta Phys. Polon. B 41 (2010) 657–683. [link].
URL https://www.actaphys.uj.edu.pl/R/41/3/657/pdf

[26] M. Blanke, A. J. Buras, S. Recksiegel, Eur. Phys. J. C 76 (4). `doi:10.1140/epjc/s10052-016-4019-7`, [link].
URL http://dx.doi.org/10.1140/epjc/s10052-016-4019-7

[27] A. J. Buras, F. De Fazio, J. Girrbach, J. High Energy Phys. 2013 (2). `doi:10.1007/jhep02(2013)116`, [link].
URL http://dx.doi.org/10.1007/JHEP02(2013)116

[28] M. Blanke *et al.*, J. High Energy Phys. 2009 (03) (2009) 108. `doi:10.1088/1126-6708/2009/03/108`, [link].
URL https://dx.doi.org/10.1088/1126-6708/2009/03/108

[29] M. Tanimoto, K. Yamamoto, Prog. Theor. Exp. Phys. 2016 (12) (2016) 123B02. `doi:10.1093/ptep/ptw160`, [link].
URL http://dx.doi.org/10.1093/ptep/ptw160

[30] G. D' Ambrosio *et al.*, J. High Energy Phys. 2022 (9). `doi:10.1007/jhep09(2022)148`, [link].
URL http://dx.doi.org/10.1007/JHEP09(2022)148

[31] D. Marzocca, S. Trifinopoulos, E. Venturini, Eur. Phys. J. C 82 (4). `doi:10.1140/epjc/s10052-022-10271-7`, [link].
URL http://dx.doi.org/10.1140/epjc/s10052-022-10271-7

[32] C.-H. Chen, T. Nomura, Journal of High Energy Physics 2018 (8). `doi:10.1007/jhep08(2018)145`, [link].
URL http://dx.doi.org/10.1007/JHEP08(2018)145

[33] W.-S. Hou, G. Kumar, J. High Energy Phys. 2022 (10). `doi:10.1007/jhep10(2022)129`, [link].
URL http://dx.doi.org/10.1007/JHEP10(2022)129

[34] S. Kanemura, Y. Mura, J. High Energy Phys. 2023 (153). `doi:10.1007/JHEP09(2023)153~`, [link].
URL https://doi.org/10.1007/JHEP09(2023)153

[35] Reports on Progress in Physics 86 (1) (2023) 016201. `doi:10.1088/1361-6633/ac9cee`, [link].
URL https://dx.doi.org/10.1088/1361-6633/ac9cee

[36] X.-G. He *et al.*, J. High Energy Phys. 2020 (4). `doi:10.1007/jhep04(2020)057`, [link].
URL http://dx.doi.org/10.1007/JHEP04(2020)057

[37] X.-G. He *et al.*, J. High Energy Phys. 2020 (8). `doi:10.1007/jhep08(2020)034`, [link].
URL http://dx.doi.org/10.1007/JHEP08(2020)034

[38] R. Ziegler, J. Zupan, R. Zwicky, J. High Energy Phys. 2020 (7). `doi:10.1007/jhep07(2020)229`, [link].
URL http://dx.doi.org/10.1007/JHEP07(2020)229

[39] E. Cortina Gil *et al.*, J. High Energy Phys. 2021 (6). `doi:10.1007/jhep06(2021)093`, [link].
URL http://dx.doi.org/10.1007/JHEP06(2021)093

[40] K. Fuyuto, W.-S. Hou, M. Kohda, Phys. Rev. Lett. 114 (2015) 171802. `doi:10.1103/PhysRevLett.114.171802`, [link].
URL https://link.aps.org/doi/10.1103/PhysRevLett.114.171802

[41] K. Fuyuto, W.-S. Hou, M. Kohda, Phys. Rev. D 93 (2016) 054021. `doi:10.1103/PhysRevD.93.054021`, [link].
URL https://link.aps.org/doi/10.1103/PhysRevD.93.054021

[42] F. Jegerlehner, A. Nyffeler, Physics Reports 477 (1) (2009) 1–110. `doi:https://doi.org/10.1016/j.physrep.2009.04.003`, [link].
URL https://www.sciencedirect.com/science/article/pii/S0370157309001306

[43] T. Aoyama *et al.*, Physics Reports 887 (2020) 1–166, the anomalous magnetic moment of the muon in the Standard Model. `doi:https://doi.org/10.1016/j.physrep.2020.07.006`, [link].
URL https://www.sciencedirect.com/science/article/pii/S0370157320302556

[44] D. P. Aguillard *et al.*, Phys. Rev. Lett. 131 (2023) 161802. `doi:10.1103/PhysRevLett.131.161802`, [link].
URL https://link.aps.org/doi/10.1103/PhysRevLett.131.161802

[45] G. W. Bennett *et al.*, Phys. Rev. D 73 (2006) 072003. `doi:10.1103/PhysRevD.73.072003`, [link].
URL https://link.aps.org/doi/10.1103/PhysRevD.73.072003

[46] N. Collaboration, J. High Energy Phys. 2021 (58). `doi:https://doi.org/10.1007/JHEP03(2021)058`, [link].
URL https://doi.org/10.1007/JHEP03(2021)058

[47] T. Kitahara *et al.*, Phys. Rev. Lett. 124 (2020) 071801. `doi:10.1103/PhysRevLett.124.071801`, [link].
URL https://link.aps.org/doi/10.1103/PhysRevLett.124.071801

[48] C. Lin, PoS DISCRETE2020-2021 (2022) 069. `doi:10.22323/1.405.0069`, [link].
URL https://pos.sissa.it/405/069/

[49] C. Lin, Ph.D. thesis, National Taiwan University (2021). [link].
URL https://doi.org/10.6342/NTU202102308

[50] J. K. Ahn *et al.*, Phys. Rev. Lett. 122 (2019) 021802. `doi:10.1103/PhysRevLett.122.021802`, [link].
URL https://link.aps.org/doi/10.1103/PhysRevLett.122.021802

[51] E. Cortina Gil *et al.*, Journal of High Energy Physics 2021 (2). `doi:10.1007/jhep02(2021)201`, [link].
URL http://dx.doi.org/10.1007/JHEP02(2021)201

[52] L. S. Littenberg, Phys. Rev. D 39 (1989) 3322–3324. doi:10.1103/PhysRevD.39.3322, [link].
URL https://link.aps.org/doi/10.1103/PhysRevD.39.3322

[53] G. Graham *et al.*, Physics Letters B 295 (1) (1992) 169–173. doi:https://doi.org/10.1016/0370-2693(92)90107-F, [link].
URL https://www.sciencedirect.com/science/article/pii/037026939290107F

[54] M. Weaver *et al.*, Phys. Rev. Lett. 72 (1994) 3758–3761. doi:10.1103/PhysRevLett.72.3758, [link].
URL https://link.aps.org/doi/10.1103/PhysRevLett.72.3758

[55] J. Adams *et al.*, Physics Letters B 447 (3) (1999) 240–245. doi:https://doi.org/10.1016/S0370-2693(98)01593-7, [link].
URL https://www.sciencedirect.com/science/article/pii/S0370269398015937

[56] A. Alavi-Harati *et al.*, Phys. Rev. D 61 (2000) 072006. doi:10.1103/PhysRevD.61.072006, [link].
URL https://link.aps.org/doi/10.1103/PhysRevD.61.072006

[57] J. K. Ahn *et al.*, Phys. Rev. D 74 (2006) 051105. doi:10.1103/PhysRevD.74.051105, [link].
URL https://link.aps.org/doi/10.1103/PhysRevD.74.051105

[58] J. K. Ahn *et al.*, Phys. Rev. Lett. 100 (2008) 201802. doi:10.1103/PhysRevLett.100.201802, [link].
URL https://link.aps.org/doi/10.1103/PhysRevLett.100.201802

[59] J. K. Ahn *et al.*, Phys. Rev. D 81 (2010) 072004. doi:10.1103/PhysRevD.81.072004, [link].
URL https://link.aps.org/doi/10.1103/PhysRevD.81.072004

[60] J. K. Ahn *et al.*, Prog. Theor. Exp. Phys. 2017 (2) (2017) 021C01. doi:10.1093/ptep/ptx001, [link].
URL https://doi.org/10.1093/ptep/ptx001

[61] J. K. Ahn *et al.*, Phys. Rev. Lett. 126 (2021) 121801. doi:10.1103/PhysRevLett.126.121801, [link].
URL https://link.aps.org/doi/10.1103/PhysRevLett.126.121801

[62] J. Comfort *et al.*, Proposal for $K_L \to \pi^0 \nu \overline{\nu}$ experiment at j-parc (2006).
URL http://j-parc.jp/researcher/Hadron/en/pac_0606/pdf/p14-Yamanaka.pdf

[63] S. Nagamiya, Prog. Theor. Exp. Phys. 2012 (1) (2012) 02B001. doi:10.1093/ptep/pts025, [link].
URL https://doi.org/10.1093/ptep/pts025

[64] J. K. Ahn *et al.*, Proposal of the koto ii experiment (2025). arXiv:2501.14827.
URL https://arxiv.org/abs/2501.14827

[65] J. K. Ahn *et al.*, Phys. Rev. Lett. 134 (2025) 081802. doi:10.1103/PhysRevLett.134.081802, [link].
URL https://link.aps.org/doi/10.1103/PhysRevLett.134.081802

[66] S. Shinohara, J. Phys. Conf. Ser. 1526 (1) (2020) 012002. doi:10.1088/1742-6596/1526/1/012002.

[67] T. Yamanaka, for the KOTO Collaboration, Prog. Theor. Exp. Phys. 2012 (1) (2012) 02B006. doi:10.1093/ptep/pts057, [link].
URL https://doi.org/10.1093/ptep/pts057

[68] Y. Maeda, Ph.D. thesis, Kyoto University (2016). [link].
URL https://www-he.scphys.kyoto-u.ac.jp/member/maeda_y/documents/dt_maeda_y.pdf

[69] S. Agostinelli *et al.*, Nuclear Instruments and Methods in Physics Research Section A: Accelerators, Spectrometers, Detectors and Associated Equipment 506 (3) (2003) 250–303. doi:https://doi.org/10.1016/S0168-9002(03)01368-8, [link].
URL https://www.sciencedirect.com/science/article/pii/S0168900203013688

[70] J. Allison *et al.*, IEEE Transactions on Nuclear Science 53 (1) (2006) 270–278. doi:10.1109/TNS.2006.869826.

[71] J. Allison *et al.*, Nuclear Instruments and Methods in Physics Research Section A: Accelerators, Spectrometers, Detectors and Associated Equipment 835 (2016) 186–225. doi:https://doi.org/10.1016/j.nima.2016.06.125, [link].
URL https://www.sciencedirect.com/science/article/pii/S0168900216306957

[72] M. Ikegami, Prog. Theor. Exp. Phys. 2012 (1) (2012) 02B002. doi:10.1093/ptep/pts019, [link].
URL https://doi.org/10.1093/ptep/pts019

[73] K. Hasegawa, in: Proc. LINAC'14, no. 27 in Linear Accelerator Conference, JACoW Publishing, Geneva, Switzerland, 2014, pp. 417–422. [link].
URL https://jacow.org/LINAC2014/papers/TUIOB03.pdf

[74] H. Hotchi *et al.*, Prog. Theor. Exp. Phys. 2012 (1) (2012) 02B003. doi:10.1093/ptep/pts021, [link].
URL https://doi.org/10.1093/ptep/pts021

[75] T. Koseki *et al.*, Prog. Theor. Exp. Phys. 2012 (1) (2012) 02B004. doi:10.1093/ptep/pts071, [link].
URL https://doi.org/10.1093/ptep/pts071

[76] K. Agari *et al.*, Prog. Theor. Exp. Phys. 2012 (1) (2012) 02B008. doi:10.1093/ptep/pts034, [link].
URL https://doi.org/10.1093/ptep/pts034

[77] H. Takahashi *et al.*, J. Radioanal. Nucl. Chem. 305. doi:10.1007/s10967-015-3940-9, [link].
URL https://doi.org/10.1007/s10967-015-3940-9

[78] M. Saito *et al.*, Phys. Rev. Accel. Beams 25 (2022) 063001. doi:10.1103/PhysRevAccelBeams.25.063001, [link].
URL https://link.aps.org/doi/10.1103/PhysRevAccelBeams.25.063001

[79] H. Ohnishi, F. Sakuma, T. Takahashi, Prog. Part. Nucl. Phys. 113 (2020) 103773. `doi:https://doi.org/10.1016/j.ppnp.2020.103773`, [link].
URL https://www.sciencedirect.com/science/article/pii/S014664102030020X

[80] T. Shimogawa, Nucl. Instrum. Methods Phys. Res., Sect. A 623 (1) (2010) 585–587. `doi:https://doi.org/10.1016/j.nima.2010.03.078`, [link].
URL https://www.sciencedirect.com/science/article/pii/S016890021000642X

[81] K. Sato, Ph.D. thesis, Osaka University (2015). [link].
URL https://osksn2.hep.sci.osaka-u.ac.jp/theses/doctor/2015/dt_sato.pdf

[82] T. Masuda et al., Prog. Theor. Exp. Phys. 2016 (2016) 013C03. `doi:10.1093/ptep/ptv171`, [link].
URL http://dx.doi.org/10.1093/ptep/ptv171

[83] K. Nakagiri, Ph.D. thesis, Kyoto University (2019). [link].
URL https://www-he.scphys.kyoto-u.ac.jp/theses/doctor/nakagiri_dt.pdf

[84] T. Matsumura *et al.*, Nucl. Instrum. Methods Phys. Res., Sect. A 885 (2018) 91–97. `doi:https://doi.org/10.1016/j.nima.2017.12.019`, [link].
URL https://www.sciencedirect.com/science/article/pii/S0168900217313736

[85] K. Sato *et al.*, Nucl. Instrum. Methods Phys. Res., Sect. A 982 (2020) 164527. `doi:https://doi.org/10.1016/j.nima.2020.164527`, [link].
URL https://www.sciencedirect.com/science/article/pii/S0168900220309244

[86] A. Alavi-Harati *et al.*, Phys. Rev. D 67 (2003) 012005. `doi:10.1103/PhysRevD.67.012005`, [link].
URL https://link.aps.org/doi/10.1103/PhysRevD.67.012005

[87] M. Osugi, Journal of Instrumentation 15 (05) (2020) C05067. `doi:10.1088/1748-0221/15/05/C05067`, [link].
URL https://dx.doi.org/10.1088/1748-0221/15/05/C05067

[88] N. Shimizu, for the KOTO collaboration, Journal of Physics: Conference Series 1162 (1) (2019) 012030. `doi:10.1088/1742-6596/1162/1/012030`, [link].
URL https://dx.doi.org/10.1088/1742-6596/1162/1/012030

[89] K. Kotera, Journal of Physics: Conference Series 2446 (1) (2023) 012043. `doi:10.1088/1742-6596/2446/1/012043`, [link].
URL https://dx.doi.org/10.1088/1742-6596/2446/1/012043

[90] H. Nishimiya, Master's thesis, Osaka University, (in Japanese) (2018). [link].
URL https://osksn2.hep.sci.osaka-u.ac.jp/theses/master/2017/Nishimiya_MT_Final.pdf

[91] Y. Sato, Master's thesis, Osaka University, (in Japanese) (2018). [link].
URL https://osksn2.hep.sci.osaka-u.ac.jp/theses/master/2017/yutasato_mthesis.pdf

[92] T. Mari, Master's thesis, Osaka University, (in Japanese) (2019). [link].
URL https://osksn2.hep.sci.osaka-u.ac.jp/theses/master/2018/mari_mthesis.pdf

[93] N. Hara, Master's thesis, Osaka University, (in Japanese) (2019). [link].
URL https://osksn2.hep.sci.osaka-u.ac.jp/theses/master/2018/haranobu_mthesis_final.pdf

[94] M. Osugi, Master's thesis, Osaka University, (in Japanese) (2020). [link].
URL https://osksn2.hep.sci.osaka-u.ac.jp/theses/master/2019/MasterThesis2019_Osugi.pdf

[95] K. Kotera, PoS ICHEP2018 (2019) 593. `doi:10.22323/1.340.0593`, [link].
URL https://doi.org/10.22323/1.340.0593

[96] Kuraray Co., Ltd. [link].
URL https://www.kuraray.com

[97] HAMAMATSU PHOTONICS K.K. [link].
URL https://www.hamamatsu.com/us/en.html

[98] T. C. Nunes, Master's thesis, Osaka University (2021). [link].
URL https://osksn2.hep.sci.osaka-u.ac.jp/theses/master/2021/MasterThesis2021_Taylor.pdf

[99] R. Shiraishi, Master's thesis, Osaka University, (in Japanese) (2021). [link].
URL https://osksn2.hep.sci.osaka-u.ac.jp/theses/master/2020/MasterThesis2020_Shiraishi.pdf

[100] R. Shiraishi, Journal of Physics: Conference Series 2446 (1) (2023) 012051. `doi:10.1088/1742-6596/2446/1/012051`, [link].
URL https://dx.doi.org/10.1088/1742-6596/2446/1/012051

[101] Y. Tajima *et al.*, Nucl. Instrum. Methods Phys. Res., Sect. A 592 (3) (2008) 261–272. `doi:https://doi.org/10.1016/j.nima.2008.04.080`, [link].
URL https://www.sciencedirect.com/science/article/pii/S0168900208006505

[102] N. Kawasaki, PoS KAON13 (2013) 040. `doi:10.22323/1.181.0040`, [link].
URL https://doi.org/10.22323/1.181.0040

[103] N. Kawaski, Master's thesis, Kyoto University, (in Japanese) (2009). [link].
URL https://www-he.scphys.kyoto-u.ac.jp/theses/master/kawasaki_mt.pdf

[104] S. Seki, Master's thesis, Kyoto University, (in Japanese) (2013). [link].
URL https://www-he.scphys.kyoto-u.ac.jp/theses/master/seki_mt.pdf

[105] S. Shinohara, Ph.D. thesis, Kyoto University (2021). [link].
URL https://www-he.scphys.kyoto-u.ac.jp/theses/doctor/dt_shinohara.pdf

[106] T. Hineno, Master's thesis, Kyoto University, (in Japanese) (2014). [link].
URL https://www-he.scphys.kyoto-u.ac.jp/theses/master/hineno_mt.pdf

[107] R. Murayama *et al.*, Nucl. Instrum. Methods Phys. Res., Sect. A 953 (2020) 163255. `doi:https://doi.org/10.1016/j.nima.2019.163255`, [link].
URL https://www.sciencedirect.com/science/article/pii/S0168900219315268

[108] R. Murayama, Ph.D. thesis, Osaka University (2017). [link].
URL https://osksn2.hep.sci.osaka-u.ac.jp/theses/doctor/2017/dt_murayama.pdf

[109] D. Naito *et al.*, Prog. Theor. Exp. Phys. 2016 (2) (2016) 023C01. `doi:10.1093/ptep/ptv191`, [link].
URL https://doi.org/10.1093/ptep/ptv191

[110] D. Naito, Ph.D. thesis, Kyoto University (2016). [link].
URL https://www-he.scphys.kyoto-u.ac.jp/theses/doctor/dt_naito.pdf

[111] T. Matsumura *et al.*, Nucl. Instrum. Methods Phys. Res., Sect. A 795 (2015) 19–31. `doi:https://doi.org/10.1016/j.nima.2015.05.036`, [link].
URL https://www.sciencedirect.com/science/article/pii/S0168900215006762

[112] H. M. Kim, for the KOTO Collaboration, Journal of Physics: Conference Series 1526 (1) (2020) 012032. `doi:10.1088/1742-6596/1526/1/012032`, [link].
URL https://dx.doi.org/10.1088/1742-6596/1526/1/012032

[113] K. Miyazaki, Master's thesis, Osaka University, (in Japanese) (2016). [link].
URL https://osksn2.hep.sci.osaka-u.ac.jp/theses/master/2015/miyazaki_mthesis.pdf

[114] H. Kim, Master's thesis, Jeounbuk National University, (in Korean) (2020).

[115] K. Nakagiri, PoS FPCP2015 (2015) 081. `doi:10.22323/1.248.0081`, [link].
URL https://pos.sissa.it/248/081

[116] I. Kamiji, K. Nakagiri, Journal of Physics: Conference Series 800 (1) (2017) 012041. `doi:10.1088/1742-6596/800/1/012041`, [link].
URL https://dx.doi.org/10.1088/1742-6596/800/1/012041

[117] I. Kamiji, Ph.D. thesis, Kyoto University, (in Japanese) (2020). [link].
URL https://www-he.scphys.kyoto-u.ac.jp/theses/doctor/kamiji_dt.pdf

[118] Y. Maeda *et al.*, Prog. Theor. Exp. Phys. 2015 (6) (2015) 063H01. `doi:10.1093/ptep/ptv074`, [link].
URL https://doi.org/10.1093/ptep/ptv074

[119] S. Shinohara, PoS FPCP2015 (2015) 079. `doi:10.22323/1.248.0079`, [link].
URL https://pos.sissa.it/248/079

[120] S. Shinohara, Journal of Physics: Conference Series 800 (1) (2017) 012044. `doi:10.1088/1742-6596/800/1/012044`, [link].
URL https://dx.doi.org/10.1088/1742-6596/800/1/012044

[121] Y. Sugiyama *et al.*, IEEE Transactions on Nuclear Science 62 (3) (2015) 1115–1121. `doi:10.1109/TNS.2015.2417312`.

[122] S. Su *et al.*, IEEE Transactions on Nuclear Science 64 (6) (2017) 1338–1345. `doi:10.1109/TNS.2017.2694040`.

[123] C. Lin *et al.*, Journal of Physics: Conference Series 1526 (1) (2020) 012034. `doi:10.1088/1742-6596/1526/1/012034`, [link].
URL https://dx.doi.org/10.1088/1742-6596/1526/1/012034

[124] M. Bogdan, J.-F. Genat, Y. Wah, in: 2010 17th IEEE-NPSS Real Time Conference, 2010, pp. 1–2. doi:10.1109/RTC.2010.5750452.

[125] M. Bogdan, J.-F. Genat, Y. Wah, in: 2009 16th IEEE-NPSS Real Time Conference, 2009, pp. 443–445. doi:10.1109/RTC.2009.5321611.

[126] R. Muto, in: Proc. IPAC'24, no. 15 in IPAC'24 - 15th International Particle Accelerator Conference, JACoW Publishing, Geneva, Switzerland, 2024, pp. 1905–1910. doi:10.18429/JACoW-IPAC2024-WEYD1, [link].
URL https://accelconf.web.cern.ch/ipac2024/pdf/WEYD1.pdf

[127] T. Masuda, Ph.D. thesis, Kyoto University (2014). [link].
URL https://www-he.scphys.kyoto-u.ac.jp/theses/doctor/taka_dt.pdf

[128] Y. Noichi, Master's thesis, Osaka University, (in Japanese) (2021). [link].
URL https://osksn2.hep.sci.osaka-u.ac.jp/theses/master/2020/MasterThesis2020_Noichi.pdf

[129] A. Hoecker *et al*. (2009). arXiv:physics/0703039, [link].
URL https://arxiv.org/abs/physics/0703039

[130] R. A. Fisher, Annals Eugen. 7 (1936) 179–188. doi:10.1111/j.1469-1809.1936.tb02137.x.

[131] Y.-C. Tung *et al*., Nucl. Instrum. Methods Phys. Res., Sect. A 1059 (2024) 169010. doi:https://doi.org/10.1016/j.nima.2023.169010, [link].
URL https://www.sciencedirect.com/science/article/pii/S0168900223010100

[132] R. D. Cousins, V. L. Highland, Nucl. Instrum. Methods Phys. Res., Sect. A 320 (1) (1992) 331–335. doi:https://doi.org/10.1016/0168-9002(92)90794-5, [link].
URL https://www.sciencedirect.com/science/article/pii/0168900292907945

[133] G. J. Feldman, R. D. Cousins, Phys. Rev. D 57 (1998) 3873–3889. doi:10.1103/PhysRevD.57.3873, [link].
URL https://link.aps.org/doi/10.1103/PhysRevD.57.3873

[134] K. Ono, In-beam charged particle detector using 0.2-mm thick plastic scintillator for the J-PARC KOTO experiment, PoS ICHEP2024 (2025) 969. doi:10.22323/1.476.0969.

[135] K. Taishi, Master's thesis, Osaka University, (in Japanese) (2022). [link].
URL https://osksn2.hep.sci.osaka-u.ac.jp/theses/master/2021/MasterThesis2021_Kato.pdf

[136] M. Gonzalez, The Data-Acquisition System and new GPU-based HLT of the KOTO Experiment, PoS ICHEP2024 (2025) 1009. doi:10.22323/1.476.1009.

[137] M. G. Carpintero, Ph.D. thesis, Osaka University (2024). [link].
URL https://osksn2.hep.sci.osaka-u.ac.jp/theses/doctor/2024/DoctorThesis2024_Mario.pdf